Fabrication and Characterization of Multilayers for Focusing Hard X-Ray Optics

by

Adrian Ivan

M.S. Physics
University of Bucharest, Romania

SUBMITTED TO THE DEPARTMENT OF NUCLEAR ENGINEERING
IN PARTIAL FULFILLMENT OF THE REQUIREMENTS FOR THE DEGREE OF

DOCTOR OF PHILOSOPHY IN NUCLEAR ENGINEERING
AT THE
MASSACHUSETTS INSTITUTE OF TECHNOLOGY

JUNE 2002

©2002 Massachusetts Institute of Technology. All rights reserved

Signature of Author: _____
Department of Nuclear Engineering
February 27, 2002

Certified by: _____
Suzanne Romaine
Harvard-Smithsonian Astrophysical Observatory
Thesis Supervisor

Certified by: _____
Sow-Hsin Chen
Professor of Nuclear Engineering
Chairman of Thesis Committee and MIT Supervisor

Certified by: _____
Paul Gorenstein
Harvard-Smithsonian Astrophysical Observatory
Thesis Reader

Accepted by: _____
Jeffrey A. Coderre
Associate Professor of Nuclear Engineering
Chairman, Department Committee on Graduate Students

MASSACHUSETTS INSTITUTE OF TECHNOLOGY
DEC 0 5 2003
LIBRARIES

ARCHIVES

FABRICATION AND CHARACTERIZATION OF MULTILAYERS FOR FOCUSING HARD X-RAY OPTICS

by

Adrian Ivan

Submitted to the Department of Nuclear Engineering,
Massachusetts Institute of Technology on February 27, 2002,
in partial fulfillment of the requirements for
the Degree of Doctor in Philosophy in Nuclear Engineering

Abstract

This study investigated the growth of multilayers with depth-graded thicknesses and their performance as x-ray mirrors for the next generation of focusing telescopes. Different material combinations were studied for the first time employing a consistent methodology for the DC magnetron sputtering growth of the multilayers and their characterization by x-ray reflectivity (XRR) measurements. The width of the interfaces was identified as the most important factor that must be controlled and minimized to achieve high reflectivity. The optimization of the process parameters led to interface widths (σ) of 3.0-4.5 Å for both W/Si and Pt/C, the most interesting materials for this application. The other material combinations studied were: W/C, Mo/Si, Ni/C, Ni-V/C, WSi_2/Si, and Nb/Si. The interface widths for W/C were about 4 Å, but wider ($\sigma \geq 7$ Å) for Mo/Si and Ni/C. The analysis indicated that the large Mo/Si interface width was due to the formation of a silicide compound. In the case of Ni/C, TEM and XRR measurements concurred to an island growth mode of nickel for thicknesses less than 17 Å, resulting in a high roughness at the C-on-Ni interface. A trial with WSi_2/Si multilayers showed values of σ comparable to the simpler W/Si system. For Nb/Si the interface widths were larger than 9 Å.

Depth graded W/Si, Pt/C, and W/C multilayers were deposited on flat substrates in process conditions optimized for low σ (3-5 Å). Their x-ray reflectivity was measured at high energy using synchrotron radiation sources and confirmed the designs for the structure of the multilayers and the reflection bandpass. The reflectivity was between 20 and 40 % for grazing incidence angles used in hard x-ray focusing telescopes.

One of the deposition chambers built for this study has the unique capability to coat with multilayers the inside of integral conical shells that compose the telescope mirror system. We have accomplished for the first time this type of coatings and present results from their x-ray measurements.

Advisor: Dr. Suzanne E. Romaine
Harvard-Smithsonian Astrophysical Observatory
60 Garden St., Cambridge, MA 02138

Acknowledgments

I am first and foremost thankful to my advisor, Dr. Suzanne Romaine, for giving me the opportunity to work in a new field and constantly offering directions all these years, starting with the installation of the first sputtering cathode at the Multilayer Facility and ending with the final revision of this thesis. Together with Dr. Paul Gorenstein, Suzanne managed every year to come up with resources to support my off-campus work at SAO. I am grateful to both of them also for funding my travel to conferences and to visit other research institutes, as they all had an impact on my professional development. Much of these resources were made available by support from NASA grants NAG 5-5095, NAG8-1194, and NSG-5138.

Even more important to me was the coherence of the small team to which I belonged for five years and the direct assistance that I have received from them along the way. Many thanks to Suzanne for sharing with me her expertise in the field of thin films and her guidance in such unique challenging project. Her presence in the lab made a difference in overcoming the countless problems that can occur in an experimental endeavor and helped us stay focused on goals. At the same time, she allowed me to explore new directions for my research and gave me the resolution to do so. Dr. Paul Gorenstein was an invaluable source of information related to x-ray astrophysics and always gave a fresh perspective in his thought-provoking questions. I appreciate the friendly discussions we have had in our lab and his guidance in collaborating with other groups. Ric Bruni was by far the best colleague I have ever had: always encouraging, cheerful, and open, he was a sounding board for my ideas at work and also a good friend. I cannot express enough gratitude for the numerous occasions when he sacrificed his time to help me solve a problem or for making the time spent in a noisy lab quite enjoyable. To these three "core members" of my group at SAO, my heartfelt gratitude for your assistance and patience shown all these years.

Many others that joined our group for a while during my research are also acknowledged. I am indebted to John Everett for his mastery of programming in IDL and CVI and his trusted program still running one of the deposition chambers. Special thanks go also to Scott Sanders for his software contribution and to Jason St.John for help with setting up our own x-ray reflectometer. Kyung Byun performed many AFM analyses and participated in two of the measurement sessions at Brookhaven. Last, but not least, I am indebted to Brad Cenko for his help with x-ray reflectivity measurements, both at SAO and at Brookhaven.

I am also grateful to the MIT members of my thesis committee for helping me stay focused on my project and for the feedback provided every semester in the committee meetings. Professor Sow-Hsin Chen graciously accepted to serve as the MIT-side supervisor after the leave of Professor Xiao-Lin Zhou. He was of inestimable help in interfacing with the department while I was carrying out my research off campus. I am indebted to Dr. Kathryn Flanagan for the encouragement shown from the beginning of my thesis program and the shared enthusiasm for the progress of x-ray astrophysics.

Some of this work depended essentially on collaboration with other institutions and I would like to extend my thanks to a group of people that were instrumental in achieving important goals.

I am grateful to Prof. Oberto Citterio and Dr. Giovanni Pareschi at Brera Observatory, Italy, for supplying the replicated shells and flats that were used as substrates for multilayers, as well as for offering to share beam time at the ESRF synchrotron. The long-standing collaboration between our labs is bound to continue in the future.

During his visit at SAO, Dr. Finn Christensen (Danish Space Research Institute) assisted directly with setting up the first version of the reflectometer. He was helpful in acquiring slumped glass foils and float glass substrates that were coated with multilayers in our facility. More important, he was also available for discussions related to x-ray telescopes. Ahsen Hussain (DSRI) spent some time in our lab at the beginning stage of the

development of our prototype production chamber. He helped with the first coating of a multilayer on an integral cylindrical surface at SAO and measured its x-ray reflectivity at DSRI.

I am also personally indebted to several x-ray groups for allowing me to conduct x-ray reflectivity measurements using their facilities before we had set up our own reflectometer. Foremost, I thank Prof. Carl Ludwig (BU) not only for the beam time on his diffractometer but also for his suggestions for the design of the reflectometer. I am also grateful for having the opportunity to do x-ray measurements in the lab led by Prof. Peter Pershan at Harvard University.

Other important material characterizations (AFM, profilometry, and TEM) have been performed at the MIT Center for Material Science and Engineering and I would like to thank Libby Shaw, Tim McClure, and Mike Frongillo, for their patience during my training and their continual support along the years.

Some of the most significant results for this work were obtained last year on the X17B1 beamline of the National Synchrotron Light Source at Brookhaven. They would have not been possible without the skills of Dr. Zhong Zhong, who helped setting up the experiment. I have to thank again the members of the SAO team led by Dr. Suzanne Romaine: Ric Bruni, Brad Cenko, and Kyung Byun. We have worked together in long shifts to make sure that we use 100% of the precious little beam time available.

Besides the financial and technical support, I am also indebted to many other people that worked in the background, both at MIT and at SAO. Thanks to Larry Knowles and the Harvard Model Shop, the machining of new parts or the replacement of broken ones was less of a problem. The administrative staff at SAO was very supportive and I would like to thank all of them for the help with my "dual status". On the MIT side, I am grateful to Clare Egan and Jennifer Gwinn-DeVries, as well as to others that helped me to transcend this problem every year.

I consider myself fortunate to be able to accomplish this project with the patient support of my wife Valeria, who sacrificed much so that I could go to graduate school. I am also grateful to her and my son for showing me that there is more to life than work.
I am indebted to my parents for the educational support they had offered to me and I would like to dedicate this work to their memory.

Table of Contents

ACKNOWLEDGMENTS **5**

PREFACE **13**

Motivation *13*
Goals *16*
Methods *17*
Thesis organization *17*

CHAPTER 1: ASTROPHYSICS IN THE HARD X-RAY BAND **20**

1.1 X-RAY PROCESSES IN ASTROPHYSICS 21
1.1.1 Bremsstrahlung *21*
1.1.2 Synchrotron radiation *22*
1.1.3 Compton scattering *24*
1.1.4 Inverse Compton scattering *25*
1.2 ASTROPHYSICAL OBJECTIVES IN THE HARD X-RAY BAND 26
1.2.1 The x-ray background *26*
1.2.2 Clusters of galaxies *26*
1.2.3 Supernovae (SN) and supernovae remnants *26*
1.2.4 Unidentified sources *27*
1.2.5 Quasars *27*
1.2.6 Neutron stars *28*
1.2.7 White dwarfs *28*
1.2.8 Seyfert galaxies *28*
1.3 X-RAY ORBITING TELESCOPE MISSIONS 28
1.3.1 The first decade *28*
1.3.2 The Einstein Observatory *29*
1.3.3 The specialized missions *30*
1.3.4 The latest missions *31*
1.3.5 The next generation of missions *34*
1.4 X-RAY TELESCOPE MIRRORS 36
1.4.1 Wolter Type I telescopes *36*
1.4.2 Performance of hard x-ray telescopes for future missions *38*
REFERENCES FOR CHAPTER 1 40

CHAPTER 2: X-RAY REFLECTIVITY OF MULTILAYERS **41**

2.1 X-RAY REFLECTIVITY: THEORETICAL PRELIMINARIES 42
2.2 FRESNEL REFLECTIVITY 44
2.3 THE PENETRATION DEPTH 47
2.4 X-RAY REFLECTIVITY IN STRATIFIED MEDIA 49
2.4.1 Reflectivity of a flat substrate *52*
2.4.2 Reflectivity from a single layer on a substrate *53*
2.5 KINEMATICAL THEORY 54
2.6 THE TREATMENT OF ROUGHNESS IN SPECULAR REFLECTIVITY 57

2.7 THE FIRST BORN APPROXIMATION 61
2.8 DISTORTED WAVE BORN APPROXIMATION 63
2.9 THE SCATTERED INTENSITY 63
2.10 EXPERIMENTAL STUDY OF X-RAY REFLECTION 64
2.10.1 Resolution 67
2.10.2 Data normalization 67
2.10.3 Footprint correction 67
2.10.4 Correction for time variations 69
2.10.5 Background corrections 69
2.10.6 The deadtime correction 69
2.10.7 Computation of the specular reflectivity of multilayered structures 70
2.10.8 The x-ray reflectometer setup 72
2.10.9 Sample alignment 75
REFERENCES FOR CHAPTER 2 77

CHAPTER 3: SPUTTERING DEPOSITION 78

3.1 PHYSICS OF SPUTTERING 78
3.1.1 General aspects of sputtering 78
3.1.2 The SRIM simulation code 80
3.1.3 Sputter yield dependence 81
3.1.4 Energy and angular distribution of sputtered atoms 83
3.1.5 Other energetic processes during sputtering 84
3.2 MAGNETRON DC SPUTTERING 88
3.2.1 DC diode sputtering 88
3.2.2 RF diode sputtering 89
3.2.3 Magnetron sputtering systems 90
3.3 DESCRIPTION OF DEPOSITION SYSTEMS 93
3.3.1 R&D sputtering system 93
3.3.2 The prototype coating system 95
3.4 NUCLEATION AND GROWTH OF THIN FILMS 99
3.4.1 Crystalline growth on surfaces 100
3.4.2 Nucleation and cluster formation 101
3.4.3 Zone models for evaporated and sputtered films 103
3.4.4 Influence of energetic atoms on the growth surface morphology 104
REFERENCES FOR CHAPTER 3 108

CHAPTER 4: STUDIES OF DIFFERENT MATERIAL SYSTEMS FOR HARD X-RAY MULTILAYERS 109

4.1 W/SI MULTILAYERS 110
4.1.1 X-ray optical constants for W/Si 111
4.1.2 Surface morphology of W single layers 112
4.1.3 Surface morphology of Si single layers 115
4.1.4 Thermodynamical properties of the W/Si system 118
4.1.5 W/Si multilayers in literature 118
4.1.6 Thickness control for W/Si multilayers 120
4.1.7 Minimum period for W/Si multilayers 122
4.1.8 The W thickness fraction γ and the interface widths in W/Si 124
4.1.9 Optimization of the deposition process using the Taguchi approach 126
4.2 WSi_2/SI MULTILAYERS 130
4.2.1 X-ray optical constants for WSi_2/Si 131
4.2.2 Interface widths of WSi_2/Si multilayers 132
4.3 W/C MULTILAYERS 136
4.3.1 X-ray optical constants for W/C 136

4.3.2 Surface morphology of C single layers *137*
4.3.3 Thermodynamical properties of the W/C system *138*
4.3.4 Magnetron sputtered carbon and W/C multilayers in literature *140*
4.3.5 Interface width in W/C multilayers *142*
4.4 Pt/C multilayers 142
4.4.1 X-ray optical constants *143*
4.4.2 Surface morphology of Pt single layers *143*
4.4.3 Pt single layers and Pt/C multilayers in literature *146*
4.4.4 Thickness calibration for Pt/C multilayers *148*
4.4.5 Minimum period of Pt/C multilayers *149*
4.4.6 Optimization of the interface width using a Taguchi experiment *151*
4.5 Mo/Si multilayers 155
4.5.1 X-ray optical constants for Mo/Si *155*
4.5.2 Surface morphology of Mo single layers *156*
4.5.3 Molybdenum films and Mo/Si multilayers in literature *157*
4.5.4 Constant period Mo/Si multilayers and interface widths *160*
4.6 Nb/Si multilayers 163
4.6.1 Nb/Si multilayers in literature *163*
4.6.2 Nb/Si interface widths for constant period multilayers *164*
4.7 Ni/C multilayers 166
4.7.1 X-ray optical constants for Ni/C *166*
4.7.2 Ni/C multilayers in literature *166*
4.7.3 Surface morphology of Ni layers *171*
4.7.4 Minimum period of Ni/C multilayers *172*
References for Chapter 4 174

CHAPTER 5: X-RAY REFLECTIVITY MEASUREMENTS AT HIGH ENERGIES 179

5.1 Reflectivity setup for high energy measurements 179
5.1.1 The X-ray source and beamline layout *179*
5.1.2 Sample motion *180*
5.1.3 Detectors *181*
5.2 Data acquisition and normalization 182
5.3 Measurement of a calibration sample 185
5.4 Depth graded multilayers design 186
5.5 W/Si graded multilayers 189
5.6 Pt/C graded multilayers 195
5.7 W/C graded multilayers 196
5.8 Conclusions 197
References for Chapter 5 199

CHAPTER 6: COATINGS OF SEGMENTED AND INTEGRAL OPTICS 201

6.1 First multilayer coating inside an integral cylinder 201
6.2 Periodic W/Si multilayer coating inside an integral glass cylinder 202
6.3 Depth graded W/Si multilayer coating inside an integral glass cylinder 204
6.4 W/Si multilayer coatings of thermally slumped glass foils 205
6.5 Multilayer coatings on replicated substrates 211
6.5.1 Integral replicated shells *211*
6.5.2 W/Si multilayer coatings on flat replicas *214*
6.5.3 W/Si multilayer coatings on nickel replicated shells *215*
6.5.4 Replicated nickel alloy shells *222*
6.6 Conclusions 223
References for Chapter 6 224

CONCLUSIONS 226

APPENDIX A: DERIVATION OF THE FRESNEL COEFFICIENTS 230

APPENDIX B: EXAMPLES OF X-RAY REFLECTIVITY SCANS 234

APPENDIX C: PROCEEDINGS PAPERS 241

Preface

Motivation

At the time of this writing, a series of major discoveries regarding the structure of our galaxy and the Universe are reported at a rapid pace in the astrophysics community[1]. With an impact that one can only estimate as immense for our understanding of the evolution of stars, galaxies, and clusters of galaxies, these findings are based on high-resolution observations in the x-ray band up to 10 keV by imaging telescopes in orbit around the Earth. Two telescope missions are at the forefront of the new discoveries: the NASA Chandra X-Ray Observatory and the European mission XMM-Newton. They were both launched in 1999 and are currently at the peak of their observational stage. The common characteristic of the two missions is their ability to focus x-rays from astrophysical objects onto the focal plane where detectors can acquire and form an image with an angular resolution of arcseconds and a high signal-to-noise ratio. In addition, diffraction gratings add spectroscopic capabilities to the observations.

The mirror system is fundamental in obtaining the x-ray image and for both telescopes it was based on state-of-the-art technologies for preparing atomically smooth substrates and coating them with a metal layer[2]. The focusing of the x-rays is achieved by total external reflection from the metal coating at grazing angles smaller than the critical angle for reflection. Because the critical angle varies inversely proportional with the energy of the x-ray photon, even the best reflector materials have prohibitively low reflectivity[3] above 10

[1] 199th Meeting of the American Astronomical Society, Washington, DC, Jan. 6-10, 2002
[2] Iridium was used for Chandra and gold for XMM-Newton.
[3] For example, at 20 keV the reflectivity of iridium is only 1% at 0.4°, even with a perfectly smooth surface.

keV at reasonable values for the grazing angles. The mirrors based on total external reflection by a layer of metal are thus limited to imaging only in the soft x-ray band.

As it will be described in Section 1.2, the astrophysical objectives in the band above 10 keV ("hard x-rays") demand observational capability with sub-arcminute angular resolution and sensitivity comparable to the soft x-ray telescopes. It is not possible to satisfy these requirements with coded-aperture telescope designs due to poor signal-to-noise ratio in large detectors. Also, the current single-layer mirror designs cannot be extended into the hard x-ray band for two major reasons related to the smallness of the critical angles at high energies:

- extremely shallow grazing angles require focal distances in excess of 10 m and are incompatible with current spacecraft architectures.
- the area projected by the mirrors onto a plane perpendicular to the telescope optical axis is very small, thus a single layer coating mirror system would be much heavier and more costly to launch than a multilayer coated mirror with equal effective area.

The solution is to extend the bandwidth of the mirrors by using Bragg-reflection instead of total external reflection. For a spatially periodic structure with a period d, strong reflections occur at incidence angles θ_B which satisfy the Bragg relation:

$$2d\sin\theta_B = m\lambda$$

where λ is the x-ray wavelength and m is the order of the reflection. Based on this relation, the periods needed to reflect (in first order) photons of 10 to 50 keV at a grazing angle of 0.4° would be 88.8 Å and 17.8 Å, respectively. They are too large for crystals, but multilayers with periods in this range can be deposited using existing technologies. The multilayers for hard x-ray telescopes are actually not periodic, but depth graded with the d spacing varying according to the relation above in order to cover the desired band of wavelengths (or equivalently, of energy).

Several projects of multilayer-based focusing x-ray telescopes (balloon-borne[4] or aboard orbiting satellites) are currently in different phases of design and development. Operating at energies above 10 keV, they will provide an improvement in sensitivity by orders of magnitude over non-focusing instruments while imaging with sub-arcminute resolution. Their science program is too vast to be completely described here, but a list of important objectives includes:

- study of hard x-ray emissions from quasars, close binary systems, and high magnetic fields around neutron stars.
- analysis of the diffuse hard x-ray background.
- identification of the positions of known gamma sources for which no optical or soft x-ray counterpart has been detected.
- testing the standard candle hypothesis for Type Ia supernovae to help determine absolute scales for cosmological distances.

Constellation-X is the next-generation NASA X-Ray Observatory[5]. A total of four satellites will be built with each incorporating one low-energy Spectroscopy X-Ray Telescope (SXT) as the major instrument and three confocal Hard X-Ray Telescopes (HXT) with $f = 10$ m to extend the imaging capability above 10 keV. The effective area of the HXT mirrors will be 1,500 cm^2 at 40 keV. The key technology of the HXT design is the use of multilayers for enhancing the broadband reflection above 10 keV. Currently, the Smithsonian Astrophysical Observatory (SAO) is participating in the research program for the HXT mirrors. The Multilayer Facility (described in Section 3.3) and the x-ray reflectometer (Section 2.10.8) were developed at SAO for this program.

The strong interest shown by the astrophysical community for developing the technology for the next generation of imaging x-ray telescopes was the main motivation for this work.

---

[4] Two balloon-borne missions have planned to use multilayer mirrors for the hard x-ray domain: InFOCμS (NASA/Goddard and Nagoya Univ.) was designed for the 20-40 keV band and HEFT (Caltech, Columbia Univ., and DSRI) will operate in the 20-70 keV band.

[5] NASA will make the announcement for opportunity in 2004. The first satellite will be launched not earlier than 2008.

The successful discoveries of the current missions (Chandra, XMM, and other) are without doubt due to the advanced instrumentation carried aboard. The unique instruments that allowed significant gains in performance, e.g., increased sensitivity, collecting area, or energetic resolution, were the result of bold new designs and years of prototype development and optimizations by collaborating teams from academia, research institutes, NASA, and industry. The same effort is currently pursued in several research directions for extending the energy bandwidth of the x-ray telescopes above 10 keV. As described above, multilayer coatings and Bragg reflection will replace the existing technology based on single metal layer coatings and total external reflection. Although multilayers provide the solution for the problem of increasing the reflectivity at high energies, there are many requirements specific to the application that demand a systematic investigation of the design, fabrication, and characterization of multilayers for x-ray mirrors[6].

Goals

The objective of this thesis was a comparative experimental study of different material combinations for multilayers and their reflectivity performance above the current limit of 10 keV for focusing x-ray telescopes and up to at least 70 keV. The long-range goal of the research was to contribute to the development of a new instrument for astrophysics, a hard x-ray focusing telescope with better angular resolution than the competing designs for the future NASA Constellation-X Mission, as well as other telescope missions. For this purpose, a second objective was to deposit and evaluate the reflectivity of multilayers on substrate materials for imaging telescopes, including closed cylindrical shells.

[6] Some of the results of this work are also relevant to fields outside of x-ray astronomy. Examples of applications using multilayers with a structure similar to those studied are neutron mirrors, XUV mirrors for "next generation lithography", synchrotron optics, medical x-ray imaging, and optics for laboratory x-ray sources.

Methods

The work for this thesis started with my participation in the design and construction of the SAO multilayer deposition facilities that are unique in their ability to accommodate large substrates of different geometries including closed cylindrical shells. For characterization of the thin film coatings, I have used the instruments available at the MIT Center for Material Science and Engineering for Atomic Force Microscopy (AFM) and profilometry. At the initial stage of my work, I have performed x-ray reflectivity measurements using the equipment of different x-ray diffraction groups in the area (MIT, Harvard Univ., Boston Univ.). Based on the experience gained, a dedicated reflectometer instrument was assembled at SAO and was used for all low-energy reflectivity scans described in this work. On the basis of these measurements, I have optimized the multilayer deposition parameters to achieve high reflectivity in the hard x-ray band and have tested the performance of selected samples using the high photon flux and the energy tuning capability of the X17B1 beam line at the Brookhaven National Laboratory.

Thesis organization

The following thesis material will present in detail the premises and the results of this work. The "Conclusions" section (p.226) will summarize the results, highlight the original accomplishments of the author, and discuss further perspectives of the topic. For a synopsis of this work, the reader can proceed directly to page 226.

Chapter 1 is an introduction to x-ray astrophysics with the aim to help the reader to understand the developments in this field. Section 1.1 is an overview of the basic x-ray processes in cosmic sources that are exemplified in Section 1.2 by presenting some of the objects of interest for astrophysics. A brief history of the x-ray orbiting telescope missions in Section 1.3 is followed by a discussion of the focusing x-ray telescopes and their mirror systems (Section 1.4).

Chapter 2 is essentially a comprehensive introduction to the subject of x-ray reflectivity for the interested reader. Sections 2.1-2.9 are entirely theoretical and build the foundation for understanding how the reflectivity of a multilayer can be calculated based on known structure parameters (thicknesses, densities, interface widths, and optical constants). These theoretical considerations are also important to understand the requirements for the design of an x-ray reflectometer and the procedures used for data acquisition and interpretation. For the benefit of the reader who wishes to skip the theory but still gain a practical understanding of the x-ray reflectivity scans, **Appendix B** offers examples of scans for different structures commonly encountered in this work (single layer, constant period multilayer, depth graded multilayers). Section 2.10 is addressing specifically the experimental side of x-ray reflectivity measurements and presents the operating procedures for sample alignment and data processing.

Chapter 3 describes the magnetron sputtering process and the coating facilities that have been developed at SAO and used in this work. Sections 3.1 and 3.2 present the physical processes involved in sputtering. The deposition chambers are described in Section 3.3. The relation between the process conditions and the growth and structure of thin films is discussed in general terms in Section 3.4 and will be addressed for specific materials in Chapter 4.

Chapter 4 presents an original investigation of different multilayer material combinations proposed for hard x-ray mirrors. Their performance as reflectors in this energy range was studied for the first time by using a consistent methodology for their growth and characterization. The width of the interfaces[7] in the multilayer is recognized as the most important factor that must be controlled and minimized to achieve high reflectivity. The relation between reflectivity and the interface width σ is given by the exponential Debye-Waller factor in Section 2.6, eq.(2.48). In order to increase the reflectivity up to the

[7] The interface is the region of transition between two consecutive layers of materials with pure composition. The imperfections at the interface are due to interdiffusion or to roughness (see Figs. 3.13 and 3.14, pp. 106-107).

theoretical limit, the width σ must be reduced as much as possible by optimizing the deposition parameters. The optimization of the deposition process led to values of σ (measured by x-ray reflectivity) of 3.0-4.5 Å for W/Si, Pt/C, and W/C, the most interesting materials for this application. Other material combinations studied and presented in this chapter are Mo/Si, Ni/C, Ni-V/C, WSi_2/Si, and Nb/Si. Their interface widths σ were larger than 7 Å and additional problems related to their reflectivity performance are discussed in the corresponding sections.

Chapter 5 describes the high-energy reflectivity measurements that were performed on depth graded multilayers using synchrotron radiation. The samples selected were W/Si, W/C, and Pt/C multilayers and displayed a reflectivity of at least 20% for a wide energetic bandpass and at grazing angles that are of interest for future work with telescope prototype mirrors. These high energy studies completed the first stage of the program of comparing the performance of different materials.

Chapter 6 highlights the accomplishments of the work performed at SAO in collaboration with external partners for the deposition of multilayer on curved substrates. Sections 6.1-6.3 present the pioneering work in test coatings of multilayers on the inside surface of integral cylindrical glass substrates. Section 6.4 discusses the uniformity of the coatings in the light of measurements of the reflectivity of multilayers deposited on thermally formed thin glass foils. Section 6.5 describes the ongoing effort to achieve a lightweight prototype telescope shell with better angular resolution than the competing techniques for Constellation-X mission. The coatings and measurements were performed at SAO with substrates supplied by collaborators at Brera University (Italy) and NASA-Marshall Space Flight Center.

In the **"Conclusions"** section, the scientific relevance of the experimental results is summarized and further research directions are discussed. A list of references of proceedings papers published as part of this work is provided in **Appendix C**.

Chapter 1: Astrophysics in the hard x-ray band

The exploration of the Universe in the x-ray spectrum had to wait for technological progress in the detection systems and the capability to launch them above the Earth atmosphere. The first cosmic x-ray source was discovered in June 1962 during the flight of a sounding rocket from the White Sands range in New Mexico. Since then, x-ray observations have been increasingly important for our advancement in the understanding of the structure of the Universe. One reason for this is that x-ray photons are created in very energetic phenomena or extreme environments that occur at critical stages in the evolution of the Universe. X-ray photon energies correspond to temperatures of 10^7 K in thermal processes or to the emission of characteristic lines of heavier elements (e.g., sulfur, silicon, and iron) and they can also be associated to synchrotron radiation in magnetic fields of the order of 10^{10} T. Another reason for which x-ray observations are irreplaceable is that photons are much less absorbed by the interstellar medium in the x-ray band than in other bands (visible, IR). The same is true for absorption in the circumstellar medium of certain types of stars.

With the exponential growth since 1962 in x-ray astronomy and the new concepts and theories that have been proposed or validated by this new information came also more fundamental questions about the evolution of the Universe. Some of these questions are related to physical processes that involve photons in the energy band above 10 keV, otherwise called "hard x-rays".

The next section will review, following Rybicki and Lightman [1], the basic processes in which x-ray photons are created and their interaction with matter. These topics are

essential for the presentation in Section 1.2 of the scientific objectives for imaging in the hard x-ray band with high angular resolution and sensitivity. Section 1.3 presents a historical account of the most important satellite based x-ray missions and concludes with introducing two future missions. Section 1.4 describes in more detail the Wolter type I optics and the baseline design for the Hard X-ray Telescope (HXT) of the Constellation-X mission.

1.1 X-ray processes in astrophysics

1.1.1 Bremsstrahlung

The emission of radiation due to acceleration or deceleration of a moving charge in the Coulomb field of another charge is called Bremsstrahlung (German for "braking radiation") or free-free emission (because the two charges are not bound together).

The bremsstrahlung due to like particles (electron-electron or proton-proton) is zero in the dipole approximation because the total dipole moment is proportional to the center or mass vector, which is a constant of motion. In the dipole approximation, only systems with different types of particles radiate by bremsstrahlung. In electron-ion scattering processes the electrons can be considered as primary radiators, as the radiation intensity is inversely proportional to the mass.

The first approximation is to describe the emission by monoenergetic electrons having a velocity v and density n_e moving in the fixed Coulomb field of ions distributed with a density n_i. The total energy dW radiated per unit frequency range $(d\omega)$ per unit volume (dV) per unit time (dt) is then:

$$\frac{dW}{d\omega dV dt} = \frac{16\pi e^6}{3\sqrt{3}c^3 m^2 v} n_e n_i Z^2 g_{ff}(v,\omega) \qquad (1.1)$$

where g_{ff} is the Gaunt correction factor and is given by the expression

$$g_{ff}(v,\omega) = \frac{\sqrt{3}}{\pi} \ln\left(\frac{b_{\max}}{b_{\min}}\right) \qquad (1.2)$$

The two values of the impact parameter b are taken as following: $b_{\max} = \frac{v}{\omega}$ and $b_{\min} = \frac{h}{mv}$.

The next step in complexity is to take the above expression for monoenergetic electrons and average over the velocity v assuming a Maxwellian distribution with a temperature T:

$$\frac{dW(T,\omega)}{dVdtd\omega}=\frac{\int_{v_{min}}^{\infty}\frac{dW(v,\omega)}{dVdtd\omega}v^2\exp\left(-\frac{mv^2}{2kT}\right)dv}{\int_0^{\infty}v^2\exp\left(-\frac{mv^2}{2kT}\right)dv}=\frac{2^5\pi e^6}{3mc^3}\left(\frac{2\pi}{3km}\right)^{1/2}T^{-1/2}Z^2n_en_i\exp\left(-\frac{hv}{kT}\right)\bar{g}_{ff} \tag{1.3}$$

In CGS units,

$$\varepsilon_v^{ff}\equiv\frac{dW(T,\omega)}{dVdtd\omega}=6.8\cdot10^{-38}Z^2n_en_iT^{-1/2}\exp\left(-\frac{hv}{kT}\right)\bar{g}_{ff} \tag{1.4}$$

where $\bar{g}_{ff}(T,v)$ is the velocity averaged Gaunt factor.

Non-thermal bremsstrahlung processes occur in transient flares and other non-equilibrium dynamical events. In order to calculate the emission in non-thermal processes one needs the electron velocity distribution for the averages. In both cases (thermal and non-thermal) the Gaunt factor can be retrieved from tables or approximate analytical formulas can be used.

1.1.2 Synchrotron radiation

In the case of acceleration of charged particles by a magnetic field, radiation is also emitted. There is a distinction between the non-relativistic and relativistic case:

- If the particle is non-relativistic $(v\ll c)$, the process is called cyclotron radiation and is described by a cyclotron frequency $\omega_B=\frac{qB}{mc}$ (CGS Gauss units). The frequency of the radiation emitted is equal to the cyclotron gyration frequency ω_B.
- If the particle is relativistic, then the emitted radiation is named synchrotron radiation and the emission spectrum is very complex.

The simplest case is a system of charged particles with isotropically distributed velocity v moving in a uniform magnetic field B. The angle between the magnetic field and the particle velocity is called the pitch angle α. Using the single particle relativistic equations of motion it can be shown that:

- The angular distribution from a single particle lies close (within $1/\gamma$) to the cone with half-angle equal to the pitch angle.
- The single particle spectrum is a function of ω/ω_c and extends up to the order of the critical frequency $\omega_c = \frac{3}{2}\gamma^3\omega_B \sin\alpha$.

The next case is to allow the particles to have a velocity distribution. For relativistic electrons, it is customary to assume a power law distribution of the form: $N(E)dE = CE^{-p}dE$. Then the power spectrum of the synchrotron radiation is an integral over the energy (or equivalently, over γ) of the relativistic single electron power spectrum law:

$$P(\omega) = \frac{\sqrt{3}}{2\pi}\frac{q^3 B \sin\alpha}{mc^2} F\left(\frac{\omega}{\omega_c}\right) \qquad (1.5)$$

It can be shown that the result of the integration is also a spectral power law:

$$P_{tot}(\omega) \sim \omega^{-\frac{p-1}{2}} \equiv \omega^{-s} \qquad (1.6)$$

(s is defined as the spectral index of the synchrotron radiation).

It is interesting to note that a synchrotron emission photon can also be self-absorbed by interaction with another charged particle. Another process that can occur is stimulated emission, in which photons are already present. The (self)absorption coefficient α_ν is power-law dependent on the frequency ν : $\alpha_\nu \sim \nu^{-\frac{p+4}{2}}$. Then, for a non-thermal power law electron distribution with index p , at low frequencies the system is optically thick by self-absorption and the observed intensity is proportional to $\nu^{\frac{5}{2}}$. At high frequencies, the system becomes optically thin and the observed intensity decreases as $\nu^{-\frac{p-1}{2}}$.

1.1.3 Compton scattering

For low photon energies $\left(h\nu \ll mc^2\right)$ the scattering of the radiation can be treated in the frame of classical electrodynamics. For photons scattered off free electrons, the process is called Thomson scattering and is described by the differential cross-section

$$\frac{d\sigma_T}{d\Omega} = \frac{1}{2} r_0^2 (1+\cos^2\theta) \qquad (1.7)$$

and the total cross section $\sigma_T = \frac{8\pi}{3} r_0^2$ (r_0 is the classical electron radius).

For high photon energies, the scattering process is described by quantum mechanics. The scattering is no longer elastic because of the recoil of the charge and the scattered photon has the energy E' given by:

$$E' = \frac{E}{1+\frac{E}{mc^2}(1-\cos\theta)} \qquad (1.8)$$

The differential cross section for unpolarized incident radiation is shown in quantum electrodynamics to be given by the Klein-Nishina formula:

$$\frac{d\sigma}{d\Omega} = \frac{r_0^2}{2}\frac{E'^2}{E^2}\left(\frac{E}{E'}+\frac{E'}{E}-\sin^2\theta\right) \qquad (1.9)$$

When gamma rays emitted by unstable nuclei are Compton scattered, their spectrum is "softened" by multiple scattering down to the hard x-ray band. For a finite, thermal medium, one can define the Compton y parameter as a measure of the change in energy when traversing the medium: y = (average fractional change of energy per scattering) × (average number of scatterings). Neglecting absorption and considering thermal ensembles of electrons, the Compton y parameter is given by:

$$y_{NR} = \frac{4kT}{mc^2} Max\left(\tau_{es}, \tau_{es}^2\right) \qquad (1.10)$$

for nonrelativistic electrons and

$$y_R = \left(\frac{4kT}{mc^2}\right)^2 Max\left(\tau_{es}, \tau_{es}^2\right) \qquad (1.11)$$

for relativistic electrons, respectively. The optical depth is $\tau_{es} = \rho k_{es} R$, where k_{es} is the electron scattering opacity ($=\sigma_T / m_p$ for ionized hydrogen) and R is the size of the medium. The expressions above are useful to determine in what conditions a medium is changing significantly an emission spectrum by Compton scattering.

1.1.4 Inverse Compton scattering

Whenever a fast charged particle has sufficient kinetic energy compared to an incident photon, net energy may be transferred from the electron to the photon in a process called inverse Compton scattering.

Considering an energetic electron in a region with isotropic photons of energy E and density ν, the power lost by the electron in inverse Compton scattering is:

$$P_{i.C.} = \frac{4}{3}\sigma_T c \gamma^2 \beta^2 \int E\nu \, dE \qquad (1.12)$$

where the integral is the photon energy density (before scattering) $U_{ph} = \int E\nu \, dE$.

If we consider now that the electrons have an energy distribution given by $N(\gamma)d\gamma$ (=number of electrons per unit volume with γ in range $(\gamma, \gamma + d\gamma)$), then the total Compton power lost by the electrons is

$$P_{tot} = \int P_{i.C.} N(\gamma) d\gamma \qquad (1.13)$$

The problem of the inverse Compton spectrum can be also broken in two. First, one needs to determine the spectrum of scattered photons of initial energy E by electrons of a given energy γmc^2. Then the general spectrum can be found by averaging over the actual photon and electron energy distributions.

The solution for a power law distribution of relativistic electrons is given by the following formula for the radiation spectrum:

$$\frac{dE}{dV dE' dt} = \pi c r_0^2 C A(p) E'^{-\frac{(p-1)}{2}} \int E^{\frac{p-1}{2}} \nu(E) dE \qquad (1.14)$$

If $\nu(E)$ is the blackbody radiation distribution, then

$$\frac{dE}{dVdtdE'} = \frac{C8\pi^2 r_0^2}{h^3 c^2}(kT)^{\frac{(p+5)}{2}} F(p) E'^{-\frac{(p-1)}{2}} \qquad (1.15)$$

1.2 Astrophysical objectives in the hard x-ray band

1.2.1 The x-ray background

Based on the ROSAT and Chandra deep field surveys, the x-ray background below 10 keV is resolvable into point sources. By lack of high-resolution telescopes in the hard x-ray band, it is not known if the diffuse component is absent also at these energies. It was hypothesized by Loeb and Waxman [2] that at the time of formation of clusters of galaxies the 2.7 K microwave background photons could be upscattered (through inverse Compton effect) by high energy intracluster electrons and produce a diffuse background in the gamma and hard x-ray band. With a high-resolution hard x-ray telescope, it would be possible to decide if the background can be resolved into point sources or is due to extended sources.

1.2.2 Clusters of galaxies

The evolution of structures in clusters of galaxies at distances $z \leq 1$ is considered an important cosmological indicator. A Coma type cluster of galaxies at z=1 has a size of 1 arcminute and would require angular resolution of at least a few arcsec in order to be imaged in the hard x-ray band. This would also be a direct way of investigating the magnetic fields in the galaxy cluster and can be corroborated with radio observations. A flux sensitivity of $3\text{x}10^{-6}$ photons/cm^2/s/keV is needed together with high angular resolution for mapping the galaxy clusters and eliminating point source contributions from AGNs.

1.2.3 Supernovae (SN) and supernovae remnants

A supernova emits gamma rays from the unstable nuclides created in the core of the star precursor. During the early phases of the SN evolution, the gamma photons are scattered

by the dense debris to hard x-ray energies before they can escape. The spectrum of the Type Ia SNs are thought to be C-O white dwarfs that are below and near the Chandrasekhar limit and have a close companion star in a binary system. By accreting material from their companions they can reach the limit and collapse, triggering a thermonuclear explosion that creates an extremely luminous supernova. It is postulated that type Ia SN progenitors are very uniform throughout the Universe and it was determined that the dispersion of their maximum luminosity is very small ("standard candle" hypothesis), probably due to the small range of the masses of the progenitors. If the Type I SNs are "standard candles" indeed, then the observation of the luminosity of the Ni^{56} line would be a test for the competing theories for the SN explosion.

1.2.4 Unidentified sources

Many gamma-ray sources are detected by telescopes that lack the spatial or spectral resolution necessary to complete the identification. The EGRET catalog contains 170 such unidentified sources (out of a total of 271). Some of these sources may be of galactic origin, like radio-quiet pulsars, cosmic ray concentrations in supernova remnants, x-ray binaries, or gamma-ray flare stars. The high-latitude unidentified sources are possibly extragalactic, like radio-quiet blazars, or other types of active galaxies. For all these objects, it is likely that the gamma spectrum extends in the hard x-ray band as well. With future generation hard x-ray telescopes the position of these sources will be known with subarcminute resolution and thus the position accuracy gap between sources detected in the gamma-ray and the optical bands can be filled by hard x-rays.

1.2.5 Quasars

The redshift compresses the intrinsic spectrum of a quasar into the hard x-ray band, such that for z=2, a telescope with a bandwidth upper limit at 70 keV can cover essentially all of it. Features like jets need to be observed with an angular resolution less than an arcminute.

1.2.6 Neutron stars

The high magnetic fields existing around neutron stars create cyclotron radiation by the deviation of energetic electrons. The effect was observed in Her X-1 and in pulsating transients and it is possible that high sensitivity measurements in the hard x-ray band will allow detection of cyclotron radiation from other neutron star systems. The detailed study of cyclotron lines in the hard x-ray band is the most direct method of mapping the neutron star magnetic field.

1.2.7 White dwarfs

The higher spectral resolution of future hard x-ray telescopes is expected to be put to use in a systematic search for the hard x-ray cutoff energy versus the mass of the white dwarfs.

1.2.8 Seyfert galaxies

Seyfert galaxies typically emit x-rays up to 100 keV. A model of the Seyfert galaxies emerging from the x- and gamma-ray observations is based on a plasma-containing nucleus that emits by Compton scattering a power law spectrum. The plasma is above an accretion disk which reflects this radiation and gives rise to a broad continuum peak at ~30 keV. High resolution observations of Seyfert galaxies in the hard x-ray band would provide key information for the understanding of their galactic nucleus.

1.3 X-ray orbiting telescope missions

1.3.1 The first decade

The era of the x-ray astronomy orbiting missions was opened by the Uhuru satellite in 1970. The principal goal of the mission was the first all-sky x-ray survey. The satellite detectors were two scanning proportional counters and covered the range 2-20 keV. The final Uhuru catalog contained 339 objects, mainly binaries, supernova remnants, Seyfert

galaxies, and clusters of galaxies. The success of Uhuru was followed in the decade by the launch of many important small satellite missions such as:

- SAS-3 (launched in 1975) identified the location of the bright x-ray sources and searched for x-ray novae and transient x-ray sources
- Ariel V (1974) was one of the first satellite missions to carry crystals for high resolution x-ray spectroscopy measurements
- Copernicus (1971) was the third of the Orbiting Astronomical Observatories
- OSO-8 (1975) carried curved graphite crystals for spectroscopy and polarimetry

These small satellite missions obtained the first detailed spectra of x-ray objects, discovered new phenomena, like x-ray bursts, and showed that pulsars are also strong x-ray sources.

1.3.2 The Einstein Observatory

The next major series of satellite missions was inaugurated in 1977 by the launch of NASA's first High Energy Astrophysical Observatory (HEAO-1). The catalog of x-ray objects generated by HEAO-1 included 850 point sources and the first measurement of the diffuse x-ray background. The mission was followed in 1978 by the second HEAO satellite, also known as the Einstein Observatory. The x-ray telescope onboard of Einstein was a Wolter Type I design with four nested elements and a focal plane assembly of four complementary detectors. The telescope focal length was 3.4 m and the field of view was 1^{o} with an angular resolution of 2 arcsec rms. The optic was manufactured from fused silica with a surface roughness of 25 Å and was coated with a Cr-Ni alloy, allowing an effective area of 400 cm^2 at 0.25 keV. By combining a focusing optic with high resolution and relatively large collecting areas, the Einstein telescope reached a sensitivity gain of several hundred to almost 1,000 compared to any of the previous missions. The four detector systems represented also an advance in the field: the high-resolution imager (HRI) provided 2 arcsecond resolution over the central field of view of the telescope and was best matched with the high angular resolution of the optics. The second detector was a multiwire imaging proportional counter (IPC) with large detection efficiency. The other

detectors in the focal plane were a curved crystal Bragg spectrometer and a solid state Si(Li) detector. A grating spectrometer could be positioned in the path of the x-rays reflected by the mirrors to produce energy-dispersed images on the HRI. The Einstein Observatory was a milestone for x-ray astronomy not only due to the revolutionary increase in sensitivity over its predecessors, but also by producing a catalog of several thousand sources located with high accuracy and encompassing the entire range of x-ray astrophysics. A few highlights of the discoveries made by this mission are listed below:

- first high resolution spectroscopy study of supernova remnants
- first study of x-ray emission from gas in galaxies and clusters of galaxies
- detected x-ray jets from sources of radio jets
- first medium and deep sky x-ray surveys

1.3.3 The specialized missions

During the 1980's, the x-ray satellite missions were scaled down and mostly specialized for specific studies. The EXOSAT mission launched by ESA in 1983 made observations of 1800 objects, including active galactic nuclei, stellar coronae, white dwarfs, x-ray binaries, and supernova remnants. The low energy telescope (0.05 to 2 keV) was a Wolter type I design with a field of view of 2 degrees and a detector resolution of 18 arcsec. The focal plane detectors were a channel multiplier array (CMA) with an effective area of 10 cm^2, a position sensitive detector for low energies (<2 keV) and two proportional counters for higher energies (1-50 keV). The mission also had spectroscopic capabilities due to a transmission gratings system used in conjunction with the CMA. The EXOSAT mission pioneered the epoxy replication of the telescope optics.

The Japanese Astro-C mission (launched in 1987) used coded apertures in front of a large area (4000 cm^2) proportional counter detector to image fields of view of 0.8^o x1.7^o. An all-sky monitor mapped the energy band 1-20 keV in a 1^o x 180^o field of view and a gamma-ray burst detector mapped the whole sky in the band 1-500 keV. This mission discovered intense 6-7 keV iron line emission from the galactic center region and also evidence for

emission/absorption Fe features in Seyfert galaxies. Transients like black hole candidates or regions near the galactic ridge were also detected for the first time.

1.3.4 The latest missions

The last decade has witnessed a series of major satellite missions dedicated to x-ray astronomy. The Roentgen Satellite ROSAT launched in 1990 was the product of a multinational collaboration (Germany, US, and UK) and during its nine years of operation it explored the space in the EUV and soft x-ray band. The main x-ray telescope (XRT) consisted of a Wolter type I nested mirror system with a focal length of 2.4 m and a geometric area of 1140 cm^2. The focal plane instruments of XRT were two position sensitive proportional counters (one for the survey phase, the other for the "pointed" phase of observations) and a high resolution imager (HRI) with 2 arcsec FWHM. A wide field camera (FOV 5 degrees) used its own Wolter-Schwarzschild mirror with short focal length (0.5 m). The ROSAT mission longevity together with the performance of the instruments allowed to catalog more than 150,000 objects and perform an XUV all-sky survey. From the qualitative point of view, ROSAT produced unprecedented details of the morphology of supernova remnants and clusters of galaxies and detected the first isolated neutron stars. Launched in 1993, the ASCA mission (Advanced Satellite for Cosmology and Astrophysics) operated until July 2000 and was the first x-ray mission combining imaging in a broad energy bandwidth with good spectral resolution and large area. This x-ray mission was also the first to use CCD detectors. The four onboard telescopes were each composed of 120 nested aluminum foils coated with gold as reflector. Their total effective area was 1,300 cm^2 at 1 keV with a spatial resolution of 3 arcmin HPD at 1 keV. The ASCA detectors were two imaging gas scintillator proportional counters and a solid state imaging spectrometer based on two CCD arrays of four 420x422 square pixel chips. Some of the more remarkable scientific objectives achieved were the study of broad Fe lines from AGNs, the determination of heavy element abundances in clusters of galaxies, and spectroscopic analysis of interacting binaries.

A special capability of x-ray timing observation and a very large collecting area are the trademarks of the Rossi X-ray Timing Explorer (RXTE) satellite launched at the end of 1995. With a spectral range from 2 to 250 keV, it can cover time scales from microseconds to months. The mission carries two pointed instruments, the Proportional Counter Array (PCA) for the lower part of the energy range (2-60 keV) and the High-Energy X-Ray Timing Experiment (HEXTE) for the upper energy range (15-250 keV). An additional All-Sky Monitor covers about 80% of the sky on every orbit, allowing surveys at time scales of 90 minutes or longer. The mission's highlights include observations of x-ray afterglows from the gamma ray bursts, discovery of kHz quasi-periodic oscillations (QPOs) from neutron star binaries, observation of bursting pulsars, and other.

Beppo-SAX was the first x-ray satellite with instrumentation covering three decades of energy from 0.1 to 300 keV with a medium effective area and imaging in the band 0.1-10 keV. The satellite was launched in 1996 and carries four x-ray telescopes working with the following detectors: a Low- and a Medium-Energy Concentrator Spectrometer (LECS for 0.1-10 keV and MECS for 1.3-10 keV), a high-pressure gas scintillator proportional counter for the band 4-120 keV, and a phoswich detector system (PDS) for the band 15-300 keV. In addition, a Wide Field Camera (WFC) with a field of view of 20° X 20° is used for the energy range 2-30 keV. The Beppo-SAX mission has been very successful in imaging the sources associated with gamma-ray bursts and accurately determining their position.

The Chandra X-Ray Observatory was launched and deployed by the Space Shuttle in July 1999 for a nominal mission duration of 5 years. The telescope is capable of imaging in the 0.1-10 keV band with 0.5 arcsecond (FWHM) angular resolution due to its combination of Wolter type I mirrors and high resolution detectors. The four nested Zerodur shells shown in Figure 1.1 were coated with iridium and provide a field of view of 30 arcmin and a focal distance of 10 m. The effective area at 0.25 and 5 keV is 800 and 400 cm^2, respectively. Each of the four detectors can be inserted in the focal plane and two of them were designed to be used primarily for spectroscopic observations with the transmission gratings. The two types of detectors used are CCDs and microchannel plates. Two arrays of CCDs compose the AXAF Charged Coupling Imaging Spectrometer (ACIS) with four chips for imaging

(ACIS-I) and six chips for spectroscopy (ACIS-S). The High Resolution Camera (HRC) consists of two micro-channel plate detectors: one for imaging (HRC-I) with 0.5 arcsec resolution and the other optimized for spectroscopy (HRC-S). The transmission gratings arrays are capable of spectral resolving powers of 60-1000 for the high energy (0.5-10 keV) band and 30-2000 for the low energy band (0.08-5 keV).

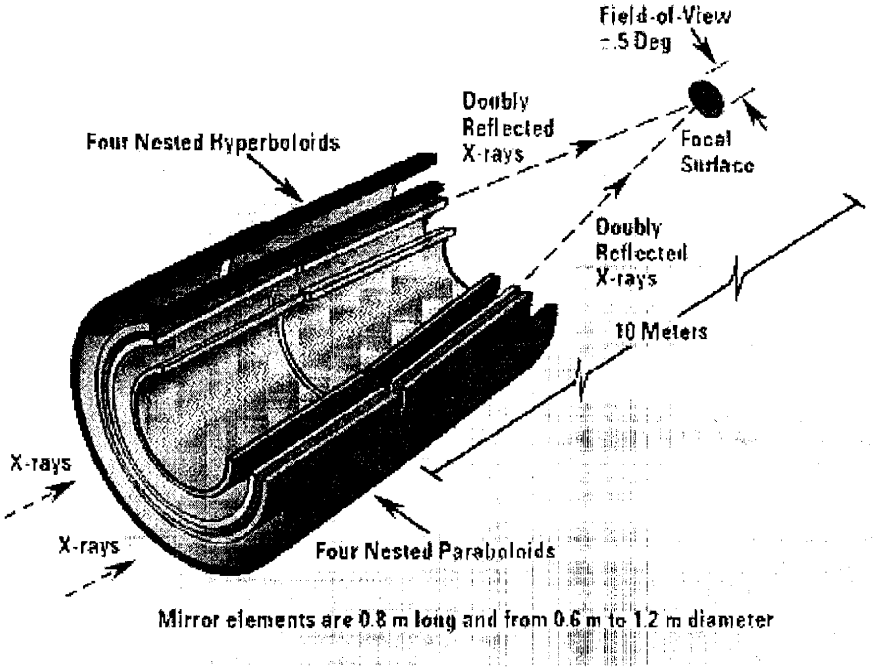

Figure 1.1: A cross-sectional perspective view of the mirror assembly onboard the Chandra telescope. The four nested shells are Wolter type I reflectors (paraboloid + hyperboloid). The polished Zerodur substrates were coated with a chromium binder layer and then with the iridium reflector layer. The soft x-ray photons are totally reflected by the iridium layer at grazing incidence angles lower than the critical value. By a double reflection off the paraboloid and the hyperboloid, an image is formed in the focal plane where the detectors are positioned.

The ESA X-ray Multi-Mirror Mission (XMM-Newton) was launched at the end of 1999 and carries three high throughput x-ray telescopes, as well as an optical monitor. The three coaligned Wolter type I telescopes were assembled from nested nickel foils coated with gold. A module with the 58 concentric nickel shells is shown in Figure 1.2 .The effective area of each telescope is 1500 cm^2 at 1 keV and the spatial resolution is 6 arcsec FWHM. Three types of instruments operate with the x-ray mirrors:

-Metal-oxide-silicon cameras (EPIC-MOS) are mounted with two of the telescopes and are used for spectral imaging. Each unit consists of an array of 7 CCDs.

-The EPIC-PN camera is an array of 12 CCDs.

-The Reflection Grating Spectrometer works with the EPIC-MOS cameras to produce spectral images with a resolution dE/E in the range 200-800.

The optical monitor (OM) is a 30 cm optical/UV telescope coaligned with the x-ray telescopes and offering a field of view of 17 arcmin with 1 arcsec spatial resolution.

The primary goal of the XMM-Newton is to perform high throughput spectroscopy in the band 0.1-10 keV, including diffuse x-ray background measurements.

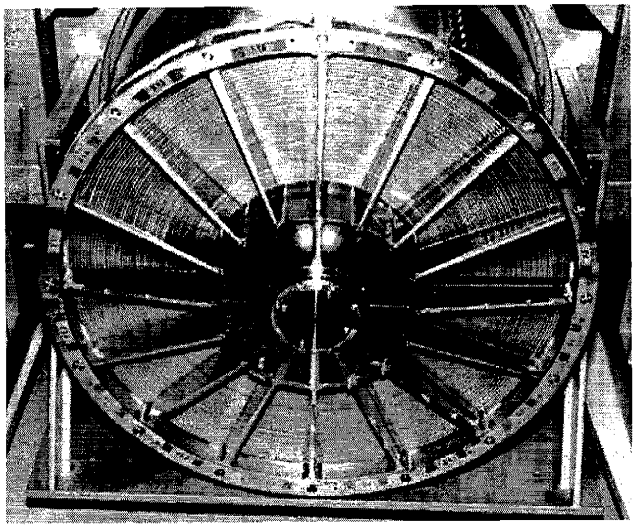

Figure 1.2: The XMM mirror module assembly of 58 nickel electroformed shells. This view is from the detector side. The effective area of each telescope is 1500 cm^2 at 1 keV and the spatial resolution is 6 arcsec FWHM.

1.3.5 The next generation of missions

Two future x-ray missions stand out by the gain in sensitivity and resolution proposed and by the fundamental science questions they will address. These are NASA's Constellation-X Mission and the European Space Agency (ESA) follow-up to XMM-Newton, the XEUS mission.

Constellation-X

Constellation-X is the NASA mission concept of a high throughput, broadband x-ray observatory based on four soft x-ray (SXT) and hard x-ray telescopes (HXT) carried aboard four satellites. The primary science objective of Constellation-X is the soft x-ray spectroscopy of emission and absorption features of all cosmically abundant metals, complemented by hard x-ray energy (10-50 keV) measurements of the non-thermal continuum. The motivation for high resolution imaging above 10 keV is provided by the existence of sources with spectral maxima in this energy range and by the astrophysical processes that are observable only in this band. Some examples of unique processes in this energy range are:

- the energy of the x-ray background peaks at ~30 keV and less than 15 % of this energy is accounted by the AGNs in the ROSAT catalog.
- the observation in this band of inverse Compton scattering radiation predicted in clusters of galaxies will allow testing of cosmological models.
- compact stellar remnants in the local group have output peaks above 10 keV and would offer information about the endpoints of stellar evolution in binaries.
- young supernova remnants (Cas A, Tycho) exhibit x-ray spectra extending to 50 keV. The spatial maps from the hard x-ray band and radio bands can be combined to test the shock acceleration theory.

XEUS

XEUS (X-ray Evolving Universe Spectroscopy) is a potential ESA mission based on a permanent space-borne x-ray observatory and with a sensitivity of about 250 times above XMM-Newton. The scientific goals include the study of massive black holes, evolution of early galaxy groups and of heavy elements abundances, the study of the intergalactic medium by absorption line spectroscopy, and other fundamental aspects of the evolution of the Universe. The large focal length of 50 m will require two separate spacecrafts, one for

the mirror system and the other for the detector, able to maintain their relative positions with 1 mm precision.

1.4 X-ray telescope mirrors

Because the x-rays are strongly absorbed in matter, the mirror systems used for x-ray focusing telescopes cannot use the same geometry as their optical counterparts. After the experimental proof of total external reflection of x-rays at very low grazing angles (less than 1°), the attempts to use parabolic mirror surfaces with small grazing incidence angles for imaging x-rays suffered from severe spherical aberrations. The aberrations increase as the grazing incidence angle is decreased, so again the simple mirror systems known from optics cannot be used for imaging x-rays even by using total reflection at angles smaller than the critical value.

1.4.1 Wolter Type I telescopes

Wolter [3] designed two-mirror systems based on aspherical (parabolic, hyperbolic, and elliptic) surfaces aligned axially symmetric and confocal. The Wolter systems are stigmatic on-axis, but not optimized for off-axis imaging. There have been different approaches to optimize the original designs with partial success [4]. The current state-of-art fabrication, metrology, and alignment errors dominate at small angles and astigmatism dominates for large field angles. For astrophysical X-ray applications, the Wolter type I design is the dominant design and will be discussed next.

A Wolter type I grazing incidence telescope consists of a paraboloid and a hyperboloid (Figure 3.1) described by the following equations:

-for the paraboloid with a vertex at z_p and the vertex radius of curvature R_p, the radius of the paraboloid at the axial position z is given by:

$$r_p^2 = 2R_p\left(z - z_p\right) \qquad (1.16)$$

-for the hyperboloid with semiaxes a and b and the center at z_h, the radius of the hyperboloid at axial position z is obtained from the equation:

$$\frac{(z-z_h)^2}{a^2}-\frac{r_h^2}{b^2}=1 \qquad (1.17)$$

The eccentricity parameter of the hyperboloid is defined as follows:

$$\varepsilon=\sqrt{1+\frac{b^2}{a^2}} \qquad (1.18)$$

The rear hyperboloid focus coincides with the paraboloid focus in the Wolter type I geometry and the front hyperboloid focus becomes the system focus. The nominal focal length of the telescope is $f'=z_f-z_0$. If the length of the paraboloid mirror is L_p and g is the gap between the paraboloid and the hyperboloid, with the origin of the coordinate system at z_1 in front of the paraboloid, the axial positions of the two vertices are:

$$z_p=z_1+L_p+\frac{g}{2}+f'+2a\varepsilon+\frac{R_p}{2} \qquad (1.19)$$

and

$$z_h=z_1+L_p+\frac{g}{2}+f'+a\varepsilon \qquad (1.20)$$

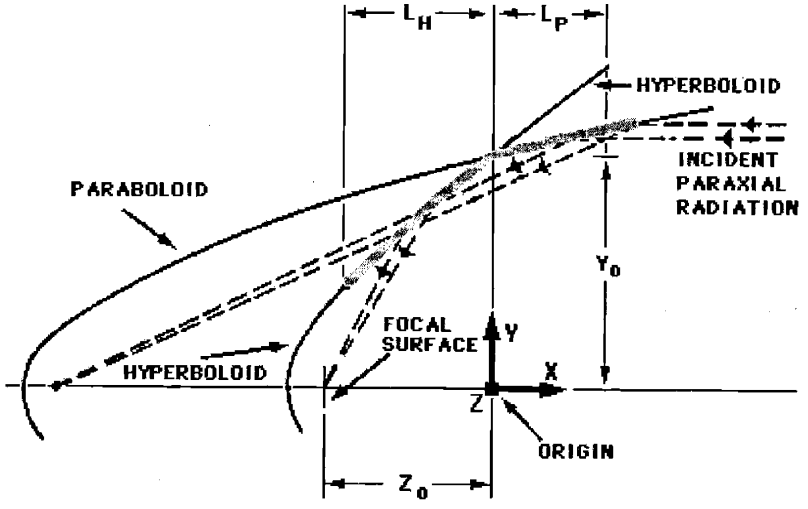

Figure 1.3: A cross section through a Wolter type I system showing the on-axis focusing for a paraxial beam by double reflection from the paraboloid and hyperboloid inner surfaces. The grazing angles are exaggerated in this figure for clarity; in fact, they must be smaller than the critical angle for total reflection. Wolter type I systems with different radii r_0 but same focal point can be nested for a higher total reflective area.

The design of a Wolter type I telescope is determined by three main independent parameters: R_p, a, and b. It is convenient to use the telescope radius r_0 at the intersection of the paraboloid and the hyperboloid as an independent parameter instead of R_p. The effective collecting area is maximized when the grazing angles of reflection at the intersection (joint) of the hyperboloid and the paraboloid are equal. The grazing angle at this joint is then related to r_0 and f' by the equation:

$$\alpha = \frac{1}{4}\tan^{-1}\left(\frac{r_0}{f'}\right) \qquad (1.21)$$

The actual focal length, measured from the system principal point, is

$$f = f' + \frac{r_0^2}{2f'} \qquad (1.22)$$

With the eq. (1.21), the number of the main independent parameters was reduced to two: r_0 and f'. A telescope has a finite length and non-zero gap, so the additional design parameters are: L_p, L_h, and g. From these input parameters, the geometrical performance of the Wolter type I telescope can be calculated for a particular application.

1.4.2 Performance of hard x-ray telescopes for future missions

Because the critical angle decreases inversely proportional with the energy, the extension of the traditional metal-coated Wolter type I mirrors to the hard x-ray band would require very small grazing angles, a condition which from eq. (1.21) is equivalent to a small ratio r_0/f .

This means that either the shells have a small radius r and are tightly nested, or that the focal point is at a large distance f. Both options have disadvantages: the small radii shells will have a lower effective area and the long focus telescopes are impractical for satellite missions (with the exception of XEUS, Section 1.3.5). The solution is to use Bragg enhanced reflection at larger angles θ by coating the Wolter type I optic with a multilayer having a period d matched to the angle θ and the x-ray wavelength λ by the Bragg equation:

$$2d\sin\theta = m\lambda \qquad (1.23)$$

For reflection in a band of wavelengths (energies), the period d can be graded in the depth of the multilayer to match the wavelengths λ of interest by using the same Bragg relation (Christensen et al. [5]). The maximum practical grazing angle θ_{max} for a multilayer based telescope is determined by the minimum achievable d and interface width of the multilayer (see Chapter 4 for different materials). The highest achievable energy E_{max} is dictated by the smallest d and by the smallest grazing angle (excluding edge absorption in the material). In a system of confocal nested shells, the highest energies are reflected from the inner shells, so a larger number of shells is required to achieve a given effective area.

The baseline characteristics for the Constellation-X Hard X-ray Telescope (HXT) calls for an effective area of 1,500 cm^2 at 40 keV, 1 arcmin HPD or better at 10 keV, a diameter of the field of view of at least 8 arcmin and a bandpass cutoff at 40 keV or higher. The prime interest of the research performed at the Multilayer Facility at Smithsonian Astrophysical Observatory (SAO) is the HXT for Constellation-X. The specific feature of our approach is to achieve high angular resolution without reducing the effective area of the mirror. For this purpose, the mirror substrates are fabricated as integral shells by nickel electroforming of a superpolished mandrel (see Section 6.5.1). Compared to other telescopes with segmented substrates (e.g., HEFT [6], InFOCμS [7]), the number of mirror units to be aligned to the common focus is lower by an order of magnitude. Also, the integral shells are more rigid and keep their figure during mounting and alignment. By taking advantage of the integral shell approach, the sensitivity of the HXT will be increased, simultaneously with a higher angular resolution that will allow observing individual sources in fields with high density of x-ray sources. The spectroscopic studies will also benefit from the increased angular resolution. For example, in the study of Cas A and other supernovae remnants, the distribution of Ti^{44} needs to be mapped from the 68 and 78 keV emission lines and correlated to the soft x-ray images from Chandra with better than one arcmin resolution.

Based on scientific and technical considerations, the research program performed at SAO and together with our collaborators has the established goal to demonstrate the feasibility of the following performance enhancements that will be used in the final baseline technology decision for HXT:

- reduced HPD to 30 arcsec or better
- extended energy band to 70-100 keV

References for Chapter 1

1. G.B. Rybicki and A.P. Lightman, *Radiative Processes in Astrophysics*. 1979, New York: John Wiley & Sons.

2. A. Loeb and E. Waxman, *"Cosmic gamma-ray background from structure formation in the intergalactic medium"*, Nature **405**, 2000, pp. 156-158.

3. H. Wolter, *"Mirror systems with glancing incidence on image producing optics for x-rays"*, Ann. Phys. (N.Y.) **10**, 1952, pp. 94-103.

4. P.L. Thompson and J.E. Harvey, *"Systems engineering analysis of aplanatic Wolter type 1 X-ray telescopes"*, Optical Engineering **39**, 2000, pp. 1677-1691.

5. F.E. Christensen, A. Hornstrup, N.J. Westergaard, H.W. Schnopper, J.L. Wood, and K. Parker. *"A graded d-spacing multilayer telescope for high energy x-ray astronomy"*, in *Multilayer and grazing incidence X-Ray/EUV optics*, 1991, *Ed.* Proceedings of SPIE, vol. 1546, pp.160-167.

6. W.W. Craig, F.E. Christensen, T. Decker, C.J. Hailey, F.A. Harrison, R.M. Hill, M. Jimenez-Garate, P. Mao, and S. Schindler. *"Hard x-ray optics for the HEFT baloon borne payload: prototype design and status"*, in *EUV, X-Ray, and Gamma-Ray Instrumentation for Astronomy IX*, 1998, *Ed.* O.H.Sigmund and M.A.Gummin, Proceedings of SPIE, vol. 3445, pp.112-120.

7. S.M. Owens, F. Berendse, T. Okajima, K. Misaki, Y. Ogasaka, K. Tamura, Y. Tawara, H. Kunieda, K.-W. Chan, et al. *"Characterization and performance of the InFOCuS 20-40 keV x-ray focusing mirror"*, in *X-Ray Optics for Astronomy: Telescopes, Multilayers, Spectrometers, and Missions*, 2001, *Ed.* P.J. Hoover and P. Gorenstein, Proceedings of SPIE, vol. 4496, pp.101-112.

Chapter 2: X-Ray Reflectivity of Multilayers

The foundation of the theory of x-ray reflectivity is presented in this chapter, starting with the use of the complex index of refraction of a medium to describe the propagation of x-rays. The boundary conditions for Maxwell's equations allow the derivation of the Fresnel reflectivity coefficients in Appendix A. Section 2.2 presents the definition of the critical angle and the total external reflection effect for x-rays. The penetration depth is discussed and calculated for some materials used in x-ray mirrors in Section 2.3. The theory of x-ray reflectivity of stratified media is introduced next using the matrix formalism of Paratt and developed explicitly for the case a single material layer on a substrate. The so-called kinematical theory is presented as an approximation that excludes multiple reflections and refraction at the interfaces. At the end of the Section 2.5 it is proven for a continuous medium that the kinematical theory is equivalent to the Born approximation for the x-ray scattering cross section. The problem of rough interfaces in multilayers is defined next in terms of the general matrix theory and it is shown that for a Gaussian height distribution at the interface an exact correction (the Névot-Croce factor) can be applied to the Fresnel reflectivity coefficient for specular reflection. The theory of off-specular reflectivity requires a recasting of the Maxwell equations in an integral form, such that the scattered field is calculated as the superposition of a "reference state" field and a "perturbation" field due to the presence of roughness at the interface. Based on the choice of the reference state, two cases are discussed in Sections 2.8 and 2.9: the first Born approximation (BA) and the distorted wave Born approximation (DWBA). The BA reference state is the field in vacuum and the approximation is correct for incidence and scattering angles larger than

the critical value. DWBA considers as the reference state the field calculated by the matrix method in multilayers with sharp interfaces (no roughness). The DWBA treatment yields better results near the critical angles and explains the presence of the Yoneda peaks in experimental off-specular scans. Of equal importance to the theoretical description of specular and off-specular reflection of the x-rays is the understanding of the measurement process. Section 2.10 is dedicated to the description of the experimental setup for x-ray reflectivity and of the corrections and normalizations used for the experimental data. An overview of the simulation software package IMD is included in Section 2.10.7.

2.1 X-ray reflectivity: theoretical preliminaries

For the wavelengths corresponding to x-rays (roughly, the range 0.1 Å $\leq \lambda \leq$ 10 Å), it can be shown [1] that a dense medium can be described by a complex index of refraction $n = 1 - \delta - i\beta$ and the classical wave theory can be used to describe the propagation of the x-rays.

The real part $1-\delta$ is associated with the phenomena of refraction and total external reflection of the x-rays. δ is positive and typically of the order of 10^{-7} to 10^{-4} for all materials. It is monotonically decreasing with energy as illustrated in Figure 2.1 for W, Mo, and amorphous Si, three materials used for x-ray multilayers and representative for the classes of materials with high, medium, and low density. The optical parameter δ is related to density ρ of atoms and the wavelength of the radiation λ by the microscopical quantity $b(0)$, the scattering length in the forward direction:

$$\delta = \frac{\lambda^2 \rho b(0)}{\pi} \tag{2.1}$$

The scattering length b can be calculated in principle using the quantum mechanical description of the atom acting as a scatter center for the incident electromagnetic field with amplitude A_i. The scattered field amplitude at large distances r is given by a spherical wave equation:

$$A_{sc}(\vec{r}) = -A_{in} b(\hat{r}) \frac{e^{-ikr}}{r} \tag{2.2}$$

The imaginary part of the index of refraction, β, is associated with absorption of the radiation in matter and can be expressed in terms of the macroscopic quantity μ (the linear absorption coefficient):

$$\beta = \frac{\lambda\mu}{4\pi} \tag{2.3}$$

Typical values for β above 10 keV (hard x-rays) are in the range $10^{-11} \div 10^{-5}$ as illustrated in Figure 2.2 for W, Mo, and amorphous Si.

Databases of x-ray optical constants (δ, β) for many materials are compiled by the Center for X-Ray Optics, Lawrence Berkeley National Laboratory, for energies up to 30 keV [2]. For x-ray form factors (from which δ and β can be calculated), the National Institute for Standards and Technology has published tables for energies up to 400 keV [3].

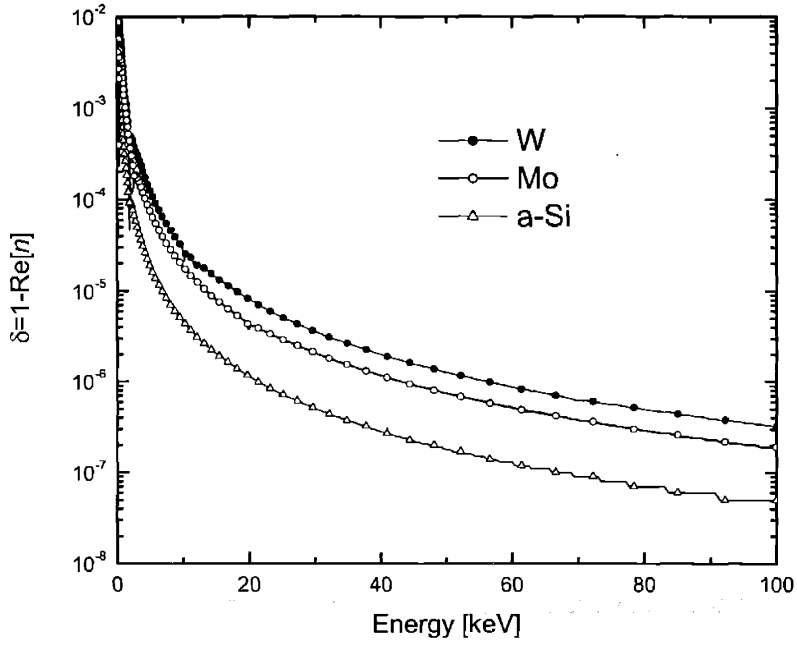

Figure 2.1: The energy dependence of $\delta = 1 - \mathrm{Re}[n]$ for tungsten, molybdenum, and amorphous silicon. For all materials δ is decreasing approximately as E^{-2} (see eq. **(2.1)**). The data shown were compiled in [2] and are updated on the website of the Center for X-ray Optics at Lawrence Berkeley National Laboratory.

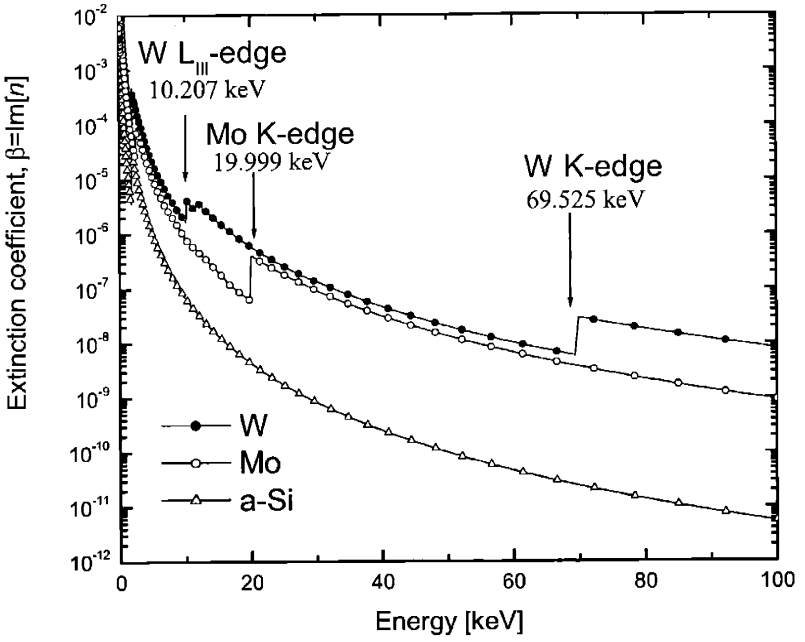

Figure 2.2: The energy dependence of the extinction coefficient $\beta = \mathrm{Im}[n]$ for tungsten, molybdenum, and amorphous silicon. The data shown are from [2]. The absorption is increased by almost an order of magnitude when the excitation energies for the K and L atomic shells are reached. The arrows and labels indicate the absorption edges and energies in the hard x-ray band for W and Mo. The K-shell absorption edge for Si is in the soft x-ray band at E_K=1.839 keV and is not labeled. For all materials, β decreases monotonically as E^{-4} for energies above the absorption edges.

2.2 Fresnel reflectivity

The reflectivity of an interface can be derived from Maxwell's equations using the conditions of continuity of the electric and magnetic fields. In the Appendix A is given the derivation of the amplitude coefficients for the reflected and the transmitted wave at the boundary between vacuum and a medium with refraction index n.

In terms of the incidence angle i_1 and refraction angle i_2 measured with respect to the normal (see Appendix A, Fig. A.1), the reflectivity coefficient for a plane wave with s-polarization is:

$$r_s = \frac{\sin(i_2 - i_1)}{\sin(i_2 + i_1)} = \frac{\cos i_1 - n\cos i_2}{\cos i_1 + n\cos i_2} \tag{2.4}$$

and for p-polarization:

$$r_p = \frac{\tan(i_2 - i_1)}{\tan(i_2 + i_1)} \tag{2.5}$$

Experimentally, it is more convenient to measure the reflectivity as a function of the grazing angle of incidence θ. The relations between i_1, i_2, and the grazing angles θ (incidence) and θ_{tr} (transmission) measured with respect to the surface of separation are given by the following set of equations:

$$\theta = \frac{\pi}{2} - i_1 \qquad \sin i_1 = n \sin i_2 \text{ (the Snell-Descartes law)} \qquad \theta_{tr} = \frac{\pi}{2} - i_2 \tag{2.6}$$

From the Snell-Descartes law: $\cos\theta = n\cos\theta_{tr}$, so the reflectivity coefficient for s-polarization can be written as a function of θ only:

$$r_s(\theta) = \frac{\sin\theta - \sqrt{n^2 - \cos^2\theta}}{\sin\theta + \sqrt{n^2 - \cos^2\theta}} \tag{2.7}$$

The critical angle θ_c for a material with index of refraction n and no absorption ($\beta = 0$) is defined as the limit value of the grazing angle θ for which $\theta_{tr} = 0$ (no transmitted wave in the material), or equivalently, using the Snell-Descartes law: $\cos\theta_c = n$. For angles $\theta < \theta_c$, the wave is totally reflected by the material and $r_s = 1$.

If we consider the small grazing angle approximation and expand the sine and cosine functions in (2.7), then the reflectivity coefficient becomes:

$$r_s(\theta) = \frac{\theta - \sqrt{\theta^2 - \theta_c^2}}{\theta + \sqrt{\theta^2 - \theta_c^2}} \tag{2.8}$$

The experimentally measured reflectivity is the flux density of the reflected wave normalized by the flux density of the incident wave $R(\theta) = I(\theta)/I_0$. Because the flux density is proportional to the square modulus of the field amplitude, it follows from the definition of the reflectivity that for the small angle approximation:

$$R(\theta) = |r_s(\theta)|^2 = \left| \frac{\theta - \sqrt{\theta^2 - \theta_c^2}}{\theta + \sqrt{\theta^2 - \theta_c^2}} \right|^2 \tag{2.9}$$

The subscript s describing the polarization state was dropped because it will be shown later that for small angles the s- and p-polarization reflectivities are identical.

For $\theta \gg \theta_c$ the asymptotic expression for $R(\theta)$ becomes:

$$R(\theta)\Big|_{\theta \gg \theta_c} = \frac{\theta_c^{\,4}}{16\theta^4} \tag{2.10}$$

To summarize, the reflectivity curve $R(\theta)$ for the interface between vacuum (or air, with a good approximation) and an absorptionless medium with a critical angle $\theta_c = \cos^{-1}(n)$ has three different regions:

- a plateau of total external reflection $R = 1$ for $\theta \leq \theta_c$
- a sharp decrease of R at θ_c
- a power law decrease of R for angles much larger than θ_c: $R \sim 1/\theta^4$

Figure 2.3 shows in a continuous line the reflectivity curve for silicon calculated at 8 keV using the exact Fresnel reflectivity coefficient from (2.7). The small angle approximation (2.8) holds very well at low grazing angles and produces a reflectivity curve indistinguishable from (2.7). For angles larger than θ_c, the asymptotic expression (2.10) can be used equally well.

As mentioned above, the medium was assumed without absorption ($\beta = 0$) to illustrate more clearly the total reflection plateau. In the presence of absorption, the "plateau" at $\theta < \theta_c$ has a reflectivity less than 1 (typically 0.8-0.9, depending on material and energy).

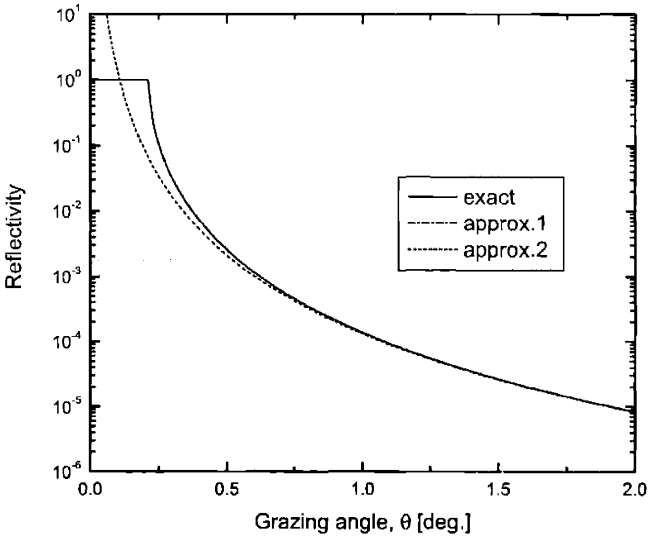

Figure 2.3: Calculated reflectivity at 8 keV for an ideal (no absorption, $\beta = 0$) vacuum-silicon interface using the exact Fresnel formula (eq.**(2.7)**) and two different approximations. The first one is the small angle approximation given by eq. **(2.9)**, which for the range of angles used (less than 2°) agrees with eq. **(2.7)** (the difference in the plots cannot be distinguished). For the second approximation, the asymptotic expression **(2.10)** was used and for angles above 1° an excellent match with the exact formula can be noticed.

2.3 The penetration depth

For the x-ray characterization of single layers it is important to determine the "penetration depth" as a function of angle. This can be calculated from the wave equation in the medium. The amplitude of the electric field of the transmitted plane wave propagating in the -z direction inside a medium of refractive index n is:

$$E_{tr} = E_0 e^{i\left(\omega t - \bar{k}\cdot\bar{r}\right)} = E_0 e^{i(\omega t - k_0 n\cos\theta_{tr} x + k_0 n\sin\theta_{tr} z)} \tag{2.11}$$

But $n\cos\theta_{tr} = \cos\theta$ and for small angles $\sin\theta_{tr} \approx \theta_{tr}$, so the terms in the exponential can be rearranged:

$$E_{tr} = E_0 e^{i(\omega t - k_0\cos\theta\cdot x)} e^{ik_0 n\theta_{tr} z} \tag{2.12}$$

The attenuation of the wave intensity in the material is given by $I(z) \sim \left|E_{tr}\right|^2 = E_0{}^2 e^{-2\mathrm{Im}(k_0 n\theta_{tr} z)} \doteq I_0 e^{-\mu z}$. If we define the penetration depth, $z_{1/e}$, as the depth in

material for which the beam is attenuated by a factor $1/e \approx 0.368$, then from the last equation:

$$z_{1/e} = \frac{1}{\mu(\theta)} = \frac{1}{2k_0 \,\mathrm{Im}\left(n \cdot \theta_{tr}\right)} = \frac{\sqrt{2}hc}{4\pi E \sqrt{\sqrt{\left(\theta^2 - 2\delta\right)^2 + 4\beta^2} - \left(\theta^2 - 2\delta\right)}} \quad (2.13)$$

Using values of β and δ from the CXRO tables [2], the penetration depth is plotted as a function of θ at E=8 keV (Fig. 2.4) and 30 keV (Fig. 2.5) for the following materials: Si, C, W, and Pt. The 8 keV values are of interest for the low-energy characterization performed routinely with Cu-K_α radiation, while the values at 30 keV are relevant for applications as hard x-ray mirrors.

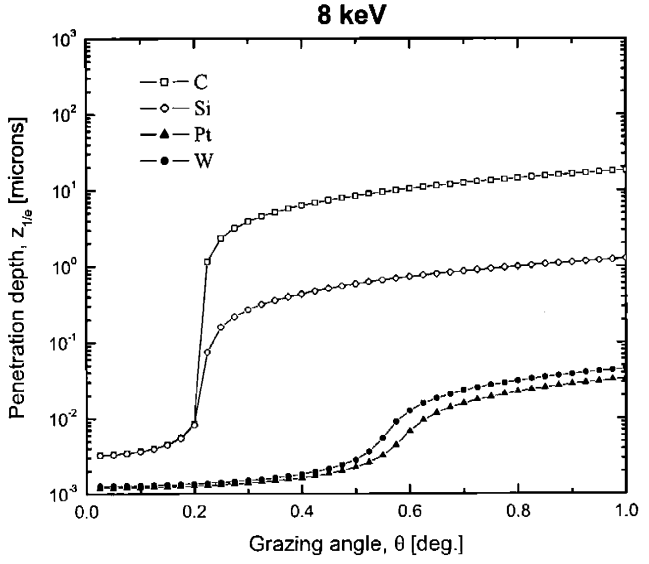

Figure 2.4: Penetration depth (1/e) in C, Si, Pt, and W, versus the grazing angle of incidence at E=8 keV. A sharp increase is noted at the critical angle for each material, followed by a slower increase in penetration at angles above the critical value. For the low-Z materials (C and Si), the penetration depth is of the order of 0.5-10 μm at large angles, while for high-Z materials (Pt and W) it is less than 0.1 μm.

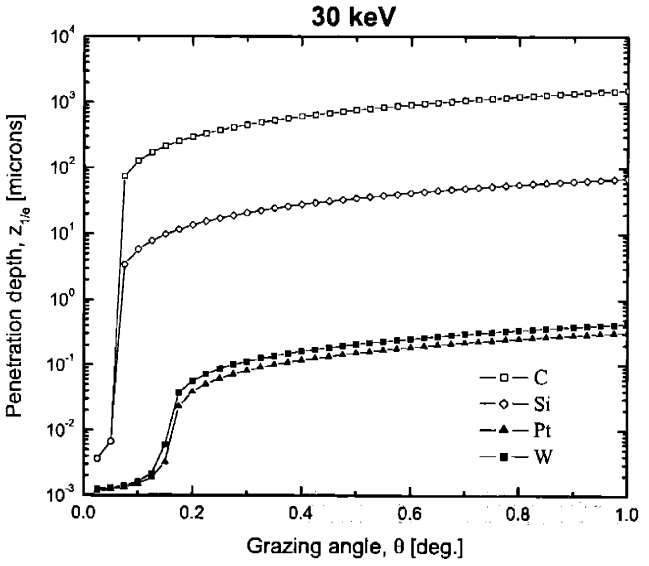

Figure 2.5: Penetration depth in C, Si, Pt, and W, versus the grazing angle of incidence at E=30 keV. For the low-Z materials (C and Si), the penetration depth is of the order of ten to hundreds of μm at large angles, while for high-Z materials it is below 1μm.

2.4 X-ray reflectivity in stratified media

In the case of multilayers, the boundary condition of continuity of the tangential component of the electric and magnetic fields must be applied at each interface. The derivation of the reflectivity coefficient for the multilayer is usually performed using the matrix method [4], which is described next.

An *s*-polarized plane wave is incident from the vacuum on a stratified medium as shown in Figure 2.6. The vacuum side is labeled with the index 0 and subsequent layers of material are labeled from 1 to *n*. Using this notation, the depth Z_{j+1} is associated with the interface between layer *j* and *(j+1)*. The wave is transmitted and reflected at each interface and we denote the upward (reflected) wave by a '+' superscript and the downward traveling wave (transmitted) by a '-' superscript. At a depth *z* inside layer *j* the electric field is a superposition of the upward and downward traveling waves:

$$E_j(x,z) = A_j^{+} e^{ik_{z,j}z} e^{i(\omega t - k_{x,j}x)} + A_j^{-} e^{-ik_{z,j}z} e^{i(\omega t - k_{x,j}x)} \qquad (2.14)$$

We introduce the notation:

$$U(\pm k_{z,j}, z) = A_j^{\pm} e^{\pm i k_{z,j} z} \tag{2.15}$$

so that the condition of continuity of the tangential component of the electric field at depth $z = Z_{j+1}$ can be written as

$$U(k_{z,j}, Z_{j+1}) + U(-k_{z,j}, Z_{j+1}) = U(k_{z,j+1}, Z_{j+1}) + U(-k_{z,j+1}, Z_{j+1}) \tag{2.16}$$

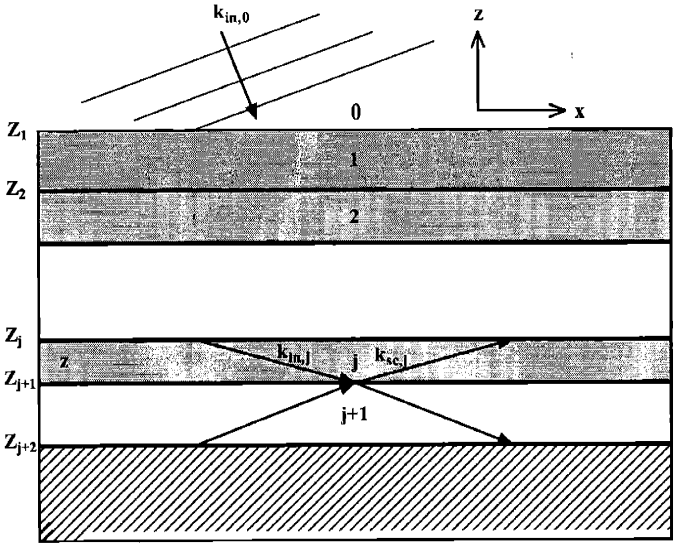

Figure 2.6: The schematics of the wavevectors for incident, reflected, and transmitted waves at the interface between layer j and $j+1$ positioned at depth Z_{j+1} from the surface.

From Maxwell's equations, the condition of continuity of the tangential component of the magnetic field is equivalent to the condition that the z-derivative of the electric field is continuous. This leads to the equation below for the interface between layer j and $j+1$:

$$k_{z,j}\left[U\left(k_{z,j}, Z_{j+1}\right) - U\left(-k_{z,j}, Z_{j+1}\right)\right] = k_{z,j+1}\left[U\left(k_{z,j+1}, Z_{j+1}\right) - U\left(-k_{z,j+1}, Z_{j+1}\right)\right] \tag{2.17}$$

The last two equations can be written in a matrix form, with the amplitudes U of the electric field in medium j on the left side and in medium $j+1$ on the right:

$$\begin{pmatrix} U\left(k_{z,j}, Z_{j+1}\right) \\ U\left(-k_{z,j}, Z_{j+1}\right) \end{pmatrix} = \begin{pmatrix} p_{j,j+1} & m_{j,j+1} \\ m_{j,j+1} & p_{j,j+1} \end{pmatrix} \begin{pmatrix} U\left(k_{z,j+1}, Z_{j+1}\right) \\ U\left(-k_{z,j+1}, Z_{j+1}\right) \end{pmatrix} \tag{2.18}$$

with

$$p_{j,j+1} = \frac{k_{z,j} + k_{z,j+1}}{2k_{z,j}} \text{ and } m_{j,j+1} = \frac{k_{z,j} - k_{z,j+1}}{2k_{z,j}} \tag{2.19}$$

The 2×2 matrix above relates the amplitudes U of the electric field on the medium j side to the medium $(j+1)$ side of the interface. It is called the refraction matrix for the interface $(j,j+1)$ and is denoted by $\mathcal{R}_{j,j+1}$. When the wave travels a distance h in the j^{th} medium from the interface $(j-1,j)$ to the interface $(j,j+1)$, the amplitudes of the field are changed by the translation matrix $\mathcal{T}_j$:

$$\begin{pmatrix} U(k_{z,j}, z) \\ U(-k_{z,j}, z) \end{pmatrix} = \begin{pmatrix} e^{-ik_{z,j}h} & 0 \\ 0 & e^{ik_{z,j}h} \end{pmatrix} \begin{pmatrix} U(k_{z,j}, z+h) \\ U(-k_{z,j}, z+h) \end{pmatrix} \tag{2.20}$$

The amplitudes of the electric field at the surface (depth $Z_1 = 0$) of the stratified medium are now related to the amplitudes at the substrate surface ($z = Z_s$) by a repeated multiplication of refraction and translation matrices:

$$\begin{pmatrix} U(k_{z,0}, Z_1) \\ U(-k_{z,0}, Z_1) \end{pmatrix} = \mathcal{R}_{0,1}\mathcal{T}_1\mathcal{R}_{1,2}\mathcal{T}_2 \ldots . \mathcal{R}_{N,s} \begin{pmatrix} U(k_{z,s}, Z_s) \\ U(-k_{z,s}, Z_s) \end{pmatrix} = \mathcal{M} \begin{pmatrix} U(k_{z,s}, Z_s) \\ U(-k_{z,s}, Z_s) \end{pmatrix} =$$

$$= \begin{pmatrix} M_{11} & M_{12} \\ M_{21} & M_{22} \end{pmatrix} \begin{pmatrix} U(k_{z,s}, Z_s) \\ U(-k_{z,s}, Z_s) \end{pmatrix} \tag{2.21}$$

The transfer matrix $\mathcal{M}$ is defined above as the product of successive refraction and translation matrices. The reflection coefficient r of the medium is now introduced as the ratio of the reflected and the incident electric fields' amplitudes at the surface of the stratified medium:

$$r = \frac{U(k_{z,0}, Z_1)}{U(-k_{z,0}, Z_1)} = \frac{M_{11}U(k_{z,s}, Z_s) + M_{12}U(-k_{z,s}, Z_s)}{M_{21}U(k_{z,s}, Z_s) + M_{22}U(-k_{z,s}, Z_s)} \tag{2.22}$$

If the substrate is much thicker than the penetration depth then the reflected component coming from the substrate is zero, $U(k_{z,s}, Z_s) = 0$, and thus the reflection coefficient of the stratified medium is given by:

$$r = \frac{M_{12}}{M_{22}} \tag{2.23}$$

For a p-polarized plane wave, a similar derivation of the refraction matrix gives the following values for its components:

$$p_{j,j+1}^{(p)} = \frac{n_{j+1}^2 k_{z,j} + n_j^2 k_{z,j+1}}{2n_{j+1}^2 k_{z,j}} \tag{2.24}$$

$$m_{j,j+1}^{(p)} = \frac{n_{j+1}^2 k_{z,j} - n_j^2 k_{z,j+1}}{2n_{j+1}^2 k_{z,j}} \tag{2.25}$$

The transfer matrix $\mathcal{M}$ and the reflectivity are calculated in an identical manner with the s-polarization case.

It is practical to express the matrix coefficients (for both s- and p-polarization) in terms of the grazing angle θ and the refractive index in each layer. For example, $k_{z,j} = -k_j \sin\theta_j = -\sqrt{k_j^2 - k_{x,j}^2}$, and because of the Snell-Descartes law at each interface, $k_{x,j} = k_j \cos\theta_j = k_{j+1}\cos\theta_{j+1} = ... = k_0 \cos\theta$. Also, $k_j = n_j k_0$, so the expression for $k_{z,j}$ is:

$$k_{z,j} = -k_0\sqrt{n_j^2 - \cos^2\theta} \tag{2.26}$$

2.4.1 Reflectivity of a flat substrate

In the simplest case of a homogeneous, semi-infinite medium, there is only one interface so there are no translation matrices. The transfer matrix is equal to the refraction matrix $\mathcal{M}=\mathcal{R}_{0,1}$ and

$$r = \frac{M_{12}}{M_{22}} = \frac{m_{0,1}}{p_{0,1}} = \frac{k_{z,0} - k_{z,1}}{k_{z,0} + k_{z,1}} \tag{2.27}$$

Using the expressions for $k_{z,j}$ from above: $k_{z,0} = -k_0 \sin\theta$ and $k_{z,1} = -k_0\sqrt{n^2 - \cos^2\theta}$ we regain for r an identical form with the Fresnel derivation:

$$r_s(\theta) = \frac{\sin\theta - \sqrt{n^2 - \cos^2\theta}}{\sin\theta + \sqrt{n^2 - \cos^2\theta}} \tag{2.28}$$

2.4.2 Reflectivity from a single layer on a substrate

If there is only one layer of thickness $h = Z_1 - Z_2$, then there is only one translation matrix $\mathcal{T}_1$: $\begin{pmatrix} e^{ik_{z,1}h} & 0 \\ 0 & e^{-ik_{z,1}h} \end{pmatrix}$ and two refraction matrices $\mathcal{R}_{0,1}$ and $\mathcal{R}_{1,2}$. The transfer matrix is the product $\mathcal{M}=\mathcal{R}_{0,1}\mathcal{T}_1\mathcal{R}_{1,2}$ and to calculate the reflectivity coefficient we need only two of the $\mathcal{M}$ matrix coefficients: M_{12} and M_{22}.

$$r = \frac{M_{12}}{M_{22}} = \frac{m_{0,1}p_{1,2}e^{-ik_{z,1}h} + m_{1,2}p_{0,1}e^{ik_{z,1}h}}{m_{0,1}m_{1,2}e^{-ik_{z,1}h} + p_{1,2}p_{0,1}e^{ik_{z,1}h}} \tag{2.29}$$

The expression for r can be recast in terms of the reflection coefficients at each interface *(i-1, i)* defined as

$$r_{i-1,i} = \frac{m_{i-1,i}}{p_{i-1,i}} = \frac{k_{z,i-1} - k_{z,i}}{k_{z,i-1} + k_{z,i}} = \frac{n_i \sin\theta_i - n_{i-1}\sin\theta_{i-1}}{n_i \sin\theta_i + n_{i-1}\sin\theta_{i-1}} \tag{2.30}$$

which we recognize from the Fresnel treatment of the reflectivity at an interface, eq. (2.4). If we express now r in terms of $r_{0,1}$ and $r_{1,2}$ by dividing (2.29) by $p_{0,1}p_{1,2}$, the final form for the single layer reflectivity coefficient is:

$$r = \frac{r_{0,1} + r_{1,2}e^{2ik_{z,1}h}}{1 + r_{0,1}r_{1,2}e^{2ik_{z,1}h}} \tag{2.31}$$

At the numerator the reflectivity coefficient of the first interface (0,1) is added to the coefficient of the second interface (1,2), corrected for the phase shift due to the distance $2h$ traveled back and forth through the layer 1 with wavevector $k_{z,1}$. The denominator contains a product term $r_{0,1}r_{1,2}$ corresponding to multiple reflections in the stratified medium.

The measured reflectivity is the squared modulus of the reflectivity coefficient and if we neglect absorption (i.e., assume all n_i are real) it can be expressed in a closed form:

$$R = rr^* = \frac{r_{0,1} + r_{1,2}e^{2ik_{z,1}h}}{1 + r_{0,1}r_{1,2}e^{2ik_{z,1}h}} \cdot \frac{r_{0,1} + r_{1,2}e^{-2ik_{z,1}h}}{1 + r_{0,1}r_{1,2}e^{-2ik_{z,1}h}} = \frac{r_{0,1}^2 + r_{1,2}^2 + 2r_{0,1}r_{1,2}\cos 2k_{z,1}h}{1 + r_{0,1}^2\, r_{1,2}^2 + 2r_{0,1}r_{1,2}\cos 2k_{z,1}h} \tag{2.32}$$

The cosine terms indicate that the reflectivity will oscillate in the reciprocal space with a period π/h. The features associated with these oscillations in the plot of R versus θ are called Kiessig fringes.

2.5 Kinematical theory

For angles much larger than the critical angle θ_c, the reflectivity coefficients $r_{i,i-1}$ have a small magnitude and could be neglected in second order and above. For the example of a single layer material on a substrate, eq. (2.31) can be written in this approximation as:

$$r = r_{0,1} + r_{1,2}e^{2ik_{z,1}h} \tag{2.33}$$

In Figure 2.7 is shown the reflectivity calculated at 8 keV using this approximation for a single layer of 60 Å of Ni on a silicon substrate. As expected, the kinematical theory diverges for angles less than θ_c and is inaccurate at angles close to θ_c, because multiple reflections are strong near the total reflection plateau. Compared with the exact simulation from IMD, it is remarkable that the kinematical theory model matches perfectly the exact reflectivity starting at 0.45°, while θ_c=0.402° at 8 keV for Ni.

The kinematical approximation can be generalized to a stratified medium composed of N layers on a substrate:

$$r = r_{0,1} + r_{1,2}e^{iq_{z,1}d_1} + r_{2,3}e^{i(q_{z,1}d_1+q_{z,2}d_2)} + \ldots + r_{j,j+1}e^{i\sum_{k=0}^{j}q_{z,k}d_k} + \ldots + r_{N,N+1}e^{i\sum_{k=0}^{N}q_{z,k}d_k} \tag{2.34}$$

where we used $q_{z,j} = 2k_{z,j} = \frac{4\pi}{\lambda}\sin\theta_j$, the wavevector transfer in medium j. The reflection coefficients $r_{j,j+1}$ can be rewritten in terms of $q_{z,j}$:

$$r_{j,j+1} = \frac{q_{z,j} - q_{z,j+1}}{q_{z,j} + q_{z,j+1}} \tag{2.35}$$

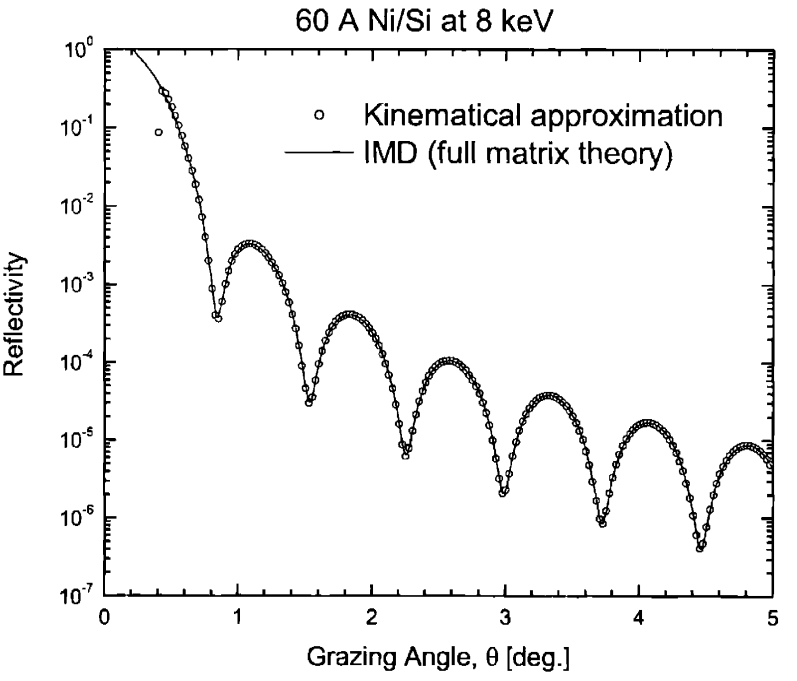

Figure 2.7: The kinematical theory approximation (eq. **(2.33)**) was used to calculate the reflectivity at 8 keV for a 60 Å Ni layer on Si, as shown by the open dots. The approximation fails at angles close to the critical angle ($\theta_c = 0.402^0$ at 8 keV for Ni) because multiple reflections are not negligible near the total reflection plateau. The continuous line represents a full theoretical calculation with IMD and it can be seen how the kinematical approximation misses the total reflection but agrees perfectly with the exact theory at angles larger than θ_c (the difference cannot be distinguished for $\theta > 0.45^0$).

By examining eq. (2.34), we observe that multiple reflections at the interfaces are now excluded because there are no products $r_{j,j+1}r_{j+1,j+2}$ present.

The next approximation would be to assume negligible refraction and take $q_{z,1} = q_{z,2} = ... = q_z$, so that eq. (2.34) becomes:

$$r = \sum_{j=0}^{N} r_{j,j+1} e^{iq_z \sum_{m=0}^{j} d_m} \tag{2.36}$$

A final approximation could be made for the $r_{j,j+1}$ reflection coefficients in (2.36) if we assume that the change in $q_{z,j}$ is not significant from one layer to the next:

$$r_{j,j+1} = \frac{q_{z,j}^2 - q_{z,j+1}^2}{\left(q_{z,j} + q_{z,j+1}\right)^2} \approx \frac{q_{c,j+1}^2 - q_{c,j}^2}{4q_z^2} = \frac{4\pi r_e\left(\rho_{j+1} - \rho_j\right)}{q_z^2} \tag{2.37}$$

where $q_{c,j}^2 = 16\pi r_e \rho_j$, r_e being the classical electron radius and ρ_j the electron density. With these approximations, the reflection coefficient can be written as

$$r = \frac{4\pi r_e}{q_z^2}\sum_{j=1}^{N}\left(\rho_{j+1} - \rho_j\right)e^{iq_z Z_{j+1}} \tag{2.38}$$

In the limit of infinitely thin layers and $N \to \infty$, the sum above becomes an integral:

$$r = \frac{4\pi r_e}{q_z^2}\int_{-\infty}^{+\infty}\frac{d\rho(z)}{dz}e^{iq_z z}dz \tag{2.39}$$

Now the expression for the reflectivity of this medium with a continuous variation of the electron density $\rho(z)$ is:

$$R(q_z) = r \cdot r^* = \left(\frac{4\pi r_e}{q_z^2}\right)^2\left|\int_{-\infty}^{+\infty}\frac{d\rho}{dz}e^{iq_z z}dz\right|^2 \doteq R_F(q_z)\left|\frac{1}{\rho_s}\int_{-\infty}^{+\infty}\frac{d\rho}{dz}e^{iq_z z}dz\right|^2 \tag{2.40}$$

The factor $R_F(q_z)$ above is the asymptotic expression for the Fresnel reflectivity:

$$R_F(q_z) = \frac{\left(4\pi r_e \rho_s\right)^2}{q_z^4} = \frac{q_c^4}{16q_z^4} \simeq \frac{\theta_c^4}{16\theta^4} \tag{2.41}$$

The expression for $R(q_z)$ can be cast in the form of a density autocorrelation function if we use the chain rule for the integral:

$$\frac{1}{\rho_s}\int_{-\infty}^{+\infty}\frac{d\rho}{dz}e^{iq_z z}dz = \frac{1}{\rho_s}\left[\rho(z)e^{iq_z z}\Big|_{z\to-\infty}^{z\to\infty} - \int_{-\infty}^{+\infty}\frac{de^{iq_z z}}{dz}\rho(z)dz\right] =$$

$$= -\frac{iq_z}{\rho_s}\int_{-\infty}^{+\infty}\rho(z)e^{iq_z z}dz \tag{2.42}$$

Back to eq. (2.40),

$$R(q_z) = \frac{\left(4\pi r_e\right)^2}{q_z^2}\left|\int_{-\infty}^{+\infty}\rho(z)\cdot e^{iq_z z}dz\right|^2 = \frac{\left(4\pi r_e\right)^2}{q_z^2}\iint\rho(z)\rho(z')e^{iq_z(z-z')}dzdz' \tag{2.43}$$

The integral in the last term of (2.43) is the autocorrelation function of the electron density in the direction normal to the medium surface. Also, eq. (2.43) is the Born approximation

formula for x-ray scattering that can be retrieved (see [1]) starting with the scattering cross section expression:

$$\frac{d\sigma}{d\Omega} = r_e^2 \iint \rho(\mathbf{r})\rho(\mathbf{r}')e^{i\mathbf{q}\cdot(\mathbf{r}-\mathbf{r}')}d\mathbf{r}d\mathbf{r}' \qquad (2.44)$$

To sum up, the approximations considered in this section were the following:

1. neglect multiple reflections from the interfaces (no second and higher order reflectivity coefficient terms are considered).
2. refraction effects are neglected for q_z.
3. the reflection coefficient at each interface is proportional to the difference in ρ, the electron density.

These approximations constitute altogether the frame of the so-called "kinematical theory" of reflectivity. The kinematical theory is equivalent to the Born approximation for scattering and is successful in describing the reflectivity from a stratified medium for $q \gg q_c$, i.e., at large momentum transfer. The advantage of this theory is a faster derivation and simpler expression for the reflectivity, also showing the physics of scattering from the interfaces.

2.6 The treatment of roughness in specular reflectivity

When the interface between the layer j and $j+1$ is not perfectly flat but has some 2-dimensional fluctuations from the average: $Z_j \to Z_j + z_{j+1}(x,y)$ with $\langle z_{j+1}(x,y)\rangle = 0$, the coefficients of reflection must be averaged over the lateral directions (x,y). Returning to the matrix treatment, eq. (2.18), we need to recast the form of the equations so that the $z_{j+1}(x,y)$ terms are in the right-hand side of the equation:

$$\begin{pmatrix} A_j^+ \\ A_j^- \end{pmatrix} = \begin{pmatrix} p_{j,j+1}e^{i(k_{z,j+1}-k_{z,j})Z_{j+1}}e^{i(k_{z,j+1}-k_{z,j})z_{j+1}(x,y)} & m_{j,j+1}e^{-i(k_{z,j+1}+k_{z,j})Z_{j+1}}e^{-i(k_{z,j+1}+k_{z,j})z_{j+1}(x,y)} \\ m_{j,j+1}e^{i(k_{z,j+1}+k_{z,j})Z_{j+1}}e^{i(k_{z,j+1}+k_{z,j})z_{j+1}(x,y)} & p_{j,j+1}e^{-i(k_{z,j+1}-k_{z,j})Z_{j+1}}e^{-i(k_{z,j+1}-k_{z,j})z_{j+1}(x,y)} \end{pmatrix} \begin{pmatrix} A_{j+1}^+ \\ A_{j+1}^- \end{pmatrix}$$

(2.45)

Taking the average over (x,y), and assuming a Gaussian distribution $z_{j+1}(x,y)$ with a variance σ_j^2 (or a power expansion of any distribution up to the second order σ_j^2), we obtain the average field components at the interface:

$$\left\langle \begin{pmatrix} A_j^+ \\ A_j^- \end{pmatrix} \right\rangle = \begin{pmatrix} p_{j,j+1} e^{i(k_{z,j+1}-k_{z,j})Z_{j+1}} e^{-(k_{z,j+1}-k_{z,j})^2 \sigma_{j+1}^2/2} & m_{j,j+1} e^{-i(k_{z,j+1}+k_{z,j})Z_{j+1}} e^{-(k_{z,j+1}+k_{z,j})^2 \sigma_{j+1}^2/2} \\ m_{j,j+1} e^{i(k_{z,j+1}+k_{z,j})Z_{j+1}} e^{-(k_{z,j+1}+k_{z,j})^2 \sigma_{j+1}^2/2} & p_{j,j+1} e^{-i(k_{z,j+1}-k_{z,j})Z_{j+1}} e^{-(k_{z,j+1}-k_{z,j})^2 \sigma_{j+1}^2/2} \end{pmatrix} \left\langle \begin{pmatrix} A_{j+1}^+ \\ A_{j+1}^- \end{pmatrix} \right\rangle \tag{2.46}$$

The effect of the averaging is thus a multiplication of the coefficient $p_{j,j+1}$ by $e^{-(k_{z,j+1}-k_{z,j})^2 \frac{\sigma_{j+1}^2}{2}}$ and of the coefficient $m_{j,j+1}$ by $e^{-(k_{z,j+1}+k_{z,j})^2 \frac{\sigma_{j+1}^2}{2}}$. We know that the reflection coefficient for the interface *j,j+1* is the ratio between $m_{j,j+1}$ and $p_{j,j+1}$ (see eq. (2.30)), so the roughness reduces the reflection coefficient by the amount

$$\frac{r_{j,j+1}^{rough}}{r_{j,j+1}^{flat}} = \frac{e^{-(k_{z,j+1}+k_{z,j})^2 \frac{\sigma_{j+1}^2}{2}}}{e^{-(k_{z,j+1}-k_{z,j})^2 \frac{\sigma_{j+1}^2}{2}}} = e^{-2k_{z,j+1}k_{z,j}\sigma_{j+1}^2} = e^{-q_{z,j+1}q_{z,j}\sigma_{j+1}^2/2} \tag{2.47}$$

The right hand side of the equation is known as the Névot-Croce [5] factor and is an exact roughness correction for the reflection coefficient of the interface. In the particular case where the Born (kinematical) approximation holds: $k_{z,j} \approx k_{z,j+1} \approx q_z/2$, then the Fresnel coefficient is reduced by the amount:

$$\frac{r_{j,j+1}^{rough}}{r_{j,j+1}^{flat}} = e^{-2k_{z,j+1}k_{z,j}\sigma_{j+1}^2} = e^{-q_z^2\sigma_{j+1}^2/2} \tag{2.48}$$

with the right hand side of (2.48) known as the Debye-Waller factor.

The treatment of the roughness effect on specular reflectivity in the frame of the matrix theory is correct, but is limited in describing only the coherent component of the reflected beam. In order to understand the off-specular scattering, a different theory must be formulated.

The starting point is to cast the Maxwell equations in an integral form, representing the total field as a resultant of the contributions of the scattering from the dipoles induced in the volume of the material. Usually, the field can be calculated for a "reference" medium with a

flat surface or a stratified medium with flat, sharp interfaces. The interface roughness can then be treated as a perturbation of the reference state and different Born approximations can be used in the integral equation for the scattered field.

Starting with the Maxwell equations:

$$\nabla \times \mathbf{E} = -\frac{\partial \mathbf{B}}{\partial t} \tag{2.49}$$

$$\nabla \times \mathbf{H} = \frac{\partial \mathbf{D}}{\partial t} \tag{2.50}$$

and applying the $\nabla \times$ operator to eq. (2.49) one obtains:

$$\nabla \times \nabla \times \mathbf{E} = -\frac{\partial}{\partial t}(\nabla \times \mathbf{B}) = -\frac{\partial}{\partial t}\left(\mu \frac{\partial \mathbf{D}}{\partial t}\right) = -\varepsilon\mu \frac{\partial^2 \mathbf{E}}{\partial t^2} = -\frac{n^2}{c^2}\frac{\partial^2 \mathbf{E}}{\partial t^2} \tag{2.51}$$

For monochromatic waves, the time dependence is of the form $e^{i\omega t}$ and $\frac{\partial^2 \mathbf{E}}{\partial t^2} = -\omega^2 \mathbf{E}$.

Introducing $k_0 = \frac{\omega}{c}$, eq. (2.51) becomes:

$$\nabla \times \nabla \times \mathbf{E} - n^2 k_0^2 \mathbf{E} = 0 \tag{2.52}$$

The perturbation of the reference state is manifested as a variation of n^2 from the reference value n_{ref}^2:

$$n^2(\mathbf{r}) = n_{ref}^2(\mathbf{r}) + \delta n^2(\mathbf{r}) \tag{2.53}$$

The field equation for a perturbed medium has now the form:

$$\nabla \times \nabla \times \mathbf{E}(\mathbf{r}) - n_{ref}^2(\mathbf{r}) k_0^2 \mathbf{E}(\mathbf{r}) = \delta n^2(\mathbf{r}) k_0^2 \mathbf{E}(\mathbf{r}) \tag{2.54}$$

The right hand side of eq. (2.54) can be interpreted equivalently as an induced dipole source due to a polarization density $\delta \mathbf{P}(\mathbf{r}) = \varepsilon_0 \delta n^2(\mathbf{r}) \mathbf{E}(\mathbf{r})$.

The formal solution of eq. (2.54) can be expressed by introducing the Green function tensor $\overline{\overline{\mathbf{G}}}(\mathbf{R},\mathbf{r}')$:

$$\begin{aligned} \mathbf{E}(\mathbf{r}) &= \mathbf{E}_{ref}(\mathbf{r}) + \varepsilon_0 \int d\mathbf{r} \delta n^2(\mathbf{r}) \overline{\overline{\mathbf{G}}}(\mathbf{R},\mathbf{r}) \cdot \mathbf{E}(\mathbf{r}) = \\ &= \mathbf{E}_{ref}(\mathbf{r}) + \int d\mathbf{r} \overline{\overline{\mathbf{G}}}(\mathbf{R},\mathbf{r}) \cdot \delta \mathbf{P}(\mathbf{r}) \end{aligned} \tag{2.55}$$

where the Green function tensor must be a solution of the propagation equation (2.54) with a Dirac delta source term in the right hand side:

$$\nabla\times\nabla\times\overline{\overline{\mathbf{G}}}(\mathbf{R},\mathbf{r}')-n_{ref}^2(\mathbf{R})k_0^2\overline{\overline{\mathbf{G}}}(\mathbf{R},\mathbf{r}')=\frac{k_0^2}{\varepsilon_0}\delta(\mathbf{R}-\mathbf{r}') \qquad (2.56)$$

and it must also satisfy the outgoing wave boundary conditions.

The Green function can be explicitly calculated for reference states, e.g., a plane boundary between vacuum and substrate, or planar multilayer structure with no interface roughness. One elegant way to calculate it is to use the reciprocity theorem [6], which states that for a given medium, two different dipole source distributions $\mathbf{P}_A$ and $\mathbf{P}_B$ and the fields they create, $\mathbf{E}_A$ and $\mathbf{E}_B$, are related by the integral identity:

$$\int d\mathbf{r}\mathbf{E}_A(\mathbf{r})\bullet\mathbf{P}_B(\mathbf{r})=\int d\mathbf{r}\mathbf{E}_B(\mathbf{r})\bullet\mathbf{P}_A(\mathbf{r}) \qquad (2.57)$$

By choosing as dipole sources: (A) a unit dipole $\hat{e}\delta(\mathbf{R}-\mathbf{r}')$ located at the detector position $\mathbf{R}$ where we measure the scattered radiation, and (B) the dipole perturbation $\delta\mathbf{P}(\mathbf{r})=\varepsilon_0\delta n^2(\mathbf{r})\mathbf{E}(\mathbf{r})$, eq. (2.57) becomes:

$$\int d\mathbf{r}'\varepsilon_0\delta n^2(\mathbf{r}')\mathbf{E}(\mathbf{r}')\cdot\mathbf{E}_{\text{det}}^{\hat{e}}(\mathbf{R},\mathbf{r}')=\delta\mathbf{E}(\mathbf{r})\cdot\hat{e} \qquad (2.58)$$

But $\delta\mathbf{E}=\mathbf{E}-\mathbf{E}_{ref}$, so (2.58) can be rewritten as:

$$\mathbf{E}(\mathbf{R})\bullet\hat{e}=\mathbf{E}_{ref}(\mathbf{R})\bullet\hat{e}+\int d\mathbf{r}'\varepsilon_0\delta n^2(\mathbf{r}')\mathbf{E}(\mathbf{r}')\bullet\mathbf{E}_{\text{det}}^{\hat{e}}(\mathbf{R},\mathbf{r}') \qquad (2.59)$$

Compared with (2.55), the Green function can be determined as the field in $\mathbf{r}'$ due to a unit dipole at $\mathbf{R}$ in the reference medium. Based on this proof, the Green function can be calculated in vacuum (the reference medium in the Born approximation) and for a planar multilayer without roughness at the interface (which is the reference for the Distorted Wave Born Approximation-DWBA theory of the diffuse reflectivity).

The solution for the vacuum reference medium is a spherical wave:

$$\mathbf{E}_{\text{det}}^{\hat{e}}(\mathbf{R},\mathbf{r}')=k_0^2(\hat{\mathbf{u}}\times\hat{\mathbf{e}})\times\hat{\mathbf{u}}\frac{e^{-ik_0R}}{4\pi\varepsilon_0R}e^{i\mathbf{k}_{sc}\bullet\mathbf{r}'} \qquad (2.60)$$

If the unit vector $\hat{e}$ is chosen normal to the scattering direction and along the *s* or *p* polarization directions, the expression above gives the field components:

$$E_{\text{det}}^{s,p}(\mathbf{R},\mathbf{r}') = k_0^2 \frac{e^{-ik_0 R}}{4\pi\varepsilon_0 R} e^{i\mathbf{k}_{sc}\cdot\mathbf{r}'} \tag{2.61}$$

The solution for a multilayer reference medium has the following form when the point $\mathbf{r}'$ is inside layer j:

$$E_{\text{det}}^{s,p}(\mathbf{R},\mathbf{r}') = k_0^2 \frac{e^{-ik_0 R}}{4\pi\varepsilon_0 R} E_j^{s,p}\left(-k_{sc,j}, z'\right) e^{i\mathbf{k}_{sc\|}\cdot\mathbf{r}_\|} \tag{2.62}$$

where $E_j^{s,p} e^{i\mathbf{k}_{sc\|}\cdot\mathbf{r}\|}$ is the field in medium j for an incident wave of s- or p-polarization and can be computed using the matrix method. The $\|$ superscript refers to vector components in a plane parallel to the interface.

Substituting the expression (2.60) in (2.59), one finds the expression of the scattered field in the Born Approximation:

$$\mathbf{E}_{sc}(\mathbf{R}) = \frac{e^{-ik_0 R}}{4\pi R} \int d\mathbf{r}\, \delta n^2(\mathbf{r}') \mathbf{E}_\perp(\mathbf{r}') e^{i\mathbf{k}_{sc}\cdot\mathbf{r}'} \tag{2.63}$$

where $\mathbf{E}_\perp = \mathbf{E} - \left(\hat{\mathbf{u}}\cdot\mathbf{E}\right)\hat{\mathbf{u}}$ is the field component normal to the direction of scattering $\hat{\mathbf{u}} = \mathbf{R}/R = \mathbf{k}_{sc}/k_0$.

The differential scattering cross section can now be calculated by integrating the flux of the Poynting vector $\mathbf{S} = \frac{nc\varepsilon_0}{2}|\mathbf{E}|^2 \hat{\mathbf{k}}_{sc}$ over the sphere of radius R, around the direction $\hat{\mathbf{k}}_{sc}$, and normalizing by the incident plane wave flux. The result is:

$$\frac{d\sigma}{d\Omega} = \frac{k_0^4}{16\pi^2 |\mathbf{E}_{in}|^2} \left| \int d\mathbf{r}' \delta n^2(\mathbf{r}') \mathbf{E}_\perp(\mathbf{r}') e^{i\mathbf{k}_{sc}\cdot\mathbf{r}'} \right|^2 \tag{2.64}$$

2.7 The First Born Approximation

The first Born approximation is valid far from the critical angle for total external reflection. The field $\mathbf{E}(\mathbf{r}')$ is approximated by the incident field in vacuum:

$$\mathbf{E}(\mathbf{r}') \approx \mathbf{E}_{in} e^{-i\mathbf{k}_{in}\cdot\mathbf{r}'} \tag{2.65}$$

Then the differential cross section (2.64) becomes:

$$\frac{d\sigma}{d\Omega}^{BA} = \frac{k_0^4}{16\pi^2}\left(\hat{\mathbf{e}}_{\mathbf{in}}\cdot\hat{\mathbf{e}}_{\mathbf{sc}}\right)^2\left|\int d\mathbf{r}\delta\, n^2 e^{i\mathbf{q}\cdot\mathbf{r}}\right|^2 \tag{2.66}$$

where $\mathbf{q}=\mathbf{k}_{sc}-\mathbf{k}_{in}$ is the wavevector transfer.

When the perturbation is a single rough surface between a medium and the vacuum, the volume integral in the cross section (2.66) is separated into an integral along the depth direction z and an integral along the plane parallel to the surface:

$$\frac{d\sigma}{d\Omega}=\frac{k_0^4}{16\pi^2}\left(n^2-1\right)^2\left(\hat{\mathbf{e}}_{in}\cdot\hat{\mathbf{e}}_{sc}\right)^2\left|\int d\mathbf{r}_{\parallel}\int_{-\infty}^{z(\mathbf{r}_{\parallel})} dz e^{i\mathbf{q}\cdot\mathbf{r}}\right|^2 \tag{2.67}$$

Integrating over z first:

$$\begin{aligned}&\frac{d\sigma}{d\Omega}=\frac{k_0^4}{16\pi^2 q_z^2}\left(n^2-1\right)^2\left(\hat{\mathbf{e}}_{in}\cdot\hat{\mathbf{e}}_{sc}\right)^2\left|\int d\mathbf{r}_{\parallel}e^{iq_z z(\mathbf{r}_{\parallel})}e^{i\mathbf{q}_{\parallel}\cdot\mathbf{r}_{\parallel}}\right|^2=\\&\frac{k_0^4}{16\pi^2 q_z^2}\left(n^2-1\right)^2\left(\hat{\mathbf{e}}_{in}\cdot\hat{\mathbf{e}}_{sc}\right)^2\int d\mathbf{r}_{\parallel}\int d\mathbf{r}_{\parallel}^{'}e^{iq_z\left(z(\mathbf{r}_{\parallel})-z(\mathbf{r}_{\parallel}^{'})\right)}e^{i\mathbf{q}_{\parallel}\cdot\mathbf{r}_{\parallel}}e^{-i\mathbf{q}_{\parallel}\cdot\mathbf{r}_{\parallel}^{'}}\end{aligned} \tag{2.68}$$

Introducing the change of variable $\mathbf{R}_{\parallel}=\mathbf{r}_{\parallel}-\mathbf{r}_{\parallel}^{'}$, eq. (2.68) becomes:

$$\frac{d\sigma}{d\Omega}=\frac{k_0^4 A}{16\pi^2 q_z^2}\left(n^2-1\right)^2\left(\hat{\mathbf{e}}_{in}\cdot\hat{\mathbf{e}}_{sc}\right)^2\int d\mathbf{R}_{\parallel}\left\langle e^{iq_z\left(z(\mathbf{R}_{\parallel})-z(0)\right)}\right\rangle e^{i\mathbf{q}_{\parallel}\cdot\mathbf{R}_{\parallel}} \tag{2.69}$$

where the average <> is a surface integral over the illuminated area A. Assuming a Gaussian distribution of the height fluctuations $z\left(\mathbf{R}_{\parallel}\right)$:

$$\left\langle e^{iq_z\left(z(\mathbf{R}_{\parallel})-z(0)\right)}\right\rangle = e^{-\frac{1}{2}q_z^2\left\langle\left(z(\mathbf{R}_{\parallel})-z(0)\right)^2\right\rangle} \tag{2.70}$$

the expression for the scattering cross section in the first Born approximation is:

$$\frac{d\sigma}{d\Omega}=\frac{k_0^4 A}{16\pi^2 q_z^2}\left(n^2-1\right)^2\left(\hat{\mathbf{e}}_{in}\cdot\hat{\mathbf{e}}_{sc}\right)^2 e^{-q_z^2\langle z\rangle^2}\int d\mathbf{R}_{\parallel}e^{q_z^2\left\langle z(\mathbf{R}_{\parallel})z(0)\right\rangle}e^{i\mathbf{q}_{\parallel}\cdot\mathbf{R}_{\parallel}} \tag{2.71}$$

The specular component has $\mathbf{q}_{\parallel}=0$:

$$\left(\frac{d\sigma}{d\Omega}\right)_{spec.}=\frac{k_0^4 A}{4q_z^2}\left(n^2-1\right)^2 e^{-q_z^2\langle z\rangle^2}\left(\hat{\mathbf{e}}_{in}\cdot\hat{\mathbf{e}}_{sc}\right)^2\delta\left(\mathbf{q}_{\parallel}\right) \tag{2.72}$$

The diffuse component has the cross section:

$$\left(\frac{d\sigma}{d\Omega}\right)_{diff.} = \frac{k_0^4 A}{16\pi^2 q_z^2}\left(n^2-1\right)^2\left(\hat{\mathbf{e}}_{inc}\cdot\hat{\mathbf{e}}_{sc}\right)^2 e^{-q_z^2\langle z\rangle^2}\int d\mathbf{R}_{\parallel}\left(e^{q_z^2\langle z(\mathbf{R}_{\parallel})z(0)\rangle}-1\right)e^{i\mathbf{q}_{\parallel}\cdot\mathbf{R}_{\parallel}} \quad (2.73)$$

2.8 Distorted Wave Born Approximation

The next step is to consider $\mathbf{E}(\mathbf{r}')$ in (2.59) as the field calculated using the matrix method or other iterative methods. The reference state is the medium with sharply defined interfaces. This approximation yields better results than the first Born approximation near the critical angle and is widely used for x-ray scattering analysis.

For a single rough interface, the DWBA treatment yields an expression similar to (2.73) for the diffuse scattering:

$$\left(\frac{d\sigma}{d\Omega}\right)_{diff.}^{DWBA} = \frac{k_0^4 A}{16\pi^2}\left(n_1^2-n_0^2\right)^2\left|t_{0,1}^{in}\right|^2\left|t_{0,1}^{sc}\right|^2\frac{e^{-\frac{1}{2}\left(q_{z,1}^2+q_{z,1}^{*2}\right)\langle z\rangle^2}}{\left|q_{z,1}\right|^2}\cos^2\psi\int d\mathbf{R}_{\parallel}\left[e^{|q_{,1}|^2\langle z(\mathbf{R}_{\parallel})z(0)\rangle}-1\right]e^{i\mathbf{q}_{\parallel}\cdot\mathbf{R}_{\parallel}}$$

(2.74)

where $\cos\psi = \hat{\mathbf{e}}_{inc}\cdot\hat{\mathbf{e}}_{sc}$ and $t_{0,1}^{in}$ and $t_{0,1}^{sc}$ are the Fresnel transmission coefficients for the angle of incidence θ_{in} and θ_{sc}. At the critical angle for total external reflection $\theta_{in}=\theta_c$, the transmission coefficients $t_{0,1}^{in}$ and $t_{0,1}^{sc}$ have a maximum and this corresponds to a maximum in the scattered intensity. Using the reciprocity theorem, it can be shown that there is another maximum for $\theta_{sc} = \theta_c$. These two maxima are called Yoneda peaks and they can be explained only in the frame of the DWBA theory.

2.9 The scattered intensity

The previous sections dealt with calculating the differential scattering cross section using different approximations, but in experiments what is directly measured is a convolution of the cross section with the incident beam divergence and the detector acceptance solid angle Ω_D.

Assuming an incident beam cross section $l_x \times l_y$ and a Gaussian distribution of the divergence of the incident beam:

$$I_{inc} = I_0 e^{-\frac{\delta\theta_{in}^2}{2\Delta\theta_{in}^2}} e^{-\frac{\delta\theta_y^2}{2\Delta\theta_y^2}} \tag{2.75}$$

where the angular standard deviation $\Delta\theta_{in}$ is measured in the plane of incidence and $\Delta\theta_y$ normal to the plane of incidence, then the scattered flux density at the detector, I_D, and the scattering cross section are related by:

$$I_D = \frac{I_0}{l_x \times l_y} \int d(\delta\theta_{in}) d(\delta\theta_y) \frac{1}{2\pi\Delta\theta_{in}\Delta\theta_y} e^{-\frac{\delta\theta_{in}^2}{2\Delta\theta_{in}^2} - \frac{\delta\theta_y^2}{2\Delta\theta_y^2}} \int \frac{d\sigma}{d\Omega} d\Omega_{\text{det}} \tag{2.76}$$

2.10 Experimental study of x-ray reflection

The details of the x-ray reflectivity setups will be discussed in Section 2.10.9. For the purpose of a brief introduction, the basic elements characteristic to many x-ray reflectometers are enumerated here:

-an x-ray source that can be conventional (sealed tube or rotating anode) or synchrotron-based (bending magnet, wiggler, or undulator)

-a monochromator with the desired resolution and throughput

-an optional beam monitor detector

-a system of slits (and/or Soller collimators) defining the incident beam divergence

-a goniometer with sample holder to control the sample position

-an optional analyzer crystal for high resolution studies

-a system of slits to define the acceptance angle of the detector

-a detector (1-D or 2-D position sensitivity optional)

The sample surface is defined as the plane (x, y) and the normal to the surface is the z axis. Depending of the number of goniometer axes available, the samples can be rotated around the θ, χ, and ϕ axes shown in Fig. 2.8.

The components of the wavevector transfer **q** are:

$$\begin{cases} q_x = k_0\left(\cos\theta_{sc}\cos\psi - \cos\theta_{in}\right) \\ q_y = k_0\cos\theta_{in}\sin\psi \\ q_z = k_0\left(\sin\theta_{in} + \sin\theta_{sc}\right) \end{cases} \tag{2.77}$$

with $k_0 = 2\pi/\lambda_0$. The angle $\theta_{in} + \theta_{sc}$ is denoted by 2θ and alternate notations for θ_{in} are θ and ω .

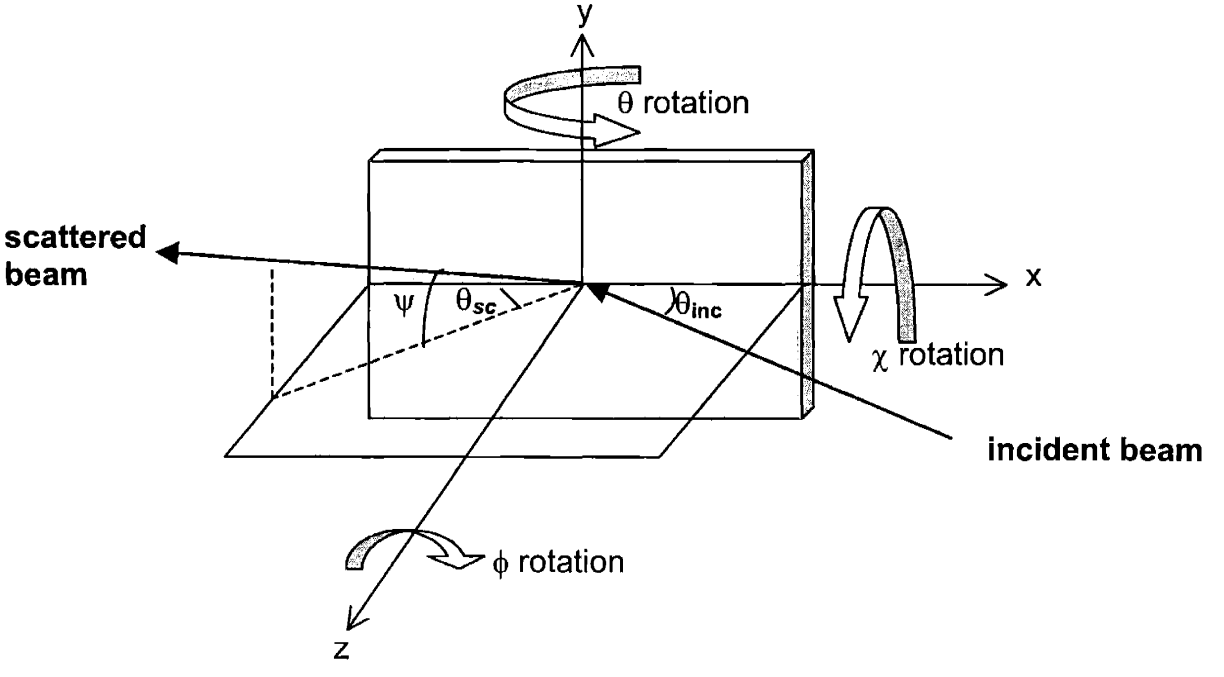

Figure 2.8: The axes and rotation angles for the general scattering geometry. The incident beam direction and the normal to the surface define the incidence plane *xz*. The scattered beam direction is described by an azimuthal angle ψ and an angle θ_{sc} in the incidence plane. The angles can be varied by rotating the sample around the *y* axis (θ rotation), *x* axis (χ angle rotation), or the *z* axis (φ rotation).

The incident beam impinges on the sample at the grazing incidence angle θ_{in}. The detector position is given by the θ_{sc} and ψ angles which are polar angles in the plane of incidence (x,z) and out of this plane in the y direction, respectively. Different combination of angle scans can be used to map different regions of the reciprocal space. Most of the scans are performed with the detector in the incidence plane $(\psi = 0)$ so the wave-vector transfer components have a simpler form:

$$\begin{cases} q_x = k_0(\cos\theta_{sc} - \cos\theta_{in}) \\ q_y = 0 \\ q_z = k_0(\sin\theta_{in} + \sin\theta_{sc}) \end{cases} \tag{2.78}$$

The standard scans in this category are:

- specular scans, with $\theta_{in} = \theta_{sc}$, or equivalently, $\omega = (2\theta)/2$. The angles ω and 2θ are scanned simultaneously while obeying the condition above. The detector measures the specularly reflected beam and maps the reciprocal space in the transversal z-direction: $\mathbf{q}:(0,0,2k_0\sin\theta)$
- offset scans, with the scattering angle 2θ varied while keeping a constant offset $\Delta\theta_0$ from the specular direction. In the reciprocal space the $\mathbf{q}$ vector tip describes a curve that can be approximated by a line making an angle $\Delta\theta_0$ with the q_z direction. This type of scan measures the diffuse component close to the specular reflection.
- rocking scans, with 2θ fixed and only the $\omega = \theta$ angle varied in the range 0 to 2θ. In the reciprocal space this describes an arc that can be approximated for small angles as a line segment parallel to the transverse q_x direction.
- detector scans, where ω is fixed and 2θ scanned above the lower limit $(2\theta)_{\min} = \omega$. This type of scan has the advantage of a constant sample illumination area during the scan.

For off-incidence plane detection $(\psi \neq 0)$ one keeps a constant ω and varies ψ. This geometry measures the q_y direction in the reciprocal space. The ψ -scan is difficult to implement because almost all reflectometers do not offer motion off the incidence plane. Usually $\psi = 0$ and the slits are open wide in the y direction so that the measured beam is integrated with a wider acceptance angle, resulting in a larger number of counts and better statistics.

2.10.1 Resolution

For in-plane scattering and small angles, the resolution in the reciprocal **q** space depends on the grazing and exit angles and the angular divergence and acceptance angles $\Delta\theta_{in}$ and $\Delta\theta_{sc}$:

$$\begin{cases} \delta q_x = k_0\sqrt{\theta_{in}^2\Delta\theta_{in}^2 + \theta_{sc}^2\Delta\theta_{sc}^2} \\ \delta q_z = k_0\sqrt{\Delta\theta_{in}^2 + \Delta\theta_{sc}^2} \end{cases} \tag{2.79}$$

The resolution in q determines the maximum length scales that can be coherently probed by the scattering experiment.

2.10.2 Data normalization

The detected photons are recorded either as counts if the detector works in pulse mode or as a current if in current mode. Irrespective of the working mode, the detector readout, I, must be proportional to the flux of photons reaching the detector. The data must be corrected for different factors due to geometry of the setup or due to time variations of the intensity of the x-ray source.

2.10.3 Footprint correction

If the sample dimension along the x axis is l and the beam width along the y axis is b_{in}, then for all grazing angles less than $\theta_{in,0} = \sin^{-1}(b_{in}/l)$ the beam footprint is larger than the sample. The fraction of beam falling off the sample will not be reflected and the intensity $I(\theta)$ will drop below the expected value. Assuming a uniform rectangular flux distribution of the incident beam, the specular data must be corrected by a factor:

$$f_{spec,in}(\theta_{in}) = \sin\theta_{in}/\sin\theta_{in,0} \tag{2.80}$$

for all $\theta_{in} \le \theta_{in,0}$. If the detector slit has a width b_{sc} smaller than the beam width b_{in}, another correction factor must be applied:

$$f_{spec,sc} = b_{in}/b_{sc} \tag{2.81}$$

In conclusion, the specular reflectivity is corrected for the finite beam size effects using the formula:

$$R(\theta) \doteq R(\theta_{in}) = f_{spec,in}(\theta_{in}) f_{spec,sc} \frac{I_{spec}(\theta_{in})}{I_0} \tag{2.82}$$

where I_0 is the intensity of the incident beam.

For diffuse measurements, when $\theta_{in} \le \theta_{in}^0 = \sin^{-1}(b_{in}/l)$, the area illuminated is less than the full sample area, so the correction factor must account for it:

$$f_{diff,in}(\theta_{in}) = \sin\theta_{in}^0 / \sin\theta_{in} \tag{2.83}$$

Similarly, if the area seen by the detector is less than the area illuminated by the beam, another correction factor must be used for diffuse intensity measurements:

$$f_{diff,sc}(\theta_{in},\theta_{sc}) = \frac{b_{sc}}{l f_{diff,in}(\theta_{in})} \text{ if } \theta_{sc} > \sin^{-1}\left(\frac{b_{sc}}{l f_{diff,in}(\theta_{in})}\right) \tag{2.84}$$

The diffuse measurement data $I_{diff}(\theta_{in},\theta_{sc})$ are to be compared with the model scattering cross section (integrated over the detector solid angle $d\Omega_{sc}$):

$$\int \frac{d\sigma}{d\Omega} d\Omega = \frac{I_{diff,in}(\theta_{in},\theta_{sc})}{I_0 f_{diff,in}(\theta_{in}) f_{diff,sc}(\theta_{in},\theta_{sc})} \tag{2.85}$$

These footprint corrections are usually applied for high energy measurements, where $\theta_{in,0}$ is comparable with the critical angle and/or the features of interest in the reflectivity plot. For example, at 60 keV, for a W/Si multilayer sample with l=50 mm, b_{in} = 0.1 mm, the critical angle is at θ_c= 0.064° and $\theta_{in,0}$ = 0.115°. The footprint correction must be clearly applied in this case in order to properly plot the reflectivity for angles less than $\theta_{in,0}$. However, when scanning the same sample at 8 keV, the critical angle position at $\theta_c \approx 0.45°$ is above the range $0 \le \theta \le \theta_{in,0}$=0.115° where the footprint correction is applied. Since the interesting features of the reflectivity plot (fringes, Bragg peaks, etc.) are at angles larger than the critical angle θ_c, the correction doesn't contribute with useful information and can be omitted.

2.10.4 Correction for time variations

If the x-ray source has either long-term variations (e.g., storage ring decay time) or short-term transients or fluctuations, a second detector is used to monitor the fluctuations of the direct incident beam. An additional correction must be factored in:

$$f_{monitor} = \frac{M_0}{M(\theta)} \tag{2.86}$$

where M_0 is the monitor current when recording the direct beam I_0 and $M(\theta)$ is the monitor readout at the time of the measurement of $I(\theta)$. For the SAO reflectometer, no monitor detector was used, because the flux from the x-ray tube is constant in time over the duration of the measurements. For reflectivity measurements at the synchrotron radiation source, the beam decay time is significant for the duration of the typical reflectivity scan, so a monitor detector was used (more details in Section 5.1.3).

2.10.5 Background corrections

The background of the detector, $B(\theta)$, must be subtracted for every readout $I(\theta)$. The formula for calculating the experimental specular reflectivity is:

$$R(\theta) = f_{spec,in}(\theta_{in}) f_{spec,sc} \frac{I_{spec}(\theta_{in}) - B(\theta_{in})}{I_0 - B_0} \frac{M_0 - B_{M,0}}{M(\theta_{in}) - B_M} \tag{2.87}$$

The background can be as low as $B_0 = 0.03$ cps in the case of the SAO XRR system using a NaI detector and a slow coincidence circuit to reject signals outside the photopeak window. In this case, the background correction is negligible. However, for ionization chamber detectors used at the Brookhaven National Laboratory synchrotron source, the background B_0 was of the order of 200 cps and produced a significant correction for the measured reflectivity.

2.10.6 The deadtime correction

An additional correction must be taken into account for detectors working in pulse mode (e.g., NaI) when the time interval between two successive counts is comparable to the dead time of the detection chain (detector, preamplifier, and amplifier). For paralyzable detectors with a dead time τ , the true count rate I_{true} and the measured count rate $I_{meas.}$ are related by the equation:

$$I_{true} = \frac{I_{meas.}}{1 - \tau \, I_{meas.}} \tag{2.88}$$

2.10.7 Computation of the specular reflectivity of multilayered structures

The measured reflectivity can be used to determine film thicknesses, densities, roughnesses, and optical constants. Once the specular reflectivity has been determined experimentally as above, it is adjusted against a computed reflectivity based on a set of parameters describing the sample investigated. This section describes the IMD software package and its general features. Some features like polarization and confidence interval computation were not used routinely for our purposes, but are introduced here for reference.

IMD [7] is a general-purpose computer program for modeling optical properties (reflectivity, transmission, absorption, and electric field distribution) of multilayers. Any number of layers can be designated and they can be grouped together to define a periodic or a depth-graded structure. The optical constants database is a directory of ASCII files listing the optical data α and β for a material for wavelengths from infrared to hard x-rays. The database contains 150 materials files compiled from published sources. User defined optical constants files can be created and added easily. The width of each interface profile function is characterized by a parameter σ, which is a measure of the r.m.s. interfacial roughness, in the case of a purely rough interface, an interface width in the case of a purely diffuse interface, or a combination of the two in the case when both roughness and diffuseness are present (as is the case for all samples discussed in this work).

The reflection and transmission coefficients are calculated for each interface using the modified Fresnel coefficients. The user can select to use either the Névot-Croce or the

Debye-Waller factors (introduced in Section 2.6) to account for roughness and diffuseness at the interfaces.

The IMD software takes in account the beam polarization and the detector sensitivity to polarization. In the case of an incident beam of mixed *s*- and *p*- polarization, the user defines the value of the incident polarization factor:

$$f = \frac{I^s - I^p}{I^s + I^p} \tag{2.89}$$

where I^s and I^p are the incident beam intensities for *s*- and *p*-polarization, respectively. The analyzer polarization sensitivity, q, is defined as the ratio between the *s*-polarization sensitivity to the *p*-polarization sensitivity. For example, an unpolarized beam has a polarization factor $f = 0$ and an *s*-polarized beam a factor $f = 1$. An ordinary detector is insensitive to the radiation polarization and thus has sensitivity $q = 1$. The IMD software calculates separately R^s, the *s*-polarization reflectivity, and R^p, the *p*-polarization, and then outputs the polarization-averaged reflectivity:

$$R^{av} = \frac{R^s q(1+f) + R^p(1-f)}{f(q-1) + (q+1)} \tag{2.90}$$

In the case of finite angular resolution, $\delta\theta$, or finite spectral resolution, $\delta\lambda$, IMD calculates the optical function requested (e.g., reflectivity) and then convolutes the result with a Gaussian distribution in angle (or energy) with a standard deviation $\delta\theta$ (or $\delta\lambda$, respectively).

The first step in modeling the experimental data is to start with the design values for the multilayer structure (thicknesses, densities, and interface roughnesses). Up to eight independent parameters can be varied and an unlimited number of parameters can be coupled so they are dependent on each other. By varying the parameters selected, the user can determine by comparison with the experimental data what values give a better agreement. Using these as initial values and providing a range of variation, a non-linear least square fitting procedure can be performed automatically. The fit routine exits when the χ^2 value is changing by less than a specified amount or when the number of maximum iterations was reached. The user can choose different weights for the experimental data:

- instrumental weighting, using experimental errors: $w[i] = \delta R_m[i]$
- statistical weighting, using: $w[i] = \sqrt{R_m[i]}$
- uniform weighting, with $w[i] = 1$.

The quantity minimized by the fitting algorithm is:

$$\chi^2 = \sum_i \frac{\left(R[i] - R_m[i]\right)^2}{w[i]^2} \tag{2.91}$$

where R is the calculated and R_m is the measured reflectivity. If the optional "logarithmic fitting" is used, the numerator uses the logarithms of the reflectivities:

$$\chi^2 = \sum_i \frac{\left(\ln R[i] - \ln R_m[i]\right)^2}{w[i]^2} \tag{2.92}$$

IMD can compute multidimensional confidence intervals associated with the best-fit values of the adjustable parameters. The confidence region, with statistical significance α, is defined as the p-dimensional region of parameter space for which the value of χ^2 is less than some limit value χ_L^2:

$$\chi_L^2 = \chi_{\min}^2 + \Delta\chi^2(\alpha) \tag{2.93}$$

with $\Delta\chi^2(\alpha)$ equal to the value of the χ^2 probability function with p degrees of freedom and statistical significance α.

2.10.8 The x-ray reflectometer setup

For the purpose of measuring the structure (thickness and interface widths) of x-ray multilayers, a dedicated reflectometer was built as part of this work at SAO. A picture with a perspective view of the reflectometer during the measurement of a coated mirror shell is shown in Figure 2.9. The dimensions and the main components of the reflectometer can be seen more clearly in the schematic drawing presented in Figure 2.10.

As a trade-off between penetration depth at high energy and better angular resolution at low energy (due to larger angular separation between peaks, etc.), the x-ray source chosen was a

copper anode tube with a characteristic line at 8.048 keV (Cu K_α). The size of the beam exiting from the x-ray tube is defined by the slit S_1 (see Figure 2.10) and is incident on an asymmetrically cut Ge <111> crystal. After the Ge monochromator, the beam is collimated by the pair of slits S_2 and S_3 (Fig. 2.10) and falls on the surface of the sample. The dimensions of the beam $l_x \times l_z$ and its divergence $\delta\theta$ are easily controlled by S_3, which has four stepper motors moving the horizontal and vertical blades of the slit. The beam reflected off the sample enters the detector acceptance slit S_4 and the scintillator detector (Fig.2.10, left).

The sample must be accurately positioned during the alignment procedure (described in the next section) and during the measurement. A small, flat sample requires a minimum of one motorized axis for translation in the z direction (perpendicular to the beam) during alignment, with 1 μm or less translation accuracy. A large sample requires in addition vertical (x axis) translation and longitudinal (y axis-along beam) horizontal translation in order to scan the beam over the surface of the sample if necessary. The SAO reflectometer has a precision table with ±75 mm travel, 1μm precision for the y and z axes and a vertical translation stage with ±50 mm travel, 2 μm precision for the x axis.

The rotations around the θ axis for the sample and 2θ axis for the detector are performed by the Huber goniometer shown in the center of Figs. 2.9 and 2.10. For figured samples (integral or segments of conical shells), an additional degree of freedom is provided by a motorized rotation stage for the ϕ axis (not shown in the figures). The total number of degrees of freedom that can be controlled for the sample is 5 (3 translation + 2 rotation), with the sixth (rotation around the χ axis) in the process of installation.

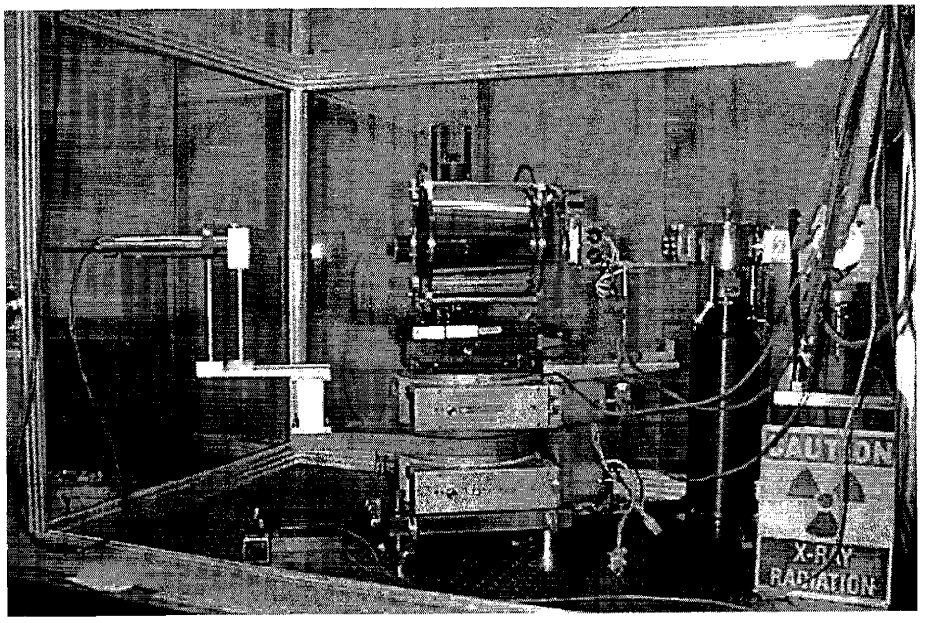

Figure 2.9: The x-ray reflectometer at SAO is shown scanning a cylindrical telescope shell (center). The copper anode x-ray tube is on the rightmost side and emits an x-ray beam to the left. The monochromator is a Ge crystal that reflects only the Cu K_α line (8.05 keV). The monochromated beam is further collimated by two slits and is incident on the sample. The beam reflected by the sample is collected by a NaI scintillator detector shown on the left side. For a schematic of the main components, see Fig. 2.10.

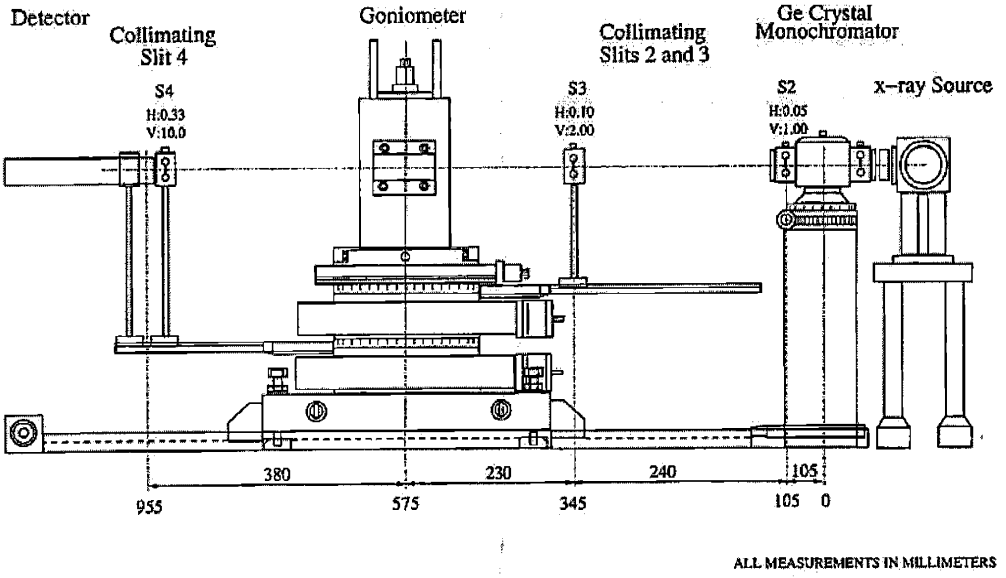

Figure 2.10: Schematics of the x-ray reflectometer with the principal components. From right to left: the x-ray tube, the monochromator box housing the Ge crystal, the collimation slits S_2 and S_3, the two-axis goniometer with the *yz* table and vertical stage, the detector acceptance slit S_4, and the scintillator crystal. (Drawing by courtesy of R.Bruni-SAO)

2.10.9 Sample alignment

In a reflectivity measurement, the first step is to verify that the origin for the detector motion 2θ is correct, i.e., if the beam is directly incident into detector and no sample is present, then $2\theta = 0^0$. After checking the zero of 2θ, the sample must be positioned such that:

1. the normal vector to its surface is in the plane defined by the incident beam direction and the detector direction
2. the goniometer rotation axis θ lies on the surface of the sample.

Any sample alignment procedure that doesn't satisfy both conditions produces an incorrect reflectivity scan, as described below.

If the sample normal vector makes an angle $\chi \neq 0$ with the specular reflection plane (condition 1 not fulfilled), then the angle of incidence on the sample θ_{inc} and the sample rotation angle θ are not identical and are related by the equation:

$$\sin\theta_{inc} = \sin\theta \cdot \cos\chi \qquad (2.94)$$

Assuming that the detector has a large acceptance angle, so that it still intercepts the full reflected beam, the measured reflectivity scan R vs. θ will be shifted due to the difference between θ_{inc} and θ. If the detector acceptance angle is small (due to a narrow slit), it is possible that some reflected photons will not reach the detector and the measured reflectivity will be less than the true reflectivity.

The second requirement for a precise sample alignment is to have the goniometer rotation axis θ lying in the plane of the sample surface. If the θ-axis is parallel to the sample, but a distance $\delta z \neq 0$ away from the sample surface (see Fig. 2.11), then the incidence angle changes from θ to $\theta + \delta\theta$, where it can be shown that $\delta\theta \approx \frac{\cos\theta \cdot \delta z}{L} \approx \frac{\delta z}{L}$, L being the distance between the x-ray source and the sample. Again, the R vs. θ scan will be shifted from the true values by the misalignment angle $\delta\theta$.

The procedure for the sample alignment is based on an iteration of a few basic translation and rotation scans until the corrections are smaller than the accuracy of the stages.

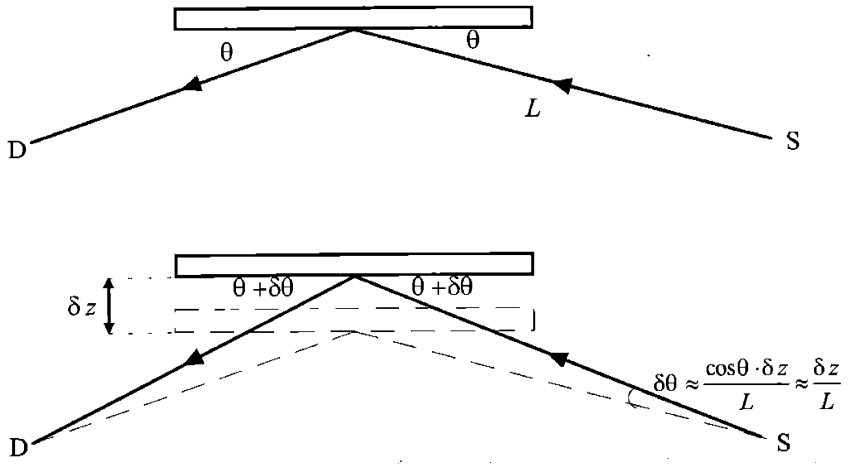

Figure 2.11: (top) Sample surface aligned correctly with the rotation axis θ in a specular reflectivity scan. **(bottom)** Same type of scan, but the sample was shifted by a distance δz from the rotation axis θ. The error in the grazing angle is $\delta\theta$.

For a rough alignment, the detector is removed and a laser beam is coaligned with the x-ray beam. With the sample not yet installed, the laser beam must pass through all the slits and impinge on the center of the monochromator crystal. Next, the sample is mounted on its holder and the rough sample alignment can be done by using the laser beam spot to indicate where the x-ray beam footprint will fall.

The scintillator detector is then mounted back and the sample is moved in the z direction until it blocks half of the flux of the direct beam I_0. A preliminary sample rocking scan determines the zero for the θ axis. Next, a quick $(\theta - 2\theta)$ scan determines the major features in the reflectivity plot, for example, the presence of a Bragg peak located at θ_B. With this information about the sample reflectivity, the alignment proceeds with a series of corrections for the zero of the z and θ positions:

1. The detector is positioned at $2\theta_B$ and a sample rocking scan is performed around $\theta = \theta_B$. If the centroid of the peak is not exactly equal to θ_B, it is set to this value.
2. The sample and detector are moved to $\theta = 0$ and $2\theta = 0$. The count rate must be exactly $I_0/2$, otherwise the sample is translated along the z axis until the count rate is equal to $I_0/2$ and the current z position is set as $z = 0$.

The iteration steps 1 and 2 are repeated until the corrections for z and θ are less than 1 μm and 0.001^0, respectively, which correspond to the accuracy of the linear stage and of the goniometer motion. For figured samples, additional iteration steps include the corrections of the zeros of the vertical stage and the rotation axis ϕ.

Once the alignment process is completed, the x-ray reflectivity measurements continue with the θ -2θ scan necessary to acquire the specular reflectivity profile $R(\theta)$.

References for Chapter 2

1. F.de Bergevin, *Interaction of X-rays (and Neutrons) with Matter*, in *X-Ray and Neutron Reflectivity: Principles and Applications*, Eds.J.Daillant and A.Gibaud, *Lecture Notes in Physics*, vol. m58, 1999, Springer: New York, p. 3-56.

2. B.L. Henke, E.M. Gullikson, and J.C. Davis, *"X-ray interactions: photoabsorption, scattering, transmission, and reflection at E=50-30000 eV, Z=1-92"*, Atomic Data and Nuclear Data Tables **54**, 1993, pp. 181-342.

3. C.T.Chantler, *"Theoretical Form Factor, Attenuation, and Scattering Tabulation for Z=1-92 from E=1-10 eV to E=0.4-1.0 MeV"*, J.Phys.Chem.Ref.Data **24**, 1995, pp. 71.

4. L.G. Parratt, *"Surface studies of solids by total reflection of X-rays"*, Physical Review **95**, 1954, pp. 359-369.

5. L. Névot, B. Pardo, and J. Corno, *"Characterization of X-UV multilayers by grazing incidence X-ray reflectometry"*, Revue Phys. Appl. **23**, 1988, pp. 1675-1686.

6. P.Lorrain and D.R.Corson, *Electromagnetic Fields and Waves*, 1970, San Francisco: W.H.Freeman and Co.

7. D.L. Windt, *"IMD: Software for modeling the optical properties of multilayer films"*, Computers in Physics **12**, 1998, pp. 360-370.

Chapter 3: Sputtering Deposition

This chapter introduces the deposition process used in this work for the preparation of x-ray multilayers and describes the apparatus and experimental conditions in which the depositions were performed. Section 3.1 discusses significant aspects of the physics of sputtering: sputtering yield, energy and angular distribution of sputtered species and energetic neutrals. Section 3.2 proceeds with a short overview of the different implementations of the sputtering process for thin film deposition applications. The focus of Section 3.3 is the description of the magnetron sputtering chambers that were set up at SAO as part of this work. The next section reviews the topics of nucleation and growth of films and introduces the zone models for sputtered films. The conclusion of Section 3.4 concentrates on the effect of energetic neutrals on the growth surface morphology, which is directly related to x-ray reflectivity performance by the interface roughness parameter σ.

3.1 Physics of sputtering

3.1.1 General aspects of sputtering

Sputtering is a physical process in which an energetic particle bombards the surface of a target material with sufficient energy to result in the ejection of one or more atoms from the target. The process is characterized by the sputter yield Y, defined as the ratio of emitted atoms to the number of bombarding particles. The most commonly used species of bombarding particles is an inert gas ion (usually Ar^+) but sputtering can result also from other types of incident particles (atoms, molecules, electrons, and photons). Ions and neutral atoms of the same element and with the same energy produce identical collisional cascades and sputtering results. This happens because the ion becomes neutralized very close to the surface by attracting an electron. However, since it is easier to generate large

fluxes of ions and accelerate them to the desired energy, all sputtering applications use ions as the bombarding species.

Depending on the kinetic energy of the incident ions, the physical processes in the sputtering target can be classified as:

1. Low energy regime (E < 20-50 eV). Also known as the subthreshold region, in this regime the energy of the incident ion is less than the binding energy of the target atoms. Experimentally, extremely small sputtering yields in the 10^{-6} range have been measured below 15 eV, suggesting that it possible for surface atoms to be displaced even at these low energies. This regime is not important for coating applications.
2. Moderate energy (50 eV < E < 1000 eV). In this range, the incident ion impacts a target atom in a primary collision and then generates a cascade of secondary collisions until the energies of the primary ion and of all the recoil atoms become less than the displacement energy for an atom in the target material. In the process, one or more recoils can be lost by leaving the material if their momentum is directed towards the surface and their energy is enough to overcome the slowing down due to electronic collisions and the surface binding energy. The schematic of the sputtering process in this regime is illustrated in Figure 3.1. It is important to note that in addition to the sputtered atoms, other particles are emitted from the target material: reflected particles (neutral atoms, ions), secondary electrons and photons (UV and soft x-rays). This is the regime used in sputtering depositions.
3. High energy (1 keV < E < 50 keV). At these energies, the ions create a region with a high density of overlapping collision cascades. In the volume of this region, the energy of the atoms is treated in a statistical mechanics approach and the theory ([1]) is well developed and accepted. The collisional cascades are created at depths larger than the escape depth for recoils, so the sputtering yield is comparable to case 2 above (moderate ion energy bombardment).
4. Very high energy (E> 50 keV). In this regime, the incident ion is implanted into the bulk of the target and very few atoms are sputtered from the surface layers.

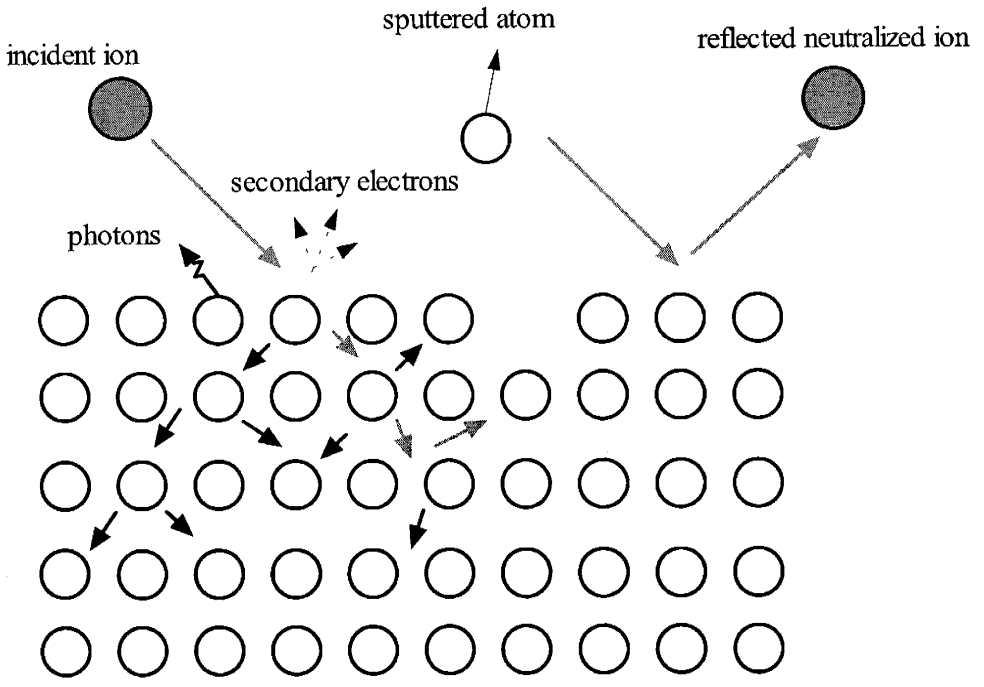

Figure 3.1: Schematic of the physical sputtering process at energies in the range 50 eV< E < 1000 eV. The incident ion (gray circle) creates a cascade of atomic collisions in the surface layers of the target material. Following this stochastic process, an average number Y (sputter yield) of target atoms are ejected from the target. Other emitted particles are: reflected neutralized ions, secondary electrons, and photons.

3.1.2 The SRIM simulation code

The sputtering process must be evaluated theoretically by Monte Carlo simulations of the interactions of a large number of incident ions and then averaging the results. The most widely used computer code is SRIM (previously known as TRIM [2]), developed in the 80's at IBM Research and constantly improved over the years. SRIM is actually a group of programs which calculate the stopping and range of ions (10 eV-2 GeV /amu) into matter using a quantum mechanical treatment of ion-atom collisions. During collisions, the ion and atom have a screened Coulomb collision, including exchange and correlation interactions between the overlapping electron shells. The ion also has long range interactions with target atoms creating electron excitations and plasmons within the target. These are described by including a description of the target's collective electronic structure and interatomic bond structure when the calculation is set up. The charge-state of the ion within the target is characterized by an effective charge, which includes a velocity

dependent charge state and long range screening due to the collective electron sea of the target. The probability of an atomic collision and the angular distribution of recoils are determined by a Monte Carlo randomization procedure. One of the options of the code is to follow the history of each collision until all atoms have energies less than the displacement energy in the respective target material. This detailed collision history mode was used in all our sputtering simulations with the SRIM code (e.g., Sect. 3.1.5).

3.1.3 Sputter yield dependence

Since sputtering is a process dominated by the momentum and energy transfer between the incident ion and the target atoms, the sputter yield is primarily dependent on the particular species used. The yields are widely different for different materials using the same ion species and energy, as shown in Figure 3.2. This is due to the differences in surface binding energies, but also to the efficiency of the momentum transfer process. In general, the sputter yield is higher for materials with lower binding energies.

The energy transferred by a projectile with mass M to the recoil atom with mass m is proportional to the ratio:

$$\frac{mM}{(m+M)^2} \tag{3.1}$$

This expression has a maximum value when $m = M$ and indicates that for kinematical reasons the sputter yield is low when the relative mass ratio m/M is either too small or too large.

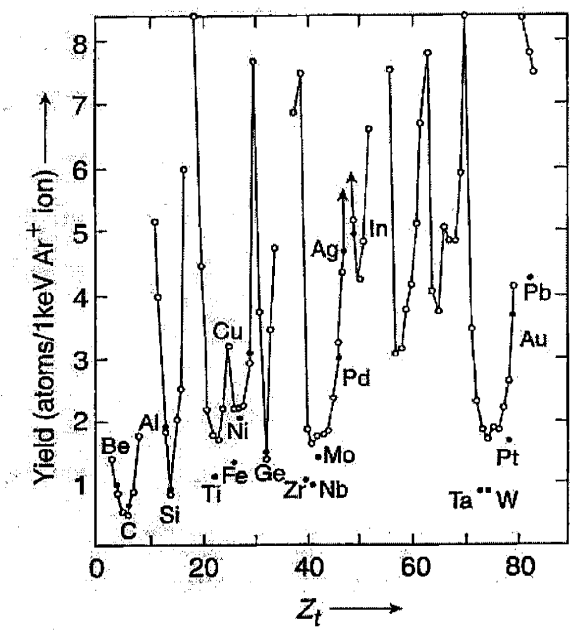

Figure 3.2: Sputtering yield versus target atomic number for incident Ar^+ ions with 1000 eV kinetic energy. (Reproduced from [3]).

The angle of incidence of the bombarding ion also influences the sputtering process. At normal incidence, the probability of escape of the recoils from an "escape depth" d is proportional with the amount of energy deposited by the ion in the surface layer with thickness d. This probability increases as $1/\cos\theta$ as the incidence angle increases from 0° (normal incidence) because the escape depth intercepts a path length $d/\cos\theta$ of the incident ion and thus the probability of collisions is increased. However, as the incidence angle becomes more grazing (θ above approaches 90°), the probability of elastic reflection increases resulting in low deposited energy and low sputtering yield. In consequence, the sputter yield peaks as a function of angle at around $70\text{-}80^\circ$. For plasma ion bombardment, as in magnetron sputtering, the ions are extracted and accelerated from the plasma sheath along the electric field lines. Because the field $\mathbf{E}$ is normal to the surface of the sputtering target, the Ar^+ ions arrive at the target at normal incidence.

3.1.4 Energy and angular distribution of sputtered atoms

Sputtering is different from other physical vapor deposition processes mainly because the kinetic energy of the atoms ejected from the target can be significantly higher. Figure 3.3 shows the calculated kinetic energy distributions for Cu atoms evaporated at 1500 K and also for Cu atoms sputtered with Ar^+ ions at 500 eV at normal incidence. The energy distribution for the evaporated copper atoms was calculated using a Maxwellian energy distribution, while for the sputtered atoms it was determined using the SRIM simulation program with full collision tracking. The average kinetic energies are 0.19 eV for evaporated atoms versus 23.3 eV for sputtered atoms. The sputtered Cu atoms will have more mobility as adatoms when growing a film on the substrate and this represents one of the advantages of sputtering over other vapor deposition methods.

The angular distribution of sputtered atoms scales as the cosine of the angle between the emission direction and the surface normal. Deviations occur at high ion energies (over-cosine distribution) and low energies (under-cosine distribution), but for plasma-based sputtering the cosine law is a good approximation. Another general departure from a cosine emission distribution occurs when the target is a single crystal or polycrystalline with texture in a preferential direction. In these cases, the sputtering emission distribution has directions along which the yield is higher (Wehner spots). To avoid these problems, we have used sputtering targets that were polycrystalline, had small grain sizes and no texture.

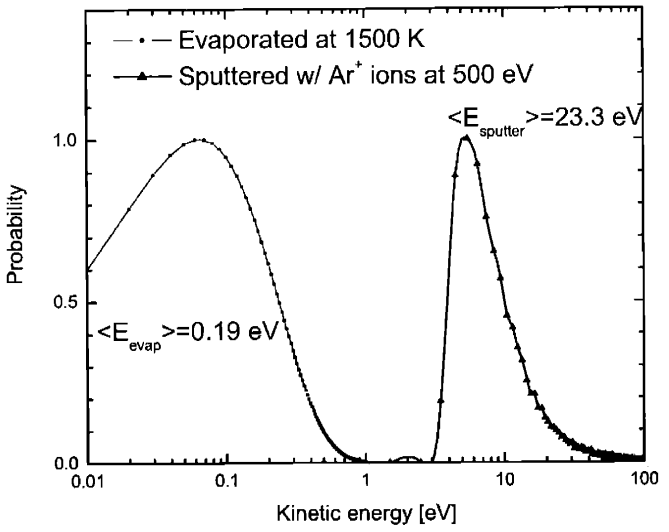

Figure 3.3: The kinetic energy (log scale) distributions for Cu atoms evaporated at 1500 K (dots) and for Cu atoms sputtered with Ar^+ ions at 500 eV (triangles). The numbers for temperature and ion energy are typical for physical vapor deposition and magnetron sputtering, respectively. For the first energetic distribution a Maxwellian function was used, while for the sputter distribution the SRIM program ran 10^4 incident ions for simulations. The energy ranges of the two distributions are widely different and therefore a log scale for energy was used. The average kinetic energy for sputtered Cu atoms is about 100 times larger than for evaporated atoms, indicating that sputtered atoms are more mobile as adatoms on the substrate.

3.1.5 Other energetic processes during sputtering

In addition to the sputtered beam, other types of particles may be ejected from the target material, as shown in Figure 3.1. In particular, two types of energetic particles associated with sputtering may have significant effects on film deposition: reflected backscattered neutrals and negative ions.

The backscattered neutrals are a kinematical effect of the ion bombardment of the target. If the mass M of the incident ion is less than the target atom mass m, the laws of momentum and energy conservation allow the ion to be reflected by the target atom. Because the ion is neutralized shortly before the impact with the surface, the backscattered particle is actually a neutral and remains unaffected by local electric and magnetic fields. The angular distribution of the reflected neutrals is also approximated by a cosine distribution in the sputtering regime used for coating applications.

The fundamental problem with reflected neutrals is that they can carry a significant fraction of the incident ion energy that is subsequently deposited to the substrate. Being uncharged, they are not deviated by electric and magnetic fields and their flux cannot be controlled in this way. The role played by the backscattered, energetic neutrals during sputtering deposition was summarized in [4]. Experimentally, the flux of energetic neutrals was measured for DC magnetron sputtering by Rossnagel [5] and their energy measured in an ion beam sputtering setup by Winters et al [6].

Theoretically, the energy and angular distribution of the energetic, backscattered neutrals can be studied using Monte Carlo simulations with the SRIM software. As described in Section 3.1.2, all the possible atomic collision processes are generated, including the backscattering of the incident ion. In Figure 3.4 are shown the calculated yields of atoms sputtered by Ar^+ ions incident on Pt, W, Si, and C targets, together with the backscattering yields from W and Pt. For each material target and energy, 10^5 incident ions were used for the Monte Carlo simulation. In the case of Si and C, the atomic masses were lower than the Ar^+ ion mass and the backscattering was forbidden by the energy and momentum conservation laws. The range of energies used for the incident ions was chosen in agreement with the voltages used in DC magnetron sputtering (200-500 eV). The angle of incidence of the ions was assumed to be normal to the target surface, which is again consistent with the situation encountered in magnetron sputtering.

The ratios between the backscattered yields and the sputtering yields are in the range 0.6-1 for W and 0.3-0.6 for Pt and they show that the sputtering process is not only a source of sputtered atoms, but also a significant source of backscattered neutrals. These values are calculated at the target surface and they can be very different at the substrate, as will be discussed later. Figure 3.5 displays the average energies of the sputtered atoms and backscattered neutrals from the same set of simulations as in Fig. 3.4.

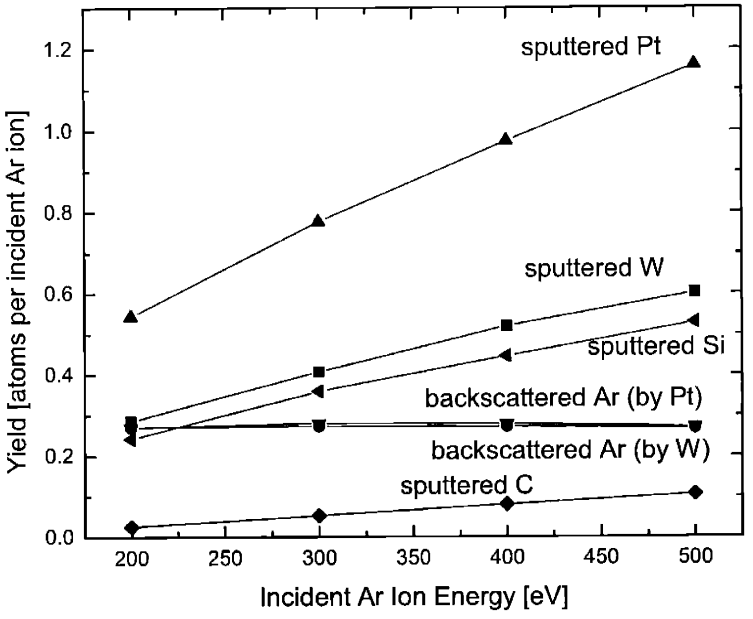

Figure 3.4: Calculated sputtering yields of Pt, W, Si, and C and calculated backscattering yields from Pt and W for Ar^+ ions. The energies of the ions were 200, 300, 400, and 500 eV, respectively, and they were incident normally on the targets. The sputtering yields and backscattering yields are calculated using the SRIM software [2]. The kinematics of the collisions allows the ions to be backscattered only in the case of targets with atomic masses larger than the ion mass (such as for Pt and W).

The average kinetic energy of the Ar neutrals backscattered from W and Pt is 2-6 times the average energy of the corresponding sputtered atoms, the ratio increasing with the incident Ar^+ energy. This is the most significant aspect of the backscattering processes at the targets, which are summarized as follows:

-for target materials with atomic mass less than the bombarding ions, the only ejected species of importance for the coating process are the sputtered atoms.

-for target materials with atoms heavier than the ions, in addition to the sputtered atoms of the target, a great number of ions (30-100% of the sputtering yield) leave the target as backscattered neutrals with up to 6 times higher average energies.

Because the multilayers for x-ray mirrors consist of alternate layers of high and low atomic mass, the film growing on the substrate during sputtering deposition will be alternatively subject to different bombarding conditions due to the presence or absence of the energetic

neutrals. The effect of the energetic neutrals on the film properties will be discussed in more detail in Section 3.4.4. The importance of the neutrals for the morphology of the interfaces and the x-ray reflectivity of multilayers will be more apparent in the studies of different materials systems presented in Chapter 4.

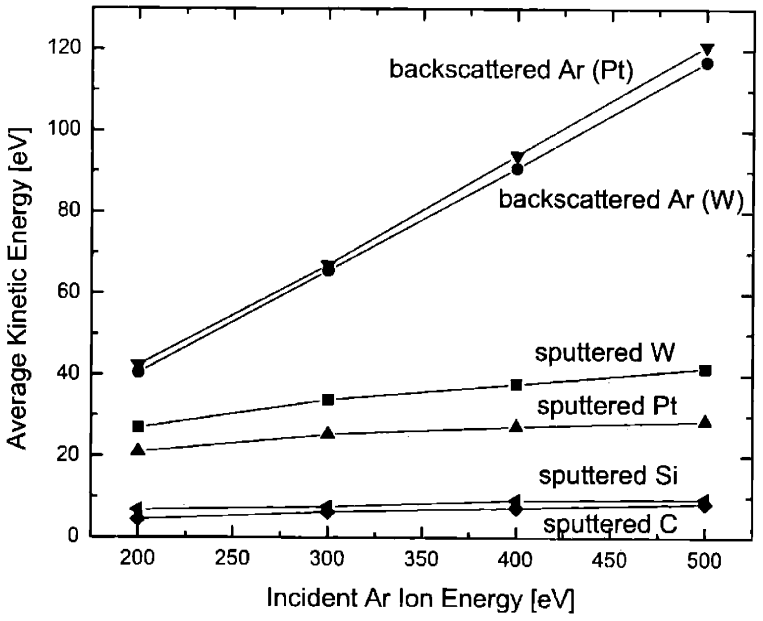

Figure 3.5: Calculated average kinetic energies of sputtered Pt, W, Si, and C atoms and calculated average kinetic energies of backscattered Ar neutrals from Pt and W targets. The energies of the ions were 200, 300, 400, and 500 eV, respectively, and they were normally incident on the targets. The energy distribution was determined in each case using the SRIM software [2] with 10^5 incident ions for the Monte Carlo simulation.

Negative ions can be ejected from the target in the case of materials containing an element with high electronegativity, such as oxygen, and another element that can readily give up an electron, such as Y, Ba, Ti, etc. With a probability dependent on the electron affinities mentioned, the oxygen atom can be sputtered as a negative ion instead of being ejected as a neutral atom. In plasma-based processes, the sputtering target is held at negative potential and further accelerates the oxygen ion towards the plasma sheath. The negative O^- ion is then stripped of its electron in the plasma by charge-exchange collisions and continues towards the substrate as a neutral with several hundred eV of kinetic energy. As with backscattered neutrals, the incidence of such energetic atoms on the growing film can

produce effects like resputtering and changes in composition (oxides) and structure (e.g., stress).

The sputtering target materials used for the deposition of x-ray multilayers are not oxides and are otherwise free of oxygen down to trace levels. The process gases for plasma have ultra-high purity (typically, Ar) with trace levels below 10^{-5} and the initial air load from the vacuum chamber is pumped out prior to the coating. These steps are taken mainly to ensure that oxygen is not present during deposition for the reasons presented above.

3.2 Magnetron DC sputtering

3.2.1 DC diode sputtering

The plasma sputtering processes have continuously evolved since the introduction of the first diode sputtering systems, which consisted of a vacuum chamber with two electrodes separated by distances typically between a few and several tens of centimeters. A process gas (usually Ar) was introduced in the system at constant flow rate and the pressure was typically in the range 0.1 to 50 mTorr. A power supply applied a high voltage between the electrodes (between 0.4-2 kV, depending on electrodes distance and gas pressure) and accelerated the background ions toward the cathode. By secondary emission at the cathode, energetic electrons could create a cascade of ionizations in the gas until a stable discharge occurred between the electrodes. The condition for the breakdown of the gas depends on the gas pressure and the electrode spacing (the Paschen curve). For most applications, the cathode is also the sputtering target: positive ions from the plasma are incident on the target material and produce sputter emission. Many diode plasma systems use the chamber walls as the anode and the substrate is placed in front of the cathode to receive the flux of sputtered atoms.

DC diode systems are limited in practice either by low currents and high voltages or by operating pressures that are too high and produce thermalization of the sputtered atoms. In either case, these systems produce films with low deposition rates, low density, and a large number of defects. The key problem of the DC diodes (and in general for plasma based

processes) is that the gas ionization cross section decreases with the increase of the energy of secondary electrons. If the voltage is increased with the purpose to give more energy to the secondary electrons to create a larger number of ionizations in the gas, the result is not satisfactory because the cross section for ionization has actually decreased. Another solution is to increase the density of the Ar atoms by raising the pressure in the chamber. The required pressures are in the range 50-100 mTorr, and the corresponding mean free paths for the sputtered atoms are of the order of a few mm at most. The result is the stopping of the sputtered atoms very close to the cathode, with diffusion as their only way to reach the substrate. This analysis shows that DC diode systems are impractical for the deposition of films and that a different mechanism must be used to increase the plasma density to levels that result in acceptable deposition rates.

3.2.2 RF diode sputtering

Instead of applying a DC voltage to the electrodes, an RF source is coupled to them by means of an impedance-matching network. The typical frequency used is 13.5 MHz and the voltage amplitude is of the order of a few hundred Volts. The RF diode sputtering system uses the difference in mobility between the electrons and the positive ions in the plasma. In an RF cycle, one of the electrodes picks up more electrons than the other gets ions, so this electrode begins to charge negatively. A capacitor in the impedance matching network prevents this charge from going to the power supply. On each succeeding RF cycle, this electrode will charge with more and more electrons, so the net result after several cycles is an average negative potential at this electrode. For a very short time, the electrode has a positive instantaneous potential and it will collect electrons. For the rest of the cycle, the instantaneous potential is negative and the electrode collects ions. The net current flow in a period is zero and there is no charging of the cathode after reaching this steady state regime. From the point of view of the sputtering application, the electrode will act as a sputtering target during the large fraction of the RF cycle when it attracts ions. One important advantage of RF diode sputtering is that the electrode can be an insulator material, as opposed to DC sputtering which requires a DC current to flow through the

cathode. For RF sputtering this is not necessary because the net current at the electrode is zero. RF diode systems are designed to exploit this advantage and are mostly used to sputter coat silicon dioxide, aluminum oxide, etc. The deposition rates are modest and the increase in power at the cathode does not increase proportionally the deposition rates for the same reasons as stated in Section 3.2.1 for DC diode sputtering (decrease of ionization cross section with the increase of electron energy). RF systems are also very complex due to the impedance matching requirements. Their operation is not very stable in time and subject to drifts and interference problems. We have not used RF sputtering systems in our studies specifically because the deposition processes for x-ray multilayers must be stable and reproducible and provide a high deposition rate.

3.2.3 Magnetron sputtering systems

The solution to the problem of increasing the plasma ionization density was to add a strong magnetic field perpendicular to the electric field, in a configuration similar to that used in magnetron vacuum tubes (hence the current name for the system). The force acting on a charged particle (electron or ion) is the Lorentz force:

$$\mathbf{F} = q\left(\mathbf{E} + \mathbf{v} \times \mathbf{B}\right) \tag{3.2}$$

where q and $\mathbf{v}$ are the charge and velocity of the particle and $\mathbf{E}$ and $\mathbf{B}$ are the local electric and magnetic fields. By applying a magnetic field perpendicular to the particle velocity, the net result is a trajectory with a radius of curvature directly proportional to the particle mass:

$$r = \frac{mv}{qB} \tag{3.3}$$

Since the ion masses are $(1{,}837 \cdot A)$ times larger than the electron mass (A is the atomic mass number), the effect of the magnetic field on ions is negligible, while the electrons trajectories are changed into circles or helical paths, depending on the field geometry and the orientation of the initial velocity of the electron, $\mathbf{v}_0$. For example, if $B = 1000$ Gauss, the radius of curvature for a 100-eV electron is 0.3 mm, while for an Ar^+ ion is 6.6 cm.

Forcing the electrons to follow a helical or cycloidal trajectory greatly improves the probability of collisions and ionization of the residual gas. Also, because the magnetic field does not increase the energy of the electron, the ionization cross section is the same as in the absence of magnetic fields.

The magnetron cathode designs were commercially developed only after rare earth magnets had become widely available. These magnetic materials (Nd-Fe-B, for example) have high magnetic energy densities and provide strong (~1000 Gauss) fields with little dependence on temperature fluctuations. Being close to the surface of the sputtering target, the magnets must still be cooled to avoid reaching the Curie temperature. Other than the cooling requirement, they are a simpler and efficient solution to the problem of creating strong magnetic fields inside the deposition chamber.

The field geometry used in current magnetron cathodes is parallel with the sputtering target surface. In this way, the electric and magnetic fields are crossed and the electrons are trapped in a plane parallel to the magnetic field using the $\mathbf{E} \times \mathbf{B}$ drift effect. The magnetic field and the drift path are sketched in Figure 3.6 for a circular planar magnetron cathode and in Figure 3.7 for a rectangular planar magnetron. Both types of cathodes are in use at SAO and will be described in Section 3.3. As a measure of the efficiency of the magnetic trapping, Rossnagel [7] determined experimentally the ratio between the drift current and the discharge (cathode) current. He found that for a 12-inch cathode the current "gain" was in the range 3 to 6, depending on the process gas and its pressure (the gain decreases with increasing pressure).

Other variants of the magnetic field geometry are used for the S-gun class of cathodes and for the post magnetrons. These types of cathodes were not used in this work because they cannot coat large areas (S-gun case) or require complex mechanical designs (in the case of post magnetron) for the coating system in order to be used for the deposition of two materials. Both coating chambers described next use planar magnetron configurations, as illustrated in Fig. 3.6 and 3.7.

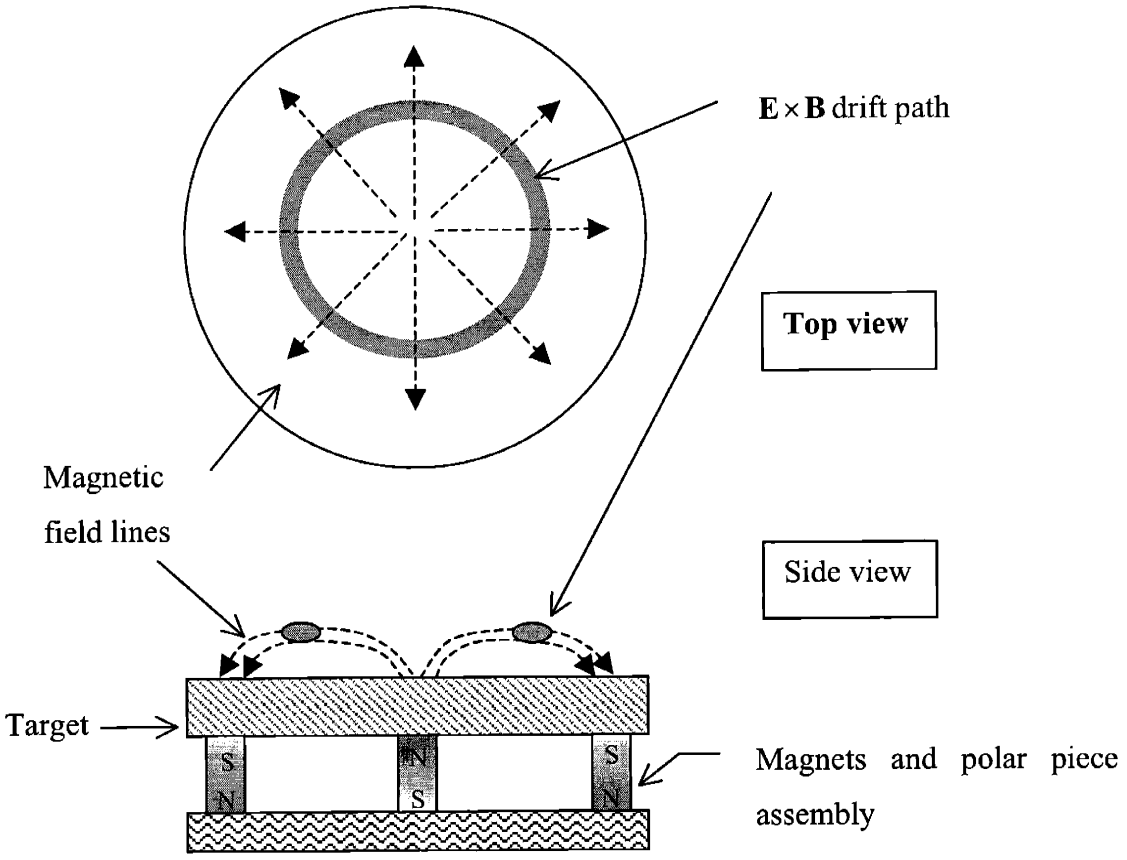

Figure 3.6: Schematics of a circular planar magnetron cathode. The top view shows the radial distribution of the magnetic field and the circular drift path for electrons. The side view shows the magnets and the polar pieces perpendicular to the surface of the sputtering target. The geometry of the electric and magnetic fields is such that the electrons are trapped in a toroidal magnetic mirror and execute several loops before being scattered out from the trap. The advantage of the magnetron cathode is the presence of an electron drift current in the plasma several times higher than the cathode current [7]. This results in high ionization densities and high sputtering rates.

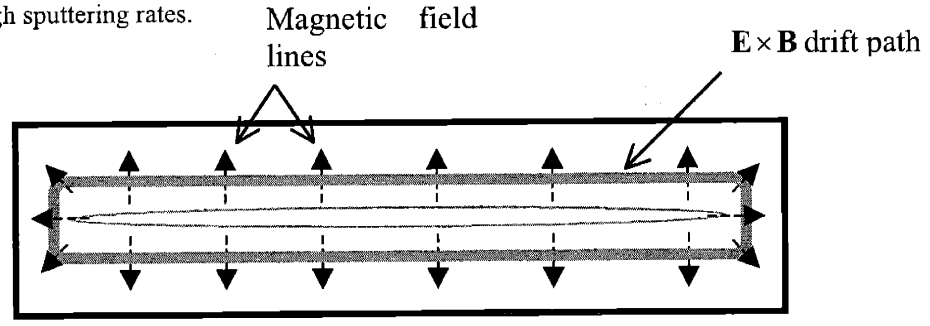

Figure 3.7: Top view schematic of a rectangular planar magnetron. The drift path for electrons is quasi-rectangular in this case. The geometry is similar to the circular cathode above, but stretched in one direction. This type of magnetron is used to coat large area substrates as they are rotated around the long axis of the cathode.

3.3 Description of deposition systems

The Multilayer Facility at the Smithsonian Astrophysical Observatory (SAO) in Cambridge, MA, has in use two magnetron sputtering systems that were developed for the purpose of studying multilayers for hard x-ray mirrors. The smaller sputtering system runs two 7.5-cm diameter DC magnetron cathodes and is used for coating samples for new materials tests and process optimization. It is usually referred to as the R&D sputtering chamber. A second vacuum chamber was designed for coating prototype optics and uses two 66-cm long linear DC magnetron cathodes. The original feature of this system is its capability to deposit multilayers on the inside of integral conical shells of 20 to 50 cm diameter. Both sputtering systems are described in more detail in the following sections.

3.3.1 R&D sputtering system

The vacuum chamber is made of stainless steel 304 and has a cylindrical configuration with an inner diameter of 61 cm and 30 cm height. The top flange was retrofitted by adding two cylindrical flanges for the magnetron cathodes. The chamber is shown on the left side of Figure 3.8. The two cathodes are oriented face down (downsputtering configuration) and the distance between the cathode axes is 30 cm. A ferrofluidic feedtrough at the center and top of the chamber allows a shaft-stepper motor assembly to support the substrate platen and spin it the horizontal plane. The platen height can be adjusted such that the distance from the cathode target to the substrates varies between 4 and 11 cm. In addition to changing the substrate position from one cathode to the other, the computer controlled stepper motor moves the substrate in an oscillatory motion with 2 RPM and 8° angular amplitude around the center of a cathode. The RPM and angle of this "sweeping" oscillatory motion were determined from test depositions on 2" wafers. The tests showed that these settings improved the thickness uniformity (±3%) and surface microroughness, compared with samples deposited in similar conditions, but without the sweeping motion.

Figure 3.9 presents the side-view schematics of the two cathodes and the platen.

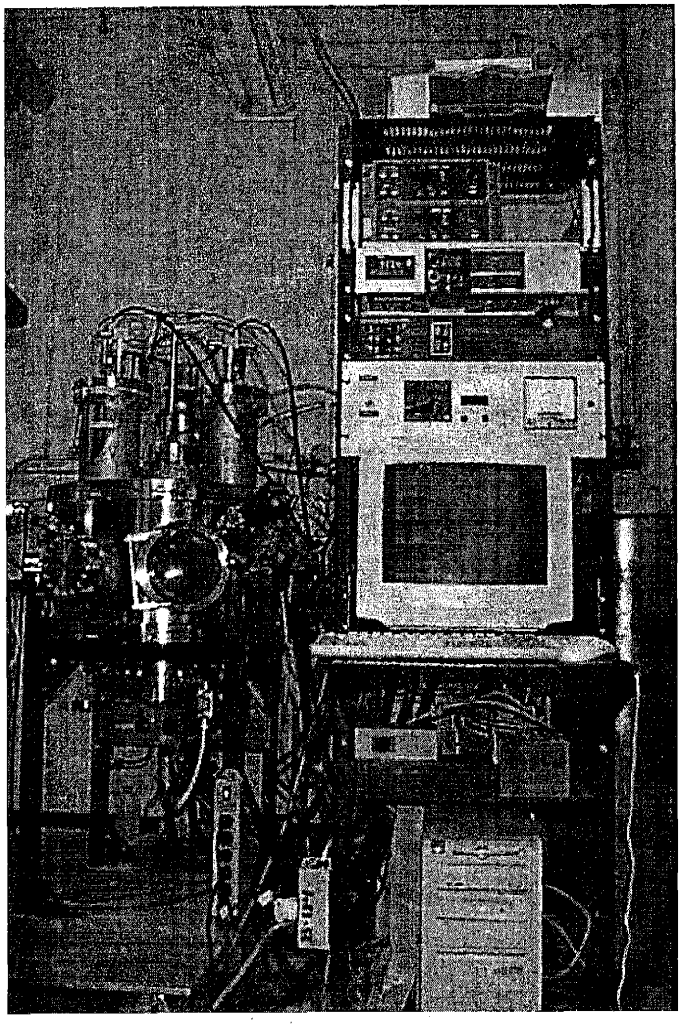

Figure 3.8: The R&D deposition system: the vacuum chamber (61 cm dia. x 30 cm height) equipped with two 7.5-cm diameter DC magnetron sputter cathodes is shown on the left. The vacuum and gas systems instrumentation is housed in the rack together with the cathode power supplies and the PC for process control (right side).

The chamber is evacuated from atmospheric pressure by using a rotary vane mechanical pump (for roughing and backing) and a turbopump. The base pressure before deposition is typically around $2\text{-}3\text{x}10^{-7}$ Torr. The process gas is ultrapure argon (99.999% purity) and its flow rate during deposition is kept constant using a mass flow controller. The pressure is measured with a capacitance manometer and can be varied in the range 1.2-7.5 mTorr by adjusting the argon the flow rate. The two magnetron cathodes are connected to power supplies which run in current controlled mode. The current settings used are in the range

20-150 mA, depending on the target material and the sputtering conditions sought. Each sputtering cathode is individually shuttered so that the substrate is exposed to the flux of sputtered atoms only for the necessary amount of time. A custom software program written in CVI (National Instruments) controls the exposure time for the deposition of each layer, based on input files with the specified layer thicknesses.

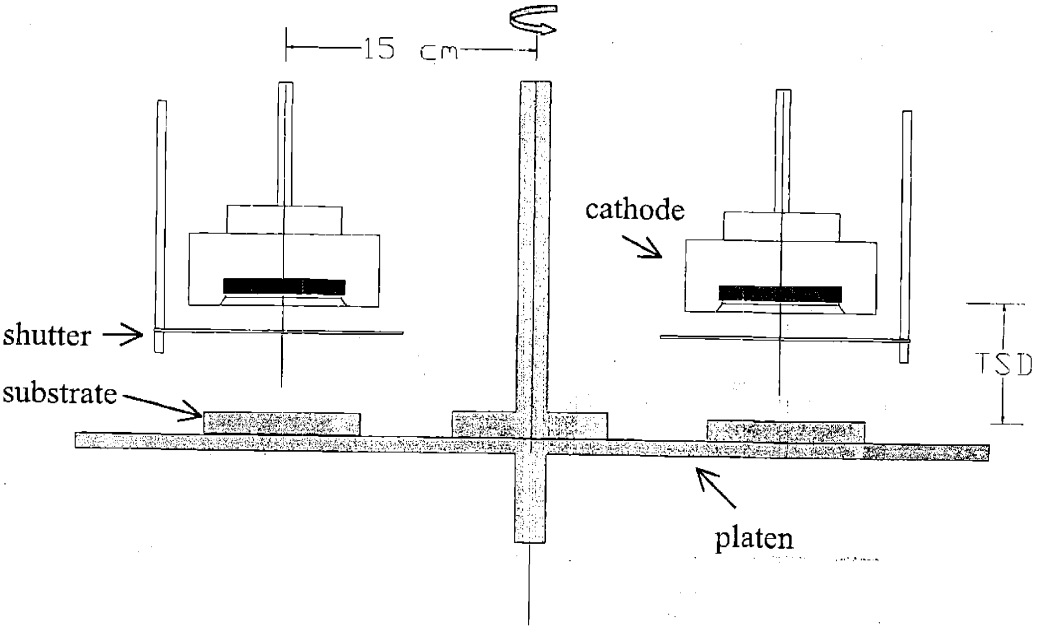

Figure 3.9: Schematics of the inside of the R&D chamber showing the platen holding the substrates below the two sputtering cathodes. The target to substrate distance (TSD) can be varied between 4 and 11 cm. The individual cathode shutters are also shown in the closed position. The central shaft rotates around the vertical during the multilayer coating in order to place a substrate alternatively under each of the two cathodes.

3.3.2 The prototype coating system

The prototype coating chamber was designed specifically to deposit on the inner surface of integral conical substrates with diameters between 20 and 50 cm. The stainless steel vacuum chamber has the shape of a cylinder with an inner diameter of 75 cm and 117 cm height (see Figure 3.10). The two linear magnetron sputtering cathodes are 66 cm long and are mounted back-to-back along the vertical axis of the chamber.

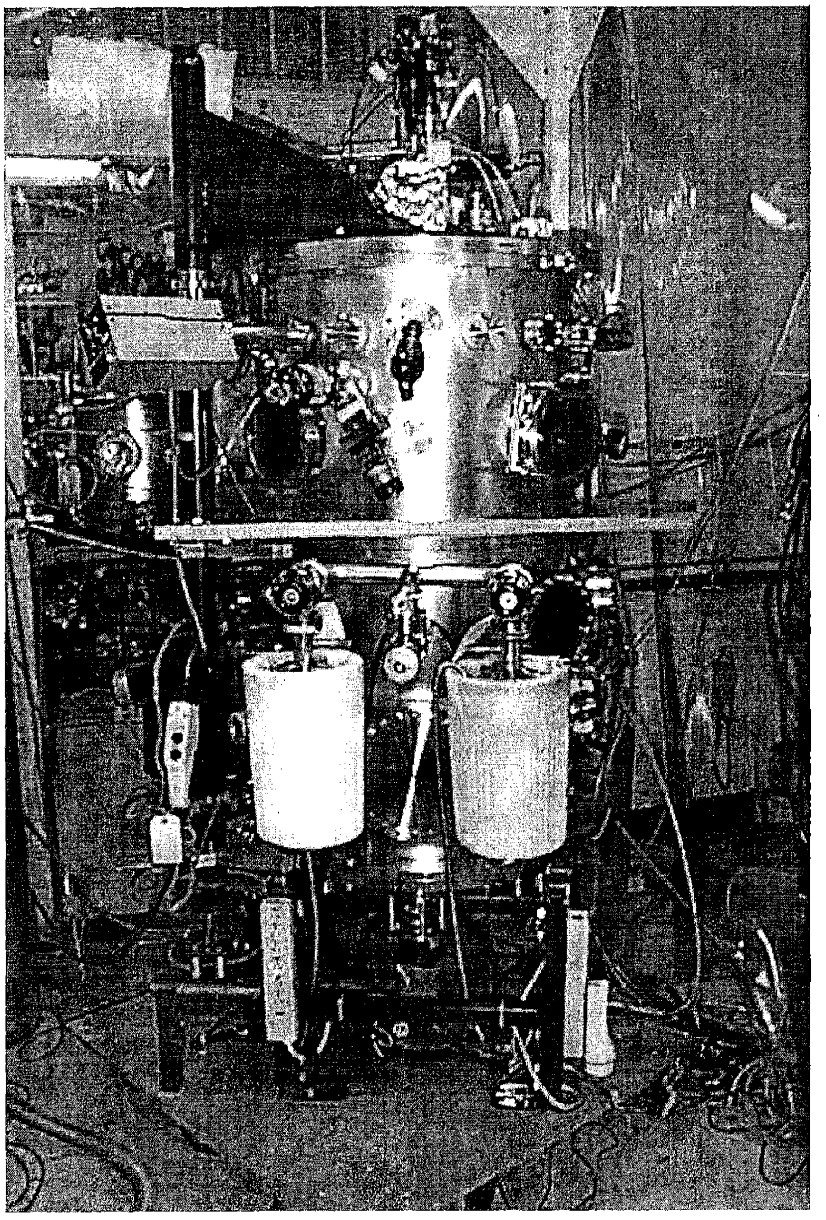

Figure 3.10: The prototype coating chamber was designed for depositing multilayers on the inner surface of integral conical substrates (20 to 50 cm dia.). The inner dimensions are 75 cm diameter by 117 cm height (1-m stick shown in picture for reference). The top half of the chamber can be raised to load the optic and then lowered to insert the two linear cathodes inside the optic.

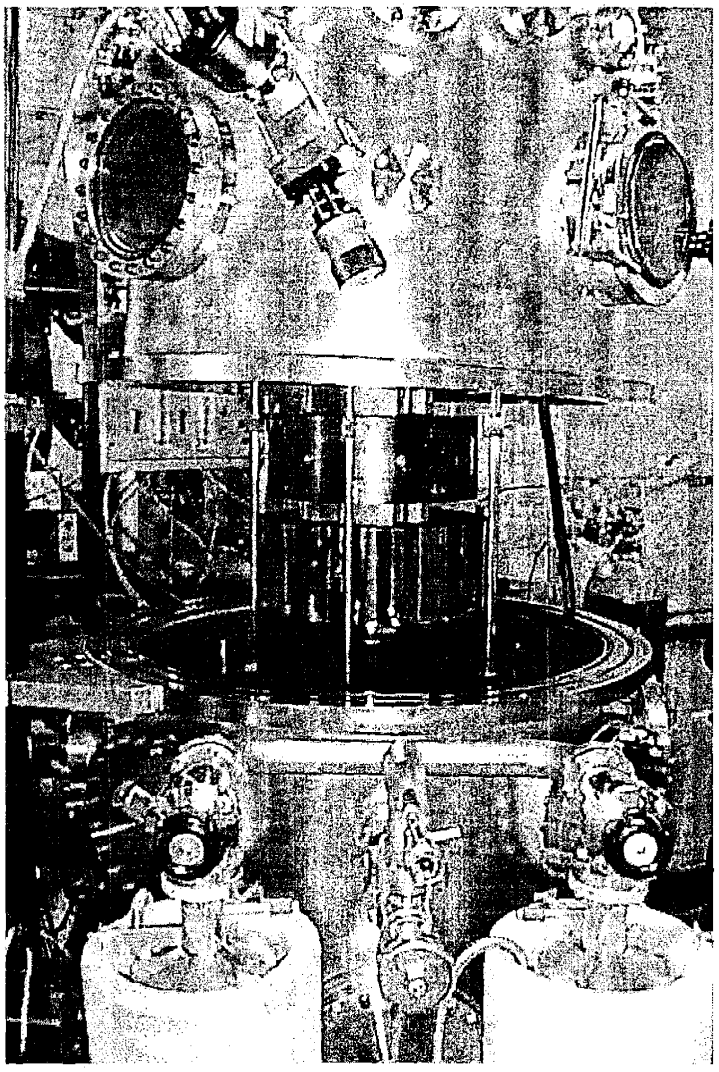

Figure 3.11: The prototype chamber is shown while being loaded with a cylindrical DURAN glass substrate (see Section 6.1 for details). The top half of the chamber (with the sputtering cathodes) was lifted by a hoist to allow for attaching the substrate to the rotating table at the bottom of the vacuum chamber. The cathodes are then inserted inside the substrate optics while the top half is lowered to close the chamber.

The top half of the chamber can be lifted by a hoist to allow for the insertion of the substrates. A rotary table on the bottom half of the chamber can hold and turn the optic during coating by using a gear-shaft assembly coupled to a stepper motor mounted outside the vacuum chamber. The table can be rotated with a speed variable between 0.5 and 12 RPM. The chamber is evacuated from atmospheric pressure using a Venturi pump for

roughing and sorption pumps to reach low vacuum. A cryosorption pump is used to lower the pressure further down to $2x10^{-7}$ Torr. The gas used for the sputtering process is ultrapure argon and the flow rate during deposition is kept constant using a mass flow controller (MFC). The pressure is measured with a capacitance manometer and can be varied in the range 2.0-7.0 mTorr by adjusting the argon flow rate at the MFC or up to 40 mTorr by using a needle valve connected to an auxiliary argon tank. The two magnetron cathodes are connected to power supplies running in current controlled mode. The current settings are in the range 200-1000 mA, depending on the target material and the sputtering process. The cathode shutters are actuated by pneumatic valves. A dedicated software program written in CVI (from National Instruments) controls the motion of the rotary table and of the cathode shutters. The deposition of a layer of material is achieved by opening the respective cathode shutter and spinning the substrate around the cathode for an integer number of revolutions, after which the cathode is shuttered. The software controls the speed and the time of exposure to the cathode, based on a table with known deposition rates and speeds for each material in specific conditions (pressure, TSD, cathode current). The schematics of the coating in the prototype chamber is shown in Figure 3.12.

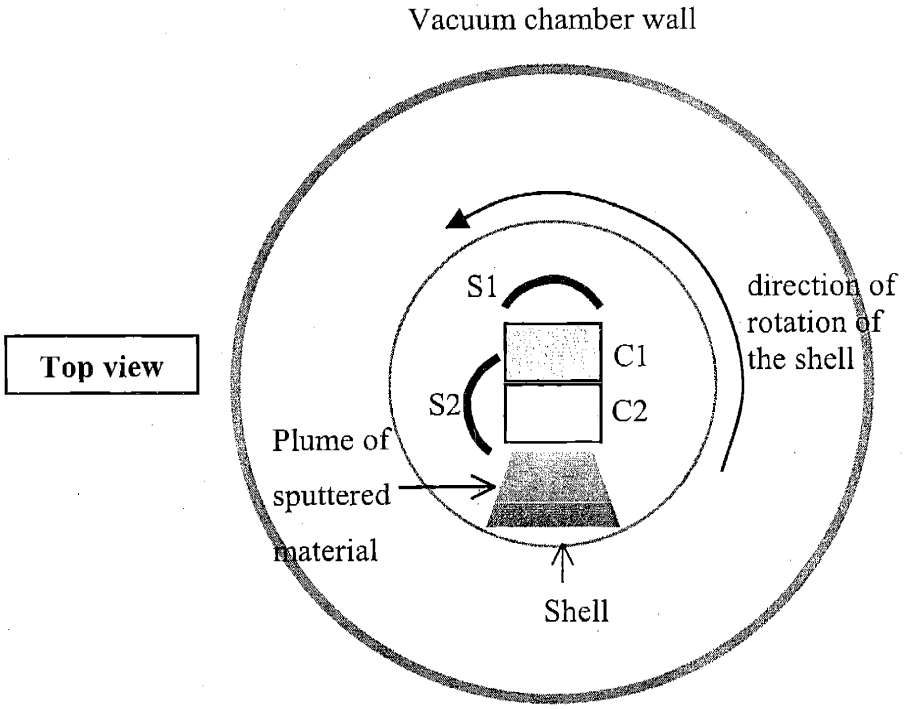

Figure 3.12: Schematics of the coating process inside the prototype coating chamber. The sputtering cathodes are stationary and connected to the top half of the chamber. They are inserted vertically along the axis of the optic. The shell is supported by a rotary table, which is turned by a stepper motor. The top view shows in this example that cathode C1 was covered by its shutter S1 and that the shutter S2 was open to allow the C2 cathode to coat the inside of the shell. The software controls the rotation of the shell such that an integer number of revs is performed around the C2 cathode until the desired thickness of material was deposited uniformly. The shutter S2 is then closed and the process can be repeated at cathode C1 to deposit the other material in a similar manner.

3.4 Nucleation and growth of thin films

The nucleation and growth of thin films depends on the deposition process chosen and the surface state of the substrate. The best knowledge of the fundamental physical processes involved in thin film deposition has derived from studies and theory of crystalline growth on clean surfaces. The differences between the situation encountered in the practice of thin layer deposition and the ideal crystalline growth are the following:

-The top atomic layer of the substrates used for multilayer deposition is not a crystalline plane. Most of the substrates are amorphous (fused silica or glass) or polycrystalline (nickel, aluminum, gold, etc.). Even monocrystalline substrates like silicon are covered by native oxide layers at the surface. The removal of the oxides can be done only in ultrahigh vacuum, usually by sputtering the surface with an Ar or Cs ion beam. This ion beam cleaning is difficult and slow for large area substrates. Most importantly, it has to be avoided because it produces roughening of the substrate. The low surface roughness requirement for substrates is incompatible with ion beam cleaning at atomic level. Most of the substrate fabrication methods involve exposure to atmosphere; the formation of oxides is even part of the polishing process for silicon wafers.

-The coatings are usually performed with high deposition rates for practical reasons and thus the atomic processes occur in non-equilibrium conditions. This is different from the quasi-equilibrium state encountered in crystalline growth processes like molecular beam epitaxy.

-In sputtering deposition (and other PVD and CVD processes), the substrate is bombarded not only by the atoms of the material to be grown as a film, but also by other particles

which are byproducts of the process (energetic neutrals, negative ions, electrons, etc.). They can have a significant influence on the structure and physical properties of the thin film.

With all these differences, the crystalline growth studies offer models and concepts that can be recognized or adapted to the description of thin film deposition processes. Many aspects of polycrystalline 2D and 3D growth are also applicable to the deposition of thin amorphous layers by magnetron sputtering, for example. Starting from this common base of phenomena, the role of energetic ion-surface interactions can be better understood.

3.4.1 Crystalline growth on surfaces

Three distinct modes of crystalline growth are generally accepted:

1. Island growth mode, or Volmer-Weber.
2. Layer mode, or Frank-van der Merwe mode.
3. Layer plus island mode, or Stranski-Krastanov.

In the island mode, small clusters are nucleated on the substrate and grow into islands. This happens when the deposited atoms are more bound to each other than to the surface of the substrate. Stated alternatively in terms of energy, when the cohesive energy exceeds the adhesive energy, this growth mode is favored. With continued deposition, the islands grow and come in contact with each other until they can make a complete path. At this point a conducting film switches to low resistivity ("percolation threshold"). By adding more deposited material, the islands form eventually a continuous film. The island growth mode is generally observed for metals deposited on insulators, such as alkali halides and graphite.

The layer growth mode is made possible by atomic forces that bind more strongly the deposited atoms to the substrate than to each other. The atoms form a single atomic layer coverage, then they build up the next atom layer, and so on. This mode was observed for rare gases on graphite and metals, some metal-metal systems, and in semiconductor growth on semiconductor substrates (same material or one with a similar lattice constant).

The layer plus island mode is an intermediate type of growth, in which after the first few layers the energetics favors island growth. Almost any factor disturbing the monotonic

decrease in binding energy towards the bulk value may be the cause of switching from layer to island growth. For example, the lattice parameter of the intermediate layer may not be continued into the bulk due to strong lattice mismatch. This growth mode is occurring in many metal-metal, metal-semiconductor, or gas-metal systems, and is generally more common than it was thought initially.

3.4.2 Nucleation and cluster formation

This section summarizes the phenomena associated with the early stages of thin film growth by atomic deposition (physical or chemical). The atoms arriving at the substrate remain on the surface for a period of time τ_s related to the surface vibrational frequency for adatoms ν (typically 10^{12} Hz) and the energy E_{des} required for desorption back to vapor state:

$$\tau_s = \frac{1}{\nu} \exp\left(\frac{E_{des}}{k_B T}\right) \tag{3.4}$$

Adatoms which are not in thermal equilibrium with the surface may perform random jumps to different sites on the surface. They have to overcome an additional energy barrier E_b (the Ehrlich barrier) when crossing step edges or the surface diffusion activation barrier E_s when moving as adatoms on the same atomic surface layer. Since $E_b > E_s$ a significant density of adatoms is usually observed near terrace steps and other substrate imperfections. The presence of impurities alters the energy barrier in a complex manner, depending on the type and distribution of atoms at the surface.

During the residence time τ_s the adatoms are capable of diffusing on a terrace by a distance from the site of incidence given by:

$$\delta x = \sqrt{2 D_s \tau_s} \tag{3.5}$$

where the surface diffusion coefficient D_s is also dependent on the substrate temperature T, the surface vibrational frequency ν, and the activation energy for surface diffusion E_s:

$$D_s = 1/2\, a_0^2 \nu \exp\left(-\frac{E_s}{k_B T}\right) \tag{3.6}$$

Following Ohring [8] the nucleation rate (nuclei/cm^{2}s) can be determined as a function of temperature and deposition rate $\dot{R}$ (atoms/cm^{2}s) in the frame of the capillarity theory. Some of the conclusions of this theory are important for practical applications:

-higher substrate temperature leads to increased size of the critical nucleus, requiring more time to develop a continuous film.

-low substrate temperatures and high deposition rates yield polycrystalline deposits.

More recent approaches to the modeling of the nucleation processes use atomistic simulations and rate equations to describe the time evolution of atomic cluster densities. For example, the rate of formation of monomers is given by:

$$\frac{dN_1}{dt} = \dot{R} - \frac{N_1}{\tau_s} - K_1 N_1^2 - N_1 \sum_{i=2}^{\infty} K_i N_i \tag{3.7}$$

where N_i is the density of clusters of i atoms and K_i are rate constants. The rate of arriving atoms is $\dot{R}$. The general form of the rate equation for clusters of size $i \geq 2$ is

$$\frac{dN_i}{dt} = K_{i-1} N_1 N_{i-1} - K_i N_1 N_i \tag{3.8}$$

indicating that clusters with $i \geq 2$ are formed by adding monomers to smaller (i-1) size clusters and disappear by reacting with monomers to produce the larger (i+1) size clusters. The rate equations form a system of i independent equations that can be increased in complexity by adding cluster surface diffusion terms of the form $\frac{\partial^2 N_i}{\partial x^2}$.

The kinetic theory of nucleation indicates that in the early stages of growth the density of stable clusters increases up to some maximum level, after which cluster coalescence takes place and their density starts to decrease. One particular type of coalescence is the Ostwald ripening. In this case, the small size clusters are added to the larger clusters present in their vicinity based on a surface diffusion mechanism. The higher density for smaller clusters is predicted by the Gibbs-Thompson equation:

$$\frac{p}{p_{vp}} = \exp\left(\frac{2\Omega\gamma}{rk_B T}\right) \tag{3.9}$$

which gives the partial pressure (and the surface density) dependence on the radius r of the cluster. The partial pressure and the cluster density are higher when the radius of the cluster

is smaller. Thus the small clusters are always present in larger concentrations than the bigger clusters and the gradient of concentration drives their diffusion. The coalescence process that occurs based on this mechanism is also called island coarsening.

3.4.3 Zone models for evaporated and sputtered films

The previous sections summarized the early stages of the formation of films. The zone models are qualitative descriptions of the structure of fully grown, thick polycrystalline films. The earliest of the zone models was proposed by Movchan and Demchishin [9] and was based on observations of very thick evaporated metals and oxides. The structure of the films was identified by three zones:

1. Zone 1 structure is columnar and less dense with a rough surface.
2. Zone 2 is columnar and nearly dense with a smoother surface.
3. Zone 3 consists of dense grains with a relatively smooth surface.

The zones are separated by transition regions with characteristic reduced temperatures: zone 1 and zone 2 are separated by a deposition temperature $T_1 = 0.3T_m$ and zones 2 and 3 are separated by the temperature $T_2 = 0.5T_m$, where T_m is the melting temperature of the material. It was shown that atomic shadowing is one of the reasons for underdense columnar growth in Zone 1. By using 2D molecular dynamics simulation for Ni with an appropriate interatomic potential, Müller [10] showed that at low substrate temperatures the film grows in columns that are shadowing the lateral growth and result in large voids and low density. Increasing the substrate temperature allowed the film to reach Zone 2-type of growth because the thermal energy promoted lateral diffusion and the growth of smooth layers.

A similar zone classification scheme was introduced by Thornton [11] based on his studies of thick sputtered metal films. The Thornton diagram has four zones:

1. Zone 1 is similar to the Movchan-Demchishin (M-D) Zone 1: large voids and columnar structures are evident in films grown at low temperatures and high Ar pressures.
2. Zone T is a transition zone to smoother, denser films. This structure is characterized by fibrous grains and dense grain boundaries and was observed for samples deposited at lower Ar pressures and/or higher substrate temperatures.

3. Zone 2 is characteristic for films sputtered at high temperatures which can still display a columnar structure with dense grain boundaries.
4. Zone 3 structure occurs for sputter coating at very high temperatures and results in large equiaxed grains.

The Thornton zone description of sputtered films is literally applicable only for thick single layer coatings of the order of μm. What is still relevant even for nm-thick layer depositions (as for x-ray multilayers) is the role played by the argon pressure in the structure of the film. The dependence of the energy of the adatoms and backscattered neutrals on the argon pressure and target-substrate distance is discussed below.

3.4.4 Influence of energetic atoms on the growth surface morphology

As it was shown in Section 3.1.5, the typical average energy of the sputtered atoms at the cathode is in the 5-30 eV range (see Fig. 3.5), which is an order of magnitude (or more) higher than for evaporative deposition. This is beneficial for the growth of smooth and dense layers because the adatoms with high energy are more likely to diffuse laterally on the surface. However, in some instances, the activation energy for surface diffusion may be still larger than the kinetic energy of the adatoms. This can happen if the adatoms lost their initial energy (as sputtered) by collisions with the argon gas atoms. The critical parameter is the ratio between the mean free path λ of the sputtered atoms and the target-substrate distance (TSD). In an argon atmosphere at 1 mTorr, the mean free path is of the order of 5 cm for the sputtered species. If $\lambda/TSD \gg 1$, then the atoms are transported in "ballistic regime" from the cathode to the substrate with no collisions and no energy loss. Films deposited in this regime tend to be small-grained, dense, and often have relatively good adhesion. If $\lambda/TSD \ll 1$, then several gas phase collisions are possible and the atoms slow down. It is important to note that the collisional cross section increases with the decrease in energy, such that a sputtered atom that suffered one collision is more likely to have additional collisions. This transport regime is known as "thermalization" and results in films with structures similar to Zone 1 in the Thornton classification (i.e., columnar structures with large voids).

The presence of energetic reflected neutrals (when $M_{ion} \leq m_{\text{target}}$) can contribute significantly to the structure and morphology of the growing film. As illustrated in Figure 3.5, the average energy of the backscattered neutrals is in the range 40-120 eV (at the cathode). The neutral arrival rate at the substrate depends on pressure and TSD and can be in the range 20-100 % of the sputter atom arrival rate. The effects of energetic neutrals on the layer growth can be mainly of two types:

- resputtering: the neutrals have sufficient energy to sputter the film in some cases. The effective resputtering rate depends on many parameters (sputtering yield of the material, relative arrival rate of neutrals vs. adatoms, etc.) and for all practical applications it is sought to be much less than the arrival rate of the sputtered atoms.
- beam mixing: when the energetic Ar neutrals do not have enough energy to sputter the film, they can still create energetic collisions in the top layers and produce mixing and rearrangements of the atoms. This is important for multilayers: if the range of the collisions generated by the neutrals reaches an underlayer of different composition, then that interface is mixed and its diffuseness increased.

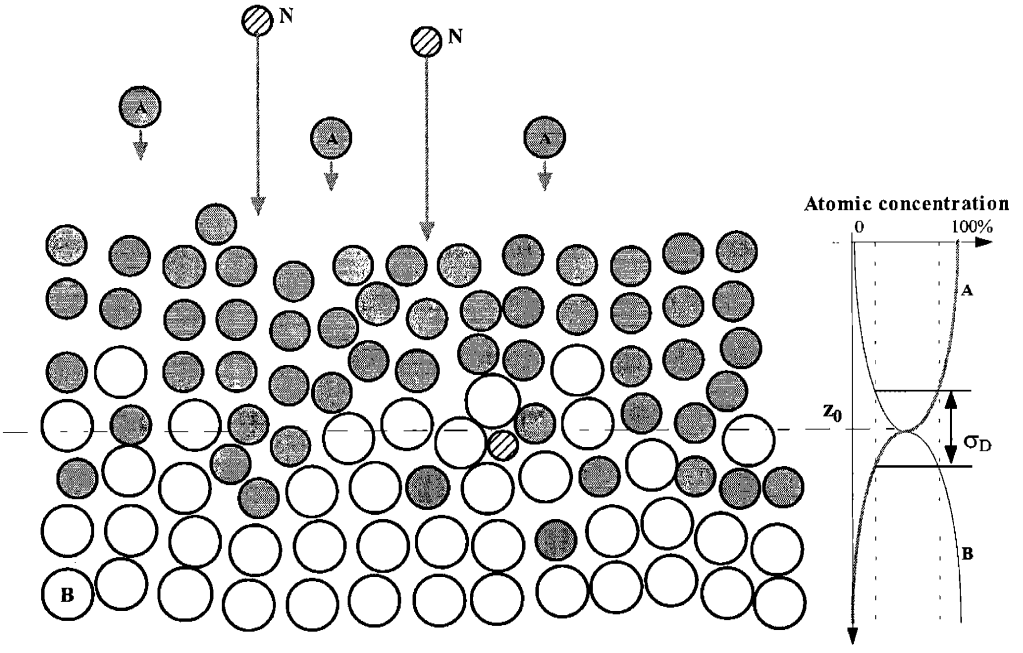

Figure 3.13: Interface mixing by energetic neutrals: atoms of type A (gray circles) are deposited by magnetron sputtering on top of a layer of material B (unfilled circles). The A atoms are assumed heavier than the ions ($m_A > M_{ion}$) and a flux of backscattered, neutralized atoms "N"(shown by dashed circles) is incident on the growing film simultaneously with the flux of A atoms. If, for example, material "A" is Pt and the ions are 400 eV Ar^+ ions (typical sputtering voltage for Pt), the backscattered neutral Ar atoms have an average kinetic energy of 90 eV and the sputtered Pt atoms have only 25 eV average energy. The range (± the straggling) for 90 eV Ar in Pt is 5±3 Å while for 25 eV Pt in Pt it is only 2±1 Å (range calculations performed with SRIM). The neutrals can thus penetrate and create collisions at the bottom of an 8 Å thick Pt layer while the arriving Pt atoms are deposited practically on the surface. The effect created by the neutrals is a mixing of the interface between atoms of type A and type B. From the point of view of the laterally averaged atomic concentration depth profiles *N(z)* (shown on right), the interface has a width σ_D ("diffuseness"). The position of the "separation plane", formally defined as the plane where the atomic concentrations are equal: $N_A(z_0) = N_B(z_0) = 50\%$ (position shown by a horizontal, dashed line), is modified during the deposition by the accumulation of B-type recoils towards the surface.

The resputtering and the neutral beam mixing effects play an important role in the formation of the interfaces in magnetron sputtered x-ray multilayers. As described previously, they consist of a sequence of alternate layers A/B repeated N times. One of the materials has a low atomic number Z, and the other one has usually a high Z to achieve the x-ray optical contrast. When depositing light atoms of type "B" ($m_B < M_{Argon}$) there are no backscattered neutrals and the only species reaching the surface are the type "B" atoms. Next, the sample is exposed to the cathode with material "A" as target. This time $m_A > M_{Argon}$ so a backscattered flux of Ar neutrals is incident on the sample simultaneously with the type A atoms (see

Figure 3.13). With energies a few times greater than the sputtered atoms, the neutrals can penetrate deeper in the forming layer of type A and even reach the interface A/B. They create collision cascades and atomic mixing at the interface. The scale on the right of Fig. 3.13 shows the atomic concentration depth profiles for A and B. The point at which they are equal is at depth z_0 and defines the location of the interface. The width of the depth profile curve gives the "diffuseness" parameter σ_D for the interface A-on-B. Because the type B atoms are light and they tend to be resputtered, the depth z_0 is shifted towards the surface compared to the initial location before the coating with type A atoms. These effects will be discussed in Chapter 4 for different material systems.

Even in the absence of energetic neutrals (as in evaporative deposition), the surface separating the atoms A from atoms B is not flat but has a complex shape described by an interface depth function z(x,y). If the average $\langle z(x,y) \rangle$ is z_0 (see Figure 3.14) then the root mean square of the deviation of z from the average is the interface roughness σ_R:

$$\sigma_R = \sqrt{\left\langle \left(z(x,y) - z_0 \right)^2 \right\rangle} \tag{3.10}$$

These two interface parameters (σ_R and σ_D) play an important role in the x-ray reflectivity theory and were discussed in Chapter 2.

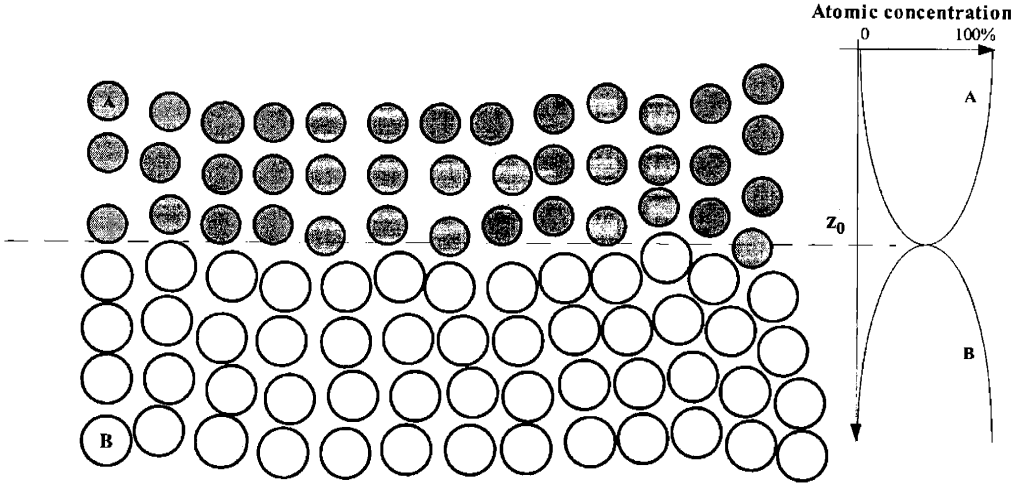

Figure 3.14: Interface roughness between materials of type A and B. The separation between the two materials is described by a function z(x,y) that fluctuates around the average value z_0. The r.m.s. deviation of z from z_0 is defined as the interface roughness σ_R(A/B) (see eq. **(3.10)**).

References for Chapter 3

1. P. Sigmund, in *Sputtering by particle bombardment*, Ed.R. Behrisch, *Topics in Applied Physics*, vol. 47, 1981, Springer Verlag: Berlin, p. 7-203.

2. J.F. Ziegler, J.P. Biersack, and U. Littmark, *The Stopping and Range of Ions in Solids*, Vol. 1, 1985, New York: Pergamon Press.

3. P. Zalm, *Quantitative Sputtering*, in *Handbook of Ion Beam Processing Technology*, Eds.J.J. Cuomo, S.M.Rossnagel, and H.R. Kaufman, vol. 1989, Noyes Publications: Park Ridge, NJ.

4. D.W. Hoffman, *"Perspective on stresses in magnetron-sputtered thin films"*, J.Vac.Sci.Technol. **12A**, 1984, pp. 953-961.

5. S.M. Rossnagel, *"Energetic particle bombardment of films during magnetron sputtering"*, J.Vac.Sci.Technol. A **7**, 1989, pp. 1025-1029.

6. H. Winters, H. Coufal, C.T. Rettner, and D.S. Bethune, *"Energy transfer from rare gases to surfaces: Collisions with gold and platinum in the range 1-4000 eV"*, Phys. Rev. B **41**, 1990, pp. 6240-6252.

7. S.M. Rossnagel, *"Induced drift currents in circular planar magnetrons"*, J.Vac.Sci.Technol. **A5**, 1987, pp. 88-91.

8. M. Ohring, *The Materials Science of Thin Films*, 1991: Academic Press.

9. B.A. Movchan and A.V. Demchishin, Phys. Met. Metallogr. **28**, 1969, pp. 83-92.

10. K.H. Müller, J. Appl. Phys. **58**, 1985, pp. 2573-2586.

11. J.A. Thornton, Ann. Rev. Mater. Sci. **7**, 1977, pp. 239-278.

Chapter 4: Studies of different material systems for hard x-ray multilayers

The field of application of hard x-ray mirrors is not restricted to astrophysics. Possible applications (but less demand at this moment) exist also in the field of synchrotron optics, medical and industrial radiography, tokamak plasma diagnostics, and other. It is rewarding to start a study of a wide class of materials for the multilayers, using a systematic approach for their fabrication and characterization, because the results help select the right combination for a particular application.

The next section is devoted to the most researched material pair for hard x-ray multilayers, namely W/Si. The two materials show a very good chemical stability and compatibility and a good contrast in the x-ray band. More important, they can be deposited as multilayers with periods as low as 15 Å and they can be grown with interface widths as low as 3 Å r.m.s. in certain conditions, thus increasing the reflectivity close to the theoretical limit (see Section 2.6). In Section 4.2 we present results from the first study of WSi_2/Si for hard x-ray multilayers. The purpose of this research was to determine the differences in x-ray reflectivity performance when one pure material (W) is replaced in the multilayer by a compound formed with the spacer material (WSi_2, in this case). Section 4.3 considered another spacer material for W with a higher optical contrast, and the selected material was carbon. In Section 4.4, carbon was paired with platinum, another metal with high melting point and higher density. For this material combination, the lowest interface width found was about 3.7 Å. The following material combinations were selected based on the requirement that the reflector material has no absorption edge above 40 keV. Multilayers based on these medium-weight materials would reflect in the upper hard x-ray band better than multilayers based on W, Pt, or other heavy metals, which have K-shell absorption edges in the region 70-80 keV. The first combination studied in this category

was Mo/Si and the results are described in Section 4.5. Mo/Si is extensively studied for EUV lithography multilayer mirrors, but their application in the hard x-ray band encounters some problems with the presence of an amorphous layer at the interface Mo-Si, which is about 7 Å wide. We have searched for replacement candidates for Mo and in Section 4.6 we discuss the case of Nb. Nickel falls in the same category of medium-heavy metal reflectors, but because it forms readily silicides, it was studied in combination with carbon as spacer material.

4.1 W/Si multilayers

Tungsten/silicon is the most studied pair of materials for hard x-ray telescope mirrors for the energy band 10-70 keV. Within this bandwidth, the low absorption and high contrast between the two materials can be exploited by preparing stacks of hundreds of W/Si bilayers to enhance reflection. More important, the magnetron sputtering deposition of W/Si multilayers results in some of the lowest interface widths achievable. The deposition rates are also advantageous for this material combination.

A systematic study of W/Si multilayers was performed in both deposition chambers presented in Chapter 3, with the dual purpose of calibrating the deposited thickness with Ångstrom-level accuracy and reducing the interface widths by optimizing the process conditions.

The study started with the investigation of the surface morphology of single layers of W and Si. The range of process settings was narrowed down to those that resulted in smooth surfaces, as measured by AFM scans of the surface. They are discussed in Sections 4.1.2 and 4.1.3. A short review of reports of other studies of W/Si multilayers can be found in Section 4.1.5. The importance of the thickness control was recognized by others when the deposition rates determined from single layer films were found in disagreement with TEM and XRR thickness measurements of multilayers with periods of a few nanometers. It was postulated by Hasan et al. [1] and later confirmed by others ([2], [3]) that the deposition of W on the Si underlayer removes some silicon material and creates an amorphous interface between W and Si. Our experiment described in Section 4.1.6 proved that the two phenomena discussed in [1] modified the effective deposition rates. The minimum period

of W/Si that can be practically deposited by magnetron sputtering was found to be about 15 Å with an average interface width σ=4.3 Å. Smaller periods result in incomplete layer coverage for W. The interface widths were in this case comparable with the layer thickness and the multilayer reflectivity decreased considerably. It was further shown that for the energy band limited by the W K-edge this minimum period is not of concern because the designs usually require larger bilayer thicknesses. Next we addressed the question of the correlation between the interface width and the fraction of W thickness, γ. The experimental results of our study on periodic multilayers with constant d=25 Å are presented in Section 4.1.8. The last and most important section discusses the minimization of the interface width in the frame of a statistical approach to the coating process. The conclusions of the experiments described were used as guidelines in the study of similar material systems. The thickness calibration data and the optimized deposition conditions were used in the fabrication of depth graded W/Si multilayers which are discussed in the next chapter.

4.1.1 X-ray optical constants for W/Si

The real and imaginary parts of the W and a-Si refraction indices are plotted versus energy in Figures 4.1 and 4.2. The x-ray optical contrast between the two materials is high due to the difference in densities (Table 4.1) and in refraction indices δ (Figure 4.1). The presence of the K-shell absorption edge for W at 69.5 keV is a practical upper limit for the bandwidth of W/Si multilayers. However, there is some recovery of the extinction coefficient β above 100 keV and the possibility to use W/Si multilayers for very high energies (up to 175 keV) was studied in [4].

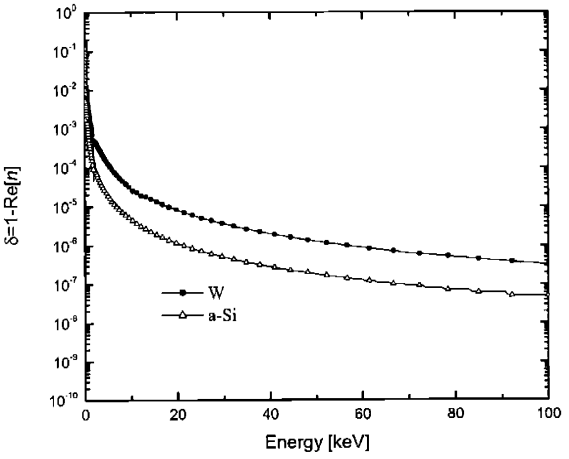

Figure 4.1: The real part of the x-ray refraction indices for W and amorphous Si. The data were compiled by the Center for X-Ray Optics (CXRO) at Lawrence Berkeley National Laboratory. Because for x-rays the real part of the refraction index is very close to unity, it is customary to represent on the vertical scale the quantity δ=1-Re[n]. The difference between δ for the two materials creates the x-ray optical contrast in a multilayer.

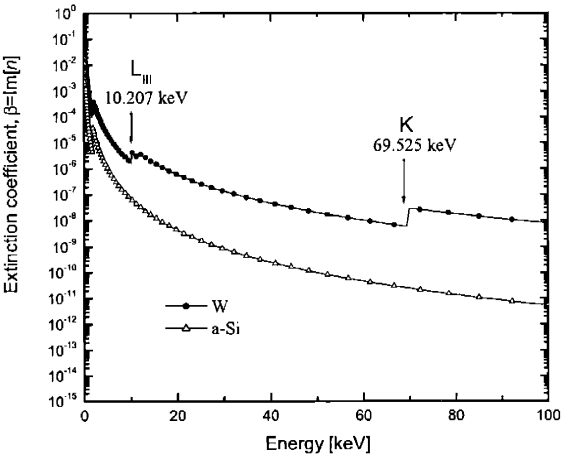

Figure 4.2: The imaginary part of the x-ray refraction indices for W and amorphous Si. The data were compiled by the Center for X-Ray Optics (CXRO) at Lawrence Berkeley National Laboratory. The K- and L-shell absorption edges of W are relevant for the hard x-ray band (E>10 keV) and arrows in the plot show their location. The jump in absorption in W at either edge is fivefold and is followed by a power law E^{-3} decrease of β with increasing energy. A low extinction coefficient β allows for higher reflectivity by adding more layers to the multilayer structure.

Table 4.1: Density and x-ray absorption edges for tungsten and amorphous silicon

Material	Density [g/cm^3]	Absorption edge for K shell [keV]	Absorption edge for L-III shell [keV]
W	19.35	69.525	10.207
a-Si	2.189	1.839	-

4.1.2 Surface morphology of W single layers

Tungsten is a refractory metal with a high melting point, T_m=3695 K. According to Thornton [5], the low temperature ratio T/T_m during magnetron sputtering results in the growth of smooth polycrystalline or amorphous W layers, depending on the argon pressure and the layer thickness. In a preliminary study for this work, single layers of W were deposited in different magnetron sputter process conditions and their surface roughness

was analyzed by AFM. The nominal W layer thickness was 1000 Å and all samples were deposited on silicon wafers positioned at TSD=7 cm from the sputtering target. The parameters that were varied were the argon flow rate and the cathode current. The flow rate determined the pressure in the chamber during the deposition and this varied between 1.5 to 2.5 mTorr for different samples as shown in Table 4.2. The DC power supply output was controlled in current mode and the cathode current was varied between 30 and 150 mA for different samples as shown. The pressure of 2.5 mTorr Ar with a current of 30 mA yielded the smoothest film with a surface microroughness of ~1.5 Å. The data indicate a correlation between the current and the surface roughness: lower current produced lower surface roughness. It is possible that the increased adatom arrival rates for high currents favor columnar growth by not allowing the deposited atoms to migrate laterally over the surface. The initial clusters grow faster as columns in the vertical direction by capturing incoming adatoms and shadowing the valleys between them. Over a few hundreds of Å thickness, the structure of the film would become columnar and polycrystalline, with many voids between the columns and ending with a rough surface.

Table 4.2: Surface microroughness of single layer W samples measured by AFM. The measurements were performed with a Nanoscope IIIa D3000 in tapping mode. The microroughness shown was determined from surface scans of 1μm x 1μm size, with 256 sampling points, and 2 Hz slow scan rate. The target-substrate distance was the same (TSD=7 cm) for the preparation of all samples. The argon backpressure and the cathode current were varied for different samples. Because the voltage depends on the gas pressure, the cathode power varied significantly from run to run and is shown on a separate column for reference.

Sample	Ar pressure [mTorr]	Cathode current [mA]	Cathode power [Watts]	AFM microroughness at 1 μm scan size
W40	2.5	90	26	11.6 Å
W41	2.5	90	26	12.6 Å
W42	2.5	30	9	1.3 Å
W43	1.5	50	16	15.2 Å
W44	1.5	100	36	15.1 Å
W46	2.0	50	16	8.5 Å
W47	2.0	150	48	11.0 Å
W48	2.5	30	9	1.7 Å
W49	2.5	60	18	11.8 Å

The surface morphology of the smooth and rough samples is different, as illustrated by Figures 4.3 and 4.4. On a 1 μm x 1 μm scan area, the sample W40 shows clusters of interconnected pores with 50-100 nm diameter covering about half of the surface area. The Power Spectrum Density (PSD) of the discrete Fourier transform of the surface scan is shown in Figure 4.5. The solid line corresponds to the 1 μm x 1 μm scan area measurement. The short dashed line is for a measurement with the same number of sampling points (256) and slow scan rate (2 Hz), but a 3 μm x 3 μm scan area was covered. The long dashed line corresponds to a 10 μm x 10 μm scan area with 512 sampling points and 1 Hz. The maximum spatial frequencies that can be sampled by each scan are given by the Nyquist theorem and were lower for the longer scans. For sample W42 (Figure 4.4), the voids sizes are close to the resolution limit. The surface morphology was measured at two different locations with 1x1 μm^2 scans to check uniformity. The two PSD spectra are shown together in Figure 4.6 and they agree very well. The average surface microroughness calculated from these scans was 1.28 Å r.m.s. and was the lowest for all the W single layers grown for this study.

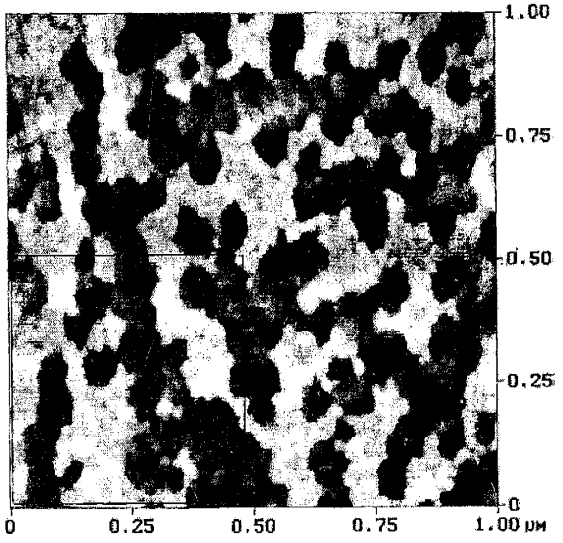

Figure 4.3: AFM scan of the surface of a single layer W sample (W40, Table 4.2). The scan size was 1x1 μm^2 and 256 lines were sampled with a slow scan frequency of 2 Hz. The darker areas show a network of pores that cover about half of the surface and result in a high surface roughness σ=11.6 Å.

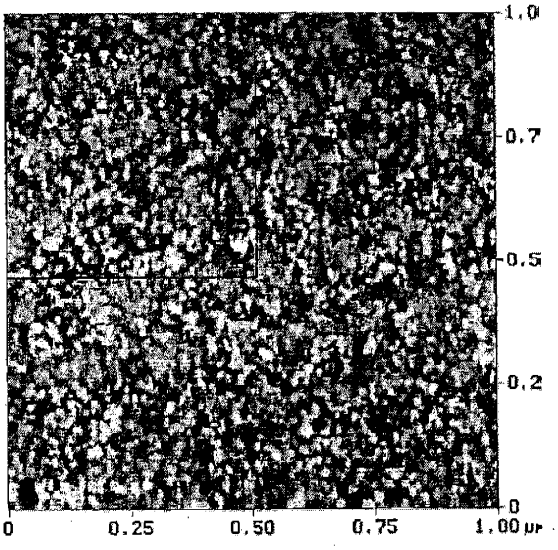

Figure 4.4: AFM scan of the surface of a single layer W sample (W42, Table 4.2). The scan size was 1x1 μm^2 and 256 lines were sampled with a scan frequency of 2 Hz. A slower deposition rate resulted in the growth of finer columns with smaller voids in between. The surface roughness

surface roughness σ=11.6 Å.

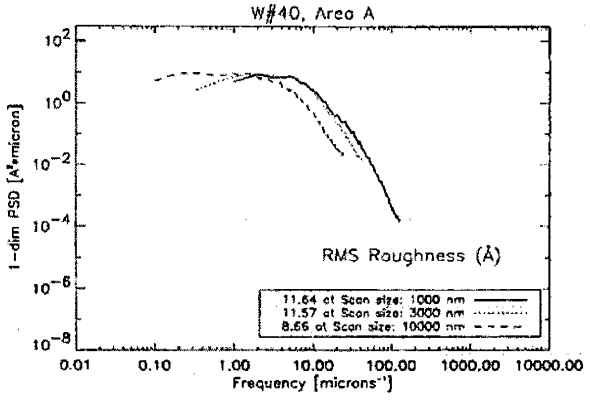

Figure 4.5: Power spectrum density for the surface of sample W40 (Table 4.2) as measured by AFM with three different scan sizes: 1x1 μm^2 (continuous line), 3x3 μm^2 (short dash line), and 10x10 μm^2 (long dash line). The maximum spatial frequency k_{max} that can be probed in a scan depends on the sampling period. The longer scans were limited to lower spatial frequencies as seen in the plot. The surface roughness is equal to the area under the PSD curve and depends on the spatial bandwidth of the measurement. The calculated values of the roughness for the three different scan sizes are 11.64 Å, 11.57 Å, and 8.66 Å, in increasing order of the scan size.

of this sample was σ=1.3 Å.

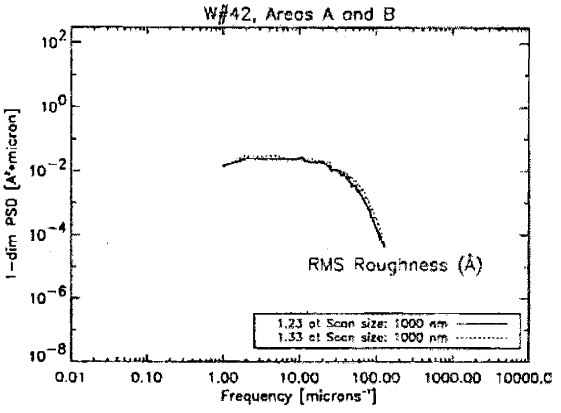

Figure 4.6: Power spectrum density for the surface of sample W42 (Table 4.2) as measured by AFM with the same scan size 1x1 μm^2 on two different locations to verify uniformity. The PSD spectra were in agreement and indicated a very smooth surface with an average σ=1.28 Å r.m.s.

4.1.3 Surface morphology of Si single layers

Silicon is a good choice as a spacer material for hard x-ray multilayers, due to its low energy K-edge at E_K=1.8 keV, a low density to contrast with the reflector, and high sputtering yields that allow fast deposition by magnetron sputtering. TEM studies [3] showed that for thicknesses less than 50 Å, which is the case for hard x-ray multilayers, the structure of the magnetron sputter-deposited silicon layers is amorphous.

We have used AFM to characterize the surface morphology of single layers of Si, deposited with different settings for the magnetron coating parameters. The substrates were silicon <111> wafers with a native oxide layer that was not removed, so that the growth took place actually on the amorphous layer of oxide. The wafers were ordered with a specified surface roughness of less than 4 Å r.m.s. and they were spot checked by AFM to

verify that they satisfied the requirements. The target-substrate distance was the same, TSD=7 cm, for all samples listed in Table 4.3. The argon flow rate in the vacuum chamber and the power supply current were the two process parameters that were varied from run to run. The samples coated at 2 and 3 mTorr (close to the optimal pressure for W) had comparable surface roughnesses of 1.5 Å on the average, but decreasing p_{Ar} below 1 mTorr resulted in an increased surface roughness.

In Figure 4.7 is shown the surface scan of the smoother sample Si12. Compared with the morphology of the W layers, the lack of features like voids indicated uniform layer growth for silicon, as opposed to columnar growth for tungsten. In Figure 4.8 is shown the PSD for the same sample at different scan sizes.

Table 4.3: Surface microroughness of single layer Si samples measured by AFM. The measurements were performed with a Nanoscope IIIa D3000 in tapping mode. The microroughness shown was calculated from surface scans of 1μm x 1μm size, with 256 sampling points, and 2 Hz slow scan rate. The target-substrate distance for the deposition was 7 cm for all samples. Other process parameter settings are listed in the table.

Sample	Ar pressure [mTorr]	Cathode current [mA]	Cathode power [Watts]	AFM microroughness at 1 μm scan size
Si11	2.0	75	28	1.8 Å
Si12	3.0	75	28	1.3 Å
Si18	0.7	45	19	6.7 Å

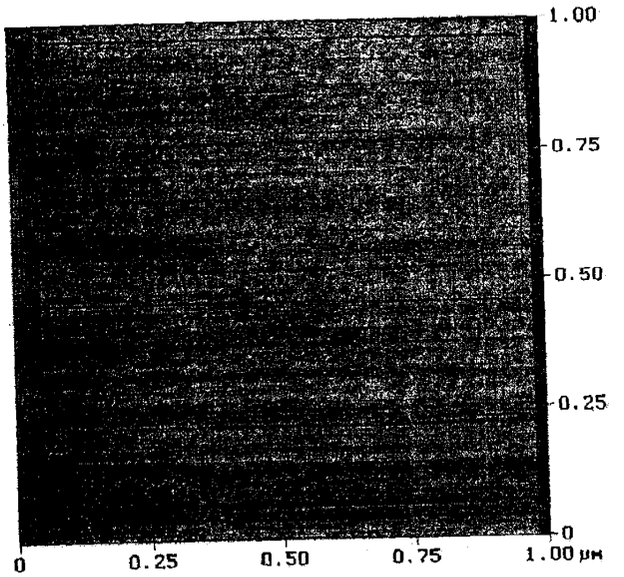

Figure 4.7: AFM scan of the surface of a single layer Si sample (Si12, Table 4.3). The scan size was 1x1 μm^2 and 256 lines were sampled with a slow scan frequency of 2 Hz.

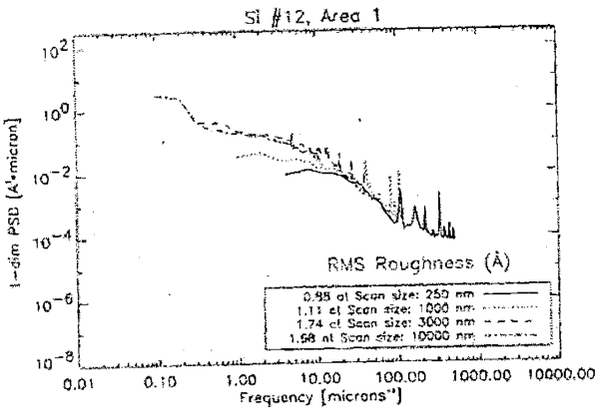

Figure 4.8: Power spectrum density for the surface of sample Si12 (Table 4.3) as measured by AFM with four different scan sizes: 0.25x0.25 μm^2 (continuous line), 1x1 μm^2 (short dash line), 3x3 μm^2 (long dash line), and 10x10 μm^2 (dash-dot line). The calculated values of the root mean square roughnesses for the four different scan sizes are 0.88, 1.11, 1.74, and 1.68 Å, in increasing order of the scan size. The spikes in the PSD curves are due to noise sources present during this measurement.

4.1.4 Thermodynamical properties of the W/Si system

The thermochemical data and the phase diagrams for the W/Si system show that two compounds can be formed: WSi_2 and W_5Si_3. The enthalpies of formation are –57.986 kJ/mole and –33.541 kJ/mole, respectively [6], which indicate that the formation of the WSi_2 compound is energetically more favored. However, the processes that occur at the interface between W and Si depend strongly on the deposition process type and parameters. In magnetron sputtering the growth takes place away from thermodynamical equilibrium and therefore we do not expect WSi_2 or W_5Si_3 to necessarily be formed at the interface.

4.1.5 W/Si multilayers in literature

The first high-resolution electron microscopy study of a W/Si multilayer produced by magnetron sputtering was reported by Petford-Long et al. [2]. The average bilayer thickness was d=28 Å and the expected thicknesses were 5 Å for W and 20 Å for Si. However, the TEM images showed that the layers had 13±4 Å of W and 15±4 Å of Si. The layer reported as W showed actually an amorphous mixture of W and Si, caused by resputtering of the Si underlayers while depositing the W material (see next section). The interfaces for Si growing on W were sharper than for W on Si. With the exception of a few crystalline islands, most of the silicon layer had an amorphous structure. In a similar multilayer also deposited by magnetron sputtering, Shih and Stobbs [7] found an interface width of 12 Å in a periodic multilayer with a period of 23 Å.

Salditt et al. [8] studied intensively the interface height-height correlations in W/Si multilayers by using non-specular reflectivity measurements. They found that the self-correlation functions show the logarithmic scaling behavior predicted by the Edwards-Wilkinson-Langevin equation, which describes the kinetic roughening of a growing surface.

The thermal activation of the interface in W/Si multilayers annealed at temperatures between 400 and 500° C [9] showed important changes in the appearance of

the Bragg peaks. They were attributed to the expansion of the W layers and the diffusion of Si atoms into W. In a later paper [10], the same authors studied the dependence of the W/Si interface width on the number of bilayers N, for N in the range 3 to 15. The XRR scans showed that the interface width was constant (6.5 Å r.m.s.) while N was varied in the above range.

One W/Si study by Windt [11] showed that the relation between the individual W and Si layer thicknesses, as measured by XRR, and the deposition time t_d is affected by the various processes in competition during film growth: after deposition of a Si layer, W atoms are deposited forming a new layer, but an amorphous W-Si interlayer is forming as well, reducing the thickness of W. In addition, high-energy Ar neutrals penetrate the growing W layer and resputter Si. The effect of these competing processes varies with the sputtering conditions and the relative exposure times of W and Si as well.

The HEFT telescope design was optimized [12] for W/Si multilayers. In a pencil-beam measurement at the ESRF synchrotron, Christensen et al. [13] reported an average interface width of 4.5 Å for the graded W/Si coating of the single-reflection mirror prototype for HEFT.

Windt et al. have studied by high resolution TEM and XRR the interfaces of depth graded W/Si multilayers. The interlayer widths were not only different for the two types of interfaces (W-on-Si and Si-on-W), but were also increasing as the period *d* increased, as shown in Figure 4.9, reproduced from [3]. Selected area electron diffraction (SAED) images were obtained from different regions of the multilayer and showed diffraction spots corresponding to α-phase cubic tungsten in the thicker layers, while the thinnest layers showed only a diffuse ring pattern indicating that tungsten is amorphous. Their TEM and XRR measurements suggested that the dominant component of the interface width was the diffuseness σ_d, which was due to ion beam mixing during the deposition.

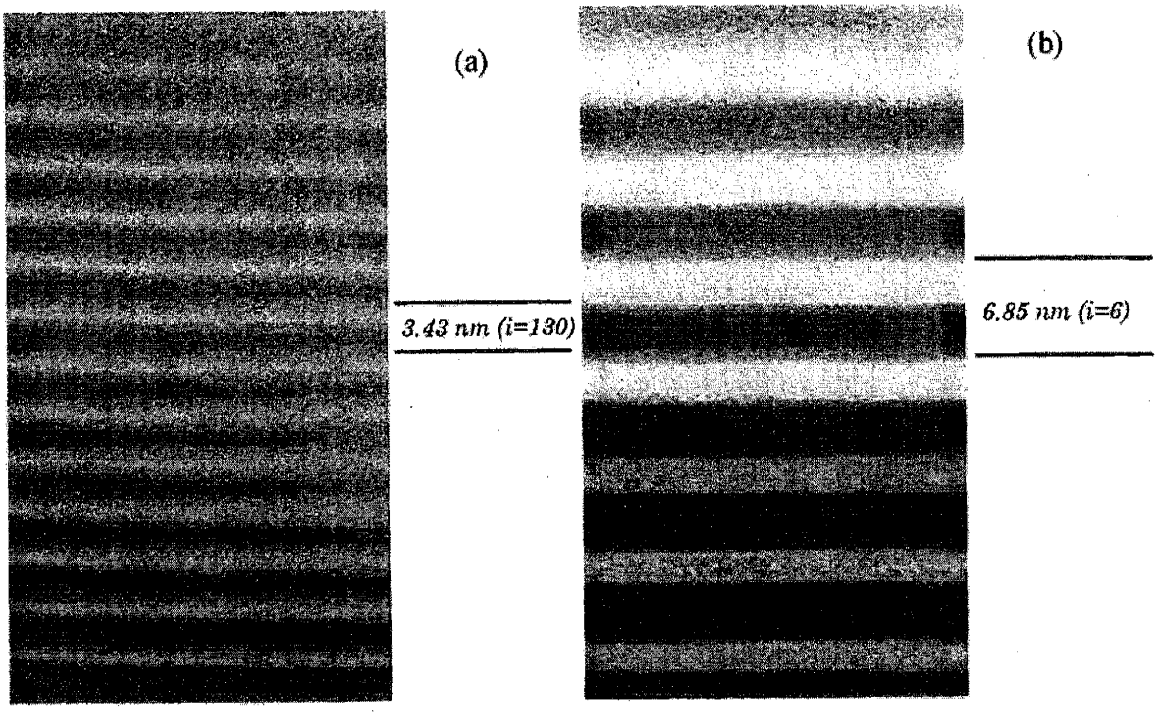

Figure 4.9: High resolution TEM images of bilayers of different thicknesses at the bottom (a) and top (b) of a graded multilayer structure. The W layers are dark and the Si layers are light. They are separated by visible gray bands that are the amorphous W-Si interlayers. The width of the interfaces increases with the thickness of the bilayer d in the stack. (Reproduced from [3], American Institute of Physics©.)

4.1.6 Thickness control for W/Si multilayers

For applications of depth graded multilayers as hard x-ray reflectors, it is imperative to control the thickness of the deposited layers with a precision of a few Ångstroms. In light of the findings reported above, the competing processes of ion beam mixing and resputtering are responsible for deviations of the actual thickness from the nominal values. Without these phenomena, the thickness d of any layer of material would be directly proportional to the deposition time t_{dep}, $d = r_{dep} \cdot t_{dep}$, where the deposition rate r_{dep} is assumed constant. Figure 4.10 presents the deposition rate calibration data for 7 multilayer samples with N=30 periodic bilayers of W/Si. The process parameters were kept constant (p_{Ar}= 2.6 mTorr Ar, 30 mA W and 75 mA Si cathode currents, 7 cm TSD) for all runs. The deposition time of only one material (tungsten) was varied while the deposition time for the second material (silicon) remained constant, t_{Si}=23.7 sec. If the deposition of Si and the

deposition of W were independent processes, i.e., without one material deposition affecting the thickness of the previously deposited material, then all the samples would have an identical Si layer thickness and a W layer thickness proportional to the time of the exposure to the W sputtering cathode, t_W. The XRR-measured thicknesses shown in Figure 4.10 lead to the following interpretation of the growth process:

-below a nominal thickness of 10 Å for W, the backscattered energetic neutrals penetrate through the W layer and create deep collisional cascades in Si. The momentum transmitted to some of the Si atoms is sufficient to remove them from the Si layer and direct them towards the W surface. A fraction of these Si atoms are lost through the surface ("resputtering"), but the rest are stopped by and incorporated in the growing W layer. The effective W thickness is larger than what a proportional law predicts: $d_W > r_W \cdot t_W$.

-for more than 10 Å W thickness, all Si atoms are stopped in the W layer. The beam mixing at the interface makes the W/Si interface wider and shifts the separation plane (by definition, the plane at which the atomic concentrations of W and Si are equal) by about 2 Ångstroms. From this point on, the W layer grows only by addition of incoming W adatoms. The thickness vs. time dependence is linear with a constant offset due to the captured Si atoms: $d_W = d_W^0 + r_W \cdot \left(t - t_W^0\right)$, where $d_W^0 \approx 10\,\text{Å}$, $t_W^0 \approx 30$ s.

Based on the effective deposition rates determined as above, we were able to grow depth graded W/Si multilayers with effective thicknesses as specified by the design. In Figure 4.11 is shown the XRR scan at 8 keV for a depth graded multilayer with N=200 bilayers, coated on a superpolished fused silica substrate. Because the effective rates (i.e., with the mixing effect included) were used to create the file with the deposition times for the computer-assisted coating, the reflectivity data are in very good agreement with the model.

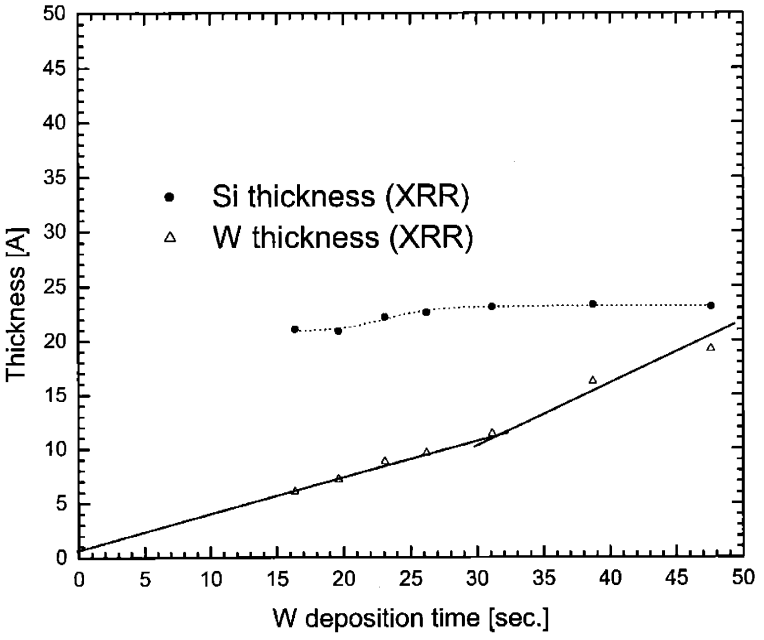

Figure 4.10: Plot of XRR-measured thicknesses of Si (dots) and W (open triangles) layers for 7 periodic W/Si multilayers deposited with the same process parameters and the same deposition time for Si. The deposition time for W was varied from sample to sample as shown on the horizontal axis. Due to the Si resputtering and mixing with W, the effective thicknesses of W and Si are interdependent (see text).

4.1.7 Minimum period for W/Si multilayers

As the period of the multilayers is decreased towards values comparable to the interface width σ, the reflectivity is much reduced due to the lower contrast at the interface. The W/Si multilayer with the smallest period that was prepared for this study had d=15.9 Å and an average interface width σ=4.3 Å about equal to the Si layer thickness d_{Si}=4.8 Å. Because σ and d_{Si} were comparable, the intensity of the first Bragg peak (Fig. 4.12) at 8 keV was very low: 0.47%. An IMD simulation for the same multilayer structure but with perfectly smooth interfaces (i.e., σ=0 Å) predicted a Bragg peak reflectivity of 6.1%.

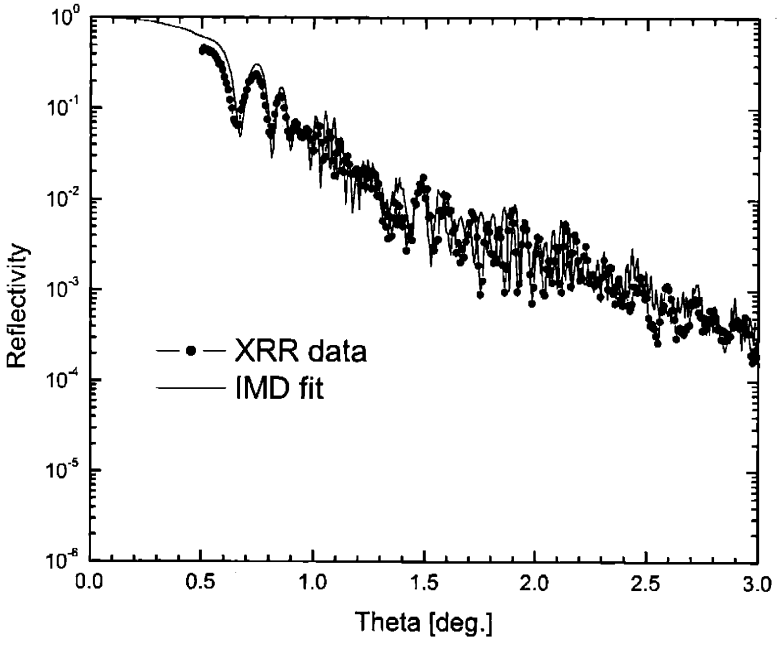

Figure 4.11: X-ray reflectivity scan at 8 keV of a graded W/Si multilayer with N=200 bilayers. The bilayers thickness *d* varied from 205 Å at the surface to 25 Å at the substrate. In order to achieve effective thicknesses identical with the design, a series of thickness calibration runs were performed using periodic multilayers with *d* varying in the range 25 to 200 Å. The agreement between the design and the deposited thicknesses is illustrated by the good match between the reflectivity data and the model fit presented above.

Deposition trials of multilayers with design periods below 15 Å resulted in high interface widths and in consequence very low peak reflectivity. For any practical application, the minimum period that can be used in multilayer designs is about 15 Å. In a depth graded multilayer, the existence of a lower limit for *d* translates into an upper limit for the energy of the photons that can be reflected. For a grazing angle of incidence θ=20 arcmin, a minimum period d_{min}=15 Å would correspond to 71.7 keV, which is above the K-shell absorption edge of W. Therefore, for W/Si multilayers used as reflectors at low grazing angles, the upper limit of the energy bandwidth (E_{max}) is dictated by the absorption edge and not by the minimum achievable period d_{min}. For Ni/C multilayers grown by magnetron sputtering it will be shown in Section 4.4 that E_{max} is determined by the minimum period, since there is no absorption edge above 10 keV for Ni.

This example also demonstrates the need to minimize the interface widths by optimizing deposition process parameters and by eliminating variations of the process parameters to which the interface width is more sensitive. This topic will be discussed in Section 4.1.9.

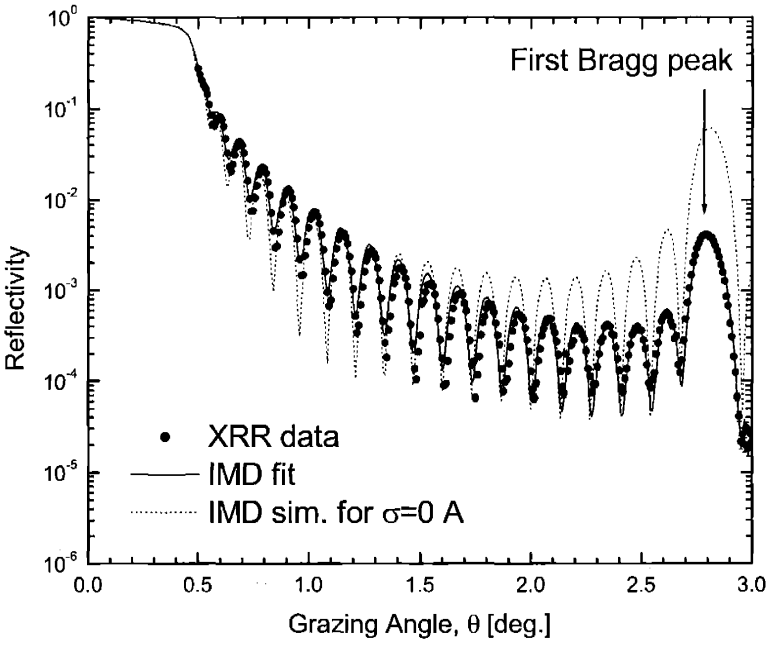

Figure 4.12: Plot of x-ray reflectivity versus grazing angle at E=8 keV for a W/Si multilayer with N=20 periodic bilayers of 11.1 Å W and 4.8 Å Si. The features present in the plot are: the total reflection plateau (for $\theta<0.45°$), the Kiessig fringes, and the first order Bragg peak (indicated by arrow). The average interface width, σ=4.3 Å, is comparable to the Si layer thickness and reduces the reflectivity of the first Bragg peak to 0.47%. An ideal multilayer with the same thicknesses but with smooth interfaces would have a peak reflectivity of 6.1% according to an IMD simulation, shown with a dotted line.

4.1.8 The W thickness fraction γ and the interface widths in W/Si

The correlation of the interface width and the reflector thickness γ (defined as $\gamma = \frac{d_W}{d_W + d_{Si}}$) was studied by analyzing a series of 12 samples deposited under the same conditions: p_{Ar}= 2.6 mTorr Ar, 30 mA W and 75 mA Si cathode currents, 7 cm TSD. The number of bilayers was N=30 and the period d=25 Å. The W thickness fraction γ was varied between 0.2 and 0.8 and the samples were analyzed by XRR at 8 keV. The interface W-on-Si is consistently wider than Si-on-W, therefore the reflectivity is largely dominated by the W-

on-Si interface. In Figure 4.13, σ(W/Si) is plotted versus the fraction of W thickness. The interface width was determined using the IMD software with a typical error of ±1 Å. The trend for the set of data shows that the interface widths are smaller when the thickness fraction of W is smaller, down to a lower limit of ~0.2. Below this limit, the W thickness is too low to achieve continuous layer growth.

Most of the multilayer design procedures "freeze" the reflector thickness fraction γ and the interface widths in order to reduce the number of free parameters for optimization. The study of the interdependence between σ(W/Si) and γ indicates that any design selection of γ in the interval 0.2 to 0.5 would result in interface widths of 4 Å on the average for multilayers with a period d=25 Å (typical d_{min} value for graded designs).

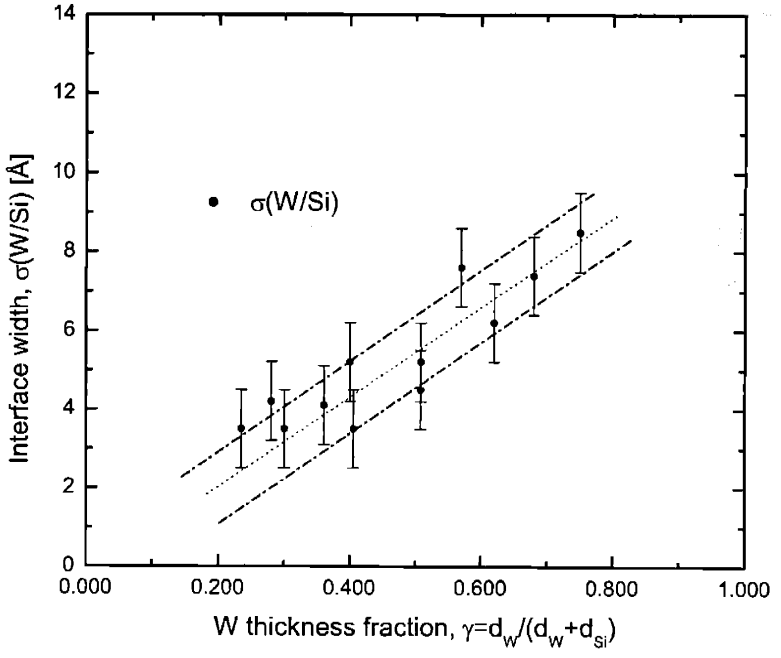

Figure 4.13: Correlation between the interface width σ(W/Si) and the thickness fraction of W, $\gamma=d_W/d$. The total thickness of the bilayer was held constant at d=25 Å. The ratio between the W layer thickness and d was varied as shown in the plot. The interface widths σ were determined with ±1 Å error from IMD fits of the XRR data. The dotted line is not a fit to the data, but shows the average trend for σ (see text). The two dot-dash lines indicate ±1 Å deviation from the average trend (dotted line).

4.1.9 Optimization of the deposition process using the Taguchi approach

It is known from Section 2.6 that the reflectivity depends exponentially on the interface roughness σ (the Debye-Waller factor, eq. (2.48)) and in order to approach the maximum reflectivity one must reduce σ to the lowest possible value. The problem of minimizing the interface width was next studied with regard to the deposition parameters. A complete theory of the dependence of σ on the particular magnetron sputtering conditions is not possible due to the complexity of the process. Any simulation would require many unknown microscopic parameters (cross sections, field distributions, etc.) and would be computationally prohibitive. At the other extreme, an empirical study would involve the production of an equally prohibitive large number of samples in different sputtering conditions. For the purpose of investigating the interface width in relation to the deposition process, we adopted a standardized statistical approach, namely the design of experiment (DOE) method, also known as the Taguchi method [14]. A screening experiment was performed with a series of eight samples and it was based on a choice of four influential parameters: argon pressure p_{Ar}, target-substrate distance TSD, and the currents in the cathodes, I_W and I_{Si}.

A repeatability test was done first to verify that the magnetron sputtering process is well controlled and that each sample is representative for the sputtering conditions. Five W/Si multilayers with N=20 periods and d=28 Å were coated for this test using the same set of parameters (p_{Ar}, TSD, I_W, I_{Si}). The centroid and the maximum reflectivity of the first Bragg peaks were determined from 8 keV XRR scans and are shown in Table 4.4. Being extracted directly from the experimental data, both quantities are free of artifacts due to multiparametric fits. The standard deviation of the Bragg peak angle was 0.31%, indicating excellent reproducibility of the period d from sample to sample (~0.1 Å st.dev.). The peak reflectivity had a standard variation of 3.6%. If we make the simplifying assumption that the peak reflectivity R is correlated with the interface width σ by the Debye-Waller formula: $\ln R \propto -\sigma^2$, then the estimated variation of σ from sample to sample is 1.5% st.dev. The conclusion of this test is that when the coating runs are repeated, the period and the interface width are reproduced within a few percents. Therefore, a single sample

produced in a particular set of sputtering conditions is representative for that coating run and, if necessary, can be replicated by subsequent repeat runs within these standard deviation limits.

Table 4.4: The reflection angle and the maximum reflectivity at 8 keV for the first order Bragg peaks of five W/Si multilayers. The design of all samples had N=20 bilayers with a period d=28 Å. They were deposited using the same set of process parameters (p_{Ar}=2.6 mTorr, I_W=30 mA, I_{Si}=75 mA, TSD=7 cm). The peak positions were reproduced within 0.31% standard deviation and the peak reflectivity had a standard deviation of 3.6%. The purpose of this test was to verify the reproducibility of the magnetron sputtering process.

Sample	First Bragg peak angle [deg.]	First Bragg peak reflectivity [%]
WSi227	1.617	28.66
WSi228	1.625	27.33
WSi229	1.625	29.06
WSi230	1.625	29.06
WSi231	1.633	30.66

Due to the complexity of the magnetron sputtering process, it is not possible to predict the dependence of the interface width σ on the particular process conditions. A theoretical treatment would require many unknown microscopic quantities and would be computationally prohibitive. A factorial experiment in which all possible combinations of process parameters are tried is equally prohibitive due to exponential relation between the number of trials and the number of parameter values. We have adopted a standardized statistical approach to study the interface width relation to the deposition process. The design of experiment (DOE) method, also known as the Taguchi method, evaluates simultaneously the ability of the process "factors" (i.e., sputtering parameters) to affect the variability of a particular "process characteristic" (the measured interface width, in our case). With a choice of four influential parameters (p_{Ar}, TSD, I_W, I_{Si}) and two "levels" for each parameter, the DOE method prescribed the preparation of eight samples.

Because we want to compare samples having the same number of bilayers N and thickness distribution but different process conditions, it is impossible to achieve this common structure without first knowing the deposition rates. Thus additional coating runs

must be performed solely for rate calibration purposes and are not included in the Taguchi analysis. After the deposition rates were determined for the eight different process conditions described in Table 4.5, we could proceed with the selection of a design structure and its fabrication.

Ideally, the design structure should be that of the depth graded multilayer optimized for the particular application, e.g., the outermost shell of the telescope for the Con-X mission. This is time consuming for the fabrication of eight samples (with N=350 each) as well as for their analysis. We have simplified instead the design structure to N=20 bilayers with a period equal to the average of the bilayer thickness distribution in the graded design. The time saved with the sample preparation and analysis outweighs the small differences for σ associated with the replacement of the graded multilayer by the periodic design with the average d. In conclusion, this screening Taguchi experiment compares the interface widths of eight multilayers with the following structure: N=20, d=30 Å, and γ=0.4. The eight samples were analyzed by XRR at 8 keV and their interface widths σ(W/Si) are listed in the last column of Table 4.5.

Table 4.5: Description of the process parameters used for the Taguchi experiment. Four process parameters (argon backpressure p_{Ar}, target-substrate distance TSD, W cathode current I_W, and Si cathode current I_{Si},) were chosen as the most influential for a screening experiment. Each parameter could take one of the two values listed in the table. For the Taguchi analysis eight samples must be prepared in the conditions enumerated in each row. All samples were periodic W/Si multilayers with N=20, d=30 Å, and γ=0.4. They were characterized by XRR at 8 keV and their interface widths σ(W/Si) are presented in the last column.

Sample #	p_{Ar} [mTorr]	TSD [cm]	I_W [mA]	I_{Si} [mA]	σ(W/Si) [Å]
1	2.6	7.0	30	75	3.0
2	2.6	7.0	70	150	5.0
3	2.6	9.5	30	150	6.0
4	2.6	9.5	70	75	4.5
5	5.2	7.0	30	150	4.8
6	5.2	7.0	70	75	4.8
7	5.2	9.5	30	75	4.2
8	5.2	9.5	70	150	5.2

In the Taguchi analysis it is customary to plot the average of the results for a particular level of a factor while the other factors are allowed to take any value. For example, there were four samples for which the Si cathode current was 75 mA. The average for σ(W/Si) measured for these four samples was 4.12 Å. The other four samples were prepared at 150 mA Si cathode current and their average σ(W/Si) was larger: 5.25 Å. By plotting these partial averages for all four parameters as in Figure 4.14, one can notice that the "main effect" (in DOE terminology) is attributed to changes in I_{Si}, followed in importance by changes of TSD and I_W. The change in pressure from one level to another had the least influence on the interface width σ(W/Si). These conclusions apply to the set of levels used in the experiment and should not be extrapolated.

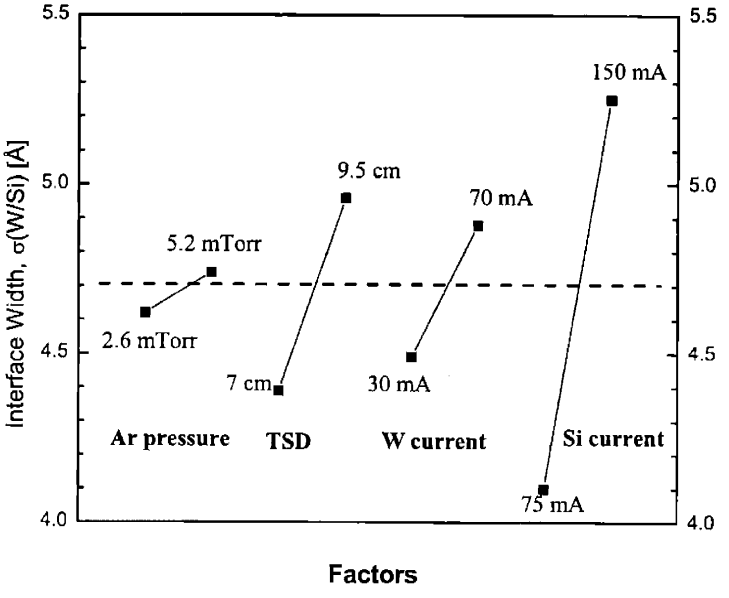

Figure 4.14: Main effect analysis for W/Si multilayer samples (N=20, d=30 Å, and γ=0.4). Four coating parameters were chosen, with two levels for each, as described in Table 4.5. The samples were characterized by XRR at 8 keV and their interface widths σ(W/Si) are listed also in Table 4.5. The square symbols represent the partial averages of σ(W/Si) for the subset of samples coated using the same level for a given process parameter (indicated by label). A line segment connects the symbols corresponding to the same process parameter. The average interface width of the whole set of samples is represented by a dashed line for reference. The strongest effect on σ(W/Si) corresponds to a level change for the Si cathode current.

The analysis of variance (ANOVA) was performed with the Qualitek-4 demo software (http://www.rkroy.com). This procedure estimates the statistical weight of each of

the controllable factors used and also estimates the weight of other factors not included in the experiment, as well as the level of noise in the experiment and measurement. For the W/Si experiment, the largest contribution of a controlled parameter to the total variance was 36.6% and it was due to I_{Si}, the Si cathode current. It is possibly related to the large change in the deposition rate of Si when switching I_{Si} from 75 to 150 mA. The other three parameters added less than 2% to the variance of σ(W/Si). The largest variance contribution (61%) was not associated with any of the four controlled factors and might have been due to statistical noise and/or other parameters that were not controlled in the experiment. The variance due to noise can be reduced by repeating the series of coating runs and producing more samples. The additional parameters that can be considered are, for example, the substrate surface roughness and the substrate temperature. A future Taguchi study will consider these means to reduce the variance of the interface width σ(W/Si).

In conclusion, the screening experiment results have indicated that the reflectivity of magnetron sputtered multilayers with d=30 Å is maximized when depositing at low Si and W cathode current levels and with the substrate closer to the cathodes. The optimum settings for these coatings were also used for the production of depth graded multilayers. The main effect on σ was due to variations of the Si cathode current. A large contribution to the variance of σ was attributed to statistical noise and process parameters that were not controlled in this screening experiment. These problems will be addressed by an extended experiment.

4.2 WSi_2/Si multilayers

Tungsten silicide (WSi_2) is a stable compound with a density of 9.3 g/cm^3 and known optical constants (CXRO-LBNL). The material is available commercially with high purity (99.95%) as a sputtering target. It is known [15] that during the sputtering of compound and alloy targets the element with the highest yield is initially depleted in the first atomic layers from the surface (preferential sputtering). An ion irradiation-enhanced diffusion current from the bulk to the surface compensates for the depletion and in a few minutes a

steady state atomic distribution is reached, having the original composition of the bulk. The relative sputtering rates of the elemental components preserve the stoichiometry of the compound/alloy. Because the atoms arrive at the substrate in the same ratio, the film grows with an identical composition as the sputtering target.

Tungsten silicide was chosen as a substitute for pure tungsten in an attempt to reduce one possible contribution to the interface width in a W/Si multilayer. If both diffusion and chemical reactions are responsible for the tendency of the two elements to form a compound at the interface, then the replacement of W by WSi_2 as reflector material would serve a double purpose:

-the diffusion of Si atoms from the spacer layer to the reflector would be blocked by a high concentration of Si in the reflector.

-the W atoms are already saturated with Si atoms in the WSi_2 compound, so they cannot enter in reactions with Si from the spacer layer.

Both effects should decrease the interface width of WSi_2/Si multilayers compared to equivalent W/Si multilayers.

4.2.1 X-ray optical constants for WSi_2/Si

The real and imaginary parts of the WSi_2 and a-Si refraction indices are plotted versus energy in Figures 4.15 and 4.16. The x-ray optical contrast between the two materials is reduced because WSi_2 has a density lower than W. The K-shell absorption edge for W at 69.5 keV presents the same practical upper limit for the energy bandwidth.

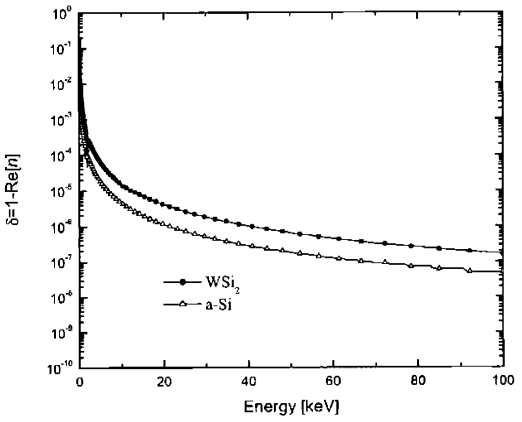

Figure 4.15: The real part of the x-ray refraction indices for WSi_2 and amorphous Si. The data were compiled by the Center for X-Ray Optics (CXRO). The vertical axis shows δ=1-Re[n]. The difference between δ for the two materials is lower than for the W/Si system.

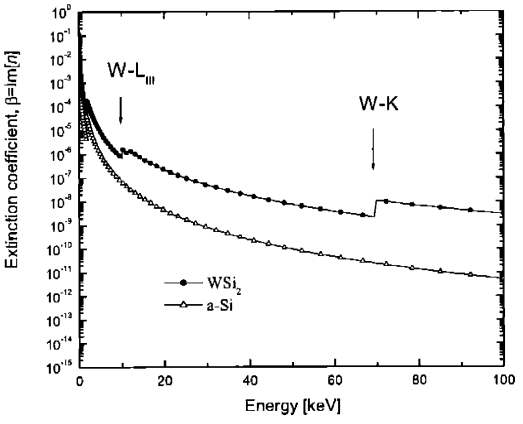

Figure 4.16: The imaginary part of the x-ray refraction indices for WSi_2 and amorphous Si. The data were provided by the Center for X-Ray Optics (CXRO). The K- and L-shell absorption edges of W are indicated by arrows.

4.2.2 Interface widths of WSi_2/Si multilayers

In Table 4.6 are presented the sputtering process conditions and the measured thicknesses and interface widths for a series of 17 multilayer samples. The argon pressure varied between 2.2 and 4.0 mTorr and the target-substrate distance was varied from 7.0 cm to 10.2 cm. With the exception of one run, the current at the cathode with the WSi_2 target was constant, I_{WSi_2} = 40 mA. For the Si cathode, the current was varied between 40 and 75 mA.

The average σ(WSi_2-on-Si) for all samples was 6.5 Å. While this number is higher than the average value σ(W/Si)=4.7 Å for the Taguchi analysis for W/Si, it must be taken in account that we are comparing different structures. The W/Si multilayers were deliberately prepared with the same period d=40 Å and γ=0.4 and relied on accurate calibrations of the deposition rates. For WSi_2 the trial runs presented in Table 4.6 were deposited without knowing a priori the deposition rates, so their periods d were not controlled and varied from 15.2 to 53.6 Å.

By lack of a Taguchi analysis for WSi_2/Si, it is more relevant to note that the minimum σ(WSi_2/Si) was ~ 3.0 Å (Figure 4.17) and was comparable with the minimum

σ(W/Si) interface width, hence there was no improvement by using the silicide instead of the pure tungsten sputtering target. The minimum σ(WSi_2/Si) occurred at TSD=8.3 cm instead of TSD=7.0 cm for W/Si. The fact that W/Si and WSi_2/Si have the same minimum σ rules out the diffusion + reaction model and strongly suggests that only the beam mixing of W and Si by energetic Ar neutrals is responsible for the interface width. The backscattering and neutralization of the Ar^+ ions is a byproduct of the sputtering process that uses the same Ar^+ ions to remove material from the target. The ratio of backscattered neutrals and sputtered atoms is independent of the cathode current. By lack of means of reducing this flux ratio, one can try at least to lower the average energy of the neutrals, e.g. from 100 eV to 50 eV, by changing the cathode voltage from 425 Volts to 225 Volts. In current controlled operation of the cathode, the decrease in voltage can be achieved only by increasing the pressure (above 7 mTorr for our cathodes). This will decrease the mean free path and create conditions for more collisions of the sputtered atoms with the Ar gas, leading to their thermalization. Since thermalization lowers the average adatom energy below 1 eV, the film will grow with a high roughness and the result is opposite to what was sought. From these arguments it seems that the measured interface width of 3.0 Å is very close to the absolute minimum value. The interface mixing by Ar neutrals must be recognized as a phenomenon intrinsically coupled with sputtering and unavoidable for all practical purposes. Theoretically, replacing Ar with a heavier noble gas like Xe should decrease the backscattering yield and reduce the flux of energetic neutrals. We have attempted this test with only two coating runs (due to the limited amount of Xe available) and we did not found an improved interface width. It is possible that the deposition conditions for the new gas (Xe) were not near optimum, so this study must be resumed with a larger number of test runs that would include process optimization.

Having the same minimum σ as W/Si, the new material combination WSi_2/Si is at disadvantage when applied for a depth graded design. Due to the lower optical contrast between WSi_2 and Si, a larger number of bilayers are required to obtain the same reflectivity as for W/Si. If the coating time is important, then it is impractical to use tungsten silicide as a substitute reflector material for tungsten.

Table 4.6: Deposition conditions for WSi_2/Si multilayers and measured layer thicknesses and interface widths.

Sample number	Argon pressure [mTorr]	TSD [cm]	WSi_2 cathode current [mA]	Si cathode current [mA]	WSi_2 thickness [Å]	Si thickness [Å]	$\sigma(WSi_2/Si)$ [Å]	$\sigma(Si/WSi_2)$ [Å]
WSi_2/Si#1	2.5	7.0	40	75	31.3	22.7	7.0	2.0
WSi_2/Si#2	2.5	7.0	40	75	26.9	26.1	8.5	2.0
WSi_2/Si#4	2.5	8.3	40	75	23.2	33.5	9.0	2.0
WSi_2/Si#5	2.5	8.3	40	40	34.1	18.7	3.1	2.0
WSi_2/Si#6	2.5	9.5	40	75	24.4	31.0	9.0	3.0
WSi_2/Si#7	2.5	9.5	40	40	21.6	27.4	8.2	2.0
WSi_2/Si#8	2.2	7.0	40	75	31.0	22.4	4.9	2.4
WSi_2/Si#9	3.0	7.0	40	75	26.3	24.8	7.5	2.5
WSi_2/Si#10	3.5	7.0	40	75	26.1	22.2	9.0	1.0
WSi_2/Si#11	4.0	7.0	40	75	25.6	22.0	7.5	3.0
WSi_2/Si#12	2.5	8.3	40	40	34.6	19.0	4.0	3.0
WSi_2/Si#13	2.5	8.3	40	40	34.6	19.0	4.0	3.0
WSi_2/Si#16	2.6	8.3	40	40	20.6	11.4	3.0	5.0
WSi_2/Si#17	3.5	8.3	40	40	11.9	17.6	3.0	3.5
WSi_2/Si#18	2.6	7.0	40	40	5.4	16.6	5.0	3.8
WSi_2/Si#19	3.5	7.0	40	40	13.7	6.7	7.0	1.6
WSi_2/Si#20	2.5	10.8	40	40	11.4	3.8	8.0	4.2
WSi_2/Si#21	2.5	10.8	80	80	24.8	8.3	9.9	4.3

The smallest period achieved for WSi_2/Si was 20.4 Å with an average interface width of 6.8 Å equal to the silicon layer thickness. The 8 keV reflectivity plot is shown in Figure 4.18.

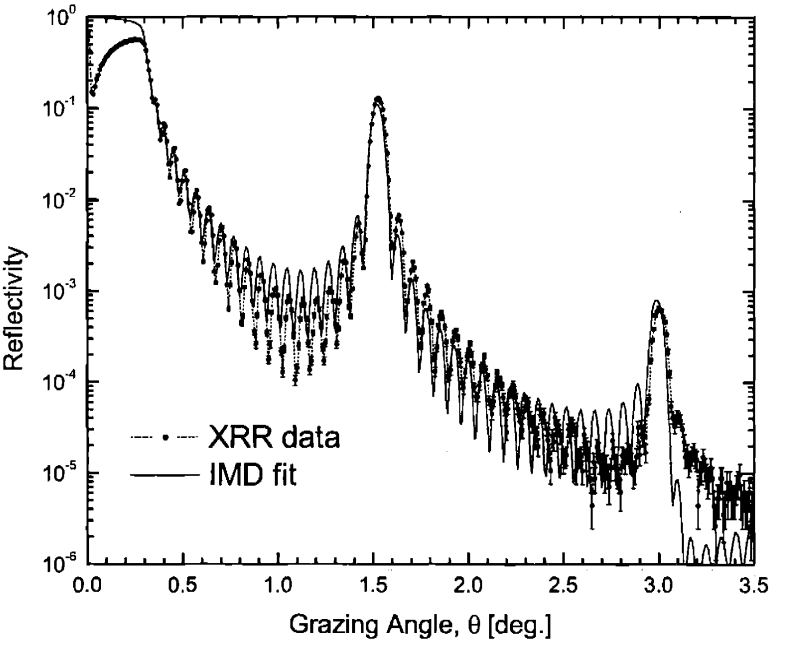

Figure 4.17: X-ray reflectivity at 8 keV for a WSi_2/Si multilayer (sample WSi_2/Si#17) with N=20 periodic bilayers of 11.9 Å WSi_2 and 17.6 Å of Si. The interface width was one of the lowest for this material combination: $\sigma(WSi_2/Si)$=3.0 Å and $\sigma(Si/WSi_2)$=3.5 Å, as determined from the IMD fit. The values for σ are comparable with the minimum σ obtained for W/Si multilayers.

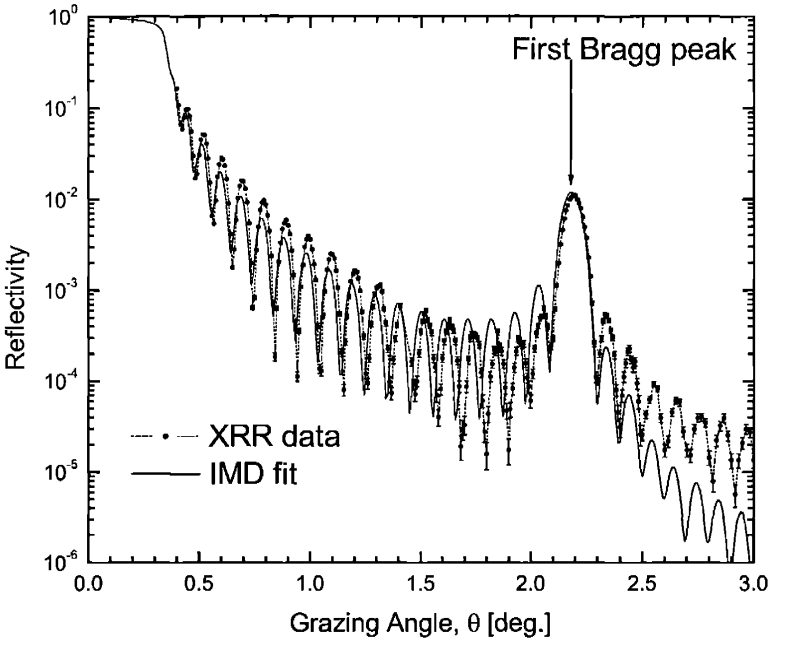

Figure 4.18: X-ray reflectivity at 8 keV for a WSi_2/Si multilayer (WSi_2/Si #19) with N=20 periodic bilayers of 13.7 Å WSi_2 and 6.7 Å Si. The interface width for WSi_2-on-Si is 7 Å r.m.s. and is larger than the Si layer thickness. This was the smallest period achieved with WSi_2/Si multilayers.

4.3 W/C multilayers

Carbon as a spacer material has the advantage of a low absorption coefficient. However, the sputtering yield is very low and coating multilayers with hundreds of periods can be very time consuming. For the study of this material system, 30 samples with periodic and depth graded multilayers were coated.

4.3.1 X-ray optical constants for W/C

The real and imaginary parts of the W and a-C refraction indices are plotted versus energy in Figures 4.19 and 4.20. Over the hard x-ray band the imaginary part of the refraction index β(C) is only 5% of β(Si). Since the reflectivity of a multilayer increases with the number of bilayers (up to a saturation limit), the advantage of using C instead of Si as

spacer consists in the possibility of adding more layers with less total absorption in the multilayer.

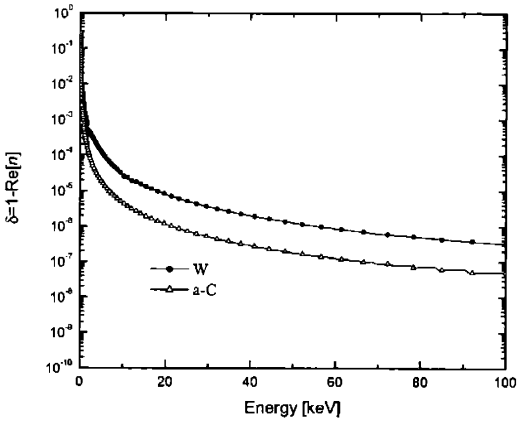

Figure 4.19: The real part of the x-ray refraction indices for W and amorphous C. The data were compiled by the Center for X-Ray Optics (CXRO). The vertical axis shows δ=1-Re[n].

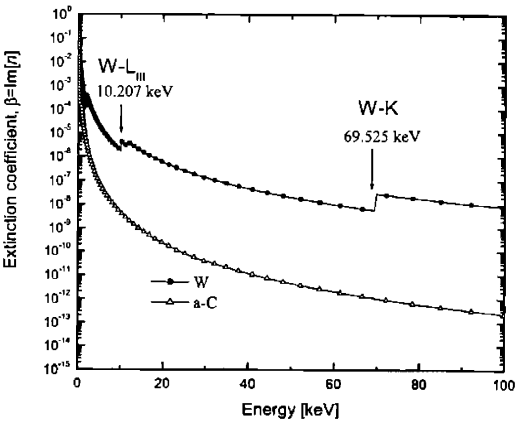

Figure 4.20: The imaginary part of the x-ray refraction indices for W and amorphous C. The data were provided by the Center for X-Ray Optics (CXRO). The absorption of C is very low in the hard x-ray band. The arrows indicate the K- and L-shell absorption edges of W.

4.3.2 Surface morphology of C single layers

AFM was used to characterize the surface morphology of single layers of C deposited with different settings for the magnetron coating parameters. The substrates used were silicon <111> wafers with surface microroughness below 4 Å r.m.s. In Table 4.7 are presented for comparison the AFM results for samples prepared in different conditions and with different thicknesses. The target-substrate distance was set to TSD=7 cm (same as for smooth W single layer coatings) and then other parameters were varied to minimize the surface roughness. For the samples deposited with the same cathode current I_C=90 mA, the roughness increased from 1.5 to 9.0 Å r.m.s. as the carbon layer thickness was increased from 30 to 730 Å. TEM studies of carbon layers deposited by magnetron sputtering showed (Petford-Long *et al.*, [2]) that amorphous carbon was grown for thicknesses under 50 Å and that some graphitic structure was formed in thicker layers. Although we have not analyzed by TEM our samples, the increased surface roughness measured for films thicker than 300 Å indicated an agreement to a rougher polycrystalline structure.

Table 4.7: Surface microroughness of single layer C samples measured by AFM. The measurements were performed with a Nanoscope IIIa D3000 in tapping mode. The microroughness shown was calculated from surface scans of 1μm x 1μm size, with 256 sampling points, and 2 Hz slow scan rate.

Sample	Ar pressure [mTorr]	Cathode current [mA]	Cathode power [Watts]	Film thickness [Å]	AFM microroughness at 1 μm scan size [Å]
C19	2.5	90	41	300	2.7
C26	3.0	90	39	730	9.0
C27	3.0	180	89	1320	8.6
C28	2.5	90	39	114	2.5
C35	2.5	90	39	30	1.5

The setting of the cathode current at I_C=90 mA was a compromise between the low deposition rates at low currents and the generation of arcs and hot particulates at the cathode when operating at high currents. Also, an increase to 2.3 mm of the gap between the ground shield and the target raised the voltage and helped maintain the plasma stable, without arcs and particulate generation. It is important to note the large difference between the deposition rates for C and Si at cathode current levels that result in comparable surface microroughness. For carbon at I_C=90 mA, the deposition rate was 0.15 Å/s versus 1.02 Å/s for Si at I_{Si}=75 mA. This is a major drawback for carbon as a spacer material.

Figure 4.21 shows the AFM surface scan image of a smooth carbon layer (sample C19, Table 4.7). In Figure 4.22 the PSD plots for two different 1 x 1 μm^2 areas of the sample are in good agreement indicating a uniform roughness of 2.7 Å r.m.s.

4.3.3 Thermodynamical properties of the W/C system

Two compounds (WC and W_2C) can be formed in thermodynamical equilibrium, according to the phase diagram for the W/C system. The enthalpies of formation are -21.0 and -8.8 kJ/mole for WC and W_2C, respectively. As discussed for the W/Si system, in magnetron sputtering it is not necessarily expected to have the above compounds formed at the interface.

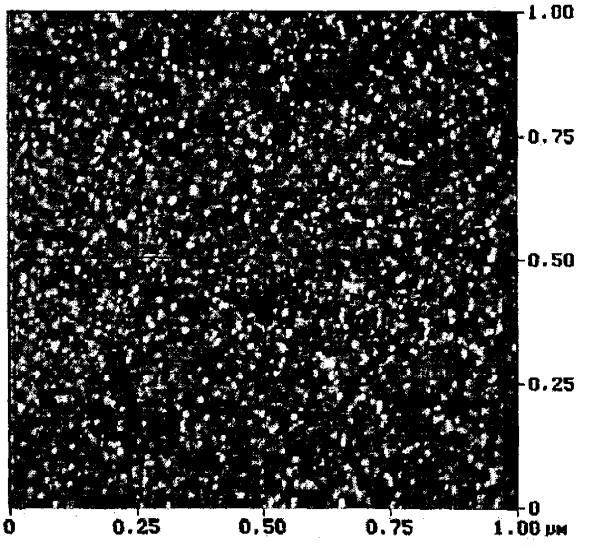

Figure 4.21: AFM scan of the surface of a single layer C sample (C19, Table 4.7). The scan size was 1x1 μm^2 and 256 lines were sampled with a slow scan frequency of 2 Hz.

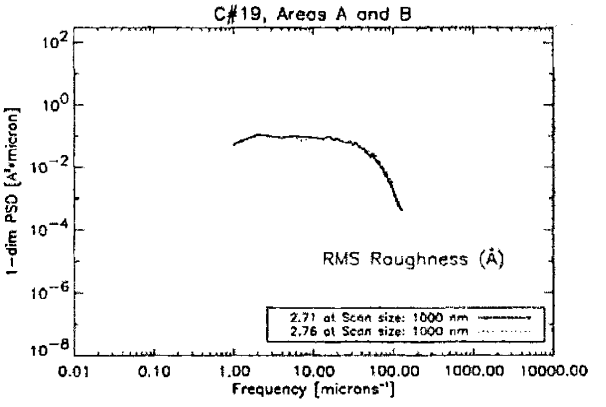

Figure 4.22: Power spectrum density for the surface of sample C19 (Table 4.7) as measured by AFM on two 1x1 μm^2 areas. The average surface roughness was 2.7 Å r.m.s.

4.3.4 Magnetron sputtered carbon and W/C multilayers in literature

The problem of stress generation in magnetron sputtered carbon films was studied by Mounier and Pauleau [16]. They have deposited micron-thick layers of carbon on biased substrates and measured their thickness by Rutherford backscattering and the intrinsic stress by the curvature method. The intrinsic stress for deposition at room temperature was dependent on the substrate voltage and reached a maximum of 2.8 GPa at -250 Volts. For unbiased substrates, the measured intrinsic stress was 0.8 GPa.

Carbon layers deposited by magnetron sputtering have been intensively investigated to understand the spatial correlation of sites with C-C bonding of type sp^3 and sp^2. Logothetidis et al. [17] have analyzed by spectroellipsometry and XRR, single layer films deposited by rf magnetron sputtering on Si <001> wafers. The substrate bias was varied from +10 to –100 V to attract Ar^+ ions from the plasma and improve the sp^3/sp^2 ratio in the carbon film. It was found that the ratio is maximized at –80 V bias and that in the initial stages of growth the sp^2 bond dominates.

A study of the thermal stability of sputtered thick a-C films is important for applications as protective coatings because it defines the useful temperature range. A comparative study of anneal-induced modifications was presented in [18]. An increase of the size of the sp^2 domains has been observed from Raman scattering.

Carbon was used as a smoothing buffer layer in [19] to reduce the substrate roughness of 8 Å r.m.s. for a Zerodur glass substrate. By depositing 40 Å of carbon on top of the glass, the surface roughness decreased to 6 Å and allowed the growth of a Mo/Si multilayer with a smaller interface width.

In a high-resolution TEM analysis of a W/C multilayer with a period d=66 Å, Petford-Long et al. [2] have found that the interface of W-on-C contained a mixture of W and C. Some of the 15-30 Å W crystallites extended into the carbon layer. These crystallites were identified as hexagonal WC using selective area diffraction. The interfaces of type C-on-W were sharper than the W-on-C interface.

High-resolution TEM images of a W/C multilayer were computer processed to provide information about the roughness and the height-height autocorrelation length at the

interfaces [20]. The multilayer was prepared by DC triode sputtering on a Si <111> wafer and had N=31 bilayers with a nominal period d=30 Å. The digitized TEM image of the cross section was scanned and processed by a computer. The r.m.s. values for the W-on-C interface were 1.5 Å and 1.2 Å r.m.s. for C-on-W. The mean autocorrelation length was of the order of 10 Å based on 1210-Å-long line profiles.

Auger electron spectroscopy (AES) was used ([21]) to determine the depth profile of W and C and the contamination with oxygen in W/C multilayers. The sample analyzed had N=20 bilayers with a period d=45 Å and was prepared by triode sputtering. The concentration depth profiling showed the existence of asymmetrical profiles and an oxygen distribution associated with W.

The effect of annealing W/C multilayers in argon at high temperatures was studied in [22] using Raman scattering. In samples where W and W-C were amorphous, which was the case for d_W < 40 Å, the reactions forming crystalline W and WC occurred at T>900° C. The period d showed an expansion of 10-15% of the original value. In multilayers with d_W > 40 Å interfacial reactions took place at temperatures of 600° and below, producing a partially oriented W_2C/C superlattice. The expansion of d was below 5%. Samples annealed in air at 300° C were progressively destroyed by oxidation of both W and C. By using cap layers of Si, the oxidation could be retarded up to 600° C.

From the references reported above, W/C multilayers with large number of bilayers (N>100) have not been previously studied. Prepared by sputtering methods (but other than DC magnetron sputtering used in this work) the W/C multilayers presented asymmetrical interfaces (σ(W-on-Si) > σ(Si-on-W)) with mixed interlayers which, when annealed at high temperature, transformed into a carbide layer.

In the following section we present the XRR measurements of a depth graded W/C multilayer with N=150 bilayers. The deposition conditions were selected based on the optimized settings for W and C single layer coatings described earlier.

4.3.5 Interface width in W/C multilayers

Information about the interface width of W/C multilayers was available indirectly from XRR measurements of depth graded multilayers. In general, they were comparable with the interface widths of W/Si multilayers. For illustration, Figure 4.23 presents the measured reflectivity at 8 keV of a depth graded multilayer with N=150 bilayers, along with the theoretical reflectivity using interface widths of 3.4 Å for W-on-C and 3.0 Å for C-on-W.

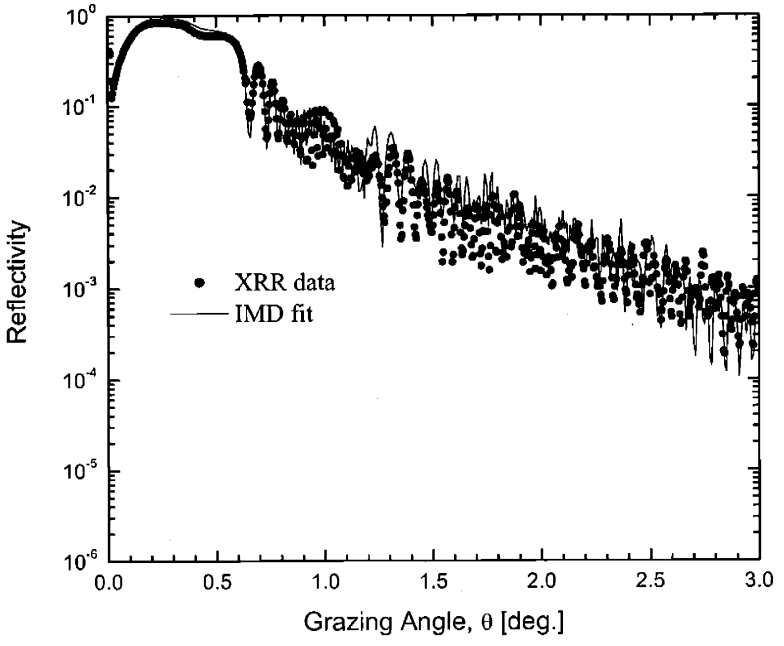

Figure 4.23: X-ray reflectivity at 8 keV for a depth graded multilayer with N=150 bilayers of W/C. The IMD fit results for the interface widths were: σ(W/C)=3.4 Å and σ(C/W)=3.00 Å.

4.4 Pt/C multilayers

The choice of platinum over tungsten as a reflector material offers two advantages:
-the density is higher (21.1 g/cm^3) and increases the optical contrast with the spacer material.

-the K-shell absorption edge is at E_K=78.4 keV and allows an extension of the bandwidth by 9 keV with respect to W.

This material combination was selected for the coating of the InFOCμS x-ray telescope [23].

4.4.1 X-ray optical constants

The real and imaginary parts of the Pt and a-C refraction indices are plotted versus energy in Figures 4.24 and 4.25.

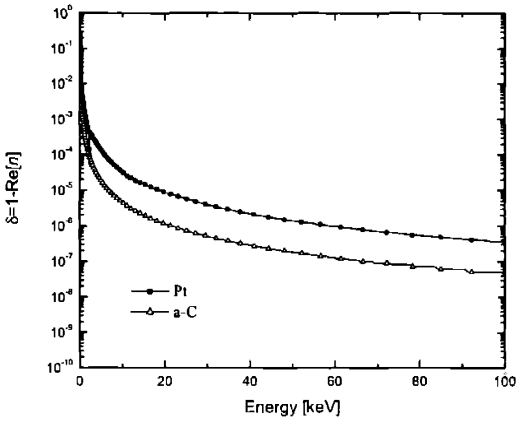

Figure 4.24: The real part of the x-ray refraction indices for Pt and amorphous C. The data were compiled by the Center for X-Ray Optics. The vertical axis shows δ=1-Re[n].

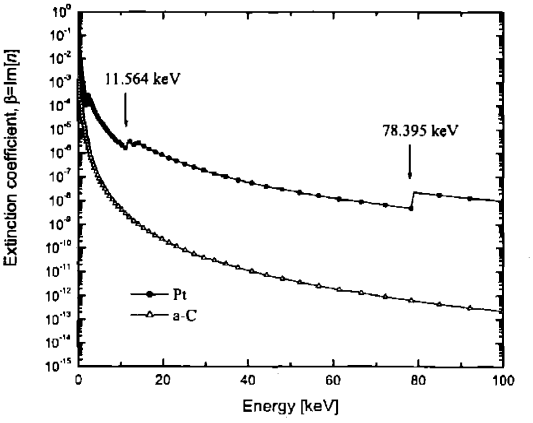

Figure 4.25: The imaginary part of the x-ray refraction indices for Pt and amorphous C. The data were provided by the Center for X-Ray Optics. The arrows indicate the K- and L-shell absorption edges of Pt.

4.4.2 Surface morphology of Pt single layers

Similarly to tungsten, platinum is a metal with a high melting point, T_m=2041 K, and fits into the Thornton classification [5] of materials with low T/T_m ratios during magnetron sputtering. The optimum deposition conditions were investigated with the cathode current kept constant at 25 mA, which resulted in a convenient deposition rate range of 0.5-1 Å/s (not excessively low and not too high to produce particulates and large roughness). The parameters that varied were the argon pressure between 2.0 and 3.5 mTorr and the substrate distance TSD from 4.5 to 9.5 cm.

Table 4.8: Surface microroughness of single layer Pt samples measured by AFM. The measurements were performed with a Nanoscope IIIa D3000 in tapping mode. The microroughness shown was calculated from surface scans of 1μm x 1μm size, with 256 sampling points, and 2 Hz slow scan rate. The cathode current I_{Pt} was kept constant for all samples at 25 mA.

Sample	Ar pressure [mTorr]	Target-substrate distance [cm]	AFM microroughness at 1 μm scan size [Å]
Pt4	2.5	7.0	5.0
Pt5	2.0	7.0	4.2
Pt6	3.0	7.0	3.2
Pt7	3.5	7.0	4.0
Pt8	2.5	9.5	2.9
Pt9	3.0	9.5	3.0
Pt10	2.5	4.5	8.8
Pt11	3.0	4.5	8.1

Since the cathode current was kept constant for all the samples, the deposition rate increased with decreasing the target-substrate distance. The higher arrival rate of adatoms at TSD=4.5 cm did not allow for surface diffusion and promoted fast growth of the surface with high roughness. The samples deposited using this distance and argon pressures of 2.5 and 3.0 mTorr had an average surface roughness of 8.8 and 8.1 Å r.m.s., respectively. The dependence between the surface roughness and the target-substrate distance is shown in Figure 4.26. The decrease of the roughness (at constant cathode current) with the increase of TSD was similar for both values of the argon pressure (2.5 and 3.0 mTorr).

For samples deposited at larger TSD, the lower deposition rates allowed for lateral growth and smoothening of the surface. The surface topography of sample Pt4, shown in Figure 4.27 for a 1μm x 1μm AFM scan, presented fine protuberances with diameters below 30 nm distributed randomly and with peak-to-valley heights below 6 nm.

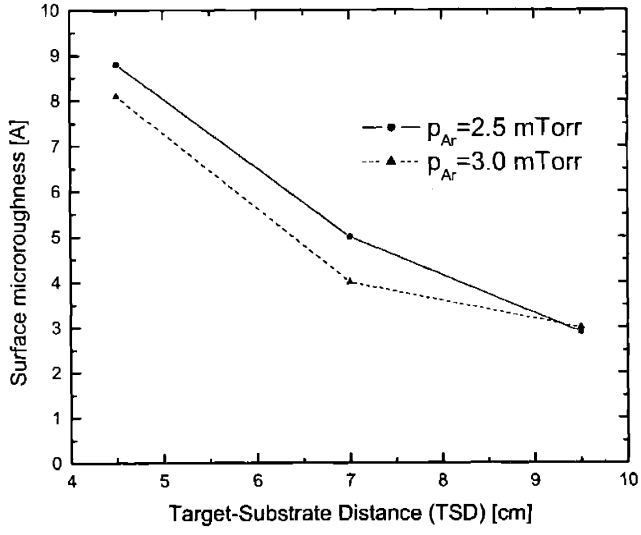

Figure 4.26: Variation of the Pt surface microroughness (measured by AFM) with the target-substrate distance for single layer samples deposited using the same cathode current, I_{Pt}=25 mA. Two different argon backpressures were used: 2.5 and 3.0 mTorr. Independent of the pressure, the deposition rate for a constant sputtering cathode current varies approximately like the inverse square of the target-substrate distance. The high deposition rate at TSD=4.5 cm resulted most probably in the growth of columnar structure with high surface roughness (> 8 Å).

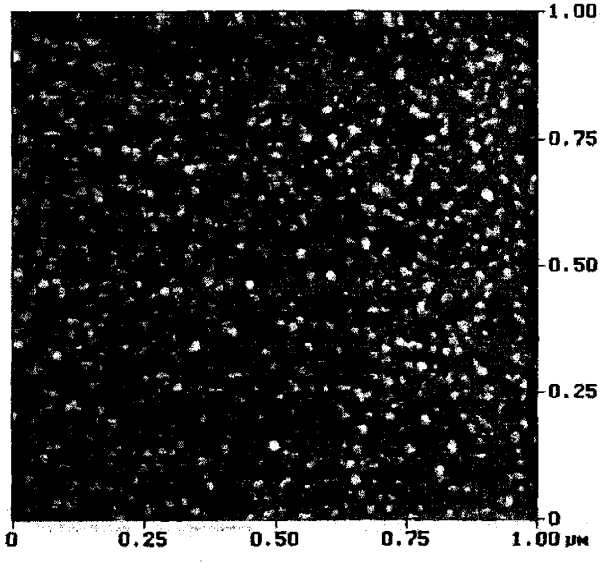

Figure 4.27: AFM scan of the surface of a single layer Pt sample (Pt4, Table 4.8). The scan size was 1x1 μm^2 and 256 lines were sampled with a slow scan frequency of 2 Hz.

4.4.3 Pt single layers and Pt/C multilayers in literature

Single layer films of platinum deposited by magnetron sputtering on <100> silicon have been investigated using XRR and X-ray photoelectron spectroscopy (XPS) [24]. The nominal layer thicknesses varied between 7 and 40 Å. The samples were prepared at 2.0 mTorr argon pressure and 16 cm TSD. The XPS data showed the presence of an amorphous interlayer Pt-Si of 30 Å thickness, independent of the nominal Pt thickness. The density of the 7 Å film was very low (13 g/cm^3) as expected for incomplete coverage of the surface due to island growth. For the 40 Å-thick film the density was 21.5 g/cm^3. The XRR roughness was on the average 3.0 Å and was independent on the thickness.

The nucleation and growth of Pt films deposited on amorphous carbon substrates by ion bean sputtering was studied by Evans et al. [25] using TEM and soft x-ray reflectivity measurements. For TEM observations, the films were deposited on a 200 Å a-C film supported by an electron microscope grid. At room temperature and for a low surface coverage, the film growth begins with the formations of clusters with ~8 Å diameter. As the deposition proceeds, the islands grow mostly two-dimensional and form a network, which then in-fills to form a continuous film at 18 Å. The energy of the Ar ions in the ion gun varied between 1 and 2.5 keV. Since the Ar ions are less energetic in the case of magnetron sputtering, the threshold thickness for layer growth is also different, as will be discussed in 4.4.5.

Lodha et al. [26] have studied the reflectivity of Pt/C multilayers deposited on fused silica, float glass, replicated foils, and oxidized wafers. The roughest substrate was the fused silica, with 8 Å r.m.s. measured by XRR at 1.48 keV (Al-K_α) and 4.0 Å measured by 10 x 10 μm^2 AFM scans. After coating with 20 bilayers of Pt/C with constant period d=50.6 Å and γ=0.57, the XRR measurements indicated 4.5 Å for the interface width, while the surface of the multilayer was rougher (6.6 Å measured by 10 x 10 μm^2 AFM scans). The gold-coated replica foil was a prototype for the InFOCμS telescope and its surface roughness was measured only by using 8.05 keV x-rays (Cu-K_α). The result of the measurement was 5.0 Å r.m.s. After coating with the same type of Pt/C multilayer as

described above, the surface roughness measured by AFM was 4.2 Å while the interface widths had 3.5 Å, as determined from XRR at 8.05 keV.

In a separate paper [27], the group of Lodha et al. have studied the variation of the period *d* with the temperature for isochronal annealings of 5 hours in vacuum. Up to 450° C, the bilayer spacing increased monotonically from 48.7 Å to 54.5 Å, accompanied by a gradual increase of the crystallite sizes and grain texture. At 500° C, the x-ray reflectivity decreased abruptly, indicating total intermixing of the layers. At the same time, the diffraction peaks of Pt showed crystalline growth with a strong texture in the [220] plane.

In an earlier study for the InFOCμS telescope, the Nagoya University group [28] have designed Pt/C multilayers and analyzed their reflectivity in the band 15-45 keV. The test multilayers were deposited by magnetron sputtering on float glass (3 Å surface roughness) and foil quadrants (4-5 Å roughness). The foils had the shape of a quarter of a cone and were made of 125 μm-thick aluminum with 15 μm of epoxy and 0.1 μm gold as separation agent from a conical glass mandrel. In the energy band of interest, the average reflectivity was 30% at 0.3° incidence angle. The interface widths were determined from the fit of the XRR scans: σ=4.1 Å for multilayers on float glass and σ=5.3 Å for those deposited on replica foils.

The InFOCμS telescope optic was built in collaboration with NASA/Goddard Space Flight Center [23]. The foils in the quadrants 1 and 2 were coated by Nagoya University with a block-graded design of the multilayers, while Goddard contributed with the coating of the foils in quadrants 3 and 4 using a power-law depth grading design. The mirror has 255 nested shells and an outer diameter of 40 cm. The target-substrate distance used for all foils was 7.5 cm and a cathode power of 500 Watts. The average interface width of the Pt/C multilayers was 5.0 Å, higher than the 4 Å expected from tests at lower power and used in the design of the depth grading distribution. Further studies will determine if the interface width can be improved by sputtering at low power.

The number of papers reporting Pt/C based multilayers and the choice of this material combination for coating the InFOCμS telescope show a wide interest in the performance of

this multilayer. In consequence, we have analyzed in more detail the Pt/C material system and we have concluded with a Taguchi optimization analysis.

4.4.4 Thickness calibration for Pt/C multilayers

The dependence between the effective thickness (below 20 Å) and the deposition time was investigated by this author by preparing a series of 10 periodic multilayers with N=20 bilayers and the same process parameters (TSD=7 cm, I_{Pt}=25 mA, I_C=90 mA). The deposition time was kept constant for C at t_C=77 seconds per layer, but it was varied for Pt from sample to sample. The C deposition time should result in a layer thickness of d_C=15 Å. If the deposition of C and the subsequent deposition of Pt were two independent processes, then all multilayers must have the same 15 Å thickness for the carbon layers and a platinum layer thickness proportional to the deposition time for this material: $d_{Pt}=r_{Pt}\cdot t_{Pt}$. The results of the XRR measurements are presented in Figure 4.28 and are interpreted as follows:

-for nominal thicknesses of Pt less than 10 Å, the Ar neutrals with an average energy of 100 eV penetrate through the ultrathin Pt layer while this material is being deposited. The Ar neutrals create collisional cascades in the carbon underlayer and can transmit to some of the C atoms enough momentum towards the surface that they travel through the Pt layer and are lost ("resputtered"). Because the atomic collisions are stochastic processes, other C atoms receive less energy than the minimum for resputtering. These C atoms are stopped in the top Pt layer and contribute to the diffuseness of the Pt-on-C interface width. In Figure 4.28, the addition of C to the Pt layer is reflected by the positive offset in the measured Pt thickness versus deposition time for the samples that had less than 10 Å Pt layer thickness. The same samples had lost about 2 Å of carbon by resputtering.

-for d_{Pt} above 10 Å, all C atoms displaced by the collision cascades have a range shorter than the Pt thickness and are totally stopped in the top layer. The growth of Pt continues only at the surface by adding newly arriving Pt atoms.

Even though the theoretical interpretation of the interdependence of Pt and C thicknesses is too complex, the data were directly useful for practical application to coatings. These

experiments were crucial for preparing depth graded multilayers with as-designed layer thicknesses. The empirically determined offsets for thickness calibration curves similar to those shown in Fig. 4.28 allowed the use of the right exposure time to obtain the design thickness.

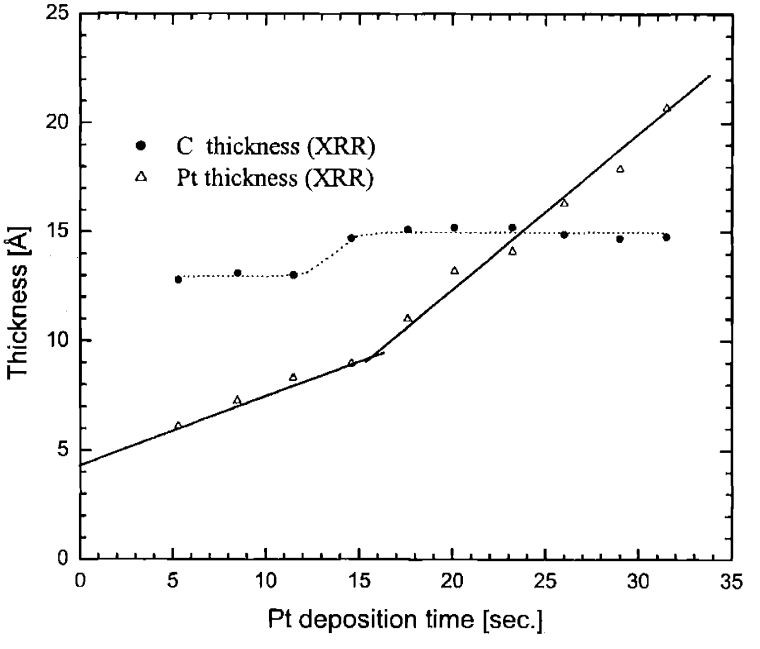

Figure 4.28: Plot of XRR-measured thicknesses of C (dots) and Pt (triangle) for 10 periodic Pt/C multilayers deposited with the same process parameters (p_{Ar}=2.5 mTorr, TSD=7.0 cm, I_{Pt}=25 mA, and I_C=90 mA) and the same deposition time for C (t_C=77 s). The deposition time for the Pt layers was varied from sample to sample and is shown on the horizontal axis. Due to C resputtering and interface mixing, interdependence between the measured thicknesses was observed (see text for discussion).

4.4.5 Minimum period of Pt/C multilayers

When decreasing the period, at some point the thickness of the individual layers becomes comparable with the interface width and the reflectivity drops to values too low to be useful. This "minimum period" limit was encountered for periodic Pt/C multilayers around d=20 Å. It was noticed also that the interface roughness of Pt was increasing when the period and implicitly the Pt layer thickness were decreasing towards the 20 Å limit. This roughening could be attributed to the three-dimensional growth of the first atomic layers of

platinum, as opposed to a layer-by-layer growth mode. Since the van der Waals radius for Pt atoms is 1.75 Å, an ideally uniform deposition of 7 Å Pt thickness would correspond to only two atomic layers. The number of incident Pt adatoms is fluctuating from one point to another on the surface and it is likely that the atoms are actually distributed in three or four atomic layers, with a large number of voids on the surface. The roughness of the surface would be of the same order as the (average) thickness of 7 Å. The effect of comparable roughness and layer thickness on the reflectivity is illustrated by the XRR scan of a sample with N=20 bilayers of Pt/C shown in Figure 4.29. The period was d=21.6 Å with d_C=13.4 Å of carbon and d_{Pt}=8.2 Å of platinum. The interface width determined from the IMD fit was 5.0 Å (for both Pt-on-C and C-on-Pt). The reflectivity of the first Bragg peak was only 6.4% at 8 keV. An ideal multilayer with the same period but with smooth interfaces would have a Bragg peak reflectivity of 27%.

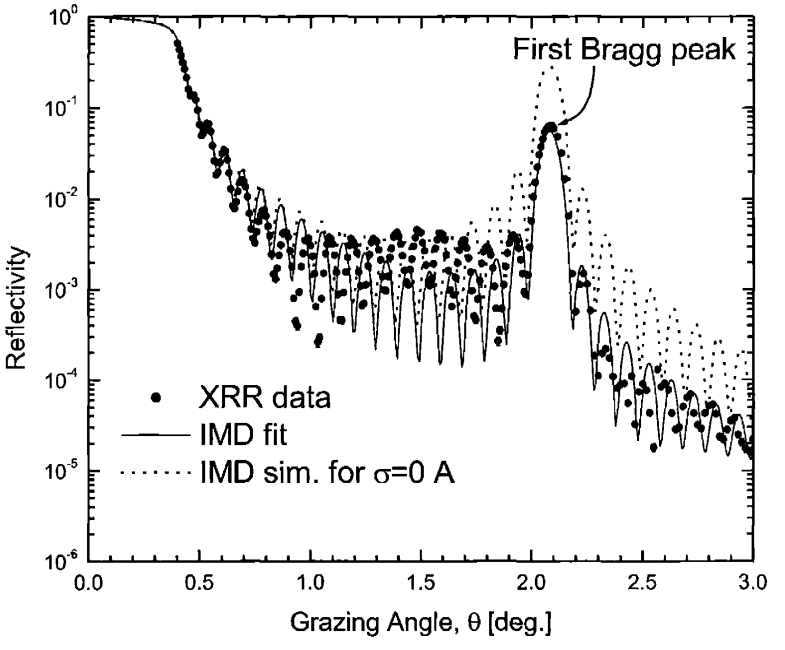

Figure 4.29: Plot of x-ray reflectivity versus grazing angle at E=8 keV for a Pt/C multilayer with N=20 periodic bilayers of 13.4 Å C and 8.2 Å Pt. The average interface width, σ=5.0 Å, was comparable to the Pt layer thickness, and produced a low Bragg peak reflectivity of 6.4%. An ideal multilayer with smooth interfaces (σ=0) would have a reflectivity curve shown by the dotted line with a maximum of 27% at the Bragg peak.

4.4.6 Optimization of the interface width using a Taguchi experiment

In the series of coating runs described above for the minimum Pt/C period, the argon pressure was kept constant at p_{Ar}=2.6 mTorr, as well as the target-substrate distance at TSD=7 cm. The smallest interface width of σ(Pt-on-C)=3.7 Å was achieved for a multilayer with a period of d = 29.6 Å. The 8 keV XRR data for this sample are shown in Figure 4.30 along with the theoretical reflectivity. In order to explore the dependence of σ with other values for the deposition parameters, a Taguchi analysis experiment was undertaken and the results are described next.

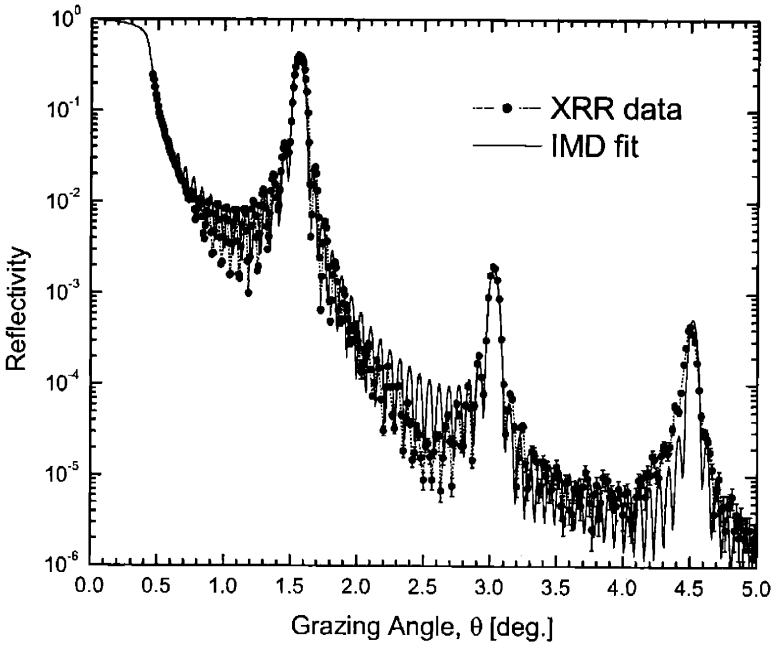

Figure 4.30: X-ray reflectivity at 8 keV for a Pt/C multilayer with N=20 bilayers, d_{Pt}=14.3 Å, and d_C=15.3 Å. The interface widths were determined from the IMD fit (shown by continuous line) and they were σ(Pt/C)=3.7 Å and σ(C/Pt)=2.5 Å.

As in the study for W/Si (Section 4.1.9) the design structure for the Taguchi test coatings was simplified to N=20 bilayers having a period equal to the average of the bilayer thickness distribution in a depth-graded multilayer. The average period taken into

account was d=30 Å with a Pt thickness fraction of γ=0.4. The same four process parameters for W/Si were considered also for this Pt/C study: argon backpressure p_{Ar}, target-substrate distance TSD, Pt cathode current I_{Pt}, and C cathode current I_C. Each parameter varied between two values ("levels") which are listed in Table 4.9. The required number of samples was eight and was determined by the previous choices for the number of parameters and the number of levels per parameter. The combination of levels assigned by the method for each of the eight samples is presented in Table 4.9.

Table 4.9: Description of the process parameters used for the Pt/C Taguchi experiment. Four process parameters (argon backpressure p_{Ar}, target-substrate distance TSD, Pt cathode current I_{Pt}, and C cathode current I_C) were chosen as the most influential for a screening experiment. Each parameter could take one of the two values listed in the table. Eight coatings were performed in the conditions enumerated in each row and then the whole series was repeated to produce another set of eight samples. All 16 samples were periodic Pt/C multilayers with N=20 bilayers of nominal period d=30 Å and γ=0.4. They were characterized by XRR at 8 keV and their interface widths σ(Pt/C) are shown in the last two columns.

Sample #	p_{Ar} [mTorr]	TSD [cm]	I_{Pt} [mA]	I_C [mA]	σ(Pt/C) [Å]	
1	2.6	7.0	25	90	3.7	3.8
2	2.6	7.0	50	180	3.7	3.7
3	2.6	9.5	25	180	4.0	3.9
4	2.6	9.5	50	90	4.1	4.3
5	5.2	7.0	25	180	3.8	3.0
6	5.2	7.0	50	90	3.0	3.2
7	5.2	9.5	25	90	4.0	4.4
8	5.2	9.5	50	180	3.8	4.0

The samples were prepared in separate coating runs and their interface widths measured by XRR at 8 keV. The last two columns in Table 4.9 show the fit value of the interface widths σ(Pt-on-C). Figure 4.31 displays the XRR data along with the model fit for the sample with the lowest σ(Pt-on-C) in this series of Pt/C multilayers.

It is instructive to plot the partial averages of σ for each of the two levels taken by a parameter in order to determine which parameter change has the most influence on the interface width ("main effect" analysis, see Figure 4.32). For example, there were eight samples prepared at 2.6 mTorr and the average of their measured σ(Pt-on-C) is 3.9 Å. The

other eight samples were deposited at 5.2 mTorr and the average σ(Pt-on-C) for these samples was 3.65 Å. Comparing the two partial averages, the change in σ was only 7% when "switching" the pressure from the low value of 2.6 mTorr to the higher value of 5.2 mTorr. Continuing this average analysis for the other deposition parameters, we found that the main effect is due to the change in target-substrate distance (TSD) from 7.0 to 9.5 cm: the average σ increases 17% from 3.5 Å at the lowest TSD to 4.1 Å for the larger distance. The Taguchi analysis helps in pinpointing the main effect but doesn't offer any information to justify it.

The trend of increasing the interface width in multilayers when the distance from the sputtering target to the substrate increases can be explained in terms of the average kinetic energy of the adatoms: for large distances, the atoms are more likely to have collisions with the Ar gas atoms and thus lose energy before reaching the substrate. Less kinetic energy on the surface means less mobility for adatoms, hence higher roughness of the growth surface. When the target-substrate distance is less than the mean free path, most of the sputtered atoms arrive at the substrate with full kinetic energy and are more likely to diffuse on the surface and grow a smooth layer.

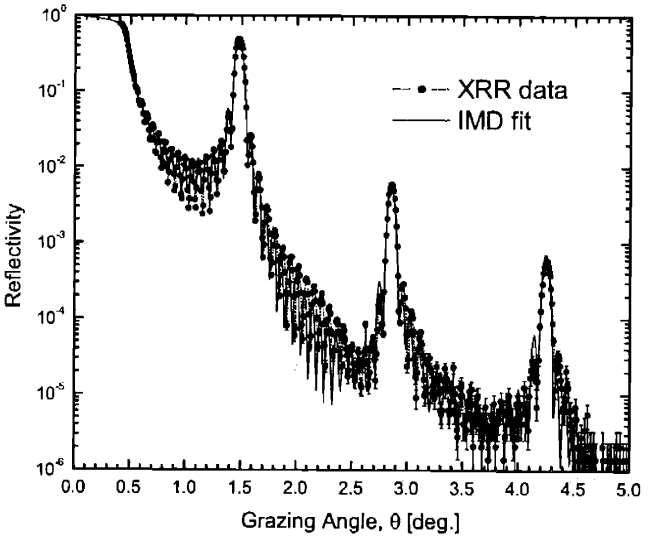

Figure 4.31: X-ray reflectivity at 8 keV for a Pt/C multilayer with N=20 bilayers, d_{Pt}=18 Å, and d_C=13 Å. The interface widths were determined from the IMD fit (shown by continuous line) and they were σ(Pt/C)=3.0 Å and σ(C/Pt)=2.6 Å. These values were the lowest measured for Pt/C multilayers.

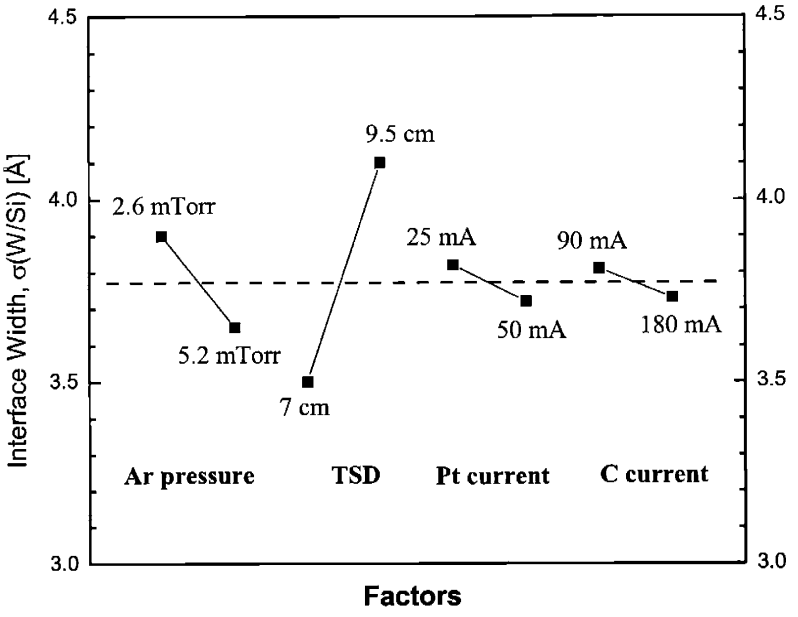

Figure 4.32: Main effect analysis for Pt/C multilayer samples (N=20, d=30 Å, and γ=0.4). The four process parameters and their chosen levels are described in Table 4.9. The samples were characterized by XRR at 8 keV and their interface widths σ(Pt/C) are shown also in Table 4.9 for all 16 samples prepared. The square symbols represent partial averages of σ(Pt/C) for the subset of samples coated using the same level for a process parameter (indicated by label, below). A line segment connects the symbols corresponding to the two levels of the parameter. The average interface width for the whole set of samples is represented by a dashed line for reference. The "main effect" is the change of the target-substrate distance from 7 to 9.5 cm, resulting in an increase of σ(Pt/C) from 3.5 to 4.1 Å.

The analysis of variance was performed with the Qualitek-4 software and the largest contribution of a controlled parameter was 54.7% for the target-substrate distance. The argon pressure parameter had a small percentage of 6.6%, indicating that the interface width of Pt/C is not too sensitive to variation of the pressure in the range 2.6-5.2 mTorr. Both cathode currents had the lowest contribution (0.1%) to the variance of the σ(Pt/C) data. For carbon this is understandable since the its deposition rate did not exceed 0.4 Å/s in any of the coating runs, but for platinum even though the deposition rates varied between 0.7 and 1.8 Å/s, their influence was not felt in the interface widths σ(Pt/C). The variance due to noise and/or other factors was 38.5%, about half the value for W/Si multilayers. It is possible that the reduction was due to better statistics for the Pt/C study, which had a double number of samples.

In the conclusion of the Taguchi experiment for magnetron sputtered Pt/C multilayers, the analysis indicated that the interface widths are minimized (and thus the reflectivity is maximized) for depositions at low substrate-target distance. The other process parameters had a low effect on σ. A 38.5% contribution to the variance of the interface width was attributed to statistical noise plus process parameters that were not controlled but will be included in a future extended experiment.

4.5 Mo/Si multilayers

Molybdenum has been used as a reflector material in EUV and soft x-ray multilayers designed for near-normal incidence. The typical periods of Mo/Si multilayers for EUV lithography are 60-70 Å because the wavelength of the source is 134 Å (92.5 eV energy). Currently, Mo/Si multilayers grown by magnetron sputtering on aspherical polished glass substrates achieve reflectivities as high as 70% at 134 Å and near normal incidence. For the hard x-ray band, the existence of the K-shell absorption edge at E_K=20 keV makes the material unsuitable for energies up to about 40 keV. At this energy the extinction coefficient β has decreased sufficiently and is comparable to that of tungsten. The advantage of Mo for energies higher than 40 keV is the absence of any other absorption edges, unlike W (E_K=69.5 keV) or Pt (E_K=78.4 keV). The density of 10.3 g/cm^3 offers a reasonable optical contrast with silicon.

4.5.1 X-ray optical constants for Mo/Si

The real and imaginary parts of the Mo and a-Si refraction indices are plotted versus energy in Figures 4.33 and 4.34. The x-ray optical contrast between the two materials is moderate due to the small difference between the refraction indices δ (see Figure 4.33). The presence of the K-shell absorption edge for Mo at 20 keV produces a jump in absorption, which recovers at about 40 keV and continues to decrease monotonically with the energy.

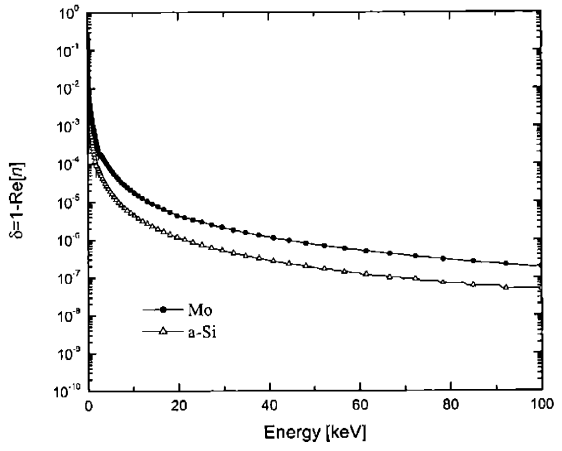

Figure 4.33: The real part of the x-ray refraction indices for Mo and amorphous Si. The data shown were compiled by the Center for X-Ray Optics (CXRO). The vertical scale the quantity δ=1-Re[n].

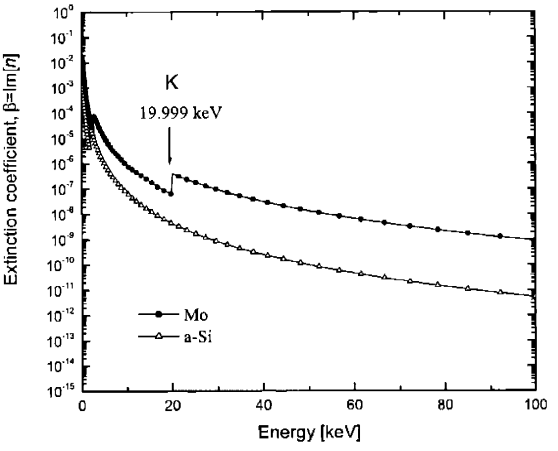

Figure 4.34: The imaginary part of the x-ray refraction indices for Mo and amorphous Si. After the increase in absorption at the K-shell edge, the coefficient β decreases monotonically with the energy.

4.5.2 Surface morphology of Mo single layers

AFM measurements were performed on thick single layers of molybdenum deposited at different argon pressures and target-substrate distances. The cathode current was kept constant at 40 mA. The argon pressure varied between 1.5 and 4.0 mTorr and the target substrate distance (TSD) from 7 to 10.8 cm. The measured deposition rates were in the range 0.25-0.50 Å/s. All samples were scanned at three locations on the surface, using 1 x 1 μm^2 scans. The average of the surface roughness measured for each sample is shown in Table 4.10. The samples were characterized also by x-ray reflectivity (except Mo1 and Mo2). All surface roughnesses measured by AFM were under 2.5 Å and they did not vary with the sputtering conditions. One possible explanation for the AFM results is that a smooth oxide layer was present at the surface of all samples. For the x-ray reflectivity measurements, the optical contrast is dominated by the interface with the metal, while an oxide layer with a low density and a few tens of Å thickness would be "transparent" to x-rays. The x-ray reflectivity provides roughness information only for the pure molybdenum layer and is insensitive to the addition of a smooth oxide layer. Thus the discrepancy between the two characterization methods is explained by the fact that AFM measured the

surface microroughness of the oxide, while the XRR method determined the roughness between the oxide and the metal. For materials that normally are not oxidized in air (platinum and gold), we found the XRR and AFM surface roughness numbers to be in very good agreement.

Table 4.10: Surface microroughness of single layer Mo samples measured by AFM and XRR. The AFM measurements were performed with a Nanoscope IIIa D3000 in tapping mode. The AFM microroughness shown was calculated from surface scans of 1μm x 1μm size, with 256 sampling points, and 2 Hz slow scan rate. The XRR measurements were performed at 8 keV. The samples were prepared with a constant cathode current I_{Mo} = 40 mA and the argon pressure and TSD were varied as shown.

Sample	Ar pressure [mTorr]	Target-substrate distance [cm]	AFM microroughness [Å]	XRR microroughness [Å]
Mo1	1.5	7.0	1.9	NA
Mo2	2.0	7.0	1.8	NA
Mo3	2.5	7.0	NA	5.6
Mo4	3.0	7.0	1.6	5.7
Mo5	2.5	8.25	1.4	9.0
Mo6	3.5	8.25	1.8	5.8
Mo7	2.5	9.5	1.6	6.3
Mo8	1.5	9.5	1.6	7.5
Mo9	2.5	10.8	1.7	5.5
Mo10	4.0	10.8	2.1	4.0

Even taking in account only the XRR data, there is still some discrepancy in the interpretation of the roughness dependence on the target-substrate distance. For example, it was expected that for a constant pressure p_{Ar}=2.5 mTorr the surface roughness would decrease by moving the substrate away from the target (as for Pt, Fig. 4.26). Instead of a monotonical decrease with TSD, the roughness reached a maximum of 9.0 Å at 8.25 cm.

4.5.3 Molybdenum films and Mo/Si multilayers in literature

The interface between molybdenum and silicon is of interest for the semiconductor industry because of the low resistivity and reproducible Shottky barrier heights. Molybdenum films have been used as gates and contacts in VLSI circuits. The work by Slaughter et al. [29] investigated the molecular beam epitaxy growth of Mo on clean (100)

and (111) Si surfaces. The interfaces were characterized by in situ reflection high-energy electron diffraction (RHEED), Auger spectroscopy, and x-ray photoelectron spectroscopy. The formation of an amorphous interfacial silicide was observed at all temperatures studied (50° C, 100° C, and 200° C). The data are consistent with an abrupt transition from Si to $MoSi_x$, where x=2 for the first 4 Å and then decays with an error function form. The interface widths were 10.0 Å at 50°C and 12.1 Å at 200° C. The silicide formation is due to a chemical reaction at the interface and is not a consequence of energetic bombardment because this is absent in MBE depositions.

The influence of the argon pressure in magnetron sputtering was studied and reported in [30]. Low deposition rates (<1 Å/s) were used for all samples prepared at p_{Ar} between 3.4 and 35 mTorr. The density decreased from 95% bulk value at 3.4 mTorr down to 50% at 35 mTorr. Small angle X-ray scattering showed the existence of columnar voids with a typical size of 100 Å in the low density samples. Films of about 300 Å thickness were amorphous for high-pressure depositions and nanocrystalline with (110) texture for low-pressure sputter depositions.

One of the first systematic TEM studies of Mo/Si multilayers was published by Petford-Long et al. [2]. They have prepared multilayered structures containing thin (10 to 120 Å) layers of Mo alternating with Si. The high-resolution TEM images showed amorphous interfaces with asymmetric widths. The following explanation was first formulated for this asymmetry: the Mo atoms deposited on the Si underlayer penetrate to a depth of 8-9 Å, knocking Si atoms out to the top surface of the structure. An amorphous mixture Mo-Si is formed with a width of ~17 Å measured from TEM. After this, the growth continues with a pure Mo layer. The next layer of Si penetrates the preceding Mo layer, but not as deeply because the crystalline Mo is more densely packed than amorphous Si. No attempt was made to compare the observed interface widths with a theoretical model based on ion range and mixing.

The temperature dependence of interfacial reactions at the Mo/Si interface was studied by rapid thermal annealing for T < 550° C [31]. The multilayers were analyzed using TEM, electron diffraction, and low-angle x-ray diffraction. It was observed that the amorphous Mo-Si mixtures at the interfaces start to nucleate at 275° C and grow hexagonal

$MoSi_2$. The bilayer period d decreased with annealing temperatures since $MoSi_2$ is denser than its constituents. The crystallization and growth limit the application of Mo/Si as x-ray mirrors at temperatures below 250° C.

X-ray specular reflectivity was used by Kim et al. [32] for the characterization of RF sputtered Mo/Si multilayers with N=30 bilayers of period d=122 Å and γ=0.58. The measured interface widths were σ(Mo-on-Si)=3 Å and σ(Si-on-Mo)=1 Å.

Multilayers with smaller periods (d=75 Å, N=50) were prepared by a combination of e-beam evaporation and ion etching with the purpose of reducing the interface widths [33]. The ion etching was performed with 300 and 2000 eV Kr^+ ions at 45° incidence on the surface of Si layers. The amount of Si removed was 10 and 30 Å, respectively. The multilayers were characterized by XRR at 8 keV and they were found to have an identical interface width of 3 Å, independent of the amount of Si removed.

Off-specular x-ray reflectivity measurements were used in recent work to probe the lateral structure of the Mo/Si multilayers. Lee et al. [34] performed longitudinal off-specular and transverse scans of a Mo/Si multilayer. The diffuseness σ_d for Si-on-Mo and Mo-on-Si interfaces was found to be 1.6 and 3.0 Å, respectively. The vertical correlation length (between layers) was estimated at 600 Å, while the lateral correlation length (in the layer planes) was 70 Å from the best fit. The analysis demonstrated that off-specular reflectivity is effective in separating the correlated roughness amplitude from the intermixing at the interfaces.

Gullikson and Stearns [35] have observed asymmetrical scattering instead of axial-symmetric scattering around the surface normal for 130 Å EUV radiation. This was in contradiction with the TEM and AFM measurements which established that the roughness is isotropic. The roughness of the top surface was 1.8 Å. The growth model was modified to include the propagation of the substrate topography. It was found that the agreement with the data was excellent after assuming that the average plane of the multilayer structure was actually tilted by 4° with respect to the substrate.

Another series of off-specular x-ray reflectivity measurements was reported by Ulyanenkov et al. [36] for two 30-period Mo/Si multilayers grown by ion beam sputtering on a silicon wafer and a polished ceramic glass (CLEARCERAM©). The periods were 70

and 72 Å, and the thicknesses of the amorphous interlayers were similar for both samples: 12 Å for Mo-on-Si and 8 Å for Si-on-Mo. The advantage of using off-specular reflectivity measurements was that the diffuseness σ_D could be determined by fit separately from the interface roughness σ_R. The values found were σ_D(Mo-on-Si)= 9 and 5 Å, respectively, and σ_D(Si-on-Mo)= 6 and 2 Å. The lateral correlation lengths were very different for the two samples: 700 Å for the first sample vs. 2500 Å for the second sample, due to the difference between the two substrates.

Although most of the deposition processes reported above were not based on DC magnetron sputtering (so they might not be relevant for our deposition method), the common finding is the presence of an amorphous interlayer that can crystallize by annealing. The formation of the interface seems to be mainly due to chemical affinity, as suggested by the low crystalline nucleation temperature (275° C) and the small diffuseness σ_D (1.6/3.0 Å). Another argument for this behavior is the relative modest backscattering yield for Ar^+ on Mo (SRIM simulation), which probably results in a low amount of intermixing at the interface due to energetic neutrals.

4.5.4 Constant period Mo/Si multilayers and interface widths

A series of 10 Mo/Si multilayers with N=20 periods of about 40 Å were deposited in different sputtering conditions on Si <111> wafers. Tables 4.11 and 4.12 present the particular process parameters for the case of a constant pressure study at p_{Ar}=2.5 mTorr and the case of a group of samples deposited at constant TSD=7 cm.

The agreement between the model and the XRR data is rather good, as shown in Figure 4.35 for sample MoSi2 (described in Table 4.11). The interface widths are practically unaffected by the change of sputtering parameters and this behavior indicates that their width is not determined by the bombardment of energetic neutrals.

Table 4.11: The measured structure and interface widths of four Mo/Si multilayers deposited at constant argon pressure p_{Ar}=2.5 mTorr. The samples have N=20 bilayers and were deposited using the same cathode current values: I_{Mo}=40 mA for the Mo cathode and I_{Si}=75 mA for Si. The measurements were performed by XRR at 8 keV.

TSD [cm]	Sample #	Period d [Å]	d_{Mo} [Å]	d_{Si} [Å]	σ(Mo/Si) [Å]	σ(Si/Mo) [Å]
5.7	MoSi9	38.0	20.5	17.5	8.5	3.4
7.0	MoSi1	35.2	19.4	15.8	8.2	3.0
8.2	MoSi7	40.1	18.4	21.7	7.5	4.5
9.5	MoSi3	32.3	17.8	14.5	8.2	3.2

Table 4.12: The measured structure and interface widths of three Mo/Si multilayers deposited at constant target-substrate distance TSD= 7cm. The samples have N=20 bilayers and were deposited using the same cathode current values: I_{Mo}=80 mA for the Mo cathode and I_{Si}=75 mA for Si. The structure and interface widths were determined from fits of XRR scans at 8 keV.

p_{Ar} [mTorr]	Sample #	Period d [Å]	d_{Mo} [Å]	d_{Si} [Å]	σ(Mo/Si) [Å]	σ(Si/Mo) [Å]
1.5	MoSi5	42.5	19.6	23.0	8.0	4.5
2.0	MoSi6	40.0	18.4	21.6	8.0	3.5
2.5	MoSi2	37.0	19.4	15.8	7.0	3.0

The interface widths measured for Mo-on-Si are in the range 7-8 Å. While these seem large for applications to hard x-ray mirrors, one can conjecture from the off-specular measurements reported in literature that the largest contribution to the interface width comes from the diffuseness σ_D and that it cannot be further reduced for the magnetron sputtering process. TEM analysis of a Mo/Si sample (MoSi10, Figure 4.36) allowed us to verify the continuity and repeatability of the layers and their relative thicknesses, but the image quality was insufficient to extract information related to the interfaces.

Another disadvantage of the Mo/Si combination for hard x-ray mirrors is the low x-ray contrast between the two materials that requires to compensate by increasing the number of bilayers up to N=300-500, depending on energy and the reflectivity level sought.

The main usefulness for the hard x-ray band remains the lack of absorption edges for E > 20 keV and thus an extinction coefficient that decreases monotonically with the energy as E^{-4}. Hard x-ray multilayer designs based on Mo/Si will probably continue to be studied, especially if the intensive research done for EUV lithography mirrors will succeed in reducing the interface widths to values comparable to W/Si. A possible improvement is to substitute Mo with an element having a similar energy for the K-shell absorption edge; this direction of research was followed and the results presented in Section 4.6.

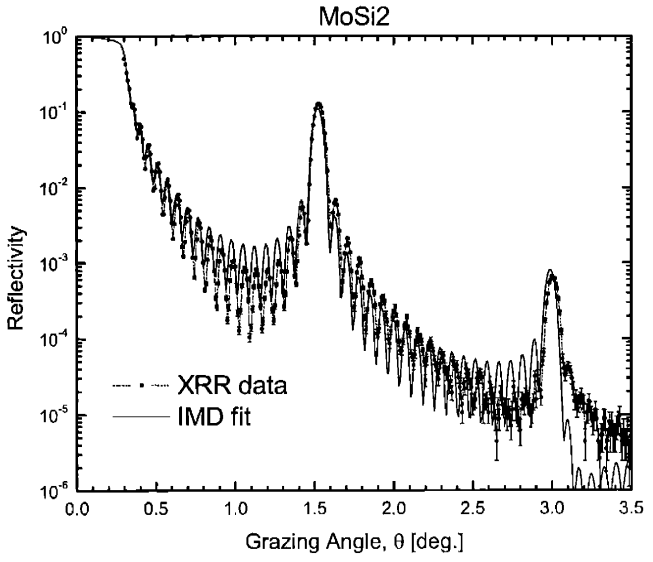

Figure 4.35: The x-ray reflectivity at 8 keV for a Mo/Si multilayer (MoSi2) with N=20 bilayers, d_{Mo}=19.4 Å, and d_{Si}=15.8 Å. The interface widths were determined from the IMD fit (shown by continuous line) and they were σ(Mo/Si)=7.0 Å and σ(Si/Mo)=3.0 Å.

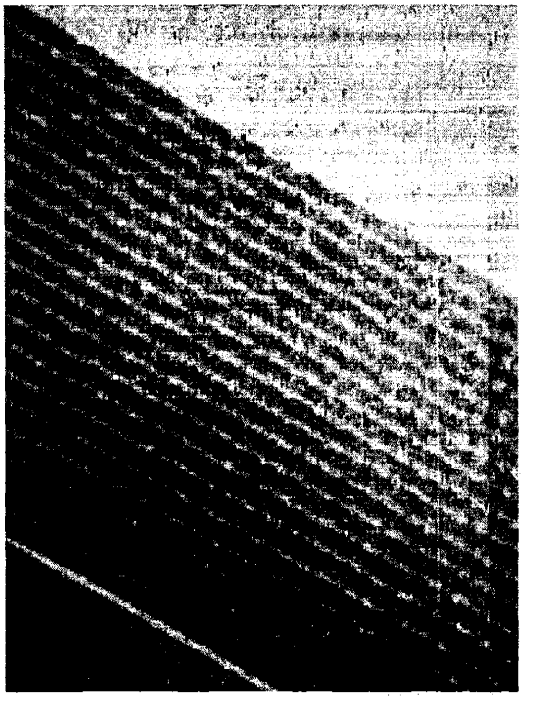

Figure 4.36: TEM image of sample MoSi10 with N=20 bilayers of Mo/Si. The period determined from XRR was d=35.3 Å. The dark bands correspond to the Mo layers, while the Si layers were more transparent to electrons and thus have a lighter appearance.

4.6 Nb/Si multilayers

Niobium is next to molybdenum in the periodic table and has similar chemical and physical properties. After the Mo/Si study we have decided to survey the literature for Nb/Si and prepare a few samples with Nb as a substitute for Mo.

4.6.1 Nb/Si multilayers in literature

The initial Nb/Si analysis by Fullerton et al. [37] found that the structure of the sputtered multilayers changed above 9 mTorr argon pressure: the interface roughness increased and the niobium formed a mosaic structure of crystallites.

Zhang and co-workers [38] found that the Nb/Si multilayers prepared had a structure dependent on the deposition temperature: the room temperature deposited multilayers were amorphous, while those deposited at 200° C started to develop a crystalline Nb_3Si phase, which they explained based on interfacial energy and heat of formation considerations.

Another study [39] used e-beam evaporation for the production of bilayers, trilayers, and multilayers of Nb/Si. The widths of the interfaces were large (20 Å for Si-on-Nb and 40 Å for Nb-on-Si). To study the role of kinetic and thermodynamic factors in the formation of the interfaces, the samples were isochronally annealed in vacuum up to 300° C. The interfacial widths increased with the temperature until the destruction of the multilayers. Close to 300° C the formation of Nb_3Si phase was detected.

The interdiffusion in amorphous Nb/Si multilayers was studied [40] using x-ray reflectivity and TEM in a temperature range from 150°C to 350°C. In the whole temperature scale, the experimental data showed that annealing caused interface shift without any other detectable change of multilayer parameters, such as period and interface roughness. A model based on diffusion of Si into Nb has been proposed, which fitted very well to the Arrhenius relation for diffusion coefficient.

The data from the literature seem to indicate that the interface widths of Nb/Si are typically large and that there must be also some dependence on the preparation mode to explain the discrepancies between the annealing observations in [40] and [39].

4.6.2 Nb/Si interface widths for constant period multilayers

A series of six samples were prepared by magnetron sputtering using different pressures and target-substrate distances but constant currents at the cathodes (I_{Si}=75 mA, I_{Nb}=40 mA). The samples were measured by XRR at 8 keV and their layer thicknesses and interface widths are presented in Table 4.13.

The XRR scans for all samples displayed an abnormally low reflectivity at small angles (see Fig.4.37). This may be explained by the bowing of the wafer substrate due to high intrinsic stress in the multilayer, but the study did not include stress measurements to corroborate this observation. The interface widths from the XRR analysis were also similar to the Mo/Si results. Therefore, this material combination was excluded from further studies.

Table 4.13: The measured structure and interface widths of six Nb/Si multilayers with N=20, deposited with constant currents I_{Si}=75 mA and I_{Nb}=40 mA. The Ar pressure and target-substrate distances were varied as shown in the table. The thicknesses and interface widths were determined from 8 keV XRR measurements

Sample #	TSD [cm]	p_{Ar} [mTorr]	Period d [Å]	d_{Nb} [Å]	d_{Si} [Å]	σ(Nb/Si) [Å]	σ(Si/Nb) [Å]
NbSi1	7.0	2.6	30.4	8.0	22.4	5.5	7.0
NbSi2	7.0	5.2	31.2	8.8	22.4	6.0	7.0
NbSi3	8.2	2.6	49.7	27.3	22.4	6.0	3.2
NbSi4	8.2	5.2	44.8	22.3	22.5	8.0	3.5
NbSi5	5.7	2.6	52.9	36.5	16.4	9.2	4.0
NbSi6	5.7	2.6	60.2	43.8	16.4	9.0	4.0

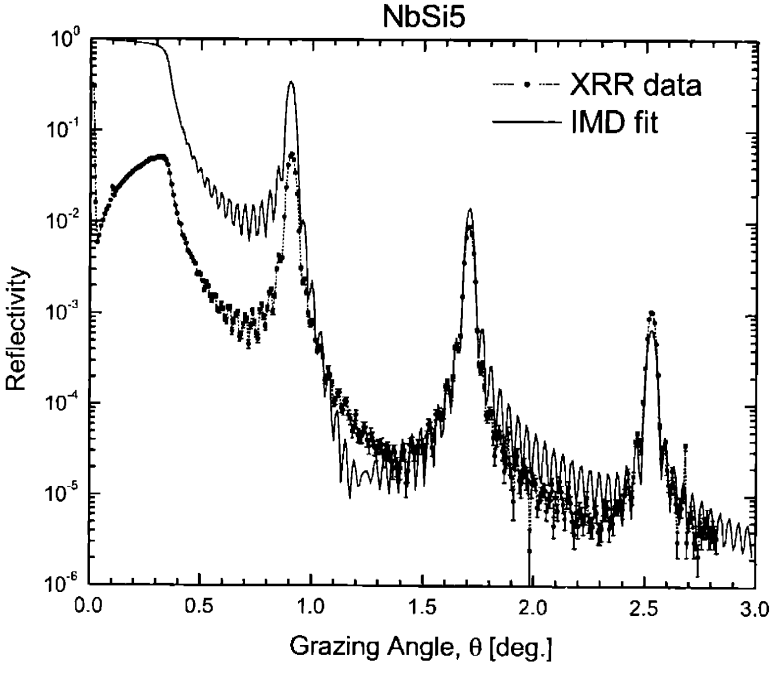

Figure 4.37: The x-ray reflectivity at 8 keV for a Nb/Si multilayer with N=20 bilayers, d_{Nb}=36.5 Å, and d_{Si}=16.4 Å. The interface widths were determined from the IMD fit (shown by continuous line) and they were σ(Nb/Si)=9.0 Å and σ(Si/Nb)=4.0 Å. All the six Nb/Si multilayer samples displayed the same anomaly at low angles: the measured reflectivity was much lower than the model for angles up to the first Bragg peak. The possible cause could be the bowing of the wafer substrates due to high intrinsic stresses in the multilayers.

4.7 Ni/C multilayers

4.7.1 X-ray optical constants for Ni/C

Nickel is another example of an element with average atomic mass that could be potentially useful for hard x-ray multilayers because its K-edge is at 8.333 keV and in consequence above that energy the extinction coefficient β can only decrease monotonically like E^{-4}. The nominal density of 8.9 g/cm^3 offers moderate contrast with spacer materials, so it must be paired with a low δ material, like carbon.

The real and imaginary parts of the Ni and a-C refraction indices are plotted versus energy in Figures 4.38 and 4.39.

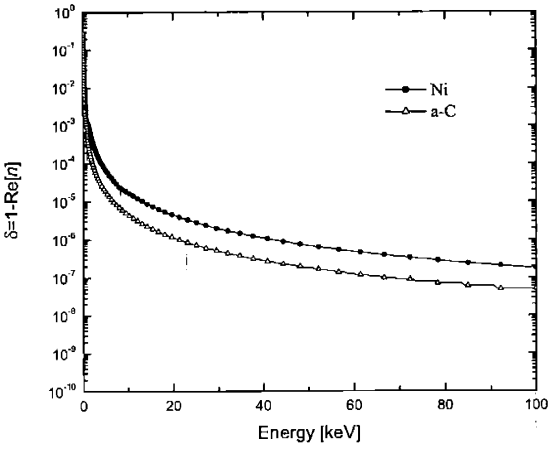

Figure 4.38: The real part of the x-ray refraction indices for Ni and amorphous C. The data were compiled by the Center for X-Ray Optics (CXRO) at Lawrence Berkeley National Laboratory. The vertical scale represents the quantity δ=1-Re[n].

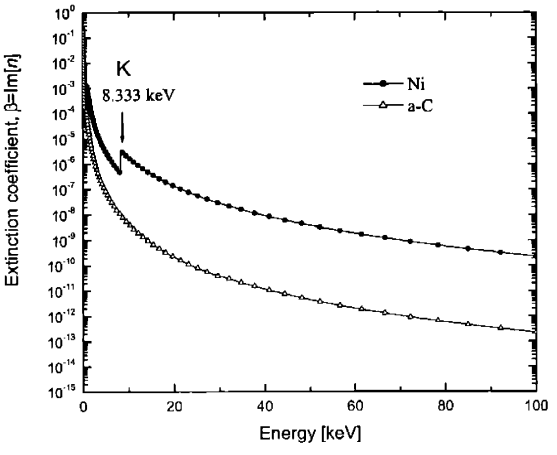

Figure 4.39: The imaginary part of the x-ray refraction indices for Ni and amorphous C.

4.7.2 Ni/C multilayers in literature

RF magnetron sputtering was chosen as the deposition process by Georgescu et al. [41] for Ni/C multilayers used as reflectors at normal incidence for λ=50 Å. The substrates were 20 mm diameter superpolished float glass disks. The power of the RF cathodes was 175 W for

C and 125 W for Ni. The first sample studied was a simple structure SiO_2\C(50 Å)\Ni(25 Å)\C(48 Å) and was measured by specular XRR using 8.05 keV Cu-K_α radiation. The roughnesses reported were 13 Å for Ni-on-C and 20 Å for C-on-Ni. It is possible that this roughness is due to conformity with the float glass substrate, which is reported to have 27 Å roughness. AFM studies of a 15 Å C single layer and a 50 Å Ni layer, each deposited on float glass, showed a surface roughness of 25 Å for C and 7 Å for Ni, on a scan area of 5x5 μm^2. TEM indicated a polycrystalline NiO structure, but it is not specified if the oxidation was present prior to sample preparation. The second sample was a multilayer with N=16 Ni/C bilayers that was prepared for electron microscopy. The TEM showed that the layer smoothness and uniformity increased with the distance from the substrate. In a follow-up paper [42], the AFM study was continued with different stylus sizes and using different scan ranges (0.5 μm, 1 μm, 4 μm, and 9 μm scan sizes). The r.m.s. roughness increased with the decrease of the tip radius (from 2.5 Å to 4.3 Å when the tip radius changed from 1000 Å to 250 Å, in a 1x1 μm^2 scan). This effect was attributed to the tip-surface convolution and there was no attempt to deconvolute the scans to retrieve the intrinsic roughness of the surface. Also, there is no discussion of the differences between the XRR and AFM roughness numbers.

Diode RF sputtered Ni/C multilayers were studied using in situ ellipsometry [43]. The substrates used were commercial Si wafers with (111) orientation or float glass flats, with surface microroughness of 5 Å for Si and 3 Å for glass. A multilayer with N=9 bilayers of Ni/C was grown and in situ kinetic ellipsometry (KE) was used to follow the growth process layer by layer. The model described below showed a good agreement with the in situ KE data: The first 7 Å of carbon deposited on Ni make a transition from a rough to a smoother growth surface. The next 24 Å of C display a mixture 25 to 60 % of pure carbon and "equivalent carbon" with optical properties different than the pure one. When the nickel deposition starts, the first 3 Å are deposited as a mixture Ni-C, followed by quasi-pure Ni of 18.75 Å thickness. The authors conclude that only after ~21 Å of nickel are deposited, the optical properties of subsequently deposited material match the values for pure nickel. The study does not include x-ray or AFM measurements of the roughness.

There is no discussion on the mechanism of diffusion of C in Ni. If the samples were not at high temperature, it is possible that the diffusion is driven by the enthalpy of reaction between Ni and C, and it must be observed also in magnetron sputtering. An IMD simulation for sample NiC154 shows no significant difference in the XRR scan models for pure Ni layer versus NiC_x mixtures, with x as high as 0.50. This is due to the low absorption of C at 8.05 keV, as opposed to the visible wavelengths used for in situ KE.

Another study of Ni growth on carbon was done using ion beam sputtering for deposition and soft x-ray reflectivity and TEM measurements for layer growth characterization [25]. In a previous paper ([44]), the authors have determined that Ni/Si and Ni/C multilayers give the maximum theoretical reflectivity over the so called "water window" wavelength range 23-46 Å. Due to interdiffusion and the formation of $NiSi_2$ compounds at the interfaces, the latter material combination was chosen for multilayers operating in high heat flux environments present in synchrotron or laser plasma experiments. For TEM analysis, a Ni film was deposited on a 200 Å thick a-C film supported by an electron microscope grid. Images with $3x10^5$ magnification and electron diffraction patterns were recorded and the images were digitized for processing. The distribution of the diameters of the islands and the fractional coverage of the surface could be computed from the digital images. An amount of nickel equivalent to 10 Å nominal thickness was ion beam sputtered on the a-C substrate maintained at three different temperatures. At 100° C the deposited Ni shows a structure of chained islands with a diameter of 10 Å. At 200° C the nickel is distributed in the form of isolated islands, some circular, which show regions of coalescence. The maximum of the diameter distribution for the islands is 90 Å. For a substrate temperature of 300° C the film consists of a sparse distribution of islands, mostly circular, with a maximum diameter of 240 Å.

In order to measure the actual thickness of the islands, a set of multilayer samples with N=50 bilayers were produced by ion beam sputtering. The thickness of carbon was constant in all samples, t_C=12.5 Å, and the nickel deposition time was different for each sample. When the thickness determined from XRR is plotted versus the deposition time for Ni, the experimental points lie on a straight line for $t_{Ni} \geq 20$ Å. For $t_{Ni} < 20$Å, the measured points lie above the straight line because the metal is distributed in islands which

are thicker than the equivalent continuous film. The paper also presents an in-depth discussion of the "doublet" (split) Bragg peaks and their association with two regions with different thicknesses of the Ni layers, dependent on the surface coverage fraction. In conclusion, the growth of ion beam sputtered nickel on amorphous carbon substrates followed according to the authors this sequence of events: cluster formation (8.7 Å diameter), island formation, two-dimensional island growth, island agglomeration in branched structure, and eventually the continuity threshold (percolation) was reached at 18.2 Å nominal Ni thickness.

Triode sputtering was used to deposit Ni/C multilayers (N=20 and C cap) that were analyzed by soft x-ray reflectivity scans [45]. The deposition rates were 0.083 Å/s for C and 0.133 Å/s for Ni on float glass substrates (<6 Å r.m.s.). A first multilayer sample was measured at 260 eV and fitted with the following parameters: d_{Ni}=21 Å, d_C=24 Å, σ(Ni/C)=5.5 Å, and σ(C/Ni)=6.5 Å. A second sample was measured first at 260 eV and the best fit results were: d_{Ni}=45 Å, d_C=15.4 Å, and σ(Ni/C)=σ(C/Ni)=7 Å. For measurements at 500 eV, there were discrepancies at the third and fourth Bragg peaks between the experimental data and the calculated reflectivity using fit values from the 260 eV scan. When the model considered 70%Ni-30%C instead of pure Ni, the results of an XRR fit indicated a lower roughness value of 4.4 Å r.m.s. Using the Ni-C mixture model and σ=4.4 Å r.m.s., the reflectivity measured at 260 eV fitted with the same set of thickness parameters. The authors conclude that the ambiguity of the model for XRR requires preliminary knowledge of either the optical constants of the materials or of the layer thicknesses by using other analytical methods. No references were made to the possibility of island growth mode for nickel.

The paper by Borchers et al. [46] provides more structural information by combining TEM with XRR. They used DC magnetron sputtering to deposit Ni/C multilayers (N=100) on Si (001) wafers with a laterally graded period of 30 to 50 Å. When an 8.05 keV pencil beam is used to perform the x-ray reflectivity scan on regions with different periods, the maximum reflectivity drops sharply from 90% to 0% for periods between 43 and 37 Å. High resolution TEM images for regions with d=45, 40, and 35 Å illustrate the change in the structure of nickel layers as their thickness decreases. For a

period of 45 Å, carbon is amorphous but nickel is polycrystalline with grains as large as 30 Å x 60 Å. For 35 Å period, there is no well defined layer structure and the Ni grains have the same size but seem to be organized in fragmented layers. Based on thermodynamic considerations, the authors conclude that the grains are *hcp* Ni and not *hcp* Ni_3C. The size of the grains measured did not fall below 20 Å x 40 Å, suggesting that below 20 Å thickness the Ni islands grown on C cannot form a continuous layer. Since in their samples $d_C=d_{Ni}$, the thin C layer deposited on top of islands of Ni cannot avoid the creation of fragmented layers and the overall result is the observed drop in reflectivity. The authors mention that the continuity limit of ~20 Å of Ni was reduced in preliminary studies to ~15 Å for ion beam deposition and pulsed laser deposition (PLD).

In a paper by Dietsch et al. [47] a double beam PLD source was integrated in a commercial MBE system and was used to deposit Ni/C over 4" diameter wafers. Two Nd:YAG lasers delivered pulses with a variable power density from 0.5 to 2 GW/cm^2 that evaporated material from the target rods and created a dense and highly ionized plasma. The interface roughness, measured by image analysis of TEM pictures, was 0.9 Å for 230 mJ/pulse and increased to 1.5 Å for 570 mJ/pulse. By changing the pulse delay from 0 to 2.5 ms, a destruction of the Ni/C layer stack is observed. Optimum irradiation conditions were met by using zero delay and moderate pulse energies. The thickness variation of a Ni/C multilayer with N=75 bilayers was 1 Å for a period of 36.5 Å.

The interface roughnesses reported in this paper are the lowest not only for the Ni/C system, but also for any x-ray multilayer encountered in the literature.

The amount of information reported in the papers above can be summarized to a few guidelines for our work using DC magnetron sputtering:

- nickel grows in islands when deposited on carbon, unless the lateral diffusion of Ni adatoms on the surface is promoted by a more energetic mode of deposition (PLD or ion beam deposition) or of assisting the deposition (beam assisted sputtering).
- there is no widely accepted agreement on the composition of the Ni-C interlayer

Since our study of different candidates for x-ray multilayers was based on DC magnetron deposition, we have proceeded with the same methodology as for the other material combinations.

4.7.3 Surface morphology of Ni layers

In this section are presented the results of XRR measurements performed on ~300-Å thick Ni layers coated on Si wafers. In one group of samples (Table 4.14) the target-substrate distance was held constant while the argon pressure was varied between 2.0 and 3.5 mTorr. For the second set of samples (Table 4.15), the pressure was constant (2.5 mTorr) and the TSD varied between 7.0 cm and 10.8 cm. In both cases, the variation of the surface roughness with the distance and the pressure was not significant, indicating that, unlike the sputter coating of heavy elements (Pt, W, etc.), the growth and surface morphology of nickel is less controllable by small adjustments of these process parameters.

Table 4.14: The thickness and surface roughness as measured from x-ray reflectivity at 8 keV for a set of single layer Ni samples deposited on silicon wafers. The Ni cathode current was constant I_{Ni} = 50 mA and the target-substrate distance was TSD = 7.0 cm.

Ar pressure [mTorr]	Thickness [Å]	Surface roughness [Å]
2.0	288	8.0
2.5	337	6.6
3.0	321	9.2
3.5	330	8.3

Table 4.15: The thickness and surface roughness as measured from x-ray reflectivity at 8 keV for a second set of single layer Ni samples deposited on silicon wafers. The Ni cathode current was constant I_{Ni} = 50 mA and the argon pressure p_{Ar}= 2.5 mTorr.

TSD [cm]	Thickness [Å]	Surface roughness [Å]
7.0	337	6.6
8.2	259	8.1
9.5	208	9.9
10.8	243	8.8

4.7.4 Minimum period of Ni/C multilayers

As it was reported recently in the literature [46], magnetron sputtered Ni grows on C in the form of 3-dimensional islands. The "percolation threshold" thickness at which nickel forms a contiguous layer is reported to be around 20 Å. For hard x-ray multilayer applications, periods of 30-40 Å are common and reflector thicknesses are under 20 Å. Due to the characteristics of the Ni growth, magnetron sputtered Ni/C multilayers would present prohibitively high C-on-Ni interface roughness or would even be discontinuous. The island growth was confirmed by our XRR measurements for a series of periodic multilayers with different thicknesses for Ni and C. Figure 4.40 presents the XRR scan at 8 keV for a periodic multilayer with 17.3 Å of Ni and 32.7 Å of C. The C-on-Ni interface width was 6.0 Å for this sample, but was significantly higher in samples with thinner nickel.

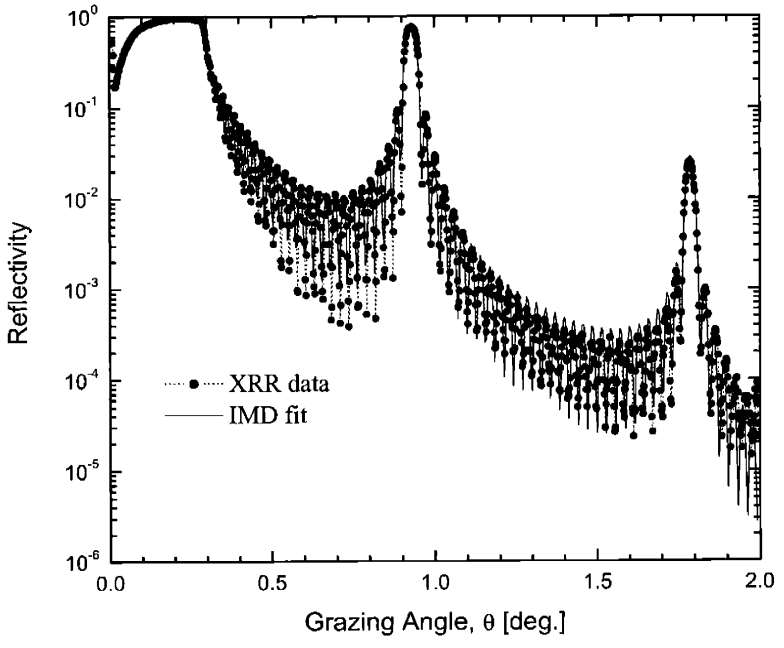

Figure 4.40: X-ray reflectivity at 8 keV for a periodic Ni/C multilayer with N=30, d_{Ni} = 17.3 Å, and d_C =32.7 Å. The interface width for Ni-on-C was 5.0 Å and 6.0 Å for C-on-Ni.

A SRIM simulation shows that the Ni adatoms reach the C layer with 10 eV average kinetic energy and the backscattering yield for Ar on Ni is very low (~10^{-2}), so there is no significant flux of energetic neutrals to assist the adatoms to achieve more mobility on the surface. Deposition processes like pulsed laser deposition [47] or ion beam sputtering can transmit sufficient energy to the Ni adatoms to overcome the cohesion forces and migrate over the surface to create a continuous layer for nominal thicknesses as low as 10 Å. However, these processes have a low deposition rate, cannot be used for coating areas larger than 10 cm with good uniformity and are not repeatable and stable as magnetron sputtering.

We have used a $Ni_{0.92}V_{0.08}$ (8% at.V) alloy sputtering target for a series of 8 periodic multilayers with *d* varying from 30 to 50 Å. The deposition parameters were similar to the Ni/C multilayers, but XRR measurements indicated interface widths comparable to or higher than Ni/C. The lowest interface width measured for the alloy-based multilayers was σ(C-on-$Ni_{0.92}V_{0.08}$) = 8.8 Å. It is possible that the concentration of V in Ni must be increased to more than 8% at. in order to produce a surfactant effect during the island growth stage.

References for Chapter 4

1. M.M. Hasan, R.J. Highmore, and R.E. Somekh, *"The uhv deposition of short-period multilayers for X-ray mirror applications"*, Vacuum **43**, 1992, pp. 55-59.

2. A.K. Petford-Long, M.B. Stearns, C.-H. Chang, S.R. Nutt, D.G. Stearns, N.M. Ceglio, and A.M. Hawryluk, *"High-resolution electron microscopy study of X-ray multilayer structures"*, J. Appl. Phys. **61**, 1987, pp. 1422-1428.

3. D.L. Windt, F.E. Christensen, W.W. Craig, C. Hailey, F.A. Harrison, M. Jimenez-Garate, R. Kalyanaraman, and P.H. Mao, *"Growth, structure and performance of depth-graded W/Si multilayers for hard X-ray optics"*, J. Appl. Phys. **88**, 2000, pp. 460-470.

4. D.L. Windt, F. Christensen, W. Craig, C. Hailey, F. Harrison, M. Jimenez-Garate, R. Kalyanaraman, and P.H. Mao, *"X-ray multilayer coatings for use at energies above 100 keV"*, in X-Ray Optics, Instruments, and Missions III, 2000, *Ed.* J.E. Truemper and B. Aschenbach, Proceedings of SPIE, vol. **4012**, pp.442-447.

5. J.A. Thornton, *"Magnetron sputtering: basic physics and application to cylindrical magnetrons"*, J.Vac.Sci.Technol. **15**, 1978, pp. 171-177.

6. L. Kaufman, *"Coupled phase diagrams and thermochemical data for transition metal binary systems-VI"*, CALPHAD **3**, 1979, pp. 45-76.

7. W.C. Shih and W.M. Stobbs, Ultramicroscopy **32**, 1990, pp. 219-239.

8. T. Salditt, T.H. Metzger, and J. Peisl, *"Characterization of roughness correlations in W/Si multilayers by diffuse X-ray scattering"*, Journal De Physique IV (Colloque C9) **4**, 1994, pp. 171 -174.

9. M. Jergel, Z. Bochnicek, E. Majkova, R. Senderak, and S. Luby, *"Thermally activated interface shift in the tungsten/silicon multilayers"*, Appl. Phys. Lett. **69**, 1996, pp. 919-921.

10. M. Jergel, E. Majkova, V. Holy, S. Luby, and R. Senderak, *"Interface study of W/Si multilayers with increasing number of periods"*, Il Nuovo Cimento **19**, 1997, pp. 439-445.

11. D.L. Windt, *"Multilayer films for figured X-ray optics"*, in Crystal and Multilayer Optics, 1998, *Ed.* A. Macrander, A.K. Freund, T. Ishikawa, and D.M. Mills, Proceedings of SPIE, vol. **3448**, pp.280-290.

12. P.H. Mao, F.A. Harrison, D.L. Windt, and F.E. Christensen, *"Optimization of graded multilayer designs for astronomical X-ray telescopes"*, Applied Optics **38**, 1999, pp. 4766-4775.

13. F.E. Christensen, W.W. Craig, C.J. Hailey, M.A. Jimenez-Garate, D. L.Windt, F.A. Harrison, P.H. Mao, E. Ziegler, V. Honkimaki, et al., *"Hard X-ray characterization of a HEFT single reflection prototype"*, in X-Ray Optics, Instruments, and Missions III, 1999, *Ed.* J.E. Truemper and B. Aschenbach, Proceedings of SPIE, vol. **4012**, pp.626-638.

14. R.K. Roy, *A Primer on the Taguchi Method*, 1990, New York: Van Nostrand Reinhold.

15. A.H. Eltoukhy and J.E. Greene, *"Diffusion enhancement due to low-energy ion bombardment during sputter etching and deposition"*, J.Appl.Phys. **51**, 1980, pp. 4444-4452.

16. E. Mounier and Y.Pauleau, *"Mechanisms of intrinsic stress generation in amorphous carbon thin films prepared by magnetron sputtering"*, Diamond and Related Materials **6**, 1997, pp. 1182-1191.

17. S. Logothetidis, P. Patsalas, M. Gioti, A. Galdikas, and L. Pranevicius, *"Growth kinetics of sputtered amorphous carbon thin films: composition studies and phenomenological model"*, Thin Solid Films **376**, 2000,

18. L.G. Jacobsohn, R. Prioli, F.L.F. Jr., G. Mariotto, M.M. Lacerda, and Y.W. Chung, *"Comparative study of anneal-induced modifications of amorphous carbon films deposited by do magnetron sputtering at different argon plasma pressures"*, Diamond and Related Materials **9**, 2000, pp. 680-684.

19. H.-J. Stock, F. Hamelmann, U. Kleineberg, D. Menke, B. Schmiedeskamp, K. Osterried, K.F. Heidemann, and U. Heinzmann, *"Carbon buffer layers for smoothing superpolished glass surfaces as substrates for molybdenum/silicon multilayer soft-X-ray mirrors"*, Applied Optics **36**, 1997, pp. 1650-1654.

20. M.O. Flaissier, C. Guichet, M. Rasigni, and G. Rasigni, *"Computer processing of electron microscope cross sections of multilayer mirrors"*, Applied Optics **36**, 1997, pp. 6491-6497.

21. D. Roux, A. Rolland, P. Renucci, and J.P. Petrakian, *"AES sputtering depth profile analysis of C/W layered synthetic microstructures"*, Applied Surface Science **28**, 1987, pp. 93-102.

22. J. Gonzalez-Hernandez, B.S. Chao, S.R.Ovishinsky, and D.D.Allred, *"The structure of W/C (0.15 < y < 0.8) multilayers annealed in argon or air"*, Journal of X-Ray Science and Technology **6**, 1996, pp. 1-31.

23. S.M. Owens, F. Berendse, T. Okajima, K. Misaki, Y. Ogasaka, K. Tamura, Y. Tawara, H. Kunieda, K.-W. Chan, et al., *"Characterization and performance of the InFOCuS 20-40 keV x-ray focusing mirror"*, in X-Ray Optics for Astronomy: Telescopes, Multilayers, Spectrometers, and Missions, 2001, *Ed.* P.J. Hoover and P. Gorenstein, Proceedings of SPIE, vol. **4496**, pp.101-112.

24. D.M. Solina, R.W. Cheary, P.D. Swift, S. Dligatcha, G.M. McCrediea, B. Gongb, and P. Lynch, *"Investigation of the interfacial structure of ultra thin platinum films using X-ray reflectivity and X-ray photoelectron spectroscopy"*, Thin Solid Films **372**, 2000, pp. 94-103.

25. B.L. Evans, A.I. Maroof, and S. Xu, *"Nucleation and growth of platinum and nickel films on amorphous carbon substrates"*, J. Appl. Phys. **76**, 1993, pp. 900-907.

26. G.S. Lodha, K. Yamashita, K. Haga, H. Kunieda, N. Nakajo, N. Nakamura, K.Tamura, Y. Tawara, J.M. Bennett, et al., *"Characterization of substrates for use in X-ray multilayer optics"*, Journal of Synchrotron Radiation **5**, 1998, pp. 693-695.

27. G.S. Lodha, S. Pandita, A. Gupta, R.V. Nandedkar, and K. Yamashita, *"Thermally induced structural modification in Pt/C X-ray multilayer mirrors fabricated by electron beam evaporation"*, Applied Physics A **62**, 1996, pp. 29-32.

28. K. Yamashita, K. Akiyama, K. Haga, H. Kunieda, G.S. Lodha, N. Nakajo, N. Nakamura, T. Okajima, K. Tamura, et al., *"Fabrication and characterization of multilayer supermirrors for hard X-ray optics"*, Journal of Synchrotron Radiation **5**, 1998, pp. 711-713.

29. J.M. Slaughter, A. Shapiro, P.A. Kearney, and C.M. Falco, *"Growth of molybdenum on silicon: Structure and interface formation"*, Physical Review B **44**, 1991, pp. 3854-3863.

30. F. Klabunde, M. Löhmann, J. Bläsing, and T. Drüsedau, *"The influence of argon pressure on the structure of sputtered molybdenum: From porous amorphous to a new type of highly textured film"*, J. Appl. Phys. **80**, 1996, pp. 6266-6273.

31. K. Holloway, K.B. Do, and R. Sinclair, *"Interfacial reactions on annealing molybdenum-silicon multilayers"*, J. Appl. Phys. **65**, 1989, pp. 474-480.

32. D.-E. Kim, D.-H. Cha, and S.-W. Lee, *"Structural characterization of a Mo/Si multilayer reflector by means of x-ray diffraction measurements"*, J. Vac. Sci. Technol. A **15**, 1997, pp. 2291-2296.

33. A.E. Yakshin, E. Louis, P.C. Gorts, E.L.G. Maas, and F. Bijkerk, *"Determination of the layered structure in Mo/Si multilayers by grazing incidence X-ray reflectometry"*, Physica B **283**, 2000, pp. 143-148.

34. D.R. Lee, Y.J. Park, D. Kim, Y.H. Jeong, and K.B. Lee, *"Nonspecular X-ray-reflectivity study of partially correlated interface roughness of a Mo/Si multilayer"*, Physical Review B **57**, 1998, pp. 8786-8789.

35. E.M. Gullikson and D.G. Steams, *"Asymmetric extreme ultraviolet scattering from sputter-deposited multilayers"*, Physical Review B **59**, 1999, pp. 13273-13277.

36. A. Ulyanenkov, R. Matsuo, K. Omote, K. Inaba, J. Harada, M. Ishino, M. Nishii, and O. Yoda, *"X-ray scattering study of interfacial roughness correlation in Mo/Si multilayers fabricated by ion beam sputtering"*, Journal of Applied Physics **87**, 2000, pp. 7255-7260.

37. E.E. Fullerton, T. Pearson, C.H. Sowers, S.D. Bader, X.Z. Wu, and S.K. Sinha, *"Interfacial roughness of sputtered multilayers: Nb/Si"*, Physical Review B **48**, 1993, pp. 17432-17443.

38. M. Zhang, W. Yu, W.H. Wang, and W.K. Wang, *"Initial phase formation in Nb/Si multilayers deposited at different temperatures"*, Journal of Applied Physics **80**, 1996, pp. 1422-1427.

39. N. Suresh, D.M. Phase, A. Gupta, and S.M. Chaudhari, *"Electron density fluctuations at interfaces in Nb/Si bilayer, trilayer, and multilayer films: An x-ray reflectivity study"*, Journal of Applied Physics **87**, 2000, pp. 7946-7958.

40. Z. Bochnicek and I. Vavra, *"Interdiffusion in amorphous Nb/Si multilayers"*, Materials Letters **45**, 2000, pp. 120-124.

41. G. Georgescu, V. Nelea, M. Ulmeanu, C. Ghica, and N. Nastase, *"Growth of carbon/nickel multilayer for X-ray-UV optics by RF reactive magnetron sputtering"*, Applied Surface Science **148**, 1999, pp. 142-146.

42. M. Ulmeanu, A. Serghei, I.N. Mihailescu, P. Budau, and M. Enachescu, *"C-Ni amorphous multilayers studied by atomic force microscopy"*, Applied Surface Science **165**, 2000, pp. 109-115.

43. P. Boher, P. Houdy, and C. Schiller, *"Interface analysis of sputtered W-C, Rh-C and Ni-C multilayers for soft X-ray applications"*, Thin Solid Films **175**, 1989, pp. 161-171.

44. S. Xu, B.L. Evans, D.I. Flynn, and C. En, *"The study of island growth of ion beam sputtered metal films by digital image processing"*, Thin Solid Films **238**, 1994, pp. 54-61.

45. J. Friedrich, I. Diel, C. Kunz, S.D. Fonzo, B.R. Müller, and W. Jark, *"Characterization of sputtered nickel / carbon multilayers with soft-X-ray reflectivitty measurements"*, Applied Optics **36**, 1997, pp. 6329-6333.

46. C. Borchers, P. Ricardo, and C. Michaelson, *"Interfacial wetting and percolation threshold in ultrathin Ni/C multilayer films"*, Philosophical Magazine A **80**, 2000, pp. 1669-1679.

47. R. Dietsch, T. Holz, H. Mai, C.-F. Meyer, R. Scholz, and B. Wehner, *"High precision large area PLD of X-ray optical multilayers"*, Applied Surface Science **127-129**, 1998, pp. 451-456.

Chapter 5: X-ray reflectivity measurements at high energies

The x-ray reflectivity of selected samples was measured using intense photon fluxes in the range 30 to 80 keV at the National Synchrotron Light Source (Brookhaven National Laboratory). The reflectivity data were analyzed to determine the structure of the multilayers. It is shown that they were compatible with the power law thickness distribution used in the design and the fit of 8 keV measurements. We present data from three different materials systems that are of practical interest for hard x-ray telescope mirrors: W/Si, Pt/C, and W/C. The average interface roughness determined was in the range 3-4 Å r.m.s. Plots of measured reflectivities versus energy show 20-30% reflectivity for the energy bandpass of interest at grazing incidence angles typical for hard x-ray telescope mirror shells.

5.1 Reflectivity setup for high energy measurements

5.1.1 The X-ray source and beamline layout

The optimal x-ray source for reflectivity measurements must be capable of producing high flux, low divergence, and monochromatic photon beams. We have used the X17B1 beamline of the National Synchrotron Light Source (NSLS) at Brookhaven National Laboratory (BNL) to satisfy these requirements. This beamline is equipped with a superconducting wiggler insertion device with a critical energy of 20 keV and is capable of delivering high flux densities up to 130 keV. At 20 keV, the typical flux density at the insertion device is $5x10^{14}$ photons/sec/mrad/(%bandwidth)/0.25A (the typical electron current in the synchrotron ring). A Bragg-Laue monochromator is located 20 m away from

the source and is tunable from 27 to 130 keV. The monochromator energy resolution was $\delta E = 0.05$ keV, as verified by single crystal diffraction. In Figure 5.1 we present the layout of the X17B1 hutch enclosure showing the collimating slits, the relative sample position, and the detectors. The four-circle goniometer, which provides (θ,φ,χ)-motion for the sample and 2θ motion for the detectors, is located 29 m from the source. The slits S_1-S_2 define an incident beam divergence of 0.4 arcsec and the slits S_3 and S_4 determine the acceptance angle of the detectors.

5.1.2 Sample motion

The samples were mounted on a translation stage attached to a four-axis goniometer. Three degrees of rotational freedom -θ,φ, and χ - were used to give the proper orientation of the sample with respect to the beam (see Fig. 3.8 showing these axes). The fourth -2θ axis rotation- was used to move the detectors. The angular resolution was 0.001°. The translation stage was used to align the surface of the sample parallel to the beam by moving the sample in a direction perpendicular to the beam with an accuracy of 0.5 μ m.

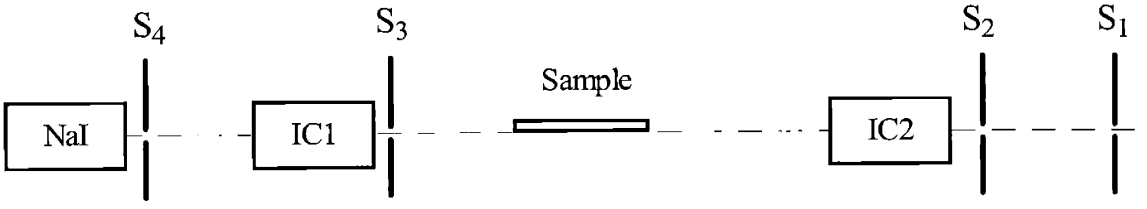

Figure 5.1: Schematics of the high-energy reflectivity setup inside the hutch X17B1 at NSLS-BNL. The slits dimensions were: S_1-0.050 mm V (vertical gap) x 2 mm H (horizontal gap), S_2-0.1 mm V x 2.2 mm H, S_3-0.3 mm V x 2 mm H, and S_4-2 mm V x 4 mm H. The beam is incident from the right and is defined by the first set of slits S_1 and S_2 to a divergence less than 0.4 arcsec. The scattering plane is horizontal and perpendicular to the page. The beam goes first through the ionization chamber IC2 ("monitor") used in current mode to monitor the beam intensity in time. The beam is reflected by the sample and then passes through the acceptance slit S_3 of the ionization chamber IC1. The NaI scintillator detector can be used to measure the beam transmitted through IC1 if the count rate is below 10^5 photons/sec.

5.1.3 Detectors

For structural analysis of the samples it is desirable to measure the reflectivity over an intensity range of 1 to 10^{-8}, which is too large to be covered by a single type of detector. We have chosen to use an ionization chamber for the high count rates and a scintillator detector for low count rates. At count rates higher than 10^5 photons/s, only the ionization chamber IC1 (Fig.5.1) was present in the beam path and the NaI scintillator was moved away to avoid detector saturation and crystal damage. The ionization chamber IC1 had two kapton windows (for the entrance and exit of the beam) and was filled with argon gas at atmospheric pressure. Due to the high flux, the ionization chamber was used in current mode by amplifying the anode signal and performing an analog/digital conversion of the current. A high noise current limited the use of this detector to high flux measurements. At fluxes below 10^5 photons/s, the scintillator detector was brought into the beam path to intercept the flux reflected from the sample. The scintillator was a NaI(Tl) crystal coupled to a photomultiplier tube and a standard preamp. When measuring the specular reflectivity of a sample, the data from the two detectors were background corrected and normalized as described in the next section.

Because the beam intensity decayed in time with a typical half-life of 24 hours and also due to other random intensity fluctuations, the beam was monitored by an ionization chamber IC2 (Fig.5.1) identical with the one used as detector (IC1). The noise current was similar to IC1, but very small compared to the current produced by the high flux of photons incident on this detector.

5.1.4 Sample alignment

In a specular reflectivity measurement, the sample must be accurately positioned to meet the conditions specified in Section 2.10.9:

- the normal of the sample surface is in the plane defined by the incident beam direction and the detector direction;

- the sample rotation axis θ lies on the surface of the sample and is perpendicular to the beam.

An initial measurement with the sample out of the way and using the ionization chamber IC1 determined I_0, the direct beam current, and B_0, the background current in the ionization chamber. The alignment procedure iterated the sequence of operations described in Section 2.10.9, plus an additional scan around the χ axis to ensure that the sample surface is parallel to the beam.

This sequence was applied until the zero-position corrections were less than 0.001° for angular motion and 0.5 μm for translation. The alignment was performed after each change of sample or change in the beam energy.

5.2 Data acquisition and normalization

Prior to each reflectivity measurement, the background was determined for all detectors by shutting off the beam and counting for 120 seconds. The background count rates were denoted by B_0 and $B_{M,0}$ for the detector (IC1) and the monitor (IC2) ionization chambers, respectively, and $B_{NaI,0}$ for the NaI scintillator. They are in essence "dark current" backgrounds and are due to sources unrelated to the beam: cosmic rays, natural radioactivity, thermal noise in the amplifiers, etc. When the beam is turned on, an additional background is present, due to primary beam photons scattered in air or leaking through the slits S_1 and S_2. This background, $B(\theta)$, can have a non-uniform spatial distribution and was determined by performing an offset scan with the beam on and the sample inserted into the beam. During the offset scan, when the sample is rotated by an angle θ, the detector ionization chamber IC1 is positioned by the goniometer at the off-specular angle $2\theta + \delta$, with $\delta = 4^0$ to keep IC1 off the direction of the strong specular reflected beam.

The background rates determined as above are necessary when computing the specular reflectivity of the sample. When using the ionization chamber IC1, the current $I(\theta)$ is

corrected for the background $B(\theta)$, normalized to the monitor current (with monitor background correction) $M(\theta)-B_{M,0}$, and then divided by the normalized, net direct beam current $(I_0-B_0)/(M_0-B_{M,0})$. The formula used is thus:

$$R_{IC}(\theta)=\frac{I(\theta)-B(\theta)}{M(\theta)-B_{M,0}}\frac{M_0-B_{M,0}}{I_0-B_0} \tag{5.1}$$

For the scintillator detector there was no possibility to measure the direct beam count rate because this detector became saturated at high photon fluxes. The reflectivity could be written as a function of the NaI count rate I_{NaI} by lumping all unknown quantities into a normalization factor η:

$$R_{NaI}(\theta)=\eta\left[I_{NaI}(\theta)-B_{NaI}(\theta)\right]/\left[M(\theta)-B_{M,0}\right] \tag{5.2}$$

Because there is an interval of overlap (region B, Fig.5.2) of the data acquired from both detectors, the normalization factor could be found by adjusting it until R_{IC} and R_{NaI} are matched over this region. In region C, Fig.5.2, the reflectivity measurements at large angles with the ionization chamber were limited by its noise floor level at 5×10^{-4} while the NaI detector presented a noise level of 10^{-9}. At very small angles (region A, Fig.5.2), the IC detector could operate at large photon fluxes while the NaI scintillator was removed from the beam to avoid saturation. Thus the two detectors were complementary to each other and by using the normalization procedure it was possible to measure the reflectivity in a dynamic range of $1:10^{-9}$. The experimental reflectivity data consisted of a combination of the data sets from the two detectors:

$$R(\theta)=\begin{cases} R_{IC}(\theta), \text{ if } \theta \text{ in region A} \\ R_{NaI}(\theta), \text{ if } \theta \text{ in region B+C} \end{cases} \tag{5.3}$$

The measurements showed that the backgrounds were essentially dominated by the dark currents for the two ionization chambers. Moreover, the background $B(\theta)$ is angle-independent (and $=B_0$ with 99% confidence) for both IC1 detector and NaI detector, as verified by offset scanning at different energies. This spatial homogeneity of the radiation

background in the hutch allowed reducing the effective measurement time per sample since only B_0 had to be measured rapidly instead of long offset scans to determine $B(\theta)$. Some typical values for the backgrounds at 40 keV with 135 mA ring current were: $B_0 = 195.3$ cps, $B_{M,0} = 185.8$ cps, $B_{NaI} = 5.3$ cps, while the direct beam count rates were $I_0 = 27387$ cps (IC1) and $M_0 = 28747$ cps (IC2). The attenuation of the beam in air over the path length t between monitor and detector accounts for the different rates in the otherwise identical detectors ($I_0 - B_0 = (M_0 - B_{M,0})e^{-\mu(E)t}$). This attenuation factor cancels itself when computing the reflectivity with eq. (5.1) because it must be present both in the numerator and the denominator.

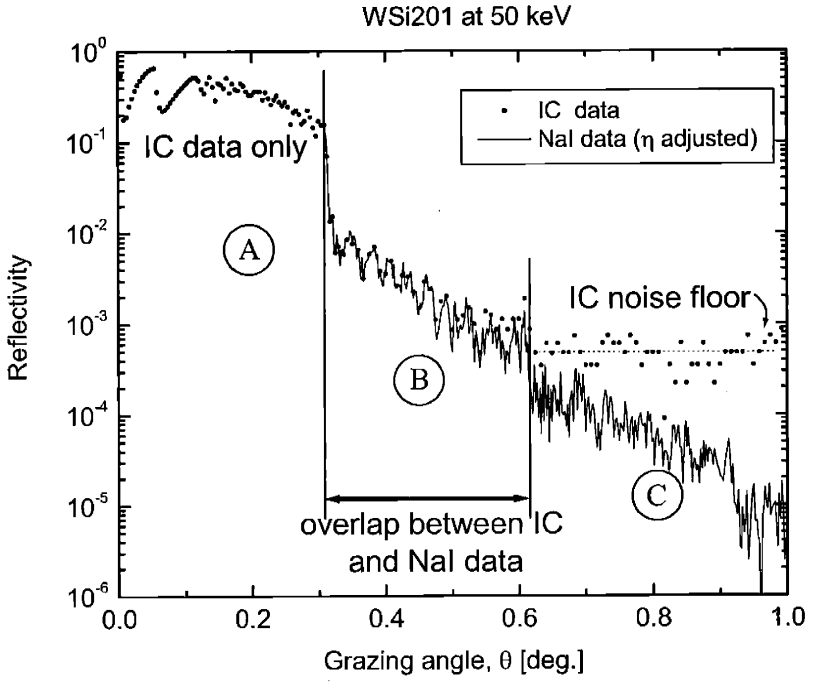

Figure 5.2: Reflectivity data normalization exemplified with measurements taken at 50 keV on sample WSi201. The ionization chamber (IC1) current was background corrected and normalized by the direct beam intensity measured by the same detector (eq. **(5.1)**). The "dark current" noise floor is equivalent to 5×10^{-4} on the reflectivity scale. The NaI scintillator count rate was corrected for background and direct beam fluctuations and multiplied by a normalization parameter. This parameter was varied until the reflectivity data from both detectors were in agreement over the overlap interval shown in figure. In the end, the reflectivity data set consisted of one subset A of the IC data and the subset B and C of the scintillator data after adjustment of the parameter η.

5.3 Measurement of a calibration sample

We have used a periodic multilayer as a calibration sample to check for repeatability of the measurements and to verify the beam energy by an independent method. A multilayer with constant period presents a simple reflectivity curve with well defined Bragg peaks and a structure with fewer parameters to fit. Our calibration sample had $N = 200$ W/Si bilayers deposited by DC magnetron sputtering on a 5 cm diameter superpolished fused silica flat with a surface roughness of 2 Å r.m.s. The nominal period of the multilayer was d=18.9 Å, of which 13.4 Å were W thickness and 5.5 Å Si thickness, separated by interfaces with an error function profile. Figure 5.3 shows the measured reflectivity of the sample at 40 keV and 80 keV versus the IMD best-fit simulations. The error bars were omitted for clarity. The first and second order Bragg peaks are the dominant features in each scan because they correspond to a strong in-phase reflection off each of the N=200 bilayers. The angles θ_m at which the peaks occur are related to the photon wavelength λ by the Bragg relation:

$$2d\sin\theta_m\sqrt{1-\frac{2(d_1\delta_1+d_2\delta_2)}{d\sin^2\theta_m}}=m\lambda \qquad m=1,2,... \tag{5.4}$$

where d_1 and d_2 are the thicknesses of the two types of materials (W and Si) and $d = d_1 + d_2$. The real part of the refractive index of each material is $\mathrm{Re}[n_i] = 1-\delta_i$.

Due to the finite beam width w and sample size l (measured along the beam direction), the footprint of the beam falls off the sample for angles less than

$$\theta_0 = \sin^{-1}\left(\frac{w}{l}\right) \tag{5.5}$$

In our experiment w=0.050 mm and the calibration sample diameter was l=51 mm, so $\theta_0 = 0.056^0$. For higher energies it is increasingly difficult to align the sample because the second step of the alignment procedure is based on a reflection from the first Bragg peak. As the energy increases, the Bragg angle θ_B falls very close to θ_0. Also, the available flux

decreases with the increase in energy and more time is needed to perform the alignment measurements with the same counting statistics.

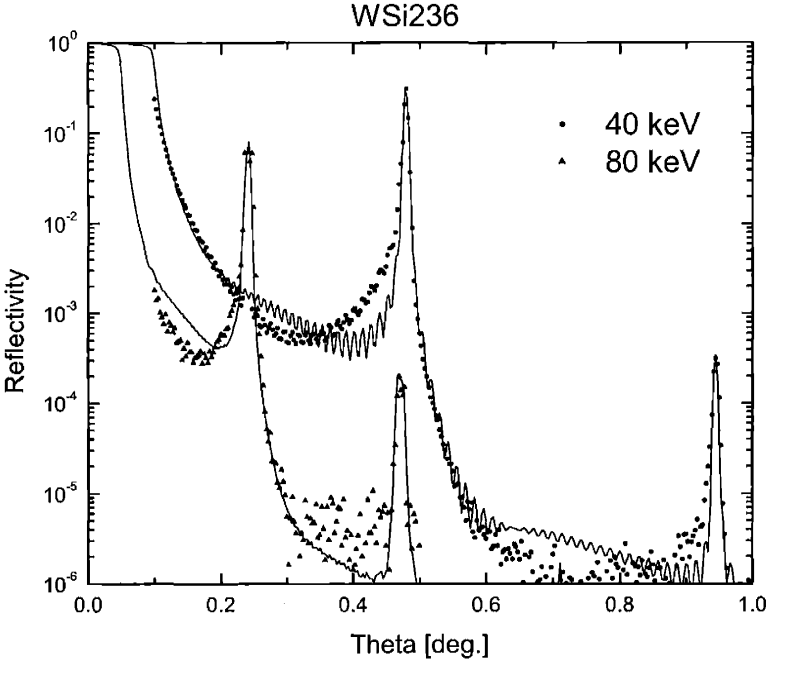

Figure 5.3: Measured reflectivity at 40 and 80 keV and IMD models for calibration sample WSi236 (W/Si multilayer with N=200 bilayers and a period d=18.9 Å). The continuous lines represent the model and the symbols are experimental points. The interface widths σ determined from the fit were 4 Å r.m.s.

5.4 Depth graded multilayers design

The depth graded multilayer samples were deposited in the R&D chamber on superpolished fused silica flats with a surface roughness of 2 Å r.m.s. The deposition rates determined from the periodic multilayer coatings (Chapter 4) were used to set the exposure times of the substrate to the flux of sputtered particles emitted by the cathodes, such that the resulting layer thicknesses are in accordance with the grading formulas.

The dependence between the bilayer thickness d and the bilayer number i was expressed by the power law formula:

$$d(i) = \frac{a}{(b+i)^c} \qquad i = 1,...,N \qquad (5.6)$$

where a, b, and c are parameters and i is the bilayer index starting with 1 at the surface. In our analysis of the high energy reflectivity measurements on graded multilayers we have used the IMD code with the power law formula and varied a, b, c, and γ (ratio of reflector and bilayer thicknesses) during the fit. Also, the widths σ of the two types of interfaces were considered independent variables. For example, in the case of W/Si multilayers we assumed that σ(W-on-Si) is not necessary identical with σ(Si-on-W). This is due to the different growth modes of the two types of interfaces and was confirmed by TEM studies [1]. In our work with constant d multilayers, we have consistently found a better fit of the X-ray reflectivity data when assuming that the two parameters σ were different. Another step up in complexity would be to consider that σ varies throughout the multilayer stack. For example, one can assume that for graded multilayers each σ obeys also a power law of the type:

$$\sigma(i) = \frac{a'}{(b'+i)^{c'}} \qquad i = 1,..,N \qquad (5.7)$$

We have decided to assume in our models that σ does not change with i, so only six parameters ($a, b, c, \gamma, \sigma_1, \sigma_2$) were allowed to vary in the IMD fit of graded multilayers.

To illustrate the features of a reflectivity scan for a graded sample and its "sensitivity" to errors of 5% in layer thicknesses, we show in Figure 5.4 the IMD calculations for a representative graded multilayer sample. The structure is a W/Si multilayer with N=350 bilayers and has the parameter values listed in Table 5.1 for sample WSi201. The solid lines represent the reflectivity at 40 keV for a multilayer with the nominal structure. The dotted line represents the reflectivity calculated for a +5% change in the deposition rate of W that corresponds to a 5% increase of $a\gamma$ in the model. Similarly, the reflectivity after a 5% increase of the Si deposition rate ($a(1-\gamma)$ increased by 5%) is shown at the bottom of Fig. 5.4 with a dashed line. The arrows in Fig. 5.4 point at the Bragg angles corresponding to first- and second-order Bragg reflections by the bilayers with the minimum thickness

d_{min}. The peaks in the region between $\theta = 0$ and the first arrow are due to first order Bragg reflections on bilayers with thicknesses from d_{max} to d_{min}, followed by second order Bragg reflections in the region between the first and second arrow marker, and so on. We notice that the most obvious "response" to changes in W and Si thickness is a shift of the edges at the locations corresponding to d_{min}.

Table 5.1: Structure of graded multilayers analyzed by x-ray reflectivity measurements. The number of bilayers is N; *a*, *b*, and *c* are described by eq. (5.6) and specify the power law distribution of the layer thicknesses. The ratio of the reflector material thickness and bilayer thickness is denoted by γ. σ(H/L) is the r.m.s. width of the interface between the heavy element on top of the light element and σ(L/H) is the r.m.s. width of the second type of interface, light element on top heavy element.

Name	N	*a*	*b*	*c*	γ	σ(H/L)	σ(L/H)
WSi201	350	76.4	-0.89	0.195	0.330	5 Å (W/Si)	3 Å (Si/W)
PtC158	200	105.2	-0.95	0.25	0.535	5 Å (Pt/C)	4 Å (C/Pt)
WC161	150	109.1	-0.94	0.25	0.379	4 Å (W/C)	3.5 Å (C/W)

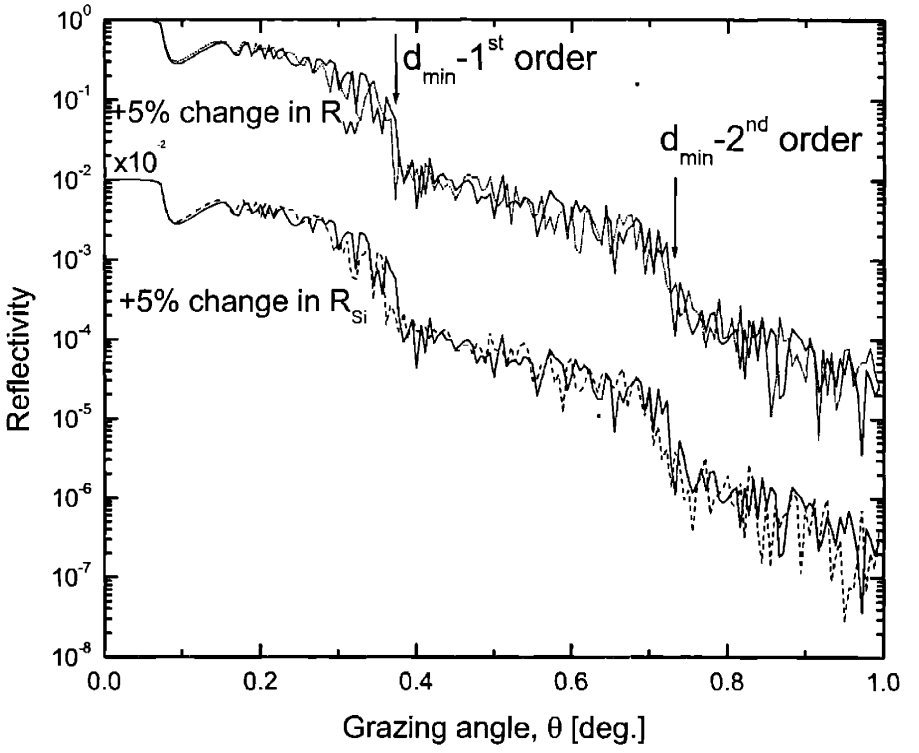

Figure 5.4: Reflectivity plots calculated at 40 keV for a graded W/Si multilayer sample with N=350 bilayers and the structure described in Table 5.1 for sample WSi201. The solid line corresponds to the nominal structure and the arrows show the Bragg angles corresponding to the smallest spacing d_{min} in the first and second order of the Bragg reflection. The top dotted line shows the reflectivity for a hypothetical sample deposited with a deposition rate for W higher by 5% that the nominal value. The bottom dashed line shows the reflectivity after a 5% increase in the deposition rate of Si.

5.5 W/Si graded multilayers

For the deposition of W/Si multilayers, the base pressure before the coating was $2x10^{-7}$ Torr and the Ar pressure 2.6 mTorr during the process. The target-substrate distance was 70 mm and the cathode currents were 75 mA for Si and 30 mA for W, respectively. The total thickness of the multilayer was 1.003 μm and the total deposition time was 8.25 hours.

We present in Figures 5.5 (a through d) the measured reflectivity R versus the grazing incidence angle θ (dots and thin dashed line) and the IMD simulation (solid line) for several of the measured energies between 30 and 60 keV for sample WSi201.

The reflectivity is well above 10% for angles $\theta<\theta_{min}$, where θ_{min} is correlated with the energy E and the minimum d spacing in the multilayer, d_{min}. The angle θ_{min} is indicated by an arrow on each plot. As the energy is increased from 30 keV to 60 keV, the useful range of angles for which the reflectivity is 10% or higher decreases down to 0.27°. This is still more than three times the critical angle θ_c (at E=60 keV) = 0.08° for Ir, one of the best reflector materials. When comparing telescope mirror shells having the same diameter, coated either with a single layer or with a multilayer, the advantage of the latter is the increased minimum grazing angle, because it allows for shorter focal lengths. Also, the effective area is larger and the slope figure errors are less significant.

The IMD fits shown in Figure 5.5 had a good agreement with the experimental data and determined an interface width of 3.5-4 Å r.m.s., which is very satisfactory for our application and encourages further work in coating such multilayers on smooth integral optic substrates.

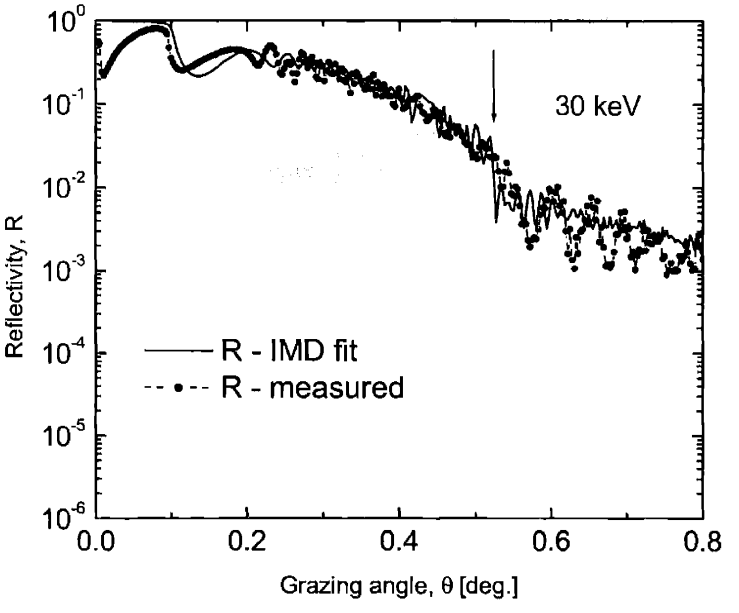

Figure 5.5 (a and b): X-ray reflectivity scans for a W/Si multilayer sample (N=350) measured at 30 keV (above) and 40 keV (below). The solid line is the IMD simulation and the measured data are represented by dots connected by a thin dashed line. The arrows indicate the angle θ_{min} corresponding to the first order Bragg reflection from the minimum period d_{min} (see text).

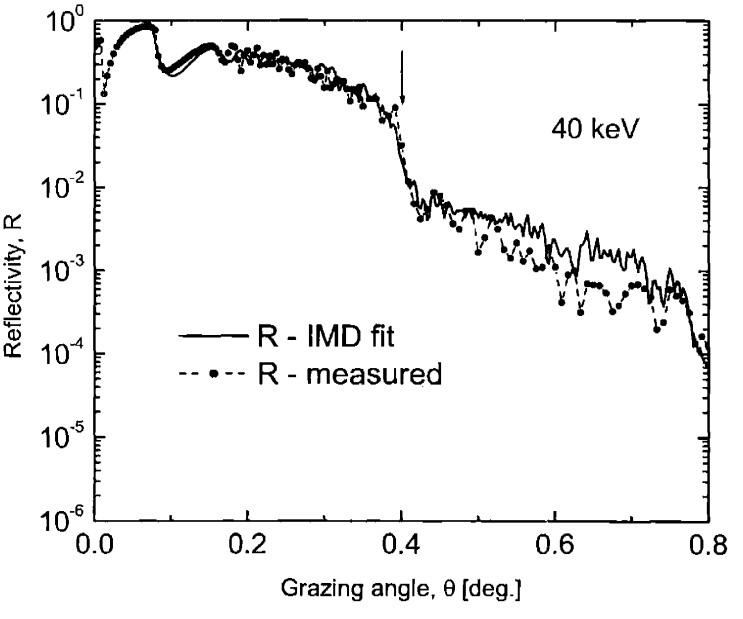

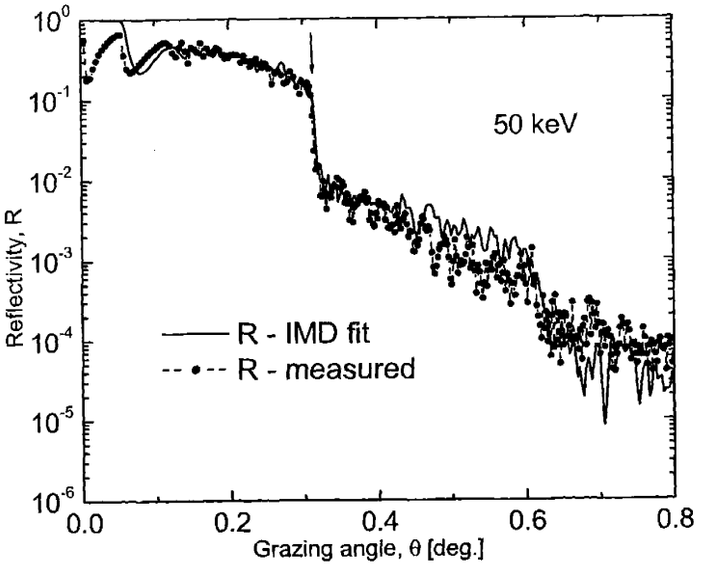

Figure 5.5 (c and d): X-ray reflectivity scans for a W/Si multilayer sample (N=350) measured at 50 keV (above) and 60 keV (below). The solid line is the IMD simulation and the measured data are represented by dots connected by a thin dashed line. The arrows indicate the angle θ_{min} corresponding to the first order Bragg reflection from the minimum period d_{min} (see text).

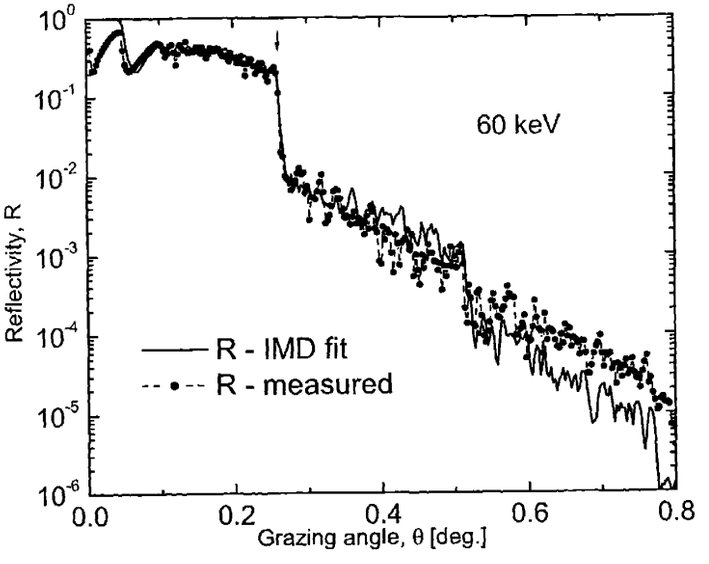

For applications like hard x-ray telescope imaging it is more relevant to plot the reflectivity versus energy for a specific angle θ_i - the grazing angle on the shell - that depends on the focal length and the shell radius (Section 1.4.1). In this way the reflective bandpass of the shell is directly displayed and can be used for determining the effective area of the telescope. For the present work all the samples were flat so there was no predetermined value for θ_i. We have chosen a set of values for θ_i from 3 to 30 arcmin with 3 arcmin stepsize. The energy scans, R vs. E, were performed by tuning the monochromator in steps of 0.5 keV. For each energy, the sample was aligned using the procedure described previously and a reflectivity scan from 3 to 30 arcmin was collected. After normalization, the reflectivity data for a given θ_i extracted and analyzed with the IMD software. We present the measured data and the model in Figs. 5.6a and 5.6b for the sample WSi201. The R vs. E scans shown are for θ_i = 15 and 18 arcmin. These values, in the case of a telescope with focal length f = 10 m, would correspond to the grazing incidence angles for shells of 35 cm and 42 cm diameter, respectively. At θ_i = 15 arcmin we have measured a reflectivity that ranges from 35% to 20% across the energy range 30-63 keV, while at the larger grazing angle θ_i = 18 arcmin the reflectivity was slightly less and cut off at 52 keV, as expected. As indicated in the figures, the IMD model agrees well with the measurement, especially considering the complexity of simulating the reflectivity of a depth graded multilayer.

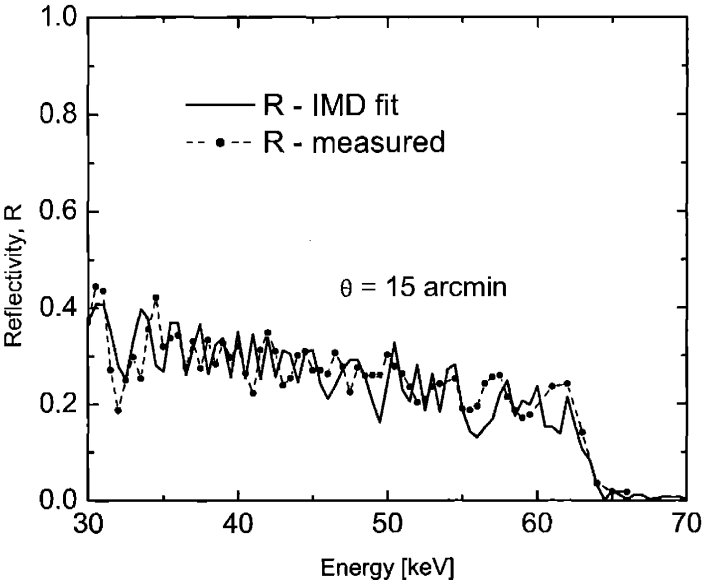

Fig. 5.6 (a and b): Reflectivity versus energy for sample WSi201 (W/Si with N=350 bilayers) in two different grazing angle geometries: a) (above) θ_i = 15 arcmin; b) (below) θ_i = 18 arcmin. The design structure is given in Table 5.1. The IMD analysis showed an interface width of 4 Å r.m.s.

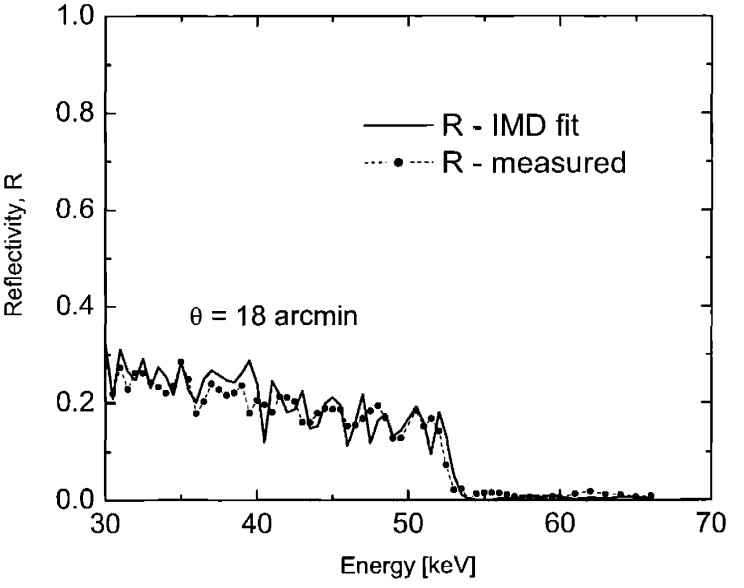

5.6 Pt/C graded multilayers

The Pt/C multilayer system has a higher energy cutoff for absorption (78.4 keV K-edge for Pt vs. 69.5 keV for W) and a stronger contrast between the two components, but a low magnetron sputter deposition rate for C, which makes the combination less efficient from the fabrication point of view. The interface widths in Pt/C are comparable with W/Si in optimal deposition conditions (3-4 Å r.m.s., see [2]). This system was used for the first multilayer-based hard x-ray imaging telescope by the InFOCμS balloon-borne mission [3]. The reflectivity of the replica foils at $\theta = 0.3^{\circ}$ was between 20 and 30 % in the energy range 24-36 keV for which it was designed ([4]).

We have coated Pt/C multilayers on flat superpolished fused silica substrates with 1 and 1.5 in. diameter and analyzed their reflectivity at high energies. One sample (PtC158) with the design parameters listed in Table 5.1 had a total thickness of 0.760 μm and was deposited in 9.25 hours. The reflectivity curve is presented in Figure 5.7 for an incident energy of 40 keV. Also shown is the IMD-calculated reflectivity using an interface width of 5 Å (Pt-on-C) and 4 Å (C-on-Pt) that agreed well with the measurements.

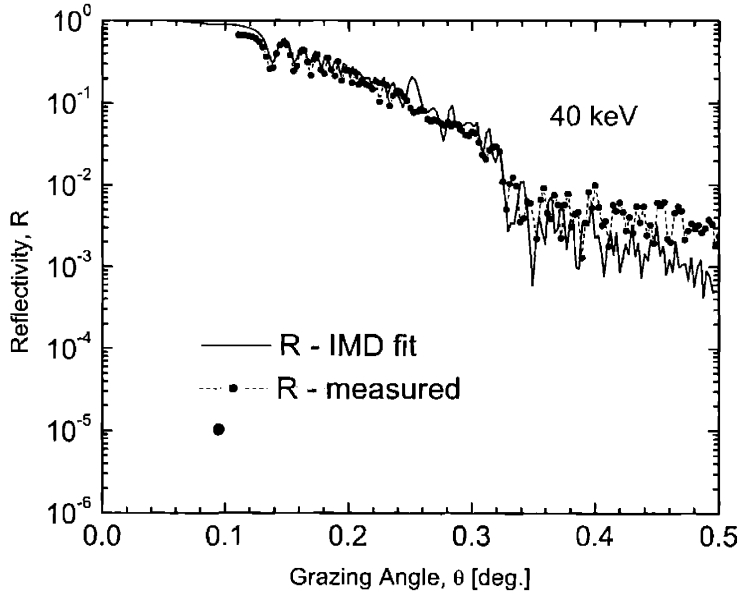

Figure 5.7: Measured (dot and dashed line) and calculated (solid line) reflectivity of a Pt/C multilayer with N=200 bilayers deposited on SPFS flat substrate. The beam energy used was 40 keV.

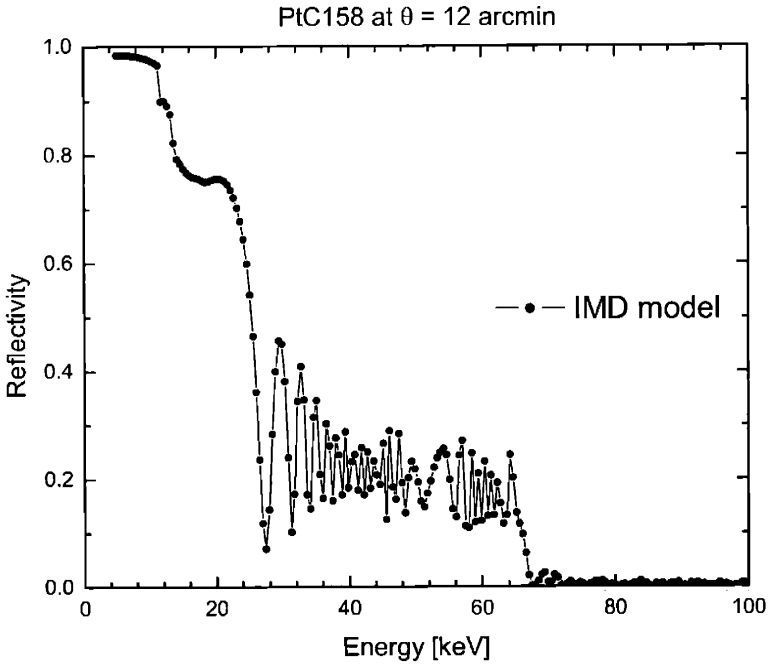

Figure 5.8: Calculated reflectivity at 12 arcmin grazing incidence angle for the Pt/C multilayer described in Table 5.1. The depth grading was designed for a broadband reflection at grazing angles around 0.2°. The reflectivity oscillates because of the finite number of bilayers with a given period *d*, but on the average, the reflectivity in the band 22-62 keV is 22%.

5.7 W/C graded multilayers

W can be paired with C instead of Si for a better optical contrast in an x-ray multilayer, but the trade-off is the longer deposition time required due to the low sputtering yield of carbon. The advantage of the higher contrast between W and C was used to reduce the number of bilayers in order to decrease the total time for the W/C deposition. The W/C sample measured was WC161 and has the structure parameters listed in Table 5.1. The total thickness of the multilayer is 0.670 μm and the total deposition time was 9 hours. In Figure 5.9 we present the measured and calculated reflectivity at 40 keV. The model had an interface width of 4 Å (W-on-C) and 3.5 Å (C-on-W) and suggests that W/C is also a potential material combination for hard x-ray multilayers, provided the disadvantage of a longer coating time is not critical for the application.

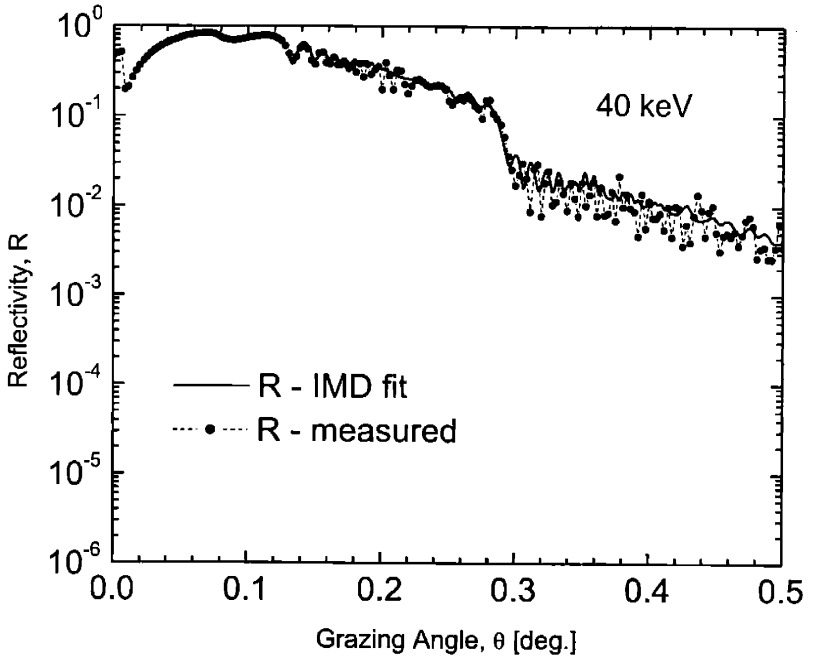

Figure 5.9: Measured (dot and dashed line) and calculated (solid line) reflectivity of a W/C multilayer with N=150 bilayers deposited on SPFS flat substrate. The incident x-ray beam energy was 40 keV.

5.8 Conclusions

The measurements presented in this chapter were the completion of the first stage of a program of multilayer depositions in the R&D chamber aimed at comparing the performance of different material combinations as candidates for high energy x-ray mirrors. Although proposed about a decade ago [5], the depth graded multilayer mirrors have been studied only by a few research groups. One of the reasons is the complexity of the multilayer structure that must be deposited with Ångstrom precision. The layer thicknesses vary in depth from a few hundreds Å down to 10-15 Å and the width of their interface must be kept below 4-5 Å in order to have a good reflectivity. For the current two missions carrying focusing hard x-ray telescopes (InFOCμS [3] and HEFT [6]), the selection of the multilayer materials (Pt/C and W/Si, respectively) was made at an early stage of the project. As part of a feasibility study for the proposed NASA Constellation-X

mission (Section 1.3.5), we accomplished in this work a more comprehensive study of the reflectivity performance of different materials.

The high energy reflectivity measurement of the depth graded multilayers allowed us to determine indirectly their structure and to validate the predicted response from the 8 keV measurements. The interface widths due to roughness and diffuseness were determined from fit and were in the range 3.5 to 5 Å r.m.s., varying according to the material composition of multilayers and the deposition process parameters. The reflectivity versus energy plots for W/Si displayed a good reflectivity for a wide bandpass at grazing angles that are of interest for future work with coated shells. Although the coating designs were "manually" optimized using IMD, the data did show a reflectivity of at least 20% at 60 keV for a grazing angle $\theta = 0.25°$.

The next stage of the Constellation-X feasibility study is to coat prototype substrate shells with depth graded multilayers and perform similar high-energy reflectivity scans, including scatter measurements.

References for Chapter 5

1. D.L. Windt, F.E. Christensen, W.W. Craig, C. Hailey, F.A. Harrison, M. Jimenez-Garate, R. Kalyanaraman, and P.H. Mao, *"Growth, structure and performance of depth-graded W/Si multilayers for hard X-ray optics"*, J. Appl. Phys. **88**, 2000, pp. 460-470.

2. A. Ivan, R.J. Bruni, K.W. Byun, P. Gorenstein, and S.E.Romaine, *"Hard x-ray multilayers: a study of different material systems"*, in Advances in X-Ray Optics, 2000, *Ed.* A.K.Freund, T. Ishikawa, A.M.Khounsary, D.C. Mancini, and A.G. Michette, Proceedings of SPIE, vol. **4145**, pp.72-79.

3. S.M. Owens, F. Berendse, T. Okajima, K. Misaki, Y. Ogasaka, K. Tamura, Y. Tawara, H. Kunieda, K.-W. Chan, et al., *"Characterization and performance of the InFOCuS 20-40 keV x-ray focusing mirror"*, in X-Ray Optics for Astronomy: Telescopes, Multilayers, Spectrometers, and Missions, 2001, *Ed.* P.J. Hoover and P. Gorenstein, Proceedings of SPIE, vol. **4496**, pp.101-112.

4. K. Yamashita, K. Akiyama, K. Haga, H. Kunieda, G.S. Lodha, N. Nakajo, N. Nakamura, T. Okajima, K. Tamura, et al., *"Fabrication and characterization of multilayer supermirrors for hard X-ray optics"*, Journal of Synchrotron Radiation **5**, 1998, pp. 711-713.

5. F.E. Christensen, A. Hornstrup, N.J. Westergaard, H.W. Schnopper, J.L. Wood, and K. Parker, *"A graded d-spacing multilayer telescope for high energy x-ray astronomy"*, in Multilayer and grazing incidence X-Ray/EUV optics, 1991, *Ed.* Proceedings of SPIE, vol. **1546**, pp.160-167.

6. W.W. Craig, F.E. Christensen, T. Decker, C.J. Hailey, F.A. Harrison, R.M. Hill, M. Jimenez-Garate, P. Mao, and S. Schindler, *"Hard x-ray optics for the HEFT baloon borne*

payload: prototype design and status", in EUV, X-Ray, and Gamma-Ray Instrumentation for Astronomy IX, 1998, *Ed.* O.H.Sigmund and M.A.Gummin, Proceedings of SPIE, vol. **3445**, pp.112-120.

Chapter 6: Coatings of segmented and integral optics

The following sections will highlight the work performed at SAO for the deposition of x-ray multilayers on figured substrates. The exact shape ("figure") of the mirrors used for x-ray telescopes is a combination of a confocal paraboloid and a hyperboloid, according to the Wolter type I design described in Section 1.4. Because the departure of the hyperboloid/paraboloid surface from two simple cones (with small taper angles) decreases with increasing focal length, for many telescope designs or for prototype mirrors the reflection surfaces are approximated by conical shells.

In Sections 6.1 to 6.3 are reported results from the earliest coating tests that used thick glass cylinders as substrates. Section 6.4 presents the uniformity and interface roughness study of multilayer coatings on thermally formed thin glass foils. These substrates are being used by the HEFT telescope mission [1]. The results of the multilayer coatings on electroformed shells are presented in Section 6.5.

6.1 First multilayer coating inside an integral cylinder

The first coating of a constant-*d* multilayer on the inner side of a cylindrical structure was performed in the prototype vacuum chamber (described in Section 3.3.2) in July 1998 (MLPC run #46). The substrate was a DURAN glass cylinder with an inner diameter of 28 cm, a thickness of 2 cm, and a height of 20 cm. The multilayer deposited for this test was W/C with N=20 bilayers. The cathodes currents were I_C=850 mA and I_W=300 mA and the argon pressure 2.7 mTorr. The automation of the deposition process was not completed at that time, so the shutters were open and closed manually. Due to the lack of precision in

timing the shutters motion, the material layers were deposited with 1.6 Å standard deviation of thickness (estimated from XRR fit).

The reflectivity of the coating was measured with an 8-keV pencil beam at 4 azimuthal locations on the inner surface of the cylinder: 0°, 90°, 180°, and 270°, with the origin for the azimuth at the location exposed to the opening and closing of the shutters. The XRR scans showed that the principal departure from an ideal multilayer was the thickness nonuniformity (due to manual shutter control). Figure 6.1 shows the inside of the DURAN cylinder after coating and its XRR scan at azimuth 0° is displayed in Figure 6.2. The period d and the W thickness ratio γ were determined from an IMD fit to be d=73.0 Å and γ=0.25. The interface widths were σ(W-on-C)=10.5 Å and σ(C-on-W)=8.5 Å. The discrepancy between the experimental points and the fit model is caused by the thickness variation in the multilayer stack due to manual control of the shutters.

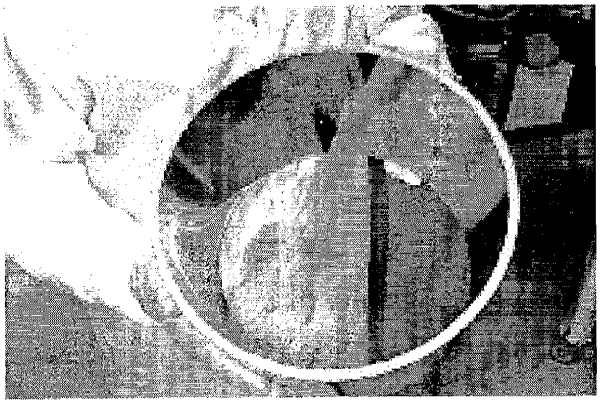

Figure 6.1: The DURAN glass after the first multilayer coating of an integral cylindrical substrate at SAO in July 1998. The cylinder shown has an inner diameter of 28 cm, 20 cm height, and 2 cm thickness. The multilayer coating consisted of 20 bilayers of W/C (d=73 Å, γ=0.25).

6.2 Periodic W/Si multilayer coating inside an integral glass cylinder

After the process automation was completed and the cathode shutters in the prototype coating chamber could be controlled by the computer, the repeatability of the exposure time during sputtering has improved significantly. This resulted in layer thickness variation of 0.1 Å or less and allowed fabrication of multilayers with imperfections dominated by the substrate figure error and roughness and by the interface width (roughness +

diffuseness) introduced by the deposition process itself. The next coating of an integral cylinder (DURAN glass with the same dimensions as in Section 6.1) was a W/Si

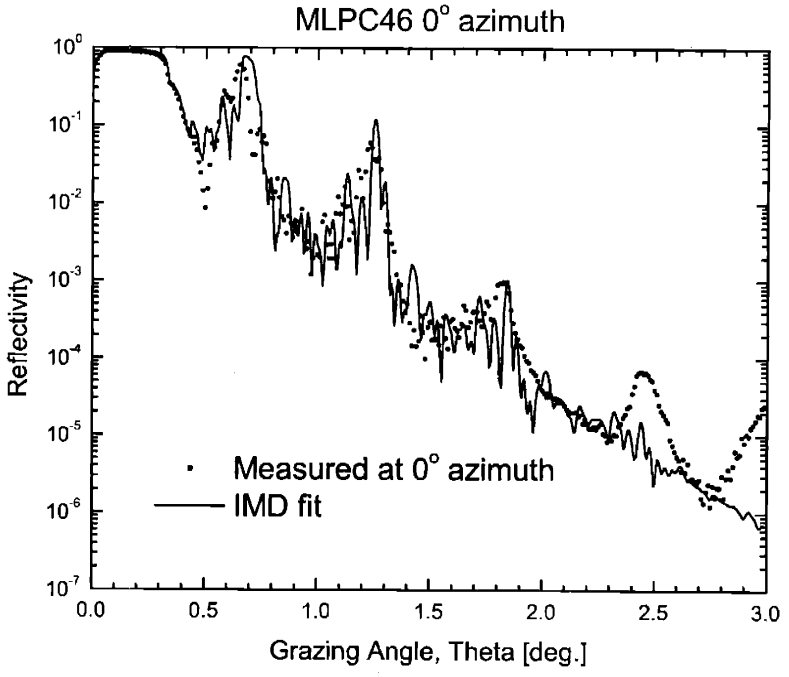

Figure 6.2: X-ray reflectivity measured at 8 keV for the W/C multilayer coated on the inside of the DURAN cylinder shown in Fig. 6.1. The IMD fit is shown by a dashed line, while the measured data are represented by dots. The discrepancy between the data and the model is due to the non-uniformity of the layer thickness in the multilayer stack and to the figure of the optic.

multilayer with N= 30 bilayers, d= 40 Å, and γ= 0.48. The cathodes currents were I_{Si}= 600 mA and I_W= 750 mA and the argon pressure 2.7 mTorr. After the multilayer deposition, the inside of the cylinder was scanned by a pencil beam of 8 keV x-rays at three azimuthal locations. In Figure 6.3 is presented the x-ray reflectivity scan for azimuth 0°, showing an improvement of the match between measured data and IMD simulation over the previous sample (shown in Fig. 6.2). Due to a variation of no more than 0.1 Å for the thicknesses d_W and d_{Si} in the multilayer stack, the Bragg peaks are clearly defined. The interface widths from the IMD model were σ(W-on-Si)=6.0 Å and σ(Si-on-W)=3.8 Å.

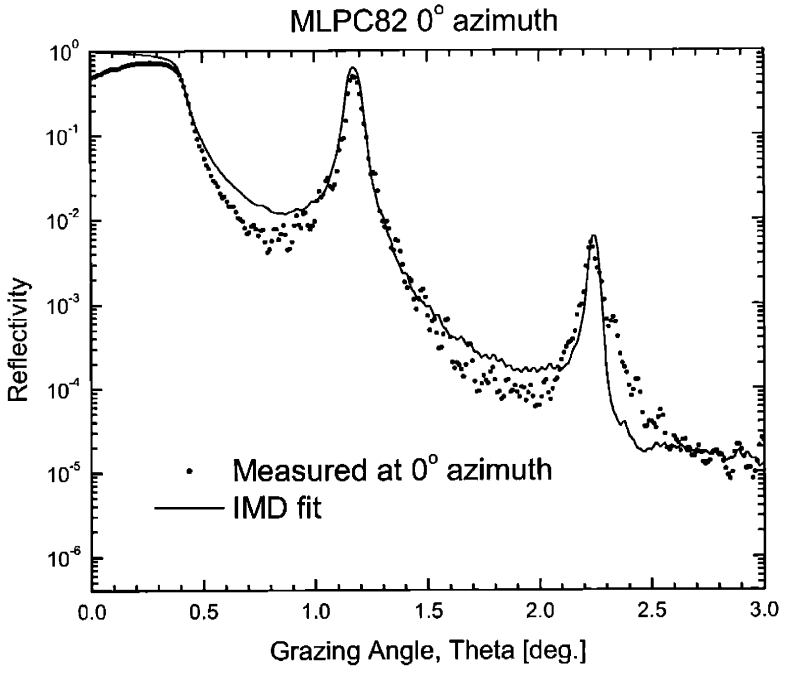

Figure 6.3: X-ray reflectivity measured at 8 keV for the W/Si multilayer coated on the inside of a DURAN glass cylinder. The IMD fit is shown by a dashed line, while the measured data are represented by dots.

6.3 Depth graded W/Si multilayer coating inside an integral glass cylinder

The last of the test coatings on thick DURAN glass cylinders was a depth graded W/Si multilayer with N=92 bilayers divided in eight "blocks". Inside each block, the bilayer thickness was constant and the values for d and γ are shown in Table 6.1. The design was optimized manually with the IMD software to yield a maximum reflectivity bandpass in the range 10-60 keV. After coating, the inside of the cylinder was scanned with an 8 keV pencil beam at four azimuthal locations separated by 90° from each other. The interface widths from the IMD fit were σ(W-on-Si)=6.1 Å and σ(Si-on-W)=3.8 Å.

Table 6.1: Number of bilayers (N_k), W thickness fraction (γ_k), and bilayer period (d_k) for the block graded W/Si multilayer coated inside a DURAN glass cylinder (MLPC run #83).

Block #	No. of bilayers N_k	γ_k	d_k [Å]
1	28	0.48	27.1
2	22	0.44	30.1
3	15	0.49	33.8
4	10	0.47	39.3
5	8	0.47	44.5
6	5	0.45	52.3
7	3	0.45	68.3
8	1	0.45	95.8

6.4 W/Si multilayer coatings of thermally slumped glass foils

The substrates for the previous coatings in the prototype chamber were in principle similar to the Chandra optic (Fig. 1.1 and Section 1.3.4), in as much as they were "thick" glass substrates with a closed cylindrical geometry. The DURAN cylinders were, however, not polished and their surface figure and roughness were not controlled. They had the advantage of being inexpensive, self-supporting and very rigid due to their thickness. The disadvantages of using substrates similar to Chandra are their cost and mass. The high cost is due to the labor-intensive polishing operation that has to be done for each substrate in order to bring the figure and the roughness within specifications. The mass and thickness can limit the effective area of the telescopes because they preclude high nesting density of the mirror shells. One solution for lightweight mirrors proposed the use of thin (< 0.5 mm) foils produced by slumping glass at a temperature above the annealing point (~750° C) into the required shape, which is given by a half-cylinder mandrel made of quartz. The technology has been used in the past to produce flat panel displays and it was adapted for curved foils and improved for the HEFT balloon mission telescope [1]. This fabrication process allows only forming segments of conical shells. In order to form a complete shell

for the telescope, the segments must be co-aligned after coating. A quadrant of a prototype mirror with 5 segments was assembled and its reflectivity measured at selected energies in the range 8 to 170 keV [2]. The half-power diameter of the prototype was 35 arcsec, based on pencil beam, single-reflection scattering measurements.

We have received several slumped glass segments from Columbia University with different curvature radii, slopes, and surface roughness. They were coated and measured at SAO in order to study the azimuthal and axial uniformity of the coating. The azimuthal span of the slump glass foils was 120° and the height was 20 cm. The average curvature radius of the foils was 11 cm. Three segments were mounted in the prototype coating chamber as shown in Figure 6.4 to form a closed surface around the sputtering cathodes. They were coated with a periodic W/Si multilayer with N=60 bilayers having a period d = 29.0 Å and a W thickness fraction γ=0.40. After coating, the reflectivity of each foil was mapped with the 8 keV pencil beam from the MLF reflectometer. The center of the beam was positioned successively for specular reflectivity scans at locations on a grid shown in Figure 6.5. The beam was collimated such that the footprint was always less than 5 cm in the axial direction, for grazing incidence angles larger than 0.20°. In the azimuthal direction, the beam width was 2°. This ensured that the specular reflectivity scan from each point does not overlap with the scan of the adjacent point on the grid. A photograph of a coated glass foil mounted on the MLF x-ray reflectometer is shown in Figure 6.6.

The results of all the reflectivity mapping scans for two samples were presented by S.Romaine *et al.* [3]. For one of them (MLPC142 S1), the average period was d = 29.7 Å with a standard deviation of 0.53 Å, while the other (MLPC142 S3) had an average d = 28.7 Å with a deviation of 0.82 Å. The relative deviation of the period across sample S1 was ±1.8% and ±2.8% across S3, which are within the limits accepted for a Constellation-X type optic (see Mao et al. [4]). A contribution to the thickness variation observed was due to the figure errors of the substrates received from the manufacturer, which were part of a test batch.

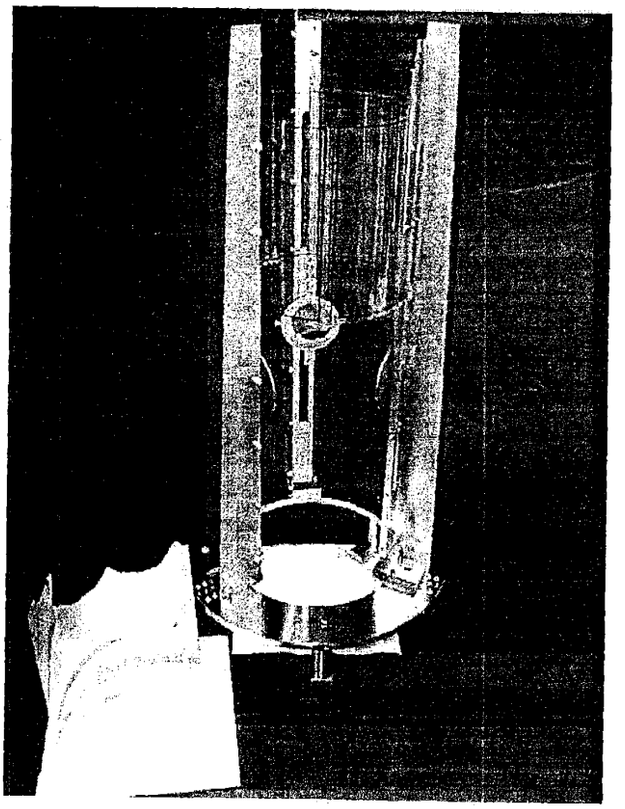

Figure 6.4: Sample holder with three slumped glass foils mounted in a cylindrical geometry, prior to the multilayer deposition in the prototype coating chamber. The foils are 20 cm high and 300 μm thick. A 2" silicon wafer is mounted below each foil as a witness sample. A coated foil is shown on the bottom left side.

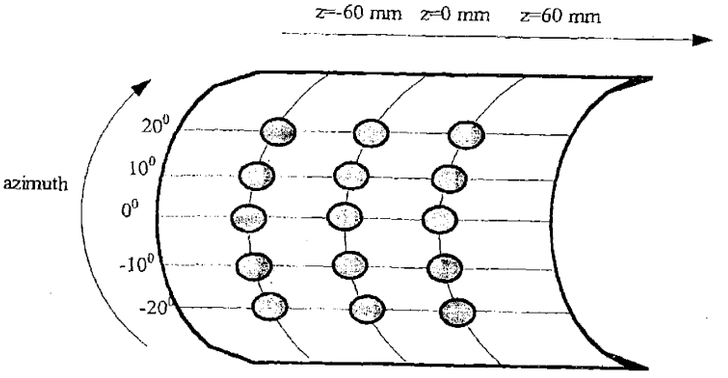

Figure 6.5: Example of a "reflectivity mapping" for slumped glass foils. The center of the pencil beam is positioned succesively on the locations of a 5×3 grid in cylindrical coordinates, shown in the drawing. The step size in the axial direction is 60 mm and 10^0 in the azimuthal directions. The beam cross sectional sizes are such that the footprint is 2^0 (azimuth) by 5 cm (axial) at grazing angles larger than 0.2^0.

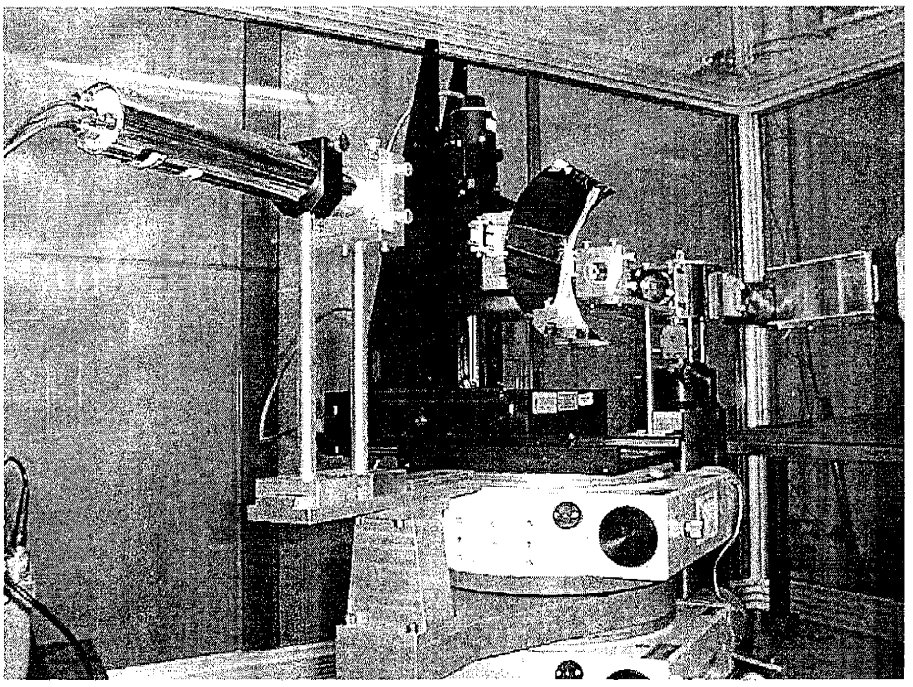

Figure 6.6: The x-ray reflectometer with a multilayer coated glass foil mounted in position for a specular measurement. The pair of collimating slits before the sample define the beam cross section dimensions to 0.2mm x 0.5 mm, such that different areas on the foil can be mapped without overlap.

Figure 6.7 presents plots of reflectivity vs. grazing angle for the center of S1 and S3, showing a difference in the Bragg peak positions corresponding to a relative deviation of the period *d* of 3% between the two samples. In Figure 6.8 are shown similar plots for sample S1 at azimuth 0° and axial coordinates z=-60, 0, and +60 mm. The deviation of *d* was ± 1.4% among these three scans.

The interface widths of the W/Si multilayers deposited on slump glass foils were in the range σ=4.5-5.5 Å, while the witness coatings deposited on 2" Si wafers showed a lower value for σ of about 3.0 Å. The difference indicated that the interface widths could be reduced, and implicitly, the reflectivity of the mirror increased, if the smoothness of the foils could be further improved.

Depth graded W/Si multilayers have also been deposited on slumped glass foils. A power law design was used with N=200, a_{Si}=43.4, a_W=50.0, b_{Si}=b_W=-0.998, c=0.3. According to this formula, the period varied in depth from 218.2 Å at the top of the stack down to 24.9 Å. The coating run was interrupted at bilayer N=165 due to an irrecoverable plasma loss at

the W cathode and was resumed after the chamber was open and the cathodes cleaned. The x-ray reflectivity scan at 8 keV is shown in Figure 6.9 and was similar to the scan of the witness samples (Si wafers). The discrepancy between the data and the IMD model is due to the frequent plasma losses at the Si cathode during the first part of the run. The relative good agreement at small angles ($\theta < 0.8^{\circ}$) corresponds to conformity to the design for the topmost, thicker layers, which were deposited in the second part of the coating run without plasma loss.

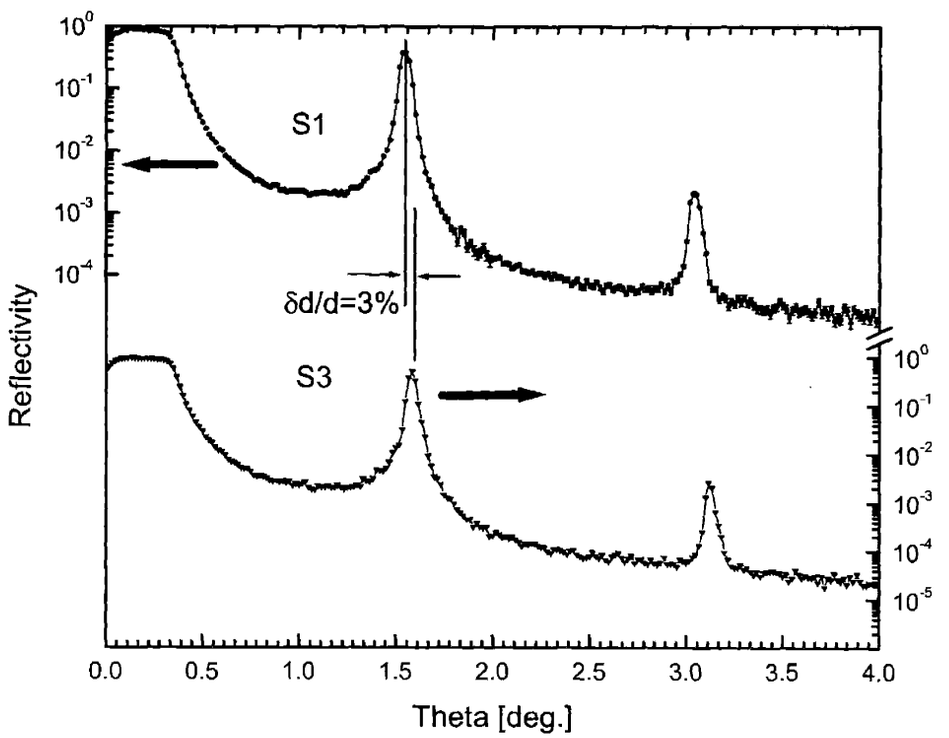

Figure 6.7: X-ray reflectivity versus grazing angle at 8 keV for the centers of two glass foils coated with a W/Si multilayer. The two foils were mounted 120° apart in the prototype coating chamber (see Fig. 6.4). The difference in the Bragg peak positions corresponds to 3% variation in period, which is indicative of the azimuthal uniformity of the coating process.

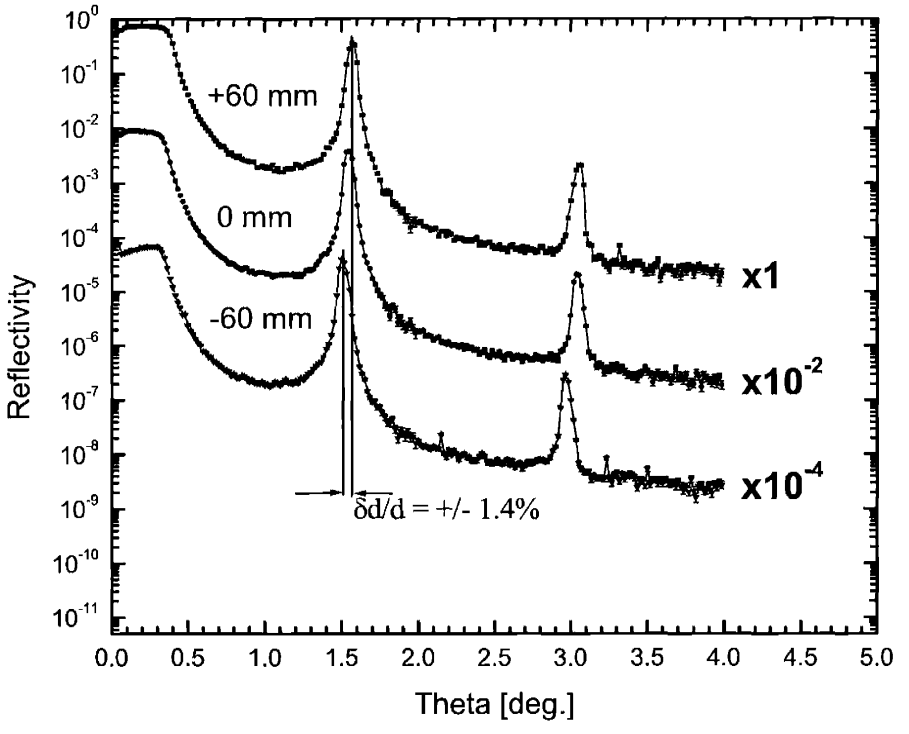

Figure 6.8: X-ray reflectivity versus grazing angle for three locations separated by 60 mm along the axis of a slumped glass foil coated with a W/Si multilayer (MLPC142 S1). The variations of the Bragg peak positions correspond to a period variation of ±1.4%.

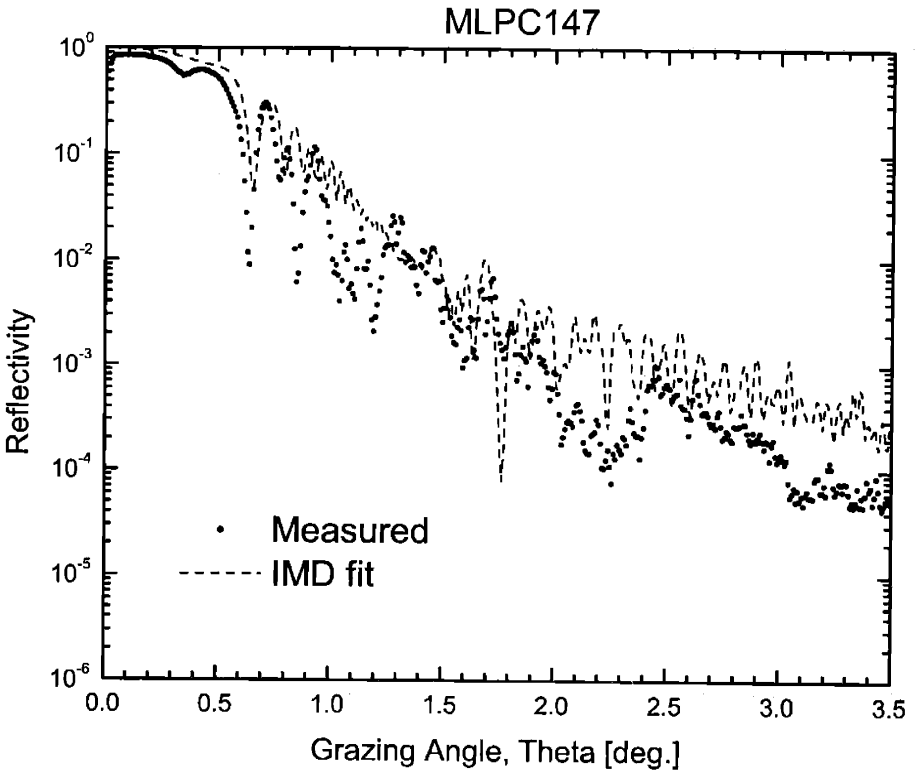

Figure 6.9: X-ray reflectivity at 8 keV for a depth graded W/Si multilayer with N=200 bilayers deposited on a slumped glass foil (MLPC run 147). The discrepancy between the data and the IMD model are due to plasma outages at both cathodes during the run (see text).

6.5 Multilayer coatings on replicated substrates

6.5.1 Integral replicated shells

Another solution pursued for the fabrication of substrates for the next generation of hard x-ray telescopes is the replication of integral shells from mandrels with the correct figure and good surface roughness. These substrates have the advantage of being rigid and keeping their figure. Therefore, assembling them in a telescope needs only alignments between shells, not within a shell, as in the case of segmented substrates. One of the disadvantages of this "closed" geometry is that it requires a deposition technique capable of coating inside the shells. The prototype coating chamber at the SAO Multilayer Facility has the

unique capability to deposit multilayers inside shells with inner diameters in the range 20-50 cm.

The most developed technology for replication is based on nickel electrodeposition on the mandrel. Electroformed shells are the only substrates which have been proven to give angular resolution of 20 arcsec., followed by epoxy replicated foils with 2 arcmin. The basic fabrication steps for the production of replicated shells are shown in Figure 6.10 and consist of:

- polishing an electroless nickel-plated aluminum mandrel until the figure and roughness specifications are met.
- evaporating on the mandrel surface a thick layer (~1000 Å) of gold, which acts as a release agent.
- electrodeposition of the required thickness of nickel on the mandrel.
- separation of the shell from the mandrel by cooling. The gold has poor adhesion on the mandrel side and separates with the shell. Gold was widely used for soft x-ray telescopes because it had a dual role of separation agent and reflector. For hard x-ray telescopes, the reflector role is taken by the multilayer, so other materials can be investigated as alternatives to gold as a separation agent. Also, the typical roughness of the gold surface that was acceptable for soft x-ray telescopes was about 8 Å (XMM telescope). For high energy telescopes, it is necessary to bring the roughness down to 3 Å r.m.s., in order to be able to avoid conformal replication of the roughness in multilayers.

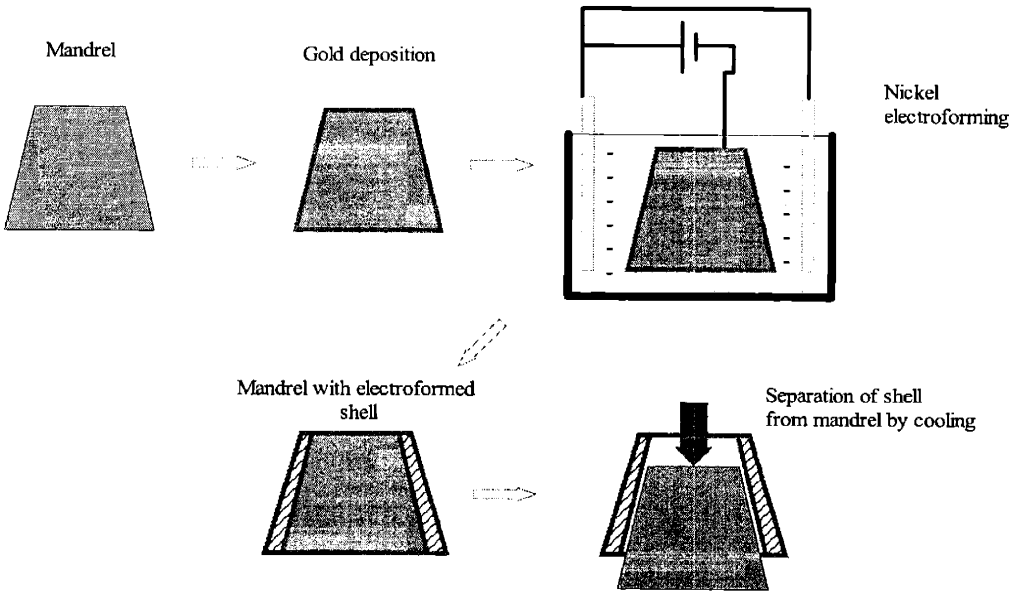

Figure 6.10: Diagram of the steps involved in replication by nickel electroforming (adapted from [5]). For simplicity, the mandrel shown above is a cone with a large slope, but in practice Wolter type I figures (paraboloid+hyperboloid) can be replicated using nickel electroforming. The process starts with a superpolished mandrel on which the separation agent (gold) is evaporated. The mandrel is then immersed in the electroforming bath, where nickel is deposited to the thickness required by the shell mirror diameter and stiffness. After removal from the bath, the mandrel core is cooled with liquid nitrogen. Because the core is made of aluminum and its thermal expansion coefficient is twice than for nickel, the shell separates from the mandrel. The gold has a poor adherence to the mandrel, so it acts as a separation agent and is released together with the nickel shell.

Multiple shells can be electroformed and separated from the same mandrel before repolishing, so the cost for the machining of the mandrel to the specified figure and the cost of the superpolishing are mitigated by repeated use of the mandrel in shell production. Successful x-ray telescope missions using replication are SAX, Spectrum-X-Gamma, JET-X, and XMM-Newton. The JET-X mirrors achieved an angular resolution of 15 arcsec, but their surface is not smooth enough to serve as a substrate for hard x-ray multilayer telescopes. More research is being carried out in the direction of reducing the roughness of the replicated shells and also for producing thinner, lighter shells while preserving the rigidity and the figure of the shell (see [6], [5]).

Some of the factors affecting the optical performance of a shell replicated by electroforming and considered in the work quoted above are:

- internal stresses during the electrodeposition process.

- plastic deformations of the shells during separation.
- incomplete separation of the gold from the mandrel.

6.5.2 W/Si multilayer coatings on flat replicas

A first coating test on replicated substrates was performed on a 7-cm diameter flat, prepared by the Brera Astronomical Observatory. The flat was coated with 60 bilayers of W/Si with d=29 Å, γ=0.34, using cathode currents of 750 mA for W and 600 mA for Si, a gas pressure p_{Ar}=2.7 mTorr, and rotating the sample around the cathodes on a 22.5 cm diameter circle. A plasma outage at the Si cathode during the deposition of the fourth bilayer reduced the thickness of that Si layer to 15.9 Å instead of 19.1 Å. The model for the x-ray reflectivity took into account this imperfection and it is shown in Figure 6.11 together with the measured data. The interface widths were σ(W-on-Si)=7.0 Å and σ(Si-on-W)=5.2 Å. These are 1.5-2 Å larger than in the case of the test coatings on slumped glass substrates, but were matched by the interface widths measured for the two witness silicon wafers, where we found σ(W-on-Si)=6.7 Å and σ(Si-on-W)=4.5 Å. It is possible that the increase observed for σ was related to the plasma outage at N=4. It is not known how the deposition conditions during the recovery stage of the plasma affect the growth process, but one can suppose that the roughness of that layer was increased and the subsequent deposition of 56 bilayers of W/Si replicated this roughness.

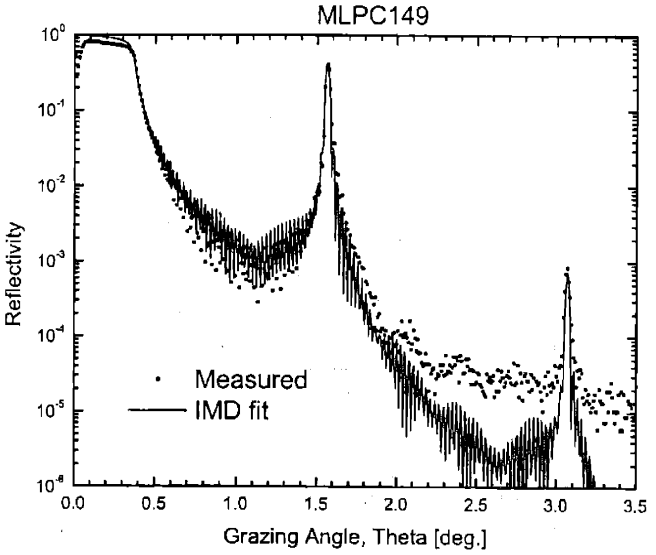

Figure 6.11: X-ray reflectivity at 8 keV for a constant period W/Si multilayer with N=60. The substrate was a flat disk replicated by nickel electroforming. The top surface of the substrate was covered by a 1700 Å thick layer of gold (used as release agent in the process) with a surface roughness of 4.5 Å. The period of the multilayer is d = 29 Å, and the interface widths are σ(W-on-Si)=7.0 Å and σ(Si-on-W)=5.2 Å.

6.5.3 W/Si multilayer coatings on nickel replicated shells

Our laboratory is collaborating with the Brera Astronomical Observatory in Italy to produce prototype mirrors for hard x-ray telescopes by coating the inside of nickel electroformed shells with multilayers. Brera is obtaining the replicated shells from the Media Lario company in Italy, which produced the XMM-Newton shells. The first SAO mandrel was fabricated and sent to Brera for superpolishing and replication. We have received a prototype replica electroformed prior to the superpolishing. After the polishing of the mandrel was completed, two other shells were replicated. The nominal inner diameter of all the shells was 28 cm. They were covered on the inside with a gold separation layer and were investigated by x-ray reflectivity measurement at four azimuthal locations prior to their coating.

The shell electroformed before the mandrel superpolishing had a 1300 Å thick gold layer with a density of 18.5 g/cm^3. The surface roughness was 6.0 Å and the interface width with

the substrate was 7.0 Å. There was no azimuthal variation of these numbers and one of the four scans is shown in Figure 6.12 (right).

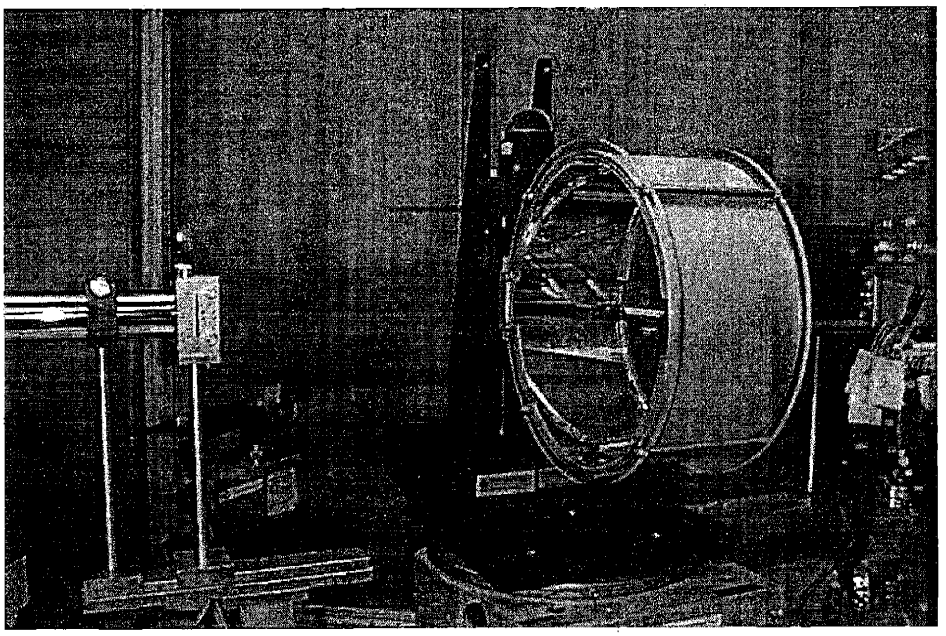

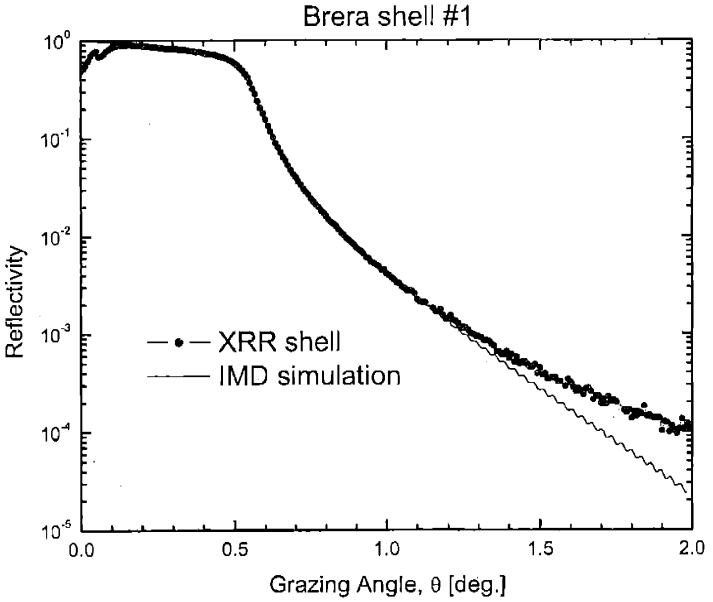

Figure 6.12: Above: The first replicated nickel shell mounted in the XRR setup for X-ray reflectivity measurements with a pencil beam. Below: the 8 keV XRR data (dots) and model (line) at azimuth 0° for the shell. The top layer is gold with 1300 Å thickness, a density of 18.5 g/cm^3 and a surface roughness of 6 Å. The substrate is electroformed nickel with a 7 Å wide interface with the gold.

This first shell was coated with a depth graded W/Si multilayer with N=200 bilayers and a power law formula optimized for measurements at 17 and 40 keV. The 200 bilayers were divided in two blocks: one block with 180 bilayers was deposited first, followed by the second block with 20 bilayers. The design parameters for the two depth graded blocks are presented in Table 6.2. The deposition was performed at 3.3 mTorr Ar pressure and the cathode currents were I_{Si}=1000 mA and I_W=750 mA. The power levels in the cathodes were 360 Watts for Si and 231 Watts for W, respectively.

Table 6.2: Thickness parameters *a*, *b*, and *c* for the two depth graded multilayers deposited on the first nickel replicated shell. The parameters were chosen to optimize the reflectivity at 17 keV and 40 keV, which were the energies intended to be used for characterization of the shell. First, the block of 180 bilayers was deposited using the corresponding parameter values in the power law equation, followed by the top 20 bilayers. The power law formula had the usual expression as introduced by Joensen et al [7] and is reproduced below. The subscript *M* stands for the material (W or Si) and the bilayer number *i* varies from 1 at the surface of the block to N_{block} for the bottom layer in the block:

$$d_M[i] = \frac{a_M}{(b_M + i)^{c_M}}$$

Block no.	N	a_W	a_{Si}	b_W	b_{Si}	c
1	180	85.36	38.67	325.8	4.077	0.25
2	20	42.14	53.95	-0.589	-0.782	0.25

The coated shell was measured by pencil beam reflectivity at different azimuthal locations and presented negligible variation. When compared with the witness samples, the reflectivity of the shell was at least one order of magnitude lower. Figure 6.13 presents a comparison with the scan of the witness coating on superpolished fused silica, which had interface widths of σ(W-on-Si)=4.5 Å and σ(Si-on-W)=3.0 Å. The interface widths of the multilayer deposited on the shell were in agreement with the measurements for values of σ in the range 15-18 Å. These large numbers were initially attributed to the different substrate roughnesses (6 Å for the shell vs. 2 Å for the superpolished silica).

After shipping to Brera, the multilayer was found delaminated from a large area of the shell. We have reconsidered the low reflectivity problem for the shell and it was hypothesized that the different thermal expansion coefficients for W ($3x10^{-6}$ K^{-1}) and Ni ($13x10^{-6}$ K^{-1}) can produce large stresses between the multilayer and the substrate when the shell cools off from the deposition temperature to room temperature. Since the deposition run for N=200 bilayers was almost 7 hour long and the cathode power levels added up to about 600 Watts, we further investigated the substrate temperature problem. For this purpose, we started to use color-changing thermal button sensors in contact with the back of the substrates. The multilayer was removed from the shell and the coating was scheduled to be repeated in identical conditions, this time with temperature sensors on the shell and on the witness substrates. After 135 bilayers were deposited, one of the cathode shutters was stuck in the open position due to a mechanical failure. The coating run was thus aborted after 4 hours. The temperatures indicated by the sensors were 50^{o} C ($\pm 4^{o}$) for the nickel shell and a 5-cm diameter nickel flat and 60^{o} C ($\pm 6^{o}$) for wafer substrates. We have changed our goals to reducing the power of the cathodes and in consequence, to decreasing the temperature of the shell during the coating.

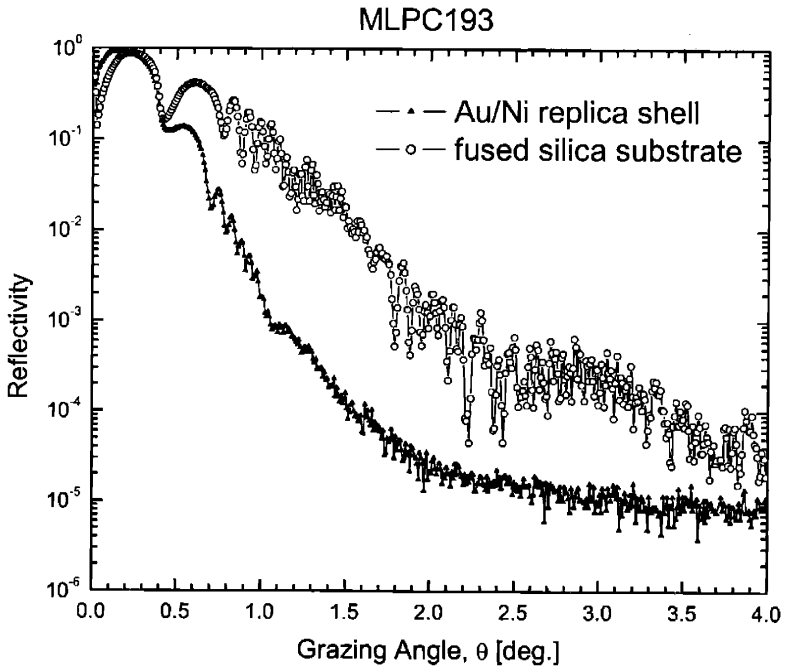

Figure 6.13: X-ray reflectivity at 8 keV for the W/Si depth graded multilayers deposited on the first nickel shell from Brera (triangle symbol) and a fused silica witness substrate (open circle symbol). The difference in reflectivity is due to the substrate roughness (6 Å for the shell vs. 2 Å for the superpolished fused silica) and also due to the poor adhesion of the multilayer to the gold surface.

The decrease of the cathodes power levels involved lower deposition rates (that had to be recalibrated) and a longer coating time for the same multilayer design. In one trial run, the currents were I_{Si}=600 mA (190 Watts power) and I_W=600 mA (177 Watts), and 200 bilayers were deposited in an 11-hour long run on silicon wafers. The temperature recorded by the sensors on the shell was 42° C (± 4°).

We have decided to lower even further the cathode currents and eventually the second shell from Brera was coated at I_{Si}=450 mA (130 Watts) and I_W=450 mA (125 Watts). The total power in the cathodes was thus about half of the power used for the coating of the first shell.

Prior to the coating, the shell was measured by x-ray reflectivity scans performed at four azimuthal locations. Again, the azimuthal uniformity was found to be excellent. This shell was smoother than the first, because it was replicated after the superpolishing of the

mandrel. The analysis of the XRR data yielded a density of 19.0 g/cm^3 and a thickness of 1500 Å for the gold layer. Its surface roughness was 4.5 Å and the Au/Ni interface width was 4.5 Å. The x-ray reflectivity scan in Figure 6.14 shows a very good match between the measured data and the IMD simulation, with a very small discrepancy at angles larger than 1.6°.

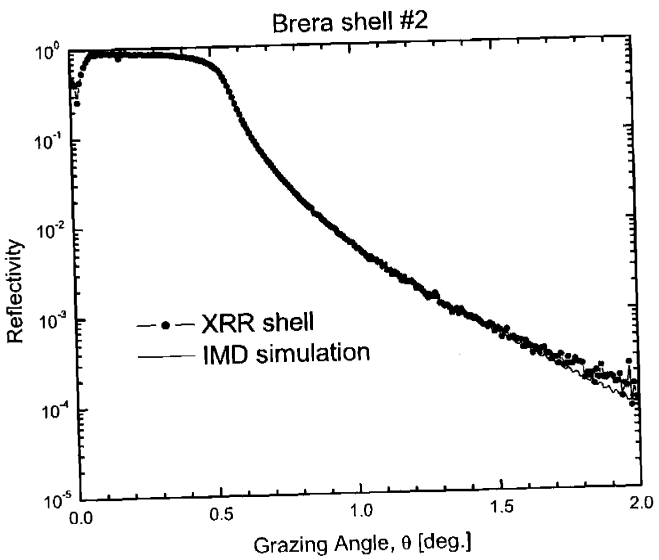

Figure 6.14: X-ray reflectivity scan at 8 keV for the second nickel replicated shell. The surface roughness is 4.5 Å. The gold separation layer was 1500 Å thick and had a density of 19.0 g/cm^3. The width of the interface Au/Ni was 4.5 Å.

The second nickel replicated shell was coated with N=115 bilayers of W/Si at the cathode current levels mentioned above. The total deposition time for this run was 7h45m and the maximum temperature recorded by the sensors on the back of the shell and witness wafers was 34° C. The shell was further characterized by x-ray reflectivity using the 8 keV pencil beam. The scan performed at 0° azimuth is shown in Figure 6.15. Although the reflectivity performance was improved from the first shell, it was still short of the goal of σ=5 Å or less. We considered the possibility of misalignments between the shell, the x-ray beam, and the scan rotation axes, or that figure errors might have reduced the measured reflectivity. However, repeating the XRR scans with narrower slits should reduce these

geometric errors. We repeated the scans in these conditions and found identical results. The IMD analysis of the data shown in Fig. 6.15 gave the following results: σ(W-on-Si)=12 Å, σ(Si-on-W)=5.8 Å. Since the substrate roughness was measured in an identical manner before coating and was 4.5 Å, a conformal growth of the multilayer cannot produce 12 Å-wide interfaces in the multilayer. The difference between the coating temperature and room temperature was about 14° C, so the thermal expansion difference between W and Ni was reduced by at least 50% compared to the first shell coating. Although the second shell coating did not delaminate as the first one, it is possible that delamination of gold from the nickel still occurs, only that it is localized on microscopic regions, enough to contribute to the large roughness measured. In that case, other separation agents or other replication methods must be researched to eliminate the gold adhesion problem.

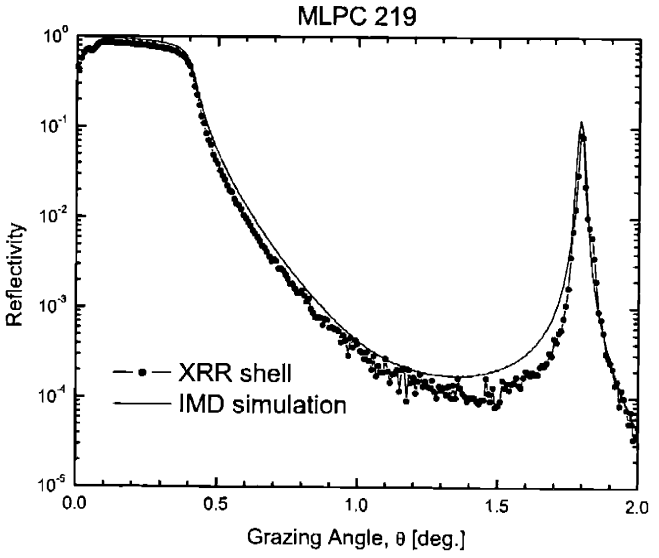

Figure 6.15: X-ray reflectivity measured at 8 keV for a constant period W/Si multilayer with N=115 bilayers. The coating was performed on the inside of the second nickel shell from Brera and the IMD simulations indicate the following thicknesses and interface widths: d_{Si}=14.4 Å, d_W=10.8 Å, σ(W-on-Si)=12.0 Å, and σ(Si-on-W)=5.8 Å. The temperature of the shell was below 34° C during the coating.

6.5.4 Replicated nickel alloy shells

Another process of integral shell replication from mandrels was developed at NASA/Marshall Space Flight Center (MSFC) and was used successfully for the production of the telescope onboard the HERO mission ([8]). The replication is based on the electrodeposition of a proprietary nickel alloy and eliminates gold as the separation agent between the mandrel and the shell. SAO has an ongoing collaboration with MSFC in which they are attempting to fabricate the mandrels and shells and SAO-MLF performs the coating and low-energy reflectivity measurements. The shells produced for HERO were smaller that the minimum shell diameter that can be coated in the SAO chamber, so a new test mandrel with a nominal diameter of 23 cm was fabricated and used to replicate three test shells with different thicknesses (0.5, 0.7, and 1.3 mm). They have the shape of a cone with a very small taper (inner diameters of 227 mm and 228.5 mm) and 198 mm height. The shells were scanned by XRR and we found a very high roughness (22-25 Å) and a density of 7.9 g/cm^3 for the alloy. To further investigate the inner surface, one of the shells was cut and characterized by atomic force microscopy. The surface scans revealed the existence of a dense distribution of "peaks" over a generally flat wide area. The peaks are uniformly distributed and cannot be avoided from the field of view when scanning with scan sizes of 0.5 μm or larger. The roughness analysis can exclude these peaks by selecting a digital box on the image of the surface. When the boxes excluded the peaks, the average roughness of the surface was 15 Å r.m.s. If the full scan area is taken into account, the average surface roughness was 37 Å, which is similar to the roughness determined by XRR. Further measurements of the surface with a WYKO interferometer instrument at x100 magnification confirmed the existence of the peaks and the large roughness introduced by them. These imperfections are thought to be due to pits in the surface of the mandrel. Additional improvement steps are being implemented for the manufacture and metrology of a new mandrel.

One of the MSFC shells was coated with a constant period Ni/C multilayer with N=20 bilayers and d=47.7 Å (20.9 Å Ni, 26.8 Å C). The interface widths were very large and

comparable to the layer thickness (σ=20 Å). The result was not surprising, considering that the shell surface roughness was corroborated by three independent characterization methods and that sputter deposited nickel is very likely to grow conformal to the substrate.

6.6 Conclusions

The success of the multilayer optics for the future generation of imaging hard x-ray telescopes depends critically on the quality of the substrates. Parameters like figure, roughness, adhesion with the multilayer, rigidity, and weight will determine the best substrate candidate for Constellation-X and similar missions. The studies at SAO were directed towards exploiting the capability of depositing multilayers inside integral substrates. The prototype chamber is unique among other coating facilities in this respect. We have proven that multilayers can be deposited with good uniformity (<3%) inside cylindrical shells and the current minimum diameter limit is 20 cm. By loading segments of shells in a closed configuration, it was also shown that the sputtering cathodes could coat segmented optics efficiently and with good uniformity. For shell diameters less than 20 cm, an approach currently being developed is to coat the outside of the mandrel with multilayers before electrodeposition.

In order to pursue the integral shell approach to the goal of high resolution telescopes, our studies showed that substantial improvements are needed for the replication process in directions like reducing the substrate roughness, solving the adhesion problem of the release agent, and decreasing shell weight while maintaining the rigidity of the shell.

References for Chapter 6

1. W.W. Craig, F.E. Christensen, T. Decker, C.J. Hailey, F.A. Harrison, R.M. Hill, M. Jimenez-Garate, P. Mao, and S. Schindler, *"Hard x-ray optics for the HEFT baloon borne payload: prototype design and status"*, in EUV, X-Ray, and Gamma-Ray Instrumentation for Astronomy IX, 1998, *Ed.* O.H.Sigmund and M.A.Gummin, Proceedings of SPIE, vol. **3445**, pp.112-120.

2. F.E. Christensen, W.W. Craig, C.J. Hailey, M.A. Jimenez-Garate, D. L.Windt, F.A. Harrison, P.H. Mao, E. Ziegler, V. Honkimaki, et al., *"Hard X-ray characterization of a HEFT single reflection prototype"*, in X-Ray Optics, Instruments, and Missions III, 1999, *Ed.* J.E. Truemper and B. Aschenbach, Proceedings of SPIE, vol. **4012**, pp.626-638.

3. S. Romaine, A. Ivan, R. Bruni, F. Christensen, F. Harrison, W. Craig, and P. Gorenstein, *"Multilayer optics for hard X-ray astronomy"*, in X-Ray Optics, Instruments, and Missions IV, 2000, *Ed.* R.B. Hoover and A.B. Walker, Proceedings of SPIE, vol. **4138**, pp.120-125.

4. P.H. Mao, F.A. Harrison, Y.Y. Platonov, D. Broadway, B. DeGroot, F.E. Christensen, W.W. Craig, and C.J. Hailey, *"Development of grazing incidence multilayer mirrors for hard x-ray focusing telescopes"*, in EUV, X-Ray, and Gamma-Ray Instrumentation for Astronomy VIII, 1997, *Ed.* O.H. Siegmund and M.A. Gummin, Proceedings of SPIE, vol. **3114**, pp.526-534.

5. O. Citterio, P. Conconi, M. Ghigo, F. Mazzoleni, and G. Pareschi, *"Progress on the use of ceramics materials for high throughput light weight X-ray optics"*, Proc. SPIE **4012**, 2000,

6. G. Pareschi, O. Citterio, M. Ghigo, and F. Mazzoleni, *"Nickel replicated multilayer optics for soft and hard X-ray telescopes"*, Proc. SPIE **4012**, 2000,

7. K.D. Joensen, P. Voutov, A.Szentgyorgyi, J.Roll, P. Gorenstein, P.Hoghoj, and F.E. Christensen, *"Design of grazing-incidence multilayer supermirrors for hard-X-ray reflectors"*, Applied Optics **34**, 1995, pp. 7935-7944.

8. B.D. Ramsey, C.D. Alexander, J.A. Apple, R.A. Austin, C.M. Benson, K.L. Dietz, R.F. Elsner, D.E. Engelhaupt, J.J. Kolodziejczak, et al., *"HERO: high-energy replicated optics*

for a hard x-ray balloon payload", in X-ray Optics, Instruments, and Missions IV, 2000, *Ed.* R.B.Hoover and A.B. Walker, Proceedings of SPIE, vol. **4138**, pp.147-153.

Conclusions

This thesis work explored the feasibility of a new design for the next generation of focusing hard x-ray telescopes. Using Bragg reflection from multilayer coatings, photons with energies above 10 keV from cosmic x-ray sources can be collected efficiently by detectors positioned in the focal plane and form images with arcminute or better angular resolution and high signal-to-noise ratio. The superior imaging performance in the hard x-ray band of the telescope designs based on multilayers -versus the existing aperture-coded telescopes or designs using single-layer coating mirrors with very long focal distances- played an important role in the selection of this technology for the NASA Constellation-X Mission and for two other hard x-ray telescope missions. The Multilayer Facility at Smithsonian Astrophysical Observatory is actively pursuing the goal of producing and testing mirror prototypes with higher angular resolution without compromising the collecting power (effective area). For this purpose, we have designed and constructed special coating facilities, which are unique in their capability to coat various substrate geometries, including integral cylindrical shells. SAO has formed collaborations with research groups at Brera Observatory in Italy and at NASA/MSFC to receive high-quality replicated shells that serve as substrates for the multilayer coatings.

As part of this research program at SAO, I have played a critical role in the following activities:

- actively participated in the design and development of the multilayer coating facilities
- initiated the x-ray reflectivity (XRR) measurements program by performing the first series of XRR analyses at external facilities
- designed and developed from the ground up the SAO reflectometer system
- coated multilayer samples in the R&D deposition chamber and participated in the multilayer coating runs performed in the prototype chamber
- investigated a large number of samples by XRR, Atomic Force Microscopy, profilometry, and other characterization methods

- participated in high energy XRR measurements using synchrotron radiation

The original aspects of the research presented in this work can be summarized in the following lines:

- the study presented in Chapter 4 was the first (and possibly the only one, so far) to adopt a consistent methodology for the growth, characterization, and optimization of multilayers for hard x-ray mirror applications.
- the set of x-ray reflectivity measurements at high energy described in Chapter 5 is one of the few studies carried out to look at the response of x-ray multilayer optics at high energies. It is also significant as the first to analyze three different material combinations for depth-graded multilayers.
- the unique capability of the SAO prototype coating chamber to deposit multilayers on the inside of both integral and segmented cylinders was proven in Chapter 6 and is expected to be decisive in achieving our goal of developing a prototype mirror with superior angular resolution.

The study of different material combinations for the multilayers (Chapter 4) reached important conclusions, which allowed selecting from the pool the best candidates for hard x-ray mirrors (W/Si, Pt/C, and W/C). The x-ray reflectivity of multilayers depends on their interface widths as described by the Debye-Waller factor (Section 2.6) and reaches the theoretical maximum when the width (due to both roughness and diffuseness) is reduced to zero. In practice, the interface widths are always finite but can be minimized by the appropriate selection of materials and deposition conditions. This was the purpose of the optimization studies described in Chapter 4. The best materials listed above could be grown in such conditions that the multilayer interface widths measured by XRR were in the range 3.0-4.5 Å. The other material combinations studied (Mo/Si, Ni/C, Ni-V/C, WSi_2/Si, and Nb/Si) did not offer the same low interface width, due to a combination of thermodynamical factors (enthalpy of mixing, surface energy, etc.) and deposition process conditions (interface mixing by energetic neutrals).

In the light of this research, future work of identification of new material combinations can be done by including new elemental or compound materials. The optimization study for the most promising material pairs can be refined by extending the number of process parameter levels in the Taguchi design of experiments (see Sections 4.1.9 and 4.4.6). Alternatively, one can explore the option of reducing the energetic neutral flux by using a heavy inert gas (Xe) instead of argon for the deposition process. The role of the substrate temperature was not investigated and could be a possible direction of research, as well as performing post-deposition annealing treatments.

The multilayer depositions on large substrates proved that the reflectivity performance of the mirrors will depend not only on the selection of materials for multilayers and their coating process parameters, but also on the quality of the substrates, through parameters like figure error, surface roughness, adhesion with the multilayer, rigidity, and density. The studies at SAO were directed towards proving the advantage of integral substrates in achieving high angular resolution. We have demonstrated that multilayers can be deposited with good lateral uniformity (<3%) inside shells with a minimum diameter of 20 cm. By loading segments of shells in a closed configuration, it was also proven that the sputtering system could coat segmented optics efficiently and with good uniformity. For shells with diameters less than 20 cm, the approach currently under development is to coat the outside of the mandrel with multilayers before the electrodeposition of the shell.

In order to pursue the goal of high resolution for integral replicated shells, our work showed that many improvements are needed in directions like reducing the roughness, solving the adhesion problem of the release agent, and decreasing the shell density while maintaining its rigidity.

Appendix A: Derivation of the Fresnel coefficients

Considering a monochromatic plane wave (Fig. A.1) incident on the boundary between medium *1* (vacuum, refraction index $n_1 = 1$) and *2* ($n_2 \doteq n = 1 - \delta - i\beta$), its propagation is described by the Helmholtz equation:

$$\nabla^2 \mathbf{E} + k_j^2 \mathbf{E} = \mathbf{0} \tag{A.1}$$

with $k_j = k_0 / n_j$ the wave vector in medium j=*1,2*. The particular solutions of eq. (A.1) are identified as the incident (*in*), reflected (*r*), and transmitted (*tr*) plane waves, and they have the plane wave expressions:

$$\mathbf{E}_m = A_m e^{i(\omega t - \mathbf{k}_m \cdot \mathbf{r})} \hat{\mathbf{e}}_y \tag{A.2}$$

where the index m stands for *in*, *r*, or *tr*, and we considered the wave to be polarized in the y direction (*s*-polarization).

The wave-vectors for the incident, reflected, and transmitted waves have the expressions:

$$\begin{aligned} \mathbf{k}_{in} &= k_0 \left(\sin i_1 \hat{\mathbf{e}}_x - \cos i_1 \hat{\mathbf{e}}_z \right) \\ \mathbf{k}_r &= k_0 \left(\sin i_1 \hat{\mathbf{e}}_x + \cos i_1 \hat{\mathbf{e}}_z \right) \\ \mathbf{k}_{tr} &= k_0 n \left(\sin i_2 \hat{\mathbf{e}}_x - \cos i_2 \hat{\mathbf{e}}_z \right) \end{aligned} \tag{A.3}$$

The angles i_1 and i_2 are measured with respect to the normal to the surface as shown in Fig. A.1. Two boundary conditions must be satisfied. First, the tangential component of the electric field must be continuous at the interface:

$$A_{in} e^{i(\omega t - k_0 x \sin i_1)} + A_r e^{i(\omega t - k_0 x \sin i_1)} = A_{tr} e^{i(\omega t - k_0 n x \sin i_2)} \tag{A.4}$$

This condition is true for any t and x. In particular, if $x = 0$, it follows that

$$A_{in} + A_r = A_{tr} \tag{A.5}$$

$$r = \frac{A_r}{A_{in}} \qquad t = \frac{A_{tr}}{A_{in}} \tag{A.9}$$

By dividing in equations (A.5) and (A.8) by A_{in}, the two continuity equations can be expressed in terms of the amplitude coefficients:

$$\begin{aligned} 1 + r &= t \\ 1 - r &= nt\frac{\cos i_2}{\cos i_1} \end{aligned} \tag{A.10}$$

Solving for r, the reflection amplitude coefficient is:

$$r^s = \frac{\cos i_1 - n\cos i_2}{\cos i_1 + n\cos i_2} = \frac{\sin(i_2 - i_1)}{\sin(i_1 + i_2)} \tag{A.11}$$

where we introduced the s superscript to indicate that this calculation is valid for an s-polarized wave. A similar derivation can be done for a plane wave polarized perpendicular to the plane of reflection (p-polarization). The result is then:

$$r^p = \frac{\tan(i_2 - i_1)}{\tan(i_2 + i_1)} \tag{A.12}$$

At small grazing incidence angles, the two reflection coefficients for s and p polarization can be considered equal with a good approximation, as shown in Figure A.2. The x-ray reflectivity at small angles is practically independent of polarization and either of the equations (A.11) or (A.12) can be used in that case. For full calculations, use of the exact equations (A.11) and (A.12) in computer codes like IMD guarantees the accuracy of the model at all possible angle values.

Using (A.5) in (A.4) and identifying the exponents, we obtain the Snell-Descartes law:

$$\sin i_1 = n \sin i_2 \tag{A.6}$$

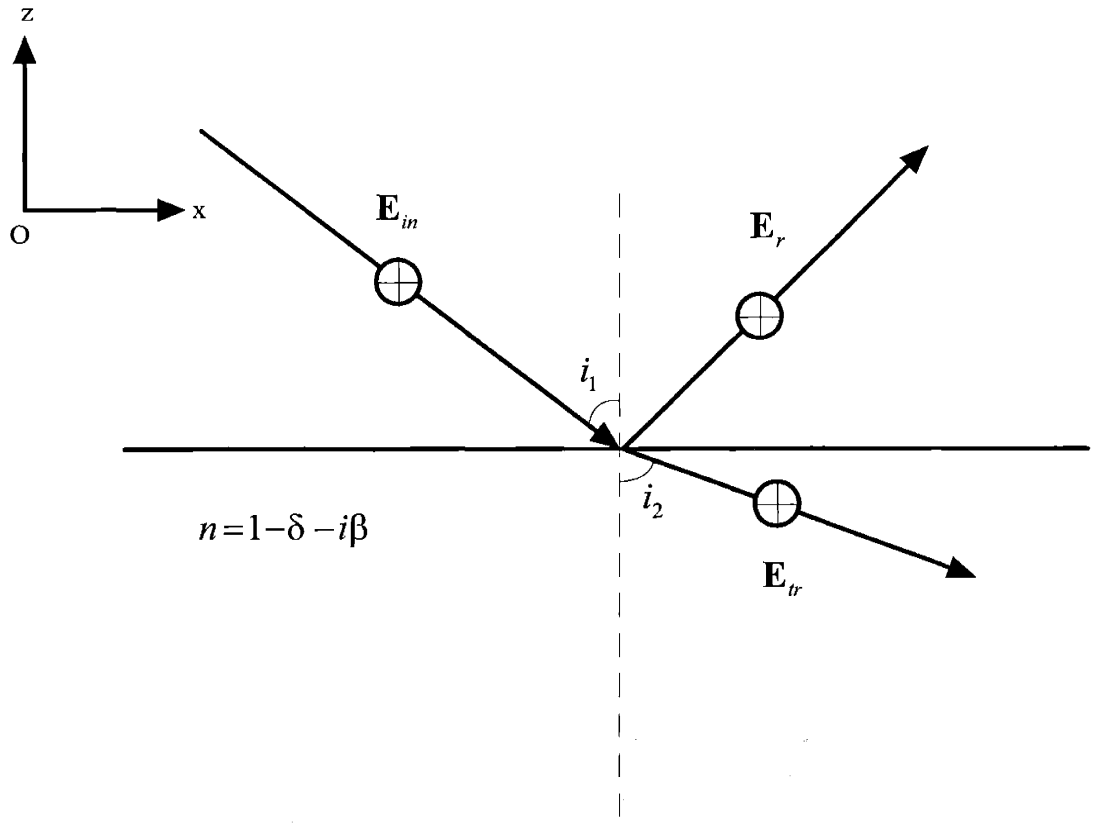

Figure A.1: Reflection and refraction of an *s*-polarized wave incident on the surface separating a medium with refraction index $n = 1 - \delta - i\beta$ from vacuum ($n = 1$).

The other boundary condition is the continuity of the tangential component of the magnetic field at the interface, B_x. The magnetic field can be calculated from the Maxwell equation:

$$\nabla \times \mathbf{E} = -\frac{\partial \mathbf{B}}{\partial \mathbf{t}} = -i\omega \mathbf{B} \tag{A.7}$$

Then $B_x = -\frac{1}{i\omega}\frac{\partial E_y}{\partial z}$, and using the equations (A.2) and (A.3), the continuity of B_x at the interface yields:

$$\left(A_{in} - A_r\right)\cos i_1 = nA_{tr}\cos i_2 \tag{A.8}$$

The amplitude coefficients for reflection *r* and transmission *t* are introduced:

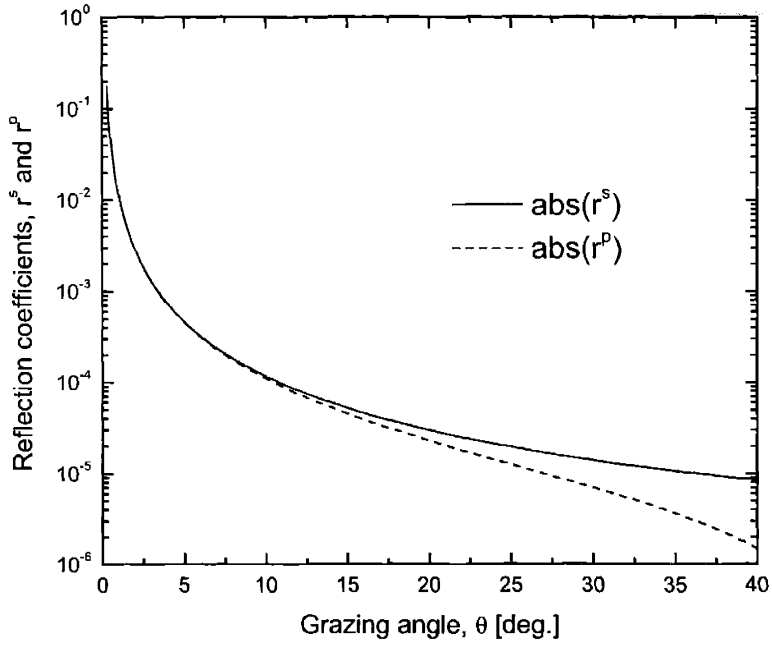

Figure A.2: Absolute values of the Fresnel reflectivity coefficients for *s*-polarized and *p*-polarized radiation with $\lambda = 1.54$ Å (Cu K_α radiation), incident on silicon at grazing angle θ. The values of r^s and r^p are identical up to 5 degrees.

Appendix B: Examples of X-Ray Reflectivity Scans

Examples of x-ray reflectivity scans for different structures encountered in this work

Although the figures shown below were presented in different sections in this thesis, they are gathered here with the purpose of offering a direct understanding, at a glance, of the features present in a reflectivity scan.
At the end of the section, Table B.1 compares the resolution of the XRR measurements with direct imaging methods like Atomic Force Microscopy (AFM) and Transmission Electron Microscopy (TEM).

Figure B.1: 8 keV reflectivity scan of a substrate prior to coating

Figure B.2: 8 keV reflectivity scan of a single layer coating

Figure B.3: 8 keV reflectivity scan of a periodic multilayer

Figure B.4: 8 keV reflectivity scan of a depth graded multilayer

Figure B.5: 40 keV reflectivity scan of a depth graded multilayer

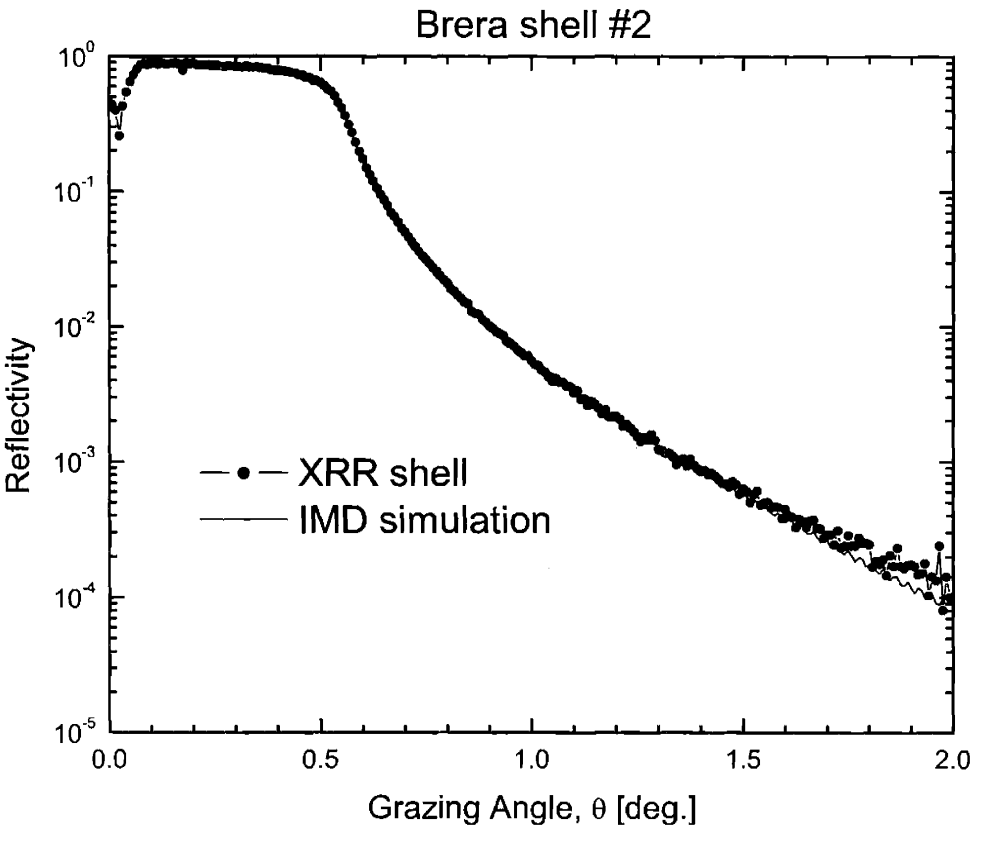

Figure B.1: 8 keV reflectivity scan of a gold substrate prior to coating. The surface roughness was 4.5 Å and the density of the gold was 19.0 g/cm^3. The critical angle for total external reflection for gold at 8 keV is 0.52°. The small dip close to 0° is due to the finite size of the sample (beam footprint effect). After the critical angle, the reflectivity decreases with the grazing angle θ like θ^{-4} (see Section 2.2) and it is necessary to use a logarithmic scale for better visualization.

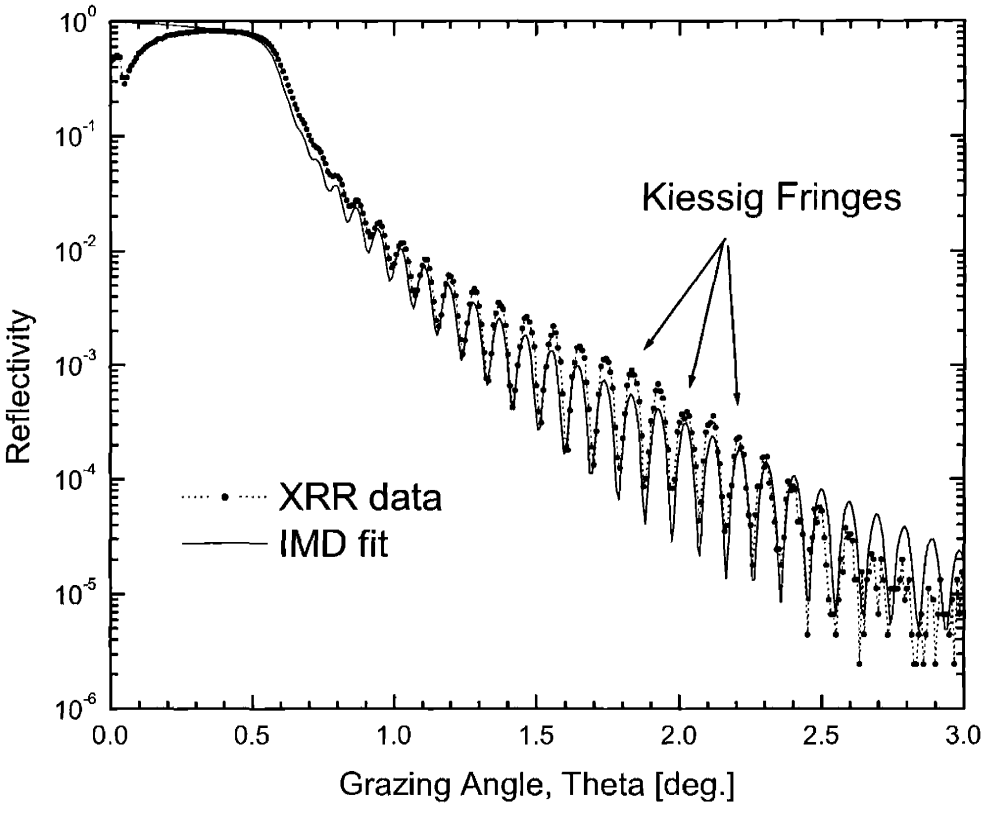

Figure B.2: 8 keV reflectivity scan of a single layer coating. The layer is Pt with a thickness of 445 Å and was deposited on a silicon wafer. The surface roughness of Pt determined from the fit was 4.5 Å and the interface between the layer and the substrate was 2.5 Å (r.m.s.) wide. The interference fringes observed have a frequency proportional to the layer thickness and are called Kiessig fringes (see Section 2.4).

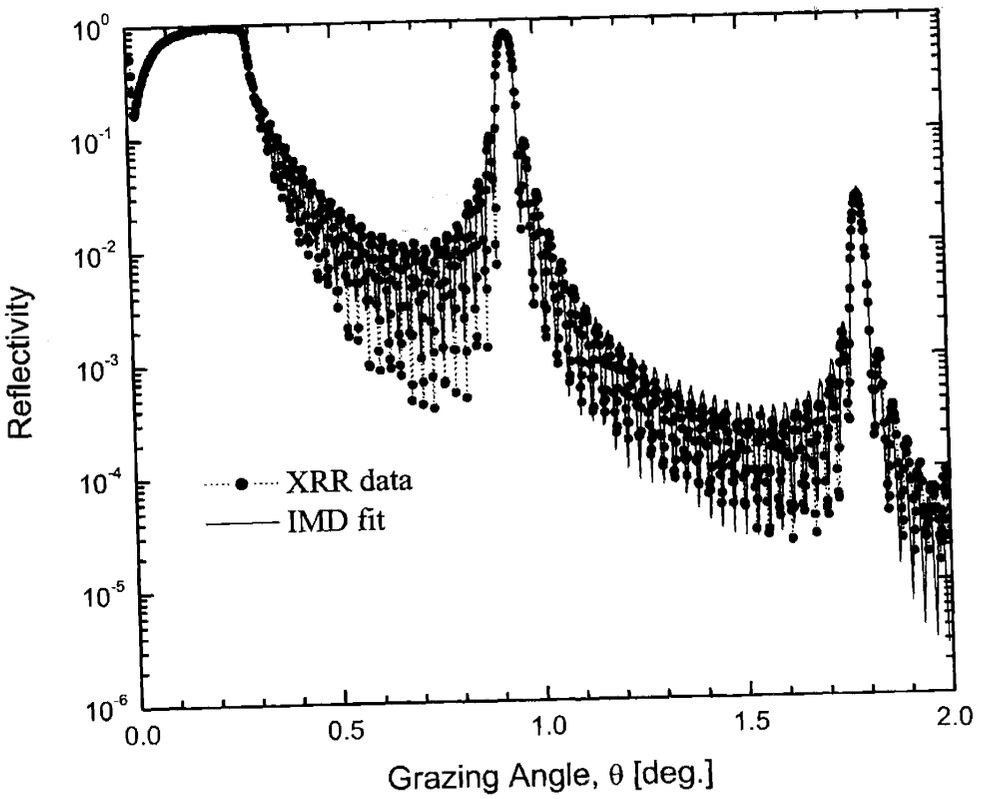

Figure B.3: 8 keV reflectivity scan of a periodic multilayer. The multilayer has N=30 periods of Ni/C bilayers, with 17.3 Å nickel thickness and 32.7 Å carbon thickness. The interface widths determined from fit are 5.0 Å for Ni-on-C and 6.0 Å for C-on-Ni. The dominant features are the two Bragg peaks at grazing angles satisfying the Bragg relation. The oscillations are actually Kiessig fringes and their frequency is proportional to the total thickness of the whole multilayer.

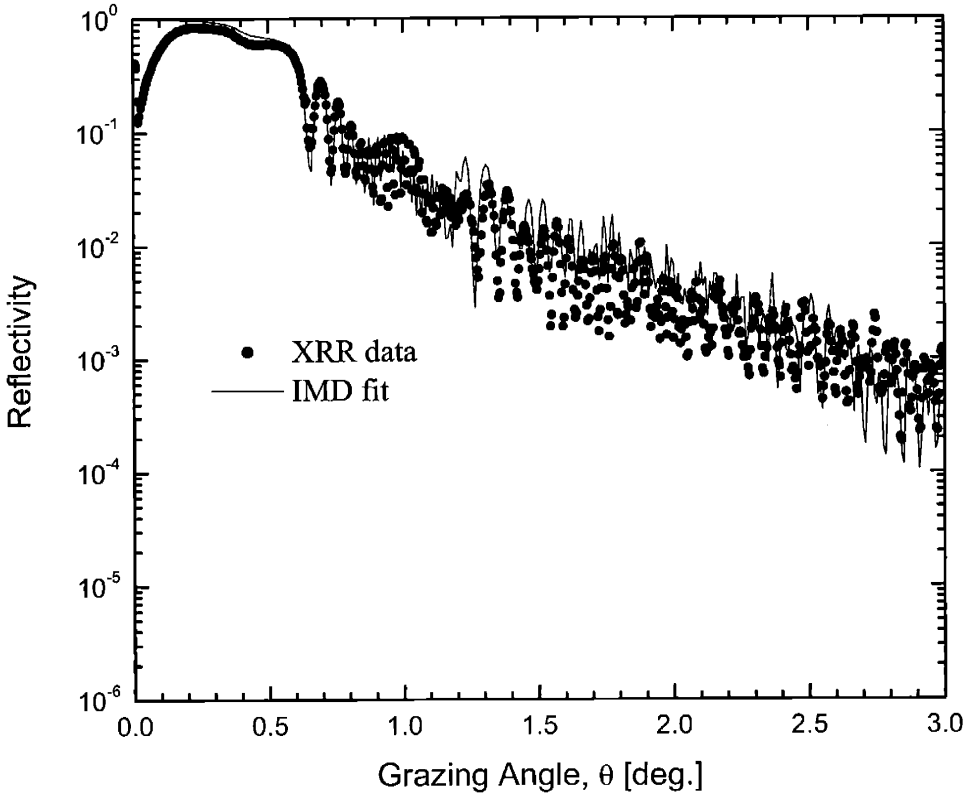

Figure B.4: 8 keV reflectivity scan of a depth graded multilayer. The bilayer thickness *d* of a graded multilayers decreases from the surface towards the substrate in order to satisfy the Bragg reflection condition for different wavelengths (energies) and thus broaden its reflectivity band. This particular sample is a W/C multilayer with 150 bilayers and the structure parameters listed in Table 5.1. The features present in the scan cannot be easily associated with the structure as in the case of Figures B1-B3 and this represents a situation were the use of the computer codes to extract information from the scans is required.

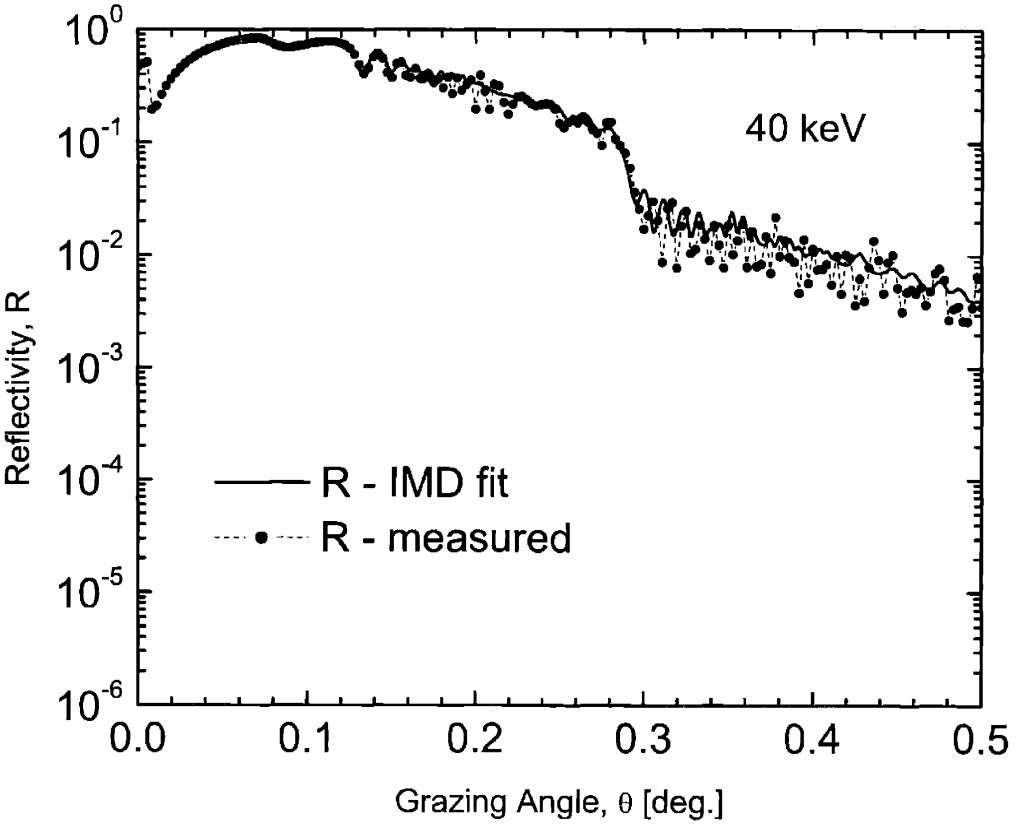

Figure B.5: 40 keV reflectivity scan of a depth graded multilayer. The multilayer is the same W/C sample as for Figure B.4. Due to the smaller wavelength corresponding to the 40 keV energy, the Bragg reflections occur at smaller angles than for 8 keV. The grazing angle was scanned only up to 0.5° and spans about the same range in the reciprocal q-space as the scan in Fig. B.4.

Table B.1: A comparison of three characterization methods for multilayers and their sensitivity to measurements of layer thicknesses and interface widths.

Characterization method	Thickness resolution	Interface information	Observations
XRR @ 8 keV (X-Ray Reflectivity)	~0.5-1 Å (depending on material densities)	-yes- capable to determine the interface width within ~0.5 Å	-non-destructive -typical analysis time 1-3 hours -requires computer analysis of the data
AFM in tapping mode (Atomic Force Microscopy)	-N/A-	-no- except for the surface roughness (0.1-100 μm^{-1} spatial frequency range)	-non-destructive for the surface -analysis time: 15-30 min. -gives only a local (μm size) image of the surface
High Resolution TEM (Transmission Electron Microscopy)	~0.5 Å (depending on magnification used)	-yes- but there are wide disagreements on what procedures to adopt for the data processing	-destructive -time for preparing the specimen: ~6 hours or more -local image of the interface, but easily to interpret visually (no computer)

Appendix C: Proceedings Papers

The following is a list of published proceedings papers based on work presented in this thesis:

1. A. Ivan, S.E. Romaine, R.J.Bruni, J.E. Everett, and P. Gorenstein, *"Characterization of graded d-spacing multilayers for hard x-ray telescopes"*, in X-Ray Optics, Instruments, and Missions, 1998, *Ed.* R.B. Hoover and A.B. Walker, Proceedings of SPIE, vol. **3444**, pp.556-563.

2. A. Ivan, R. Bruni, K. Byun, J. Everett, P. Gorenstein, and S. Romaine, *"Multilayer coatings for focusing hard X-ray telescopes"*, in Materials in Space- Science, Technology and Exploration, 1998, *Ed.* A.F. Hepp, J.M. Prahl, T.G. Keith, S.G. Bailey, and J.R. Fowler, MRS Proceedings, vol. **551**, pp.297.

3. S.E. Romaine, J.E. Everett, R.J. Bruni, A. Ivan, and P. Gorenstein, *"Characterization and multilayer coating of cylindrical x-ray optics for x-ray astronomy"*, in X-Ray Optics, Instruments, and Missions, 1998, *Ed.* R.B. Hoover and A.B. Walker, Proceedings of SPIE, vol. **3444**, pp.552-555.

4. S.E. Romaine, J.E. Everett, R.J. Bruni, A. Ivan, P. Gorenstein, M. Ghigo, F. Mazzoleni, O. Citterio, and J. Pedulla, *"Progress in replication of substrates for multilayer coatings"*, in X-ray Optics, Instruments, and Missions, 1998, *Ed.* R.B. Hoover and A.B. Walker, Proceedings of SPIE, vol. **3444**, pp.564-568.

5. A. Ivan, R.J.Bruni, K. Byun, F.E. Christensen, P. Gorenstein, and S.E. Romaine, *"Design and optimization of multilayer coatings for hard x-ray mirrors"*, in X-Ray Optics Design, Performance, and Applications, 1999, *Ed.* A.M. Khounsary, A.K.Freund, T. Ishikawa, G. Srajer, and J. Lang, Proceedings of SPIE, vol. **3773**, pp.107-112.

6. P. Gorenstein, A. Ivan, R.J. Bruni, S.E. Romaine, F. Mazzoleni, G. Pareschi, M. Ghigo, and O. Citterio, *"Integral shell mirrors for the Constellation X-ray mission hard x-ray telescope"*, in X-Ray Optics, Instruments, and Missions IV, 2000, *Ed.* R.B. Hoover and A.B. Walker, Proceedings of SPIE, vol. **4138**, pp.10-15.

7. A. Ivan, R.J. Bruni, K.W. Byun, P. Gorenstein, and S.E.Romaine, *"Hard x-ray multilayers: a study of different material systems"*, in Advances in X-Ray Optics, 2000, *Ed.* A.K.Freund, T. Ishikawa, A.M.Khounsary, D.C. Mancini, and A.G. Michette, Proceedings of SPIE, vol. **4145**, pp.72-79.

8. A. Ivan, R. Bruni, K. Byun, P. Gorenstein, and S. Romaine, *"Optimization of the broadband reflectance of graded multilayers for hard x-ray mirrors"*, in Interfacial Engineering for Optimized Properties II, 2000, *Ed.* C.B. Carter, E.L. Hall, S.R. Nutt, and C.L. Briant, MRS Proceedings, vol. **586**, pp.105-110.

9. S. Romaine, A. Ivan, R. Bruni, F. Christensen, F. Harrison, W. Craig, and P. Gorenstein, *"Multilayer optics for hard X-ray astronomy"*, in X-Ray Optics, Instruments, and Missions IV, 2000, *Ed.* R.B. Hoover and A.B. Walker, Proceedings of SPIE, vol. **4138**, pp.120-125.

10. A. Ivan, R.J. Bruni, S.B. Cenko, P. Gorenstein, and S.E.Romaine, *"High-energy characterization of multilayers for hard x-ray astronomy"*, in X-Ray Optics for Astronomy: Telescopes, Multilayers, Spectrometers, and Missions, 2001, *Ed.* P. Gorenstein and R.B. Hoover, Proceedings of SPIE, vol. **4496**, pp.112-120.

11. A. Ivan, R.J. Bruni, P. Gorenstein, and S.E. Romaine, *"Influence of deposition parameters on the reflectivity of multilayer hard x-ray mirrors"*, in X-Ray Mirrors, Crystals, and Multilayers, 2001, *Ed.* A.K. Freund, T. Ishikawa, and A.M. Khounsary, Proceedings of SPIE, vol. **4501**, pp.142-151.